Urban Flash Flood Modeling Framework Using Weather RADAR and Advanced Geospatial Technologies

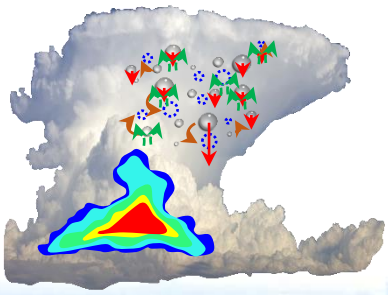

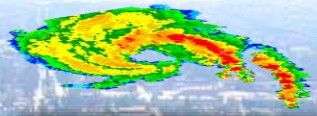

ANJANEYULU AKKIMI

Abstract-TH-2793_156104035

This Page Intentionally Left Blank
Copyright ©Anjaneyulu Akkimi 2021. All Rights Reserved.

Urban Flash Flood Modelling Framework Using Weather RADAR and Advanced Geospatial Technologies

Thesis submitted in partial fulfilment of the requirements for the award of the degree of

Doctor of Philosophy

in

Civil Engineering

by

A ANJANEYULU

with the supervision of

Prof. Subashisa Dutta

Dr. Kamaljit Ray

Department of Civil Engineering
Indian Institute of Technology Guwahati
Guwahati – 781039, Assam, India

October, 2021

Abstract-TH-2793_156104035

Urban Flash Flood Modelling Framework Using Weather RADAR and Advanced Geospatial Technologies

ANJANEYULU AKKIMI



Indian Institute of Technology Guwahati

Department of Civil Engineering, Guwahati, Assam 781039

Abstract-TH-2793_156104035

To

The Nature which creates floods and to Nature which created sapiens who fight against floods

with all my love and respect to

Sushmaa Nagari

Padma Akkimi

Vijayalakshmi T

Paramesh Akkimi

Chikkappa Nagari

Subashisa Dutta

Abstract-TH-2793_156104035

ACKNOWLEDGEMENTS

For some people, Ph.D. is a dream; for some, it is a passion; for others, it is future secure; but for me, it is a miracle. I never imagined this stage would come in my life. This phase in life is beautiful, remarkable, lonely, depressed, and horrible, not for all but most people. Accompanying many people during this phase makes this journey a cheerful, lovely learning process. I cannot express my gratitude with some words putting on a piece of paper for their support, but this is the only opportunity to express myself for their support.

I thank my supervisor, Prof. Subashisa Dutta, for not just supporting me intellectually but also introducing me to many other concurrent works. You underestimated me, understood me, then believed in me and trusted me, and then you treated me as your child. During this process, I learned an infinite number of things from you and under you. People say supervisor is the second parent for us during this process, whether it is true or not I don't know, but for me, I can't express in words the only thing I can say that in my future, whatever healthy grains I will get in my food plate, that is because of you. I extend my deepest gratitude to my other supervisor Dr. Kamljit Ray. You believed and trusted me that I could do this challenging work. You supported me and showed a lot of love in all our meetings. I am very much lucky to meet you in my life and having a co-supervisor. I thank you for all your support and love.

In our early stages of Ph.D., we behave like Einstein in an imaginary world with many dreams and impractical ideas. It is not the supervisor who brings you into the real world. It is our seniors indirectly teach us what reality is. I sincerely express my gratitude towards Dr. Shreedevi Moharana Akka. Just by observing and advice received from akka, I realised that what reality is. I learned from akka the patience required, tackling loneliness, and many other things needed to complete Ph.D. Akka is my emotional and financial supporter during this process. I am lucky to meet you in my early stages of my Ph.D. and being a part of my life. The writing stage of dissertation is horrible and nightmare for those who don't publish a single journal in their Ph.D. period like me. Everyone will be around you, but still, you will feel you are alone in this world during this process. One person came into my life like a storm, supported me emotionally, and guided me throughout this process. I heartfully thank that person.

I am thankful to two friends Vinay and Chandan. Vinay, we travelled 6 years together sharing happiness, sometime quarrels, sometimes discussion on philosophy of life, and sometimes

sitting in silence sharing thoughts, thanks to you for all these memorable moments and for supporting me during my Ph.D. career. Chandan, you are my stress buster by introducing me F1 race, football and lot of discussion about life, thanks to you for taking part in my Ph.D. travel. I want to thank my two seniors Suman and Satish, one for teaching me programming languages and academic support and another man for teaching me kindness and caring of juniors. I am very much thankful to my two junior sisters Amrutha and Aparimita, for including me in their group, caring for me a lot, and supporting me at the end stage of this process when all of my batchmates left me alone. I am thankful to my friend Bhuvana, for her friendly cooperation and togetherness. Thanks to the extended family of my senior Rupashree Panda, friends Suresh and Ashes, and Juniors Ketan, Lasya, Shivani, Nikhil, and lab helper Bazal for their friendly cooperation and togetherness. Thanks to my good friends Nama, Rajeev Gandhi, Bhatlu, Rajesh, Vishnu anna, Vinay Gadi, Viswanth, Venkatesh, Kranthi, Muni and Mukesh for their nice friendship.

Special thanks to Pramila Dutta, Subhalipsa Dutta, and especially Devilipsa Dutta for their love and treating us their family members during festivals and leaving Prof. Dutta to us when we needed. Special thanks to two of my close friends in my life Anand and Nagendra, for their love and support. Thanks to my grandparents and my family, especially my brothers Phani Nagari, Srikanth, and Vishnu, for their love, understanding, and support. The knowledge helped in this period is not just acquired in one day or these 6years; it collected thought of my life from many great teachers. I thank all the teachers who taught me from childhood to this stage, in Jaya Saraswathi School, APRS Lepakshi, Vijaya Krishna Junior College, KSRM college, and finally, IIT Guwahati. Also, I thank AP Govt. for SSC and BTech, Vijaya Krishna Group for Inter, MHRD for BTech, MTech, Ph.D. who supported me financially for providing free education to me. Also, I thank all Civil BTech batches during these 6 years in IIT Guwahati for whom I did TA and final year students whom I guided, for improving my knowledge on water resources subjects by asking difficult doubts and throwing me under bus tyre, which increased my confidence. Finally, I express my sincere thanks to Doctoral Committee members Dr. Sreeja P., Dr. Rishikesh Bharti and Prof. N. Sahoo in IIT Guwahati for their valuable suggestions, eternal encouragement, and timely help provided at various stages.

It is neither acknowledgment nor a tribute. I don't have a word to name this section. This section is for two lovely persons who sacrificed their childhood and education for my education. If they are not in my life, then I would not be here today. I might have ended as a daily wager or street vendor in my life. Those are my two younger brothers ***Akkimi Srikanth*** and ***Akkimi Vishnu***. Whatever I am enjoying all this life is snatched from their life. If really the god does exist, then they are my gods.

Abstract-TH-2793_156104035

DECLARATION

I, **A ANJANEYULU**, author of the Ph. D. thesis "**Urban Flash Flood Modelling Framework Using Weather RADAR and Advanced Geospatial Technologies**" would like to certify that

- The work presented in this thesis is original research work carried out by me.
- The research work has not been submitted for any degree or diploma or any other qualification either in this institute or in any other university.
- Whenever I have used resources [theory, concepts, texts, data, graphs, figures or any other similar nature] from other sources, a due credit by citing in the text of the thesis is clearly made.
- The work presented here is free from plagiarism to the best of my knowledge, and I take the responsibility for any issues.
- I also affirm that thesis supervisor is not responsible for any possible instance of plagiarism within this submitted work.



Date: 21-10-2021 A ANJANEYULU

Place: Guwahati [156104035]

Indian Institute of Technology Guwahati

Department of Civil Engineering, Guwahati, Assam 781039

Dr. Subashisa Dutta
Professor
Indian Institute of Technology Guwahati
Email: subashisa@iitg.ac.in
Phone: +91 361 258 2415

Dr. Kamaljit Ray
Scientist-G
Ministry of Earth Sciences
Email: raykamaljit@iitg.ac.in
Phone: +91 112 466 9514

Certificate

This is to certify that thesis entitled "**Urban Flash Flood Modelling Framework Using Weather RADAR and Advanced Geospatial Technologies**" submitted by **A ANJANEYULU**, in partial fulfilment of the requirements for the award of degree of Doctor of Philosophy, to Indian Institute of Technology Guwahati, Assam, India, is a record of the bonafide research work carried out by him under my guidance and supervision at the Department of Civil Engineering, Indian Institute of Technology Guwahati, Assam, India. To the best of my knowledge, no part of the work reported in this thesis has been presented for the ward of any degree at any other institution.

Date: 21-10-2021
Place: Guwahati

Prof. Subashisa Dutta

Date: 21-10-2021
Place: New Delhi

Dr. Kamaljit Ray

ABSTRACT

The urban landscape is one of the sensitive and drastically changing ecosystems on the earth. Throughout our civilizations, urban settlements were built proximate to water bodies such as rivers and seas. The urban landscapes also experience short time spatial scale modifications by anthropogenic activities. The change in urban morphology influences each component of meteorological and hydrological processes. It also alters the landscape's topography, which leads to change in natural and artificial drainage patterns. Precipitation is one such drastically changing variable in urban regions. In recent, the frequency of high intensity of precipitation has increased. The combined effect of rapidly changing precipitation, topography, and other hydrometeorological variables creates flash flood situations in urban regions. These variabilities also create uncertainty in urban hydrological modeling due to the representation of rapidly changing variables into the model is a challenging task. The acquiring of all these variables, such as in-advance precipitation prediction, high-resolution topography, and urban clusters, is quite complex. These variables are essential for flash flood forecasting in the urban landscape. This thesis aims to work on acquiring, understanding, finding alternatives, and incorporating these variables in a distributed urban hydrological model.

The capturing of heterogeneous convective precipitation at high spatio-temporal resolution is needed for modeling the flash flood events in an urban watershed. The Doppler Weather Radar is a powerful tool that captures all storm events at finer spatial and temporal scales where the traditional and satellite modes of measurements are insufficient. The radar rainfall is an indirect measurement derived from the measured radar reflectivity. The radar reflectivity - rainfall rate (Z-R) relationship is helpful to convert measured reflectivity into rainfall rates. The relationship is a simple empirical power law. The relationship varies with the region, storm event, ecological zone, and type of Radar. Several methodologies have been developed to establish the relationship. However, the synchronization of reflectivity and rainfall rate pairs still a challenging task for radar meteorologists. Moreover, the conversion process is subject to multiple sources of errors due to its indirect measurement. The present work introduces a Gravity – Turbulence physical based principle to synchronize the reflectivity and rainfall pairs. The proposed technique selects the reflectivity value in the vertical column of the radar scan based on spectral width thresholds. The spectral width thresholds were selected where the gravitational force on the raindrop dominates the turbulence or shear force. The proposed method identifies the appropriate radar pixel over a point rain gauge to accurately synchronize the pairs. The relationship developed using the proposed technique was compared with the existing parametric relationships such as Marshall-Palmer, TMM method, and nonparametric

Abstract-TH-2793_156104035

methods PMM and WPMM. The proposed method showed better performance than all other methods, with an error of 16% for overall storms, 12% for stratiform storms, and 18% for convective storms.

In-advance precipitation nowcasting during mesoscale convective events is essential to forecast flash floods in urban regions. Several methodologies developed includes optical flow techniques to neural network schemes. Most of the techniques focus on tracking the storm cells, and a few focuses on quantitative precipitation nowcast. They also lack in the prediction of storm growth and dispersion quantitatively during high-intensity rainfall events. This work aims to predict the mesoscale convective storm events, which produce high-intensity rainfall. The proposed technique also identifies the storm growth and dissipation stages. The prediction of high-intensity rainfall is attempted in terms of hyetograph instead of storm cell image level. A hierarchical supervised machine learning approach is developed to generate and predict the high-intensity rainfall hyetograph. The training parameters are generated stochastically with the historical datasets. The hyetograph is broken down into two segments: "Atmospheric Wave" and "Turbulence Wave." The waves are fitted with the Maxwell approximation equation then the model fitted parameters were generated. The interdependency established between all variables with each other using Cholesky decomposition factorization. The rainfall hyetograph predicted using a hierarchical random forest machine learning approach by taking an initial 30min assimilation window for training the data. The ensembles are generated and compared with the observed data. It showed that the model has well predicted the rainfall hyetograph with its growth and dissipation.

In urban settings, from street flooding to flash flood modeling, a high-resolution topography model is needed. However, it is always not possible to acquire high-resolution datasets for both developing and developed nations. It creates interest to explore open-source medium resolution elevation models for flood studies. Several research studies have been carried out in this direction. However, no such studies are identified for urban flooding. This work aims to design an assessment framework that includes statistical assessment and a zero-dimension hydrological model. A new approach based on non-dimensional angle and percentile distances of storage-elevation (zero-dimension) is included in the proposed assessment framework. The open-source elevation models were compared with field survey data using the proposed assessment framework. The designed assessment framework comprises descriptive statistics of elevations and slopes, contour lines and lengths, and a zero-dimension model. The vertical accuracy of open-source datasets with field surveyed data also computed in urban settings. The selected open-source digital elevation models provided vertical accuracy around 6m (LE90), while the ALOS AW3D model showed around 4m linear error. It is observed that ASTER global model is infused with complete noise. The results showed the potential capability of the ALOS

Abstract-TH-2793_156104035

AW3D model in the urban regions for flood modeling. The results also revealed that the elevation model, which includes few surface features such as buildings and roads, is needed than a complete bare-earth product for urban flood modeling.

In many urban hydrological models, the topography data has been used to identify the urban watershed boundary, extract the natural urban fluvial networks, overland flow paths, rim elevation for natural and artificial urban drainage networks, and terrain depressions/ponds. These are essential inputs extracted from the topographic model to reliably model the pluvial flooding in urban areas using the 1D hydrological model. The modeling outputs dependent on the resolution and source of digital elevation models (DEM). This work aims to identify the influence of digital elevation models, both high and medium resolution, on the 1D urban hydrological model. The Storm Water Management Model (SWMM) was used instead of any 2D hydrological model due to its widespread application in urban flood modeling. The results showed that the SWMM model is insensitive to DEM product type and its resolution for flood depths, peaks, and hydrograph prediction. However, it showed a high sensitivity in flood inundation extent prediction and mapping. It showed that the global DEMs and national DEMs both failed to quantify the flood inundation area outputs in 1D SWMM simulation, which showed significant errors with poor skill score of CSI (<0.4) and other binary metrics (skill scores). However, the ALOS AW3D elevation model performed better than all other global DEMs.

Several hydrological models have been developed to model the urban flood. Most of the studies focus on a local (street) scale with dense drainage datasets. These models predict sewer surcharge induced surface flooding using loosely or tightly coupled 1D/1D or 1D/2D drainage and surface flow models instead of direct surface water flooding. Moreover, surface water flood modeling at the city scale during flash floods is challenging due to a range of factors and the availability of input data. This work aims to design the distributed urban hydrological model, which includes all critical hydrological processes and surface flow routing. The proposed model works at street scale to city scale by incorporating heterogeneous precipitation measured with weather radar during an extreme event. This approach was applied to model an extreme storm event that occurred on 13 August 2014 in the highly urbanized Vally Stream, New York, USA. The results suggest that the model is able to capture the broad patterns of an inundated area at the city-scale and discharge hydrograph at the outlet of a watershed with NSE 0.9 and coefficient of determination 0.83. The sensitivity analysis reveals that the model is sensitive to low surface roughness values and hydraulic conductivity. The model also shows insensitivity to higher surface roughness (Vegetation and Urban cover).

Abstract-TH-2793_156104035

CONTENTS

Abstract i

List of Figures x

List of Tables xv

List of Symbols xvii

List of Abbreviations xix

1 INTRODUCTION

1.1 Overview 2

1.2 Role of Advanced Geo-Spatial Technologies in Urban Flash Flood Modeling 4

1.2.1 Precipitation 4

1.2.2 Topography 7

1.2.3 Imperviousness Factor (Impervious Area) 7

1.2.4 Drainage Network (Drain Discharge capacity) 8

1.2.5 Distributed Urban Hydrological Modeling 8

1.3 Research Aims 9

1.4 Structure of the Thesis 10

2 REVIEW OF LITERATURE

2.1 Introduction 14

2.2 Urban Flood Modeling 15

2.2.1 One Dimensional Models (1D) 16

2.2.2 Two Dimensional Models (2D) 16

2.2.3 1D – 1D Models 16

2.2.4 1D – 2D Models 17

Abstract-TH-2793_156104035

2.3 Weather Radar Rainfall 21
2.4 Topographic Data for Urban Floods 25
2.5 Summary 29

3 RADAR REFLECTIVITY RAINFALL RATE RELATIONSHIP

3.1 Introduction 32
3.2 Study Area, Data Collection, and Analysis 34
3.2.1 Study Area Description 34
3.2.2 Weather Radar Data and Processing 35
3.2.3 Rain Gauge Measured Rainfall Data 36
3.3 Methodology 38
3.3.1 Parametric Z-R Relationship (Traditional Matching Method, TMM) 40
3.3.2 Gravity-Turbulence Based Proposed Approach (Parametric Relation) 41
3.3.2.1 Physical Principle 41
3.3.2.2 Gravity –Turbulence based approach application 42
3.3.3 Nonparametric Z-R Relationship (Probability Matching Method, PMM) 43
3.3.4 Nonparametric (Window Probability Matching Method, WPMM) 43
3.3.5 Performance Evaluation 44
3.4 Results and Discussion 44
3.4.1 Gravity – Turbulence based Z – R Relationships 44
3.4.2 Probability Matching Method based synchronized pairs 47
3.4.3 Window Probability Matching Method based synchronized pairs 49
3.4.4 Accuracy Assessment (Evaluation) and Comparison 51
3.5 Conclusions 52

Abstract-TH-2793_156104035

4 REFLECTIVITY HYETOGRAPH PREDICTION

4.1 Introduction . . . 56

4.2 Methodology . . . 60

4.2.1 Hierarchical Machine Learning Approach . . . 60

4.2.2 Storm Reflectivity Hyetograph Analysis . . . 61

4.2.3 Storm Reflectivity Hyetograph Approximation . . . 62

4.2.4 Model Parameters and Variables . . . 66

4.2.5 Performance Evaluation . . . 66

4.3 Study Site, Data Description, and Processing . . . 66

4.3.1 Regional Setting . . . 66

4.3.2 Data Description . . . 67

4.3.3 Data Pre-Processing . . . 68

4.3.4 Reflectivity Hyetographs Abstraction . . . 68

4.4 Results and Discussion . . . 70

4.4.1 Analysis of Reflectivity Hyetograph Parameters . . . 70

4.4.2 Decomposition of Random Variables and Parameters . . . 72

4.4.2.1 Interdependency between random variables . . . 72

4.4.2.2 Probability distribution function for lifts . . . 73

4.4.2.3 Regression between depended variables . . . 75

4.4.2.4 Decomposition of Non-linear interdependent random variables . . . 75

4.4.3 Performance Evaluation of Generated Hyetographs . . . 76

4.4.4 Prediction of Storm Hyetograph . . . 79

4.5 Conclusions . . . 81

5 ASSESSMENT OF OPEN-SOURCE DEMS

5.1 Introduction . . . 84

5.2 Study Area and Data Description . . . 87

Abstract-TH-2793_156104035

5.2.1 Study Areas . . . 87
5.2.2 Datasets Description . . . 89
5.2.3 Software and Data Availability . . . 90
5.2.4 Data Pre-Processing . . . 90
5.3 Methodology . . . 91
5.3.1 Descriptive Statistics Assessment Approach . . . 91
5.3.2 Flood Inundation Assessment Approach . . . 94
5.4 Results and Discussion . . . 96
5.4.1 Descriptive Statistics of Elevation Values . . . 96
5.4.2 Descriptive Statistics of Land Slopes . . . 98
5.4.3 Analysis of Contour Lines and Lengths . . . 100
5.4.4 Analysis of DEMs of Difference (DoDs) . . . 102
5.4.5 Zero Dimension Hydrological Model . . . 108
5.4.6 Overall Assessment and Limitations . . . 110
5.5 Conclusions . . . 113

6 INFLUENCE OF DEMs ON SWMM MODEL

6.1 Introduction . . . 116
6.2 Study Area and Data Description . . . 118
6.3 Methodology . . . 118
6.4 Results and Discussion . . . 121
6.4.1 SWMM Simulated Flood Inundation Depths . . . 121
6.4.2 SWMM Simulated Flood Peaks . . . 123
6.4.3 SWMM Simulated Inflow at Outlet . . . 125
6.4.4 Flood Inundation Extents . . . 126
6.4.5 Overall Assessment . . . 128
6.5 Conclusions . . . 129

Abstract-TH-2793_156104035

7 DISTRIBUTED URBAN HYDROLOGICAL MODEL

7.1 Introduction . . . 132

7.2 Model Description . . . 134

7.2.1 Precipitation Model . . . 135

7.2.2 Evapotranspiration Model . . . 135

7.2.3 Infiltration Model . . . 136

7.2.4 Surface Flow Routing . . . 137

7.2.5 Impervious Area/ Impervious Factor (IMPF) . . . 139

7.2.6 Manning's Roughness Coefficient . . . 139

7.2.7 Soil Properties . . . 140

7.2.8 Drainage Capacity . . . 140

7.2.9 Boundary Conditions . . . 141

7.3 Model Application: Case Study and Datasets . . . 141

7.3.1 Study Site . . . 141

7.3.2 Datasets Description . . . 144

7.3.2.1 Topography data . . . 144

7.3.2.2 Discharge data . . . 144

7.3.2.3 Precipitation data . . . 146

7.3.2.4 Orthoimagery . . . 147

7.3.2.5 Soil data . . . 147

7.3.2.6 Drainage Capacity . . . 148

7.3.2.7 Evapotranspiration . . . 148

7.3.3 Derived Parameters . . . 148

7.3.3.1 Land Use and Land Cover classes . . . 148

7.3.3.2 Impervious Factor and Manning's n . . . 149

7.3.3.3 Soil infiltration parameters . . . 149

7.3.4 Model Calibration, Sensitivity and Evaluation . . . 150

Abstract-TH-2793_156104035

7.3.4.1 Sensitivity to roughness values . . . 150
7.3.4.2 Sensitivity to hydraulic conductivity (Calibration) . . 150
7.3.4.3 Evaluation . . . 150
7.4 Results and Discussion . . . 151
7.4.1 Sensitivity to Roughness Parameterisation . . . 151
7.4.2 Sensitivity and Calibration to Hydraulic Conductivity . . . 156
7.4.3 Evaluation of Model Prediction . . . 159
7.4.4 Time Series of Flow Depths . . . 160
7.5 Conclusions . . . 162

8 SUMMARY AND FUTURE SCOPE

8.1 Summary . . . 166
8.1.1 Radar Reflectivity Rainfall Rate Relationship . . . 166
8.1.2 Reflectivity Hyetograph Prediction . . . 167
8.1.3 Assessment of Open-Source DEMs . . . 168
8.1.4 Influence of DEMs on SWMM Model . . . 170
8.1.5 Distributed Urban Hydrological Model . . . 171
8.2 Recommendations for Future Research . . . 172

References . . . 175
Appendix A: Radar Reflectivity Rainfall Rate Relationship
Appendix B: Reflectivity Hyetograph Prediction
Appendix C: Assessment of Open-Source Dems
Appendix D: Influence of DEMs on SWMM Model
Appendix E: Distributed Urban Hydrological Model

Abstract-TH-2793_156104035

LIST OF FIGURES

1.1 Forms of precipitation and cause of heterogenous precipitation and local scale high intensity precipitation in Urban landscapes 3

1.2 Potential of advanced geo-spatial technologies and its applications in the field of urban flood studies 5

1.3 Modes of measurement of precipitation; 1) rain gauges (recorded, non-recorded); 2) satellite measurement; and 3) doppler weather radars 6

2.1 Schematic figure to explain 1D, 2D, 1D-1D and 1D-2D model concepts 15

2.2 PPI and RHI of Vishakapatnam, India during Hudhud tropical cyclone (Source: India Meteorological Department) 22

3.1 Selected study site with a radar coverage over the region, and Automatic Weather Stations with in study region maintained by IMD Mausam Bhawan, New Delhi, with a topography. 34

3.2 Monthly rainfall observed during the year 2013 over a study area with in the radar coverage of 100km 37

3.3 Total rainfall amount at all AWS stations observed during the year of 2013, based climate zones 37

3.4 The methodological flow chart adopted to establish radar reflectivity – rainfall rate relationship and its validation 39

3.5 (a) Traditional one to one matching of rain gauge to radar pixel to establish parametric power-law relation; (b) probability cumulative distribution wise matching for a particular rain gauge – radar pixel extracted values to establish nonparametric relationship 40

3.6 Conceptual sketch of Gravity-Turbulence based proposed approach and gravity – Turbulence forces acting on a raindrop within control volume 42

3.7 The concept of window probability matching method by cumulative distribution wise matching for a particular rain gauge at 3km × 3km window radar pixel extracted values to establish nonparametric relationship 43

3.8 Scatterplots and power-law regression fits of radar reflectivity – rainfall rate relationship for formulated scenarios: a) Traditional Matching Method; b) Traditional Matching Method considering spectral width threshold; c) Traditional Matching Method in humid subtropical climate zone; d) Traditional Matching Method considering spectral width threshold in humid subtropical climate zone; e) Traditional Matching Method in semi-arid climate zone; f) Traditional Matching Method considering spectral width threshold in semi-arid climate zone 46

Abstract-TH-2793_156104035

3.9 Scatterplots and power-law regression fits of radar reflectivity – rainfall rate relationship by Traditional Matching Method by considering all rainfall event days (Table 3.2) 47

3.10 The probability pairs (cumulative distribution functions) generated for both rainfall rate (threshold 1mm/hr.) and reflectivity (threshold 15dBZ) at point rain gauge to single radar pixel for probability matching method by considering all rainfall event days 48

3.11 Power-law regression fits of radar reflectivity – rainfall rate relationship established with a value extracted from PMM probability percentiles: a) For < 30dBZ (stratiform); b) 30-40dBZ (convective); c) >40dBZ (convective); d) Synchronized pair curve established with PMM method 49

3.12 The probability pairs (cumulative distribution functions) generated for both rainfall rate (threshold 1mm/hr.) and reflectivity (threshold 15dBZ) at point rain gauge to single radar pixel for window probability matching method by considering all rainfall event days 50

3.13 Power-law regression fits of radar reflectivity – rainfall rate relationship established with a value extracted from WPMM probability percentiles: a) For < 30dBZ (stratiform); b) 30-40dBZ (convective); c) >40dBZ (convective); d) Synchronized pair curve established with PMM method 50

4.1 Architecture of proposed hierarchical machine learning approach to synthesis and predict high intensity storm hyetograph 60

4.2 Typical storm reflectivity hyetograph comprising atmospheric response and turbulence fluctuations 62

4.3 Conceptual illustration of data preprocessing, analysis, approximation, generation and prediction of reflectivity hyetograph 64

4.4 Radar coverage over the India region by IMD operational radar network, the location and coverage (250 km) of radar over Mausam Bhawan, New Delhi, with topography 67

4.5 Radar data preprocessing (a) Raw data, (b) after removing less than 15dBZ reflectivity values, (c) Wiener filter application, processed with a 3×3-pixel Wiener filter and (d) storm cell boundary detection using Log of Gaussian (LoG) technique 69

4.6 Turbulence wave fluctuations in a reflectivity hyetograph depends on storm duration; (a) no waves if duration less than 80min, (b) 3 waves if duration is in between 90 and 130, (c) 4 waves if duration is in between 140 and 190, and (d) 5 waves if duration is in between 200 and 360 min 70

4.7 Circos plots to visualize dominant interdependency between each random variable with; a) Pearson rank coefficient of determination (linear); b) Spearman rank coefficient of determination (Non-linear) 73

4.8 cumulative Probability distribution functions for: (a) for atmospheric lift; (b) First turbulence wave lift; (c) Second turbulence wave lift; (d) Third turbulence wave lift; (e) Fourth turbulence wave lift; and (f) Fifth turbulence wave lift (numerical values within the brackets indicates Chi-square statistic value, significant at p<0.05 and p>0.95) 74

Abstract-TH-2793_156104035

4.9 Lower triangular matrices for: (a) Spearman Rank Correlation Coefficient; (b) Cholesky factorization matrix for Spearman correlation; (c) Covariance matrix; (d) Cholesky factorization matrix with covariance matrix 76

4.10 Error Analysis of hyetograph tail ends at each time step using percentage, squared, absolute, relative and scaled accuracy measures for 310min storm hyetographs (for other storm durations provided in Appendix B) 78

4.11 Predicted storm hyetograph at different storm duration (a) 6 August 2013(70min), (b) 5 August 2015(120min), (c) 20 August 2012(120min) and (d) 22 July 2013(310min) [line with triangles represents the predicted ensemble median storm hyetograph] 80

5.1 Shaded relief images of study areas with indication of places considered (Shaded relief illumination prepared with ALOS AW3D 30 data, at 315°N, 20° above the origin) 87

5.2 Shaded relief images of the Simi Valley urban settings (Fig.5.1A), the level of features depicted by A) Airborne image; B) Sentinel-2A image; C) LIDAR (1ft); D) NED (10m); E) ALOS (12.5m); F) ALOS AW3D (30m); G) NED (30m); H) ASTER (30m); I) SRTM (30m) . 89

5.3 Framework followed for assessment of digital elevation models and selection criteria of suitable DEM for urban flood modeling 92

5.4 Conceptual sketch which depicts the hypothetical urban catchments, their storage-elevation curves, normalized angle-percentile distance parameters and catchment classification graph 95

5.5 Frequency distributions of all selected DEMs at A) Simi Valley; B) New Delhi; C) Riom; D) Bangalore; E) Guwahati and F) Jorhat 97

5.6 Frequency distributions of all selected DEM slopes at A) Simi Valley; B) New Delhi; C) Riom; D) Bangalore; E) Guwahati and F) Jorhat 99

5.7 Slope values at Simi Valley corresponding to building edges or stream traces for a) surveyed data; b) ALOS AW3D; c) NED 10 m and contour characteristics at all study areas d) cumulative total of contour lengths; e) cumulative total of contour count; f) ratio between cumulative contour length to contour count 101

5.8 Difference between surveyed and other DEMs their errors. A) Dem of Differences (Surveyed–ALOS AW3D); B) Dem of Differences (Surveyed–NED 10m); C) Topographic profile from NW to SE; D) Errors/ accuracy metrics at all study areas for all DEMs 103

5.9 At Simi Valley watershed, A) Dem of Differences (Surveyed–ALOS AW3D); B) scatterplot of ALOS AW3D 30m aspect versus deviations from field surveyed; C) Dem of Differences (Surveyed–SRTM); D) scatterplot of SRTM 30m aspect versus deviations from field surveyed; E) Landsat images of October 1995, August 2002, June 2009, October 2018, satellite imagery ©Landsat/Copernicus powered by Google Earth 106

5.10 At Ashok Vihar, New Delhi watershed, A) Dem of Differences (Surveyed–ALOS AW3D); B) Dem of Differences (Surveyed–CARTOSAT); C) Dem of Differences (Surveyed–ALOS PALSAR); D) Dem of Differences (Surveyed–SRTM); E) Landsat images of May 2000, September 2006, October 2010, August 2014, satellite imagery ©Landsat/Copernicus powered by Google Earth 107

Abstract-TH-2793_156104035

5.11 The results of angle and percentile distance parameters estimated from storage-elevation curves: A) S-E curve at Simi Valley; B) Normalized SE curve; C) scatter plot between angle and h_{50}; D) scatter plot between angle and h_{25}; D) scatter plot between angle and h_{75} 109

6.1 Flow outline followed to setup and simulate SWMM model for assessment of influence of DEMs on SWMM model 119

6.2 Box-and-Whisker plots of SWMM model simulated inundation depths at all study areas for different Digital Elevation Models 122

6.3 Error diagram (RMSE vs STDE) of SWMM model simulated inundation depths at all study areas for different Digital Elevation Models relative to field surveyed data 122

6.4 Peaks at outlet and Mean Error with respect to field surveyed data plots of SWMM model simulated outputs at all study areas for different Digital Elevation Models 123

6.5 Error diagram (MAE vs RMSE) of SWMM model simulated flood peaks at all study areas for different Digital Elevation Models relative to field surveyed data 124

6.6 Inflow hydrograph its %error for each DEM with reference to field surveyed data at Simi Valley urban watershed 125

6.7 SWMM Modeled flood inundation extent maps at Simi Valley, USA for the DEMs, a) Surveyed; b) NED; c) ALOS AW3D; d) ALOS PALSAR; e) ASTER and f) SRTM 127

7.1 Generalized urban hydrological cycle and framework of the PURAHM model 134

7.2 (a) Shaded relief images of the USA with identified study area; (b) Topography of the watershed (LiDAR 1m); (c) Orthoimagery of the watershed (0.6m); and (d) watershed boundary with streams, sub watersheds and outlet (Discharge measuring site location) . . . 142

7.3 (a) Identification of cells falls inside boundary as 1 and outside boundary as 0; (b) LULC classes (0.6m); (c) Soil classes; (d) Slopes map (1m); (e) Manning's roughness, n (0.6m); (f) Impervious factor (0,1) (0.6m); (g) Hydraulic Conductivity (1m); (h) Suction Head (1m); and (i) Initial Soil Moisture deficit (1m) 143

7.4 Flow hydrograph data observed at outlet by USGS, (a) Discharge of 10year records and selected peak event discharge during August 2014; and (b) Gauge height measured at outlet of last 10 years and selected peak event gauge height during August 2014 145

7.5 Rainfall hyetograph of average amount of four stations (JFK, NY city, Lagaurdia, and Farmingadale) during the period of 13 August, 2014 (EST time zone) used in the model . . 146

7.6 Sensitivity analysis of the model simulated flood depth to surface roughness Parameterisation 152

7.7 Sensitivity analysis of the model simulated runoff at outlet to surface roughness Parameterisation 152

7.8 Sensitivity analysis of the model simulated flood depth to surface roughness Parameterisation, while keeping hydraulic conductivity (K_s) to 0.66 *cm/h* 154

Abstract-TH-2793_156104035

7.9 Sensitivity analysis of the model simulated runoff at outlet to surface roughness Parameterisation, while keeping hydraulic conductivity (K_s) to 0.66 *cm/h* 154

7.10 Sensitivity analysis of the model simulated flood depth to hydraulic conductivity 156

7.11 Sensitivity analysis of the model simulated runoff at outlet to hydraulic conductivity 157

7.12 Sensitivity analysis of the model simulated infiltration depths to hydraulic conductivity . . 157

7.13 Comparison between the model simulated and observed flow discharge at outlet during the period of peak flood occurred on 13-08-2014 (EST Time zone) 159

7.14 Performance Comparison of simulated flow with observed flow measured at outlet gauge station using error metrics RMSE, NSE and PCC during the period of peak flood occurred on 13-08-2014 (EST Time zone) 160

7.15 The predicted water depths in the Valley Stream watershed during the extreme storm event occurred on 13 August,2014 (EST Time zone) 161

Abstract-TH-2793_156104035

LIST OF TABLES

2.1 Modeling approaches developed for urban flood simulation for small city scale applications (part of this taken from Salvador et al. [2015]) . . . 18

2.2 Various Radar Reflectivity (Z) – Rainfall Rate (R) (Z = ARb) relationships for different storm types (taken from Kim et al. [2021]) . . . 22

2.3 Radar Reflectivity Rainfall Rate relationships developed for various regions (Part of it taken form Pattani [2010]) . . . 23

2.4 Major algorithms/techniques developed to track convective cells and Nowcast the high intensity of convective rainfall . . . 24

2.5 Summary characteristics on major open-source and commercial DEMs available in the world . . . 26

3.1 General Characteristics of C-band Doppler Weather Radar considered for the study . . . 35

3.2 Weather radar reflectivity data collected periods to establish relationship and for validation 36

3.3 Parameters A and B in radar reflectivity and rainfall rate relationship (eq.3.1) for different scenarios considered based on two ecological zones . . . 45

3.4 Parameters A and B in reflectivity and rainfall rate relationship (eq.3.1) computed from nonparametric synchronized pairs for different storm types by PMM and WPMM . . . 48

3.5 Pearson's r of Z – R pairs for different storm categories for PMM and WPMM methods. . . 48

3.6 Error metrics Mean Absolute Percentage Error (MAPE) computed for each method . . . 51

3.7 Error metrics Root Mean Square Error (RMSE) computed for each method . . . 51

4.1 Brief description of considered variables and model parameters in the Maxwell approximation for storm hyetographs . . . 65

4.2 Range of parameters for Turbulence waves and atmospheric response (wave) . . . 71

4.3 Linear regression equations between highly interdependent variables . . . 75

4.4 Statistical error metrics to evaluate performance of generated hyetographs (the detailed table provided in supplementary file) . . . 77

5.1 Selected study areas and their characteristics . . . 88

5.2 Error Metrics (Vertical Accuracy) compared to field surveyed data including at all urban settings. LE90: Linear error at 90%; RMSE: Root Mean Square Error (Detailed Error Metrics provided in Appendix C) . . . 105

Abstract-TH-2793_156104035

5.3 Cognizable capacity of DEMs towards urban flood modeling (all are relative to field surveyed data). (Detailed rating scores are provided in Appendix C) 112

6.1 Input datasets used for 1D urban hydrological model SWMM simulation 120

6.2 Binary metrics (Sill Scores) computed for each DEM at Simi Valley watershed 126

7.1 The broad categories of perviousness of land use and land cover classes and its impervious factors incorporated in the model (detailed subclasses provided in Appendix E) 139

7.2 The Manning's roughness values incorporated in PURAHM model for broad categories of land use and land cover classes (detailed subclasses provided in Appendix E). 140

7.3 The Soil types its map units (Figure 7.3(c)), area and percentage of occupied area by soil class (detailed soil properties provided in Appendix E) 147

7.4 Soil class based on map classes and assigned infiltration parameters by model. 149

7.5 Percentage of difference between peaks and RMSE for varying surface roughness parameters in terms of flow depth (m) and flow rate (m3/s) (reference to n = 0.001), while keeping all other parameters to field conditions 153

7.6 Percentage of difference between peaks and RMSE for varying surface roughness parameters in terms of flow depth (m) and flow rate (m3/s) (reference to n = 0.001), while keeping hydraulic conductivity Ks = 0.66 cm/h (Note: Flow rate value at n = 0.001 is ~33 m3/s) 155

7.7 Error metrics computed for model outputs at varying hydraulic conductivity values with reference to hydraulic conductivity Ks = 0.005, while keeping all parameters to field observed values 157

Abstract-TH-2793_156104035

LIST OF SYMBOLS

Symbol	Description
α	Angle with elevation axis
C_r	Courant number
D	Diameter of raindrop
D	Duration of storm event
dBZ	Radar reflectivity in decibel
$\overline{E_p}$	Mean daily potential evapotranspiration
E_p	Evapotranspiration
F	Cumulative infiltration depth
F_t	Cumulative infiltration depth at current time step t
$F_{t+\Delta t}$	Cumulative infiltration depth at next time step t+Δt
$F^{<3>}$	Score to penalize under prediction
$F^{<4>}$	Score to penalize over prediction.
f_p	Potential infiltration rate
g	Acceleration due to gravity
h_{25}	Distance from storage axis at 25 percentiles
h_{50}	Distance from storage axis at 50 percentiles
h_{75}	Distance from storage axis at 75 percentiles
K_s	Hydraulic conductivity
k_a, k_t^i	Model parameters which depends on the peak time
N(D)	Number of raindrops per unit volume
n	Manning's roughness coefficient
P(R)	Probability density function of gauge measured rainfall intensities
P(Z)	Probability density function of reflectivity
Q	Discharge
R	Rainfall rate (mm/hr)
R_i	Minimum threshold value of rainfall rate
r_a, r_t^i	Model parameters which depends on the duration of the storm
r_M	Modified correlation index
t	Base time of storm
t_D^o	Normalized unit duration
t_o^i	Time of occurrence of ith wave

Abstract-TH-2793_156104035

t_r^i	Time of response of ith wave
W	Spectral Width
Z	Radar reflectivity factor (mm^6/m^3)
Z_a	Lift of atmospheric response (atmospheric lift)
Z_i	minimum threshold value of reflectivity (or Initial Reflectivity)
$Z_a(t)$	Height of atmospheric wave
$Z^i(t)$	Height of ith turbulence wave (fluctuation)
Z_t^i	Amplitude of the ith turbulence wave

भारतीय प्रौद्योगिकी संस्थान गुवाहाटी • Indian Institute of Technology Guwahati •

Abstract-TH-2793_156104035

LIST OF ABBREVIATIONS

Terms	Abbreviations
ALOS	Advanced Land Observing Satellite
ASTER	Advanced Spaceborne Thermal and Emission and Reflection Radiometer
AWS	Automatic Weather Station
CAPPI	Constant Altitude Plan Position Indicator
CAPS	Center for Analysis and Prediction of Storms
CDF	Cumulative Distribution Function
CE	Circular Error
CFL	Courant-Freidrichs-Levy
CNN	Convolution Neural Network
COTREC	Continuity of TREC vectors
CRPS	Continuous Ranked Probability Score
CSI	Critical Success Index
DEM	Digital Elevation Model
DoD	Difference of Depths
DSD	Drop Size Distribution
DSM	Digital Surface Model
DTM	Digital Terrain Model
DWR	Doppler Weather Radar
EIA	Effective Impervious Area
EPA	Environmental Protection Agency
EU-DEM	European Digital Elevation Model
gof	goodness of fit
GMRAE	Geometric Mean Relative Absolute Error
IfSAR	Interferometric Synthetic Aperture Radar Sensor
IMD	India Meteorological Department
IMPF	Impervious Factor
ISRO	Indian Space Research Organization
JAXA	Japan Aerospace Exploration Agency
JWD	Joss – Waldovogel Distrometer

Abstract-TH-2793_156104035

LE	Linear Error
LiDAR	Light Detection and Ranging
LoG	Log of the Gaussian
LSTM	Long Short Term Memory
LULC	Land Use and Land Cover
MAE	Mean Absolute Error
MAPE	Mean Absolute Percentage Error
MAPLE	McGill Algorithm for Precipitation Nowcasting by Lagrangian Extrapolation
MASE	Mean Absolute Scaled Error
ME	Mean Error
MRMSE	Mean of ensemble Root Mean Squared Error
NAIP	National Agriculture Imagery Program
NASA	National Aeronautics Space Administration
NED	National Elevation Dataset
NOAA	National Oceanic and Atmospheric Administration
NRCS	Natural Resources Conservation Service
NSE	Nash-Sutcliffe Efficiency
NWP	Numerical Weather Prediction
PALSAR	Phased Array type L-band Synthetic Aperture Radar
PARSIVEL	Particle Size and Velocity Distribution
PCC	Pearson Correlation Coefficient
PDF	Probability Distribution Function
PMM	Probability Matching Method
PPI	Plan Position Indicator
PRISM	Panchromatic Remote-sensing Instrument for Stereo Mapping
PURAHM	Physically based Urban Runoff Accounting Hydrological Model
QPE	Quantitative Precipitation Estimation
QPF	Quantitative Precipitation Forecast
QPN	Quantitative Precipitation Nowcast
RADAR	Radio Detection and Ranging
RC	Reflectivity Core
RHI	Range Height Indicator
RMSE	Root Mean Square Error
SCIT	Storm Cell Identification and Tracking

Abstract-TH-2793_156104035

S-PROG	Spectral Prognosis
sMPAE	symmetric Mean Absolute Percentage Error
SRTM	Shuttle Radar Topography Mission
STDE	Standard Deviation Error
STEPS	Short Term Ensemble Prediction System
SVM	Support Vector Machine
SWMM	Storm Water Management Model
TIA	Total Impervious Area
TITAN	Thunderstorm Identification, Tracking, Analysis, and Nowcast
TMM	Traditional Matching Method
TWI	Topographic Wetness Index
TREC	Tracing of Radar Echoes by Correlation
USDA	U.S. Department of Agriculture
USGS	United States Geological Survey
WPMM	Window Probability Matching Method

Abstract-TH-2793_156104035

This Page Intentionally Left Blank

Abstract-TH-2793_156104035

1

INTRODUCTION

Abstract-TH-2793_156104035

1.1 OVERVIEW

Humans tried to settle as an urban conglomerate proximate to large water bodies such as rivers and coastal belts throughout the civilizations [Seyoum, 2013]. For example, ancient civilization such as Mesopotamia (Tigris–Euphrates River system), Mayan (Coastal), Egyptian (Nile River), Harappan (Indus Valley), Yellow River and modern cities such as New York (Hudson River, Coastal), London (Thames, North Sea), Paris (English Channel), Bombay (Bay of Bengal), Delhi (Yamuna), Singapore (Coastal), Hong Kong (Coastal), Tokyo (Sumida River, Tokyo bay). The urban environment is a complex, sensitive, and significantly changing ecosystem comparative to other landscapes on the earth [Das & Das, 2019]. Urban landscapes experience short spatial scale alterations by anthropogenic activities such as constructing buildings and surface coverage with impervious material. The modifications of the urban landscape create complex topographical structures with high raised buildings, which influence each component of the urban environment, such as meteorological and hydrological cycles. The changes in meteorological and hydrological processes influence local, regional, and urban watershed scales. The spatial variability of complex urban structures creates heterogeneity in hydrological processes such as precipitation, evaporation, and infiltration. These variabilities created uncertainties in flood modeling and forecasting in urban watersheds due to the representation of real-world urban landscape in hydrological modeling is a challenging task to the scientific and research community. Moreover, the dynamic spatial scale modifications in urban areas alter the rainfall patterns over complex urban topography. It leads to the generation of local scale (mesoscale) convective storms and heterogeneous precipitation pattern over urban landscapes (Fig.1.1), producing medium to high rainfall intensity [Leon et al., 2016]. These rainfall intensities create the flash flood type of situation in urban regions, and the alterations in topography and land use worsen the flash flood situation.

Flash floods are short-term events that occur within 6 hours of causative event such as high intensity of rainfall [Hapuarachchi et al., 2011], which creates a normal waterlogging situation in streets to devastate water-related catastrophes. These events are a sequence of the meteorological systems with a specified hydrological condition [Doswell et al., 1996] in an urban watershed. The higher intensities of precipitation can result in higher chances of flash floods in urban landscapes due to insufficient time

Abstract-TH-2793_156104035

to infiltrate water quickly into soil [Andjelkovic, 2001; Hardy et al., 2016], and most of the places in cities' surfaces are covered with impervious surfaces. Even though the surface impervious is the sensitive parameter to the surface runoff in urban areas, the urban landscape's high-intensity precipitation and topography create the more devastating flash floods.

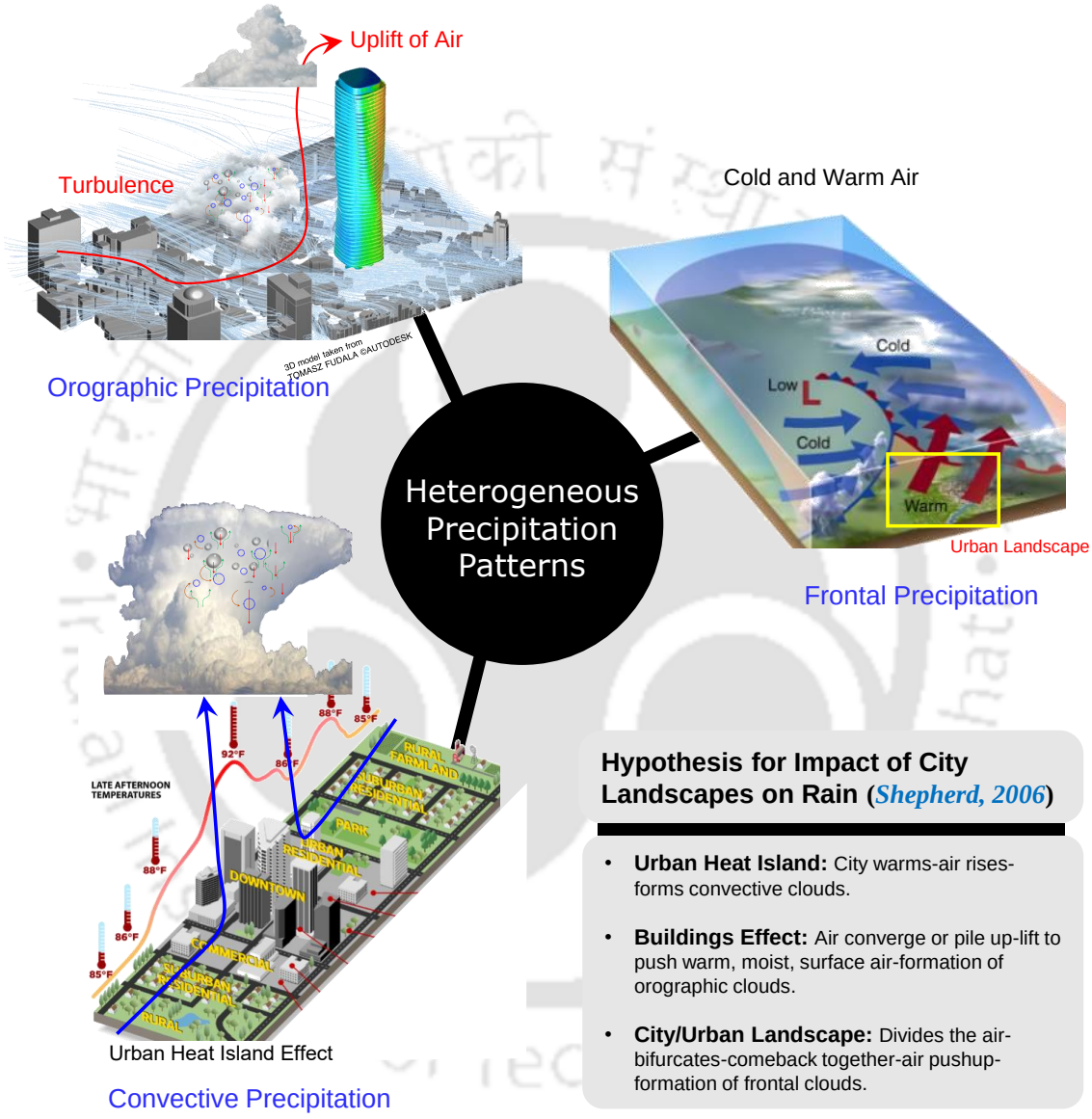

Figure 1.1. Forms of precipitation and cause of heterogenous precipitation and local scale high intensity precipitation in Urban landscapes.

Information regarding the forecasted precipitation data is necessary to design a flash flood early warning system for urban watersheds. The unknown future precipitation is the largest source of uncertainty of flash flood forecasting [Hapuarachchi et al., 2011], along with modifications in topography. Flash Flood Early

Abstract-TH-2793_156104035

Warning system design with forecasted/Nowcasted precipitation using advanced geo-spatial technologies such as topography and precipitation measurements can reduce the damage and give the early preparedness time from these events. Designing a modeling framework for flash flood early warning systems in the urban watershed has many challenges, including heterogeneous precipitation prediction, representation of topography, imperviousness, and drainage system in modeling and design of the model.

1.2 ROLE OF ADVANCED GEO-SPATIAL TECHNOLOGIES IN URBAN FLASH FLOOD MODELING

The advanced geo-spatial technologies have a wide application in urban flood modeling due to the availability of high spatial and temporal resolution of datasets (Fig. 1.2). The high spatial and temporal datasets are a must for designing an urban flash flood early warning system due to its spatial and temporal heterogeneity. The input datasets such as high-resolution in-advanced precipitation, accurate topography, impervious factor (impervious area) derived from high-resolution orthoimageries, drainage networks, and soil maps are required for urban flash flood modeling. The acquisition and availability of these datasets and incorporating them into the distributed urban hydrological model is challenging. The details of datasets required for urban flood modeling and its challenges are discussed in the sections below.

1.2.1 Precipitation

The first and far more challenging task is predicting and representing heterogeneous precipitation over the urban landscape in hydrological modeling. The forcing of conventionally measured precipitation to the model as a boundary condition is not sufficient. In general, urban hydrological applications require stringent rainfall data in terms of both resolution and accuracy. It is identified that the urban hydrological modeling applications need order of 1 *km* and 1-5 *min* spatial-temporal resolution datasets [Ocha-Rodriguez et al., 2015, 2019]. In addition to this, the Quantitative Precipitation Estimation/Forecast/Nowcast (QPE/QPF/QPN) are essential techniques to design flash flood early warning systems [Germann and Zawadzki, 2002; Seed et al., 2013]. QPE, QPF, and QPN can be carried out using advanced precipitation measurement tools such as Automatic Weather Stations (AWS), Satellite observations, and Doppler Weather Radars (Fig. 1.3).

Abstract-TH-2793_156104035

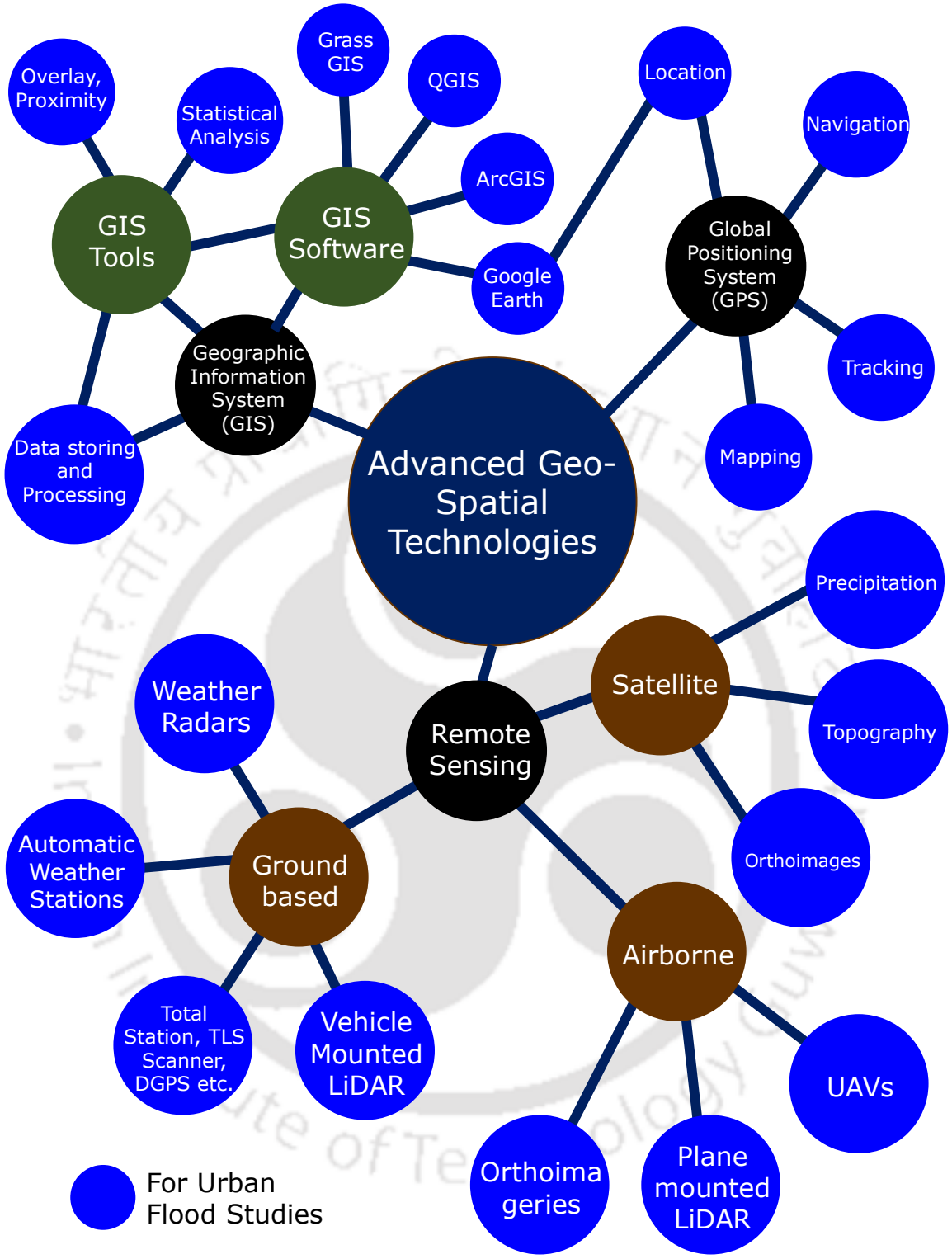

Figure 1.2. Potential of advanced geo-spatial technologies and its applications in the field of urban flood studies.

To forecast/nowcast of flash floods, a closely spaced/dense network of "in-situ" measurements is needed. Installing and maintaining very closely spaced (more) gauges are not practically feasible, which is more expensive, and they cannot sufficiently

Abstract-TH-2793_156104035

capture the spatial variability of rainfall. Designing a flash flood nowcast system applying satellite-based QPE/QPF information is incredibly troublesome and is also coarse resolution [Linsley et al., 1975; Joss, 1990]. Also, the accuracy of satellite precipitation estimation decreases when the time scale reduces (i.e., from monthly to daily to sub-daily) [Terao et al., 2017]. In contrast, Doppler Weather Radars observe precipitation fields over large areas with high spatial and temporal resolutions, thus improving the short-term predictable capacity of precipitation [Rosenfeld et al., 1993; Atlas et al., 1997]. The weather radar derived rainfall resolves the complexities as mentioned earlier by providing data at high spatial-temporal resolutions.

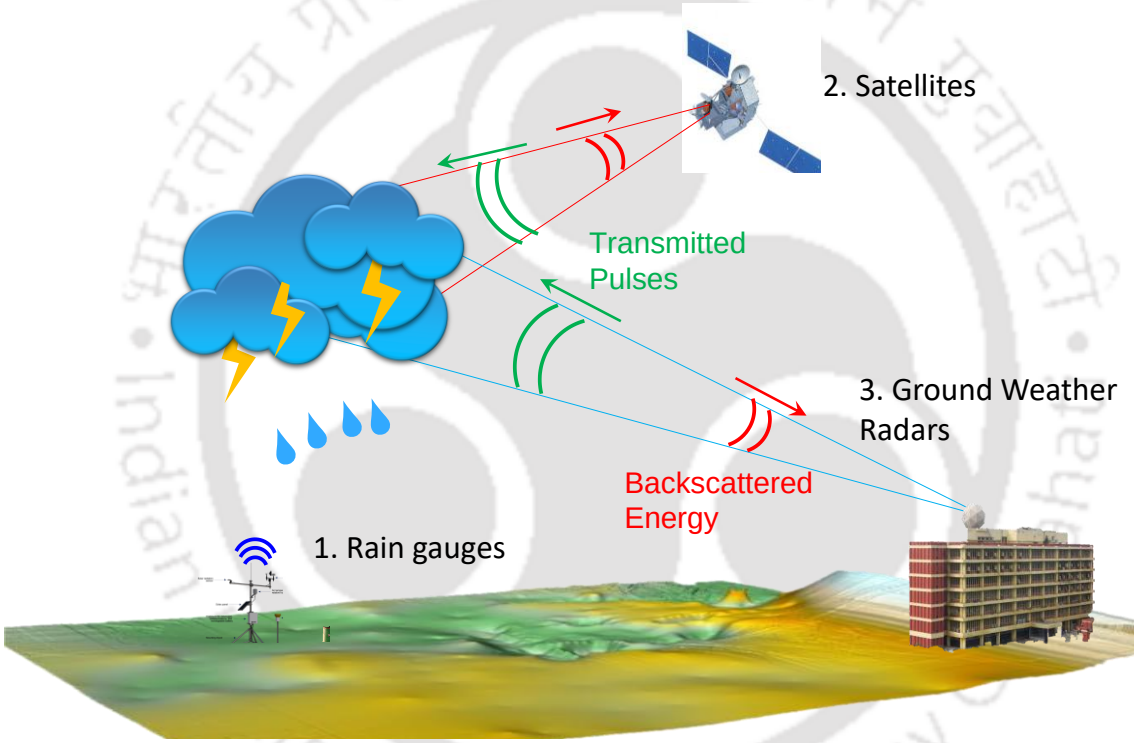

Figure 1.3. Modes of measurement of precipitation; 1) rain gauges (recorded, non-recorded); 2) satellite measurement; and 3) doppler weather radars.

In recent, all 1D and 2D urban hydrological models are incorporated radar rainfall data into their models. The significant complexity here is the retrieval of rainfall rates from radar reflectivity values, mostly in developing countries. Many researchers and scientists are marching towards this direction to increase the accuracy of rainfall rate extraction from weather radar reflectivity values [Marshall & Palmer, 1948; Blanchard, 1953; Carlson, 1970; Battan, 1973; Jorgensen & Willis, 1982;

Rosenfeld et al., 1993; Fulton et al., 1998; Zhang et al., 2011; Gochis et al., 2015]. The extensive works also have been carried to nowcast/predict the high intensity of rainfall in advance to design the flash flood forecasting system over urban landscapes.

1.2.2 Topography

The second most challenging task is to represent the topography of urban landscape in hydrological modeling applications. Many researchers studied and stated that the high-resolution topographic models (Digital Elevation Models, DEMs) such as LiDAR and IfSAR needed for urban flood modeling application due to their high Spatio-temporal resolution, vertical accuracy, and its ability to separated urban surface features (Buildings, vegetation) from bare-earth (ground) [Sanders, 2007; Abdullah, 2012; Seyoum, 2013]. However, the acquisition of LiDAR DEM is challenging to most developing and developed nations due to budget and time constraints [Sanders, 2007], which created an interest for scientists and researchers to study applications of open-source DEMs in fluvial and large-scale river basin studies. However, the application of open-source DEMs in urban hydrological flood modeling yet to be explored in depth. Along with these many questions raised to the scientific community, one of them is Digital Surface Model (DSM) or Digital Terrain Model (DTM), which is used in urban hydrological applications. The man-made artifacts are the primary obstruction for flood movement during flash floods. The DSMs represent these features in their models. However, DSMs include more noise which is not required for flood modeling. We also identified that the DSM is required to predict flood inundation area, depths, and movement accurately, but it has also created artificial storage reservoirs in the urban hydrological model. DTM helps identify natural drainage patterns, but it is also overpredicted in the flood inundation area and underpredicted in inundation depths. More research has to be carried out in this direction.

1.2.3 Imperviousness Factor (Impervious Area)

The next challenging task is representing the impervious area in an urban hydrological model application, which is the crucial parameter in urban flash flood generation and short response time of flood peak. Many researchers debate with Total Impervious Area (TIA) or Effective Impervious Area (EIA) needed for urban hydrological modeling, and more research also has been carried out towards this direction. The TIA and EIA are important when modeling is performed with 1D

Abstract-TH-2793_156104035

(lumped or semi-distributed) dimensionality models such as Storm Water Management Model (SWMM) or coupled (loosely or tightly) models such as 1D-1D and 1D-2D. In recent decades, high spatial-temporal resolution datasets of orthoimageries and advanced numerical solving techniques changed the incorporation of imperviousness in the urban hydrological modeling framework. The forcing of the impervious fraction at each sub-meter cell level for each surface covering material will be helpful to improve flash flood modeling for forecasting. Here, we tried to resolve this complexity in our newly developed model capable of modeling at a street level over a city-scale by incorporating Impervious fraction at fine resolution pixels.

1.2.4 Drainage Network (Drain Discharge Capacity)

The next complexity is to represent the real-world features of natural or man-made drainage networks in an urban hydrological modeling framework. In most of the world, the drainage networks were designed way back in the 1900-1960s, and the drainages are rapidly modifying in a short period by anthropogenic activities. The acquisition of drainage network data is challenging and expensive for both developed and developing nations. To resolve this complexity, many researchers have incorporated drainage networks in urban hydrological models as a mass loss to the system by assuming that the storm sewer system drains water away at the maximum design drainage capacity and considered no loss of capacity due to surcharge [Yu & Coulthard, 2015; Yu et al., 2016]. This assumption works fine when the drainages are functioning at their maximum design capacity, but in reality, the drainages are affected by blockage with sediment, plastic, bottles, weeds, and other materials. More research has to be done to estimate the accurate draining capacity of surface runoff without focusing much on drain channel routing during high flood events in urban areas.

1.2.5 Distributed Urban Hydrological Modeling

The primary challenging task for urban flash flood modeling is the model itself. The existing 1D models and some 2D models focus on storm sewer routing and less prioritized towards surface runoff. However, surface runoff modeling is also more critical during the high intensity of rainfall, producing the flash flood type of situation in urban settings. The changes in the local landscapes alter the slopes of the urban streets and roads and create depressions over land, which are more prominent to create floods than drainage overflow at an average intensity of rainfalls. Nowadays, the

Abstract-TH-2793_156104035

modeling of surface runoff compartment in urban modeling is essential as the drain routing compartment. In recent years, the advent of computational methods enabled the numerical modeling of both surface and drainage flow. Many modeling approaches such as storm sewer flow routing in 1D and surface flow in 2D (1D/2D) [Djordjević et al., 2005; Phillips et al., 2005; Carr & Smith, 2006; Chen et al., 2007; Vojinovic & Van Teeffelen, 2007; Vojinovic & Tutulic, 2009; Price, 2011; Abdullah et al., 2012; Seyoum, 2013] coupling or complete 2D modeling [Yu & Lane, 2006a; Bates et al., 2010; Yu & Coulthard, 2015] or dual drainage modeling, loosely or tightly coupled techniques were evolved. However, more research has to be done in this direction to develop the integrated model by incorporating all the challenges mentioned above or complexities to forecast flood within a short span and manage the water in heterogeneous urban landscapes.

1.3 RESEARCH AIMS

This research aims to develop a distributed urban hydrological model applicable at street scale to city level scale using high Spatio-temporal resolution datasets such as weather radar rainfall, topography, and orthoimageries. Considering research needs with an emphasis on the development of the model by incorporating high spatio-temporal datasets, the following objectives are outlined for the present research:

- Developing and testing an algorithm to establish the relationship to retrieve rainfall rates from weather radar reflectivity.
- Stochastic generation and prediction of high-intensity storm event rainfall hyetographs using a hierarchical supervised machine learning technique.
- To develop the assessment framework for selecting the suitable open-source medium resolution Digital Elevation Model (DEM) for urban flooding.
- To assess the impact of open-source medium resolution DEMs on 1D Storm Water Management Model (SWMM) outputs.
- Developing and testing a new city scale 2D urban hydrological modeling system to forecast urban flash floods by incorporating the high spatio-temporal resolution advanced datasets such as weather radar rainfall, LiDAR topography, orthoimageries etc.

Abstract-TH-2793_156104035

1.4 STRUCTURE OF THE THESIS

The content of this dissertation is composed of eight chapters that each represent an independent concept with independent study areas. The organization of this dissertation tracks three perspective: high spatio-temporal resolution of weather radar rainfall; topography of complex urban regions; and development of distributed urban hydrological model. The three perspectives of the thesis divided into chapters based on the aims of the present research work. Initially, the developed radar rainfall retrieval technique is tested over the study area with the observed rain gauge network data. Secondly, the in-advanced rainfall prediction technique developed with the weather radar and demonstrated its prediction capability. This is followed by an assessment of open-source DEMs with a developed novel approach for urban flood modeling. The later chapter investigates the impact of medium resolution DEMs on floods by the 1D urban hydrological model SWMM. Finally, a distributed urban hydrological model development and its demonstration with a case study of the highly urbanized watershed is carried out to evaluate the performance of the model. The chapter-wise brief description of the thesis is given below:

Chapter 1: This chapter outlines the background of work, concept ideas, an overview of general objectives, and formation of research aims related to the present research work.

Chapter 2: It presents state of the art relevant to the area of urban flood modeling framework, radar reflectivity – rainfall rate relationships, prediction of rainfall with weather radars, available digital elevation models necessary for present research work.

Chapter 3: This chapter presents a novel gravity-turbulence based technique developed to retrieve rainfall from weather radar reflectivity.

Chapter 4: This chapter represents the development of a new approach to predict the high intensity of storm events with historical weather radar reflectivity hyetograph datasets using a hierarchical based machine learning technique.

Chapter 5: This chapter provides a new assessment framework with a proposed storage-elevation function novel technique to assess the open-source digital elevation model for urban flood modeling.

Abstract-TH-2793_156104035

Chapter 6: This chapter reports the impact of the medium resolution digital elevation model (DEM) on flood characteristic by using the 1D Storm Water Management Model (SWMM) along with assessing the suitability of open-source DEMs for urban floods.

Chapter 7: This chapter covers a detailed description of the formulation and development of a distributed Physically-based Urban Runoff Accounting Hydrological Model (PURAHM) used in this research, analyzing model sensitivity and evaluating its performance.

Chapter 8: The final chapter highlights the critical finding derived from this research work, and recommendations for future work are also covered.

Abstract-TH-2793_156104035

This Page Intentionally Left Blank

Abstract-TH-2793_156104035

2

REVIEW OF LITERATURE

(State of the Art of Urban Flash Flood Modelling)

Abstract-TH-2793_156104035

2.1 INTRODUCTION

The occurrence of flash floods due to the high intensity of storm events over complex urban landscapes threatens people's lives and damage property [Smith, 2006]. In general, urban floods are flashy even at moderate rainfalls due to their land covers with impervious materials, reducing the land's carrying capacity [Seyoum, 2013]. Also, the high intensity of storm events creates more flashiness in flood movement over urbanized surfaces (Streets, gullies, parking areas, parks) [Andjelkovic, 2001] and even on non-urbanized surfaces (open lands, swamps) due to the availability of time is less to infiltrate water. The increase in population density, rapid changes in urban land use, and fast flood wave propagation due to stream channelization worsen the situation in urban regions during a flash flood. An early warning system that provides the vulnerable flash flood hot spots in urban is required to mitigate the flood, time to close roads, re-route traffic, activate danger level warnings, and deploy the emergency disaster forces before a flood occurs [Looper & Vieux, 2012]. The forecasting of floods in urban areas is a challenging task due to the fast response of the flood wave, which often makes it challenging to manually adjust inputs and parameters to the model. The forecasting of flash floods in a short time over a city scale accurately and reliably depend on efficient urban hydrological modeling structure configuration [Zang & Pan, 2014], high-resolution accurate input datasets such as precipitation, topography, and ortho-imageries. In recent years, researchers have developed the distributed hydrological models incorporating high-resolution advanced geospatial datasets such as weather radar rainfall, photogrammetry and interferometry based topographic models, and ortho-imageries (Airborne, Spaceborne). A small number of studies have been carried out which addresses the weather radar rainfall, topographic model selection, and distributed model application for urban floods. The intense research activities are ongoing worldwide to forecast flash floods and contribute to the early preparedness of urban flash flood mitigation. In this chapter review of works carried out on distributed urban flood modeling, application of weather radars towards urban flooding by predicting high intensity of rainfall, and availability of topographic models, their application in different fields, including urban flood studies, are highlighted. The last part presents the of reviewed literature. This chapter also provides the theoretical background required to develop and apply the rainfall rate – radar reflectivity relationship to retrieve rainfall from the weather radar reflectivity.

Abstract-TH-2793_156104035

2.2 URBAN FLOOD MODELING

In recent decades, a range of new modeling approaches is developed to simulate floods in urban regions, especially in the last few years. The current modeling approaches used for the urban flood significantly vary depending on its dimensionality (1D, 2D, and very rare of 3D), governing equations, solving techniques, and adopted numerical schemes. The existing models are categorized as commercial software packages (PCSWMM, XP-SWMM, MIKE) and research-oriented models (LISFLOOD, Flood Hydro-inundation). The commercial ones are more robust with well-established governing equations and well-tested numerical schemes, whereas research-oriented models developed by the hydrologist community are less robust and more heterogeneous [Leandro, 2008; Seyoum, 2013]. Part of this discussion is taken from Chen et al. [2006], Garcia-Navarro & Brufau [2006], Hunter et al. [2007], Hunter et al. [2008], Leanardo, [2008], Kuiry et al. [2010], Price [2011], Seyoum, [2013], Salvador et al. [2015]. The conceptual diagram of modeling concepts is shown in Figure 2.1.

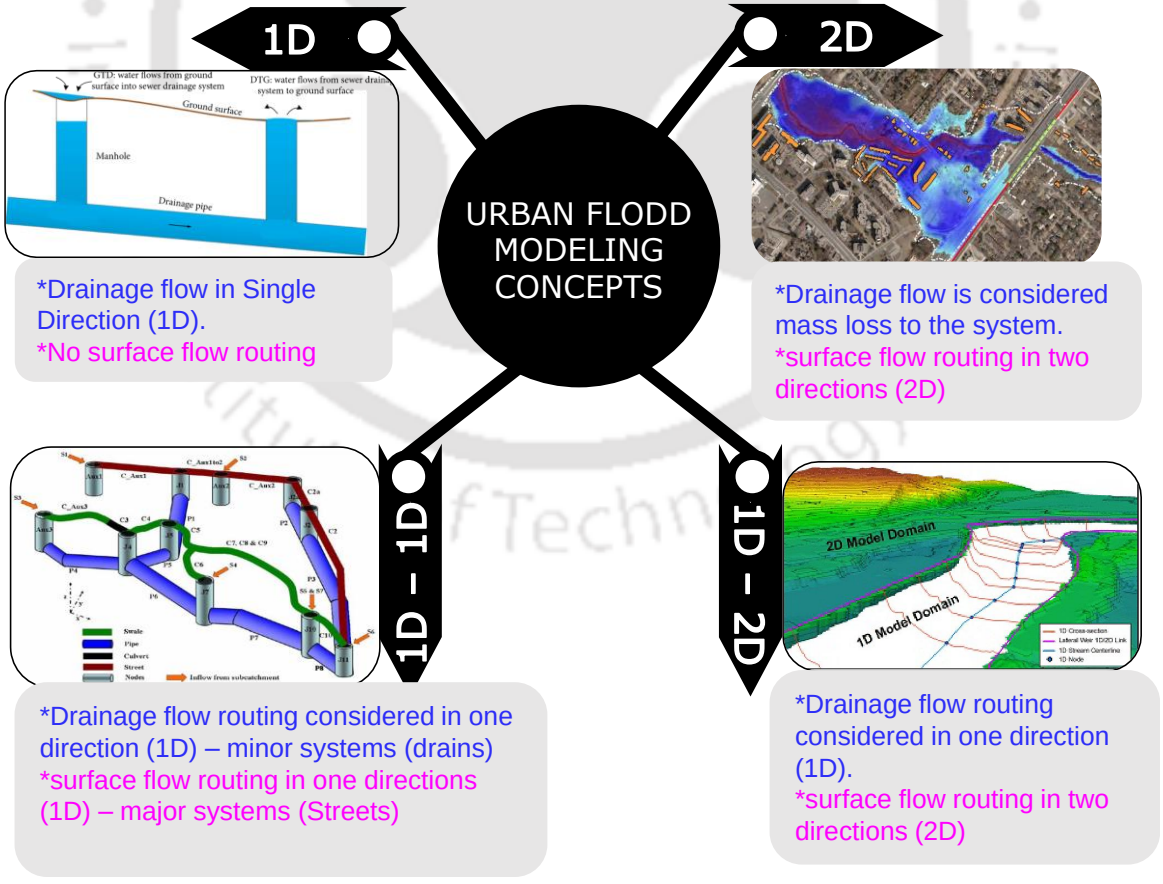

Figure 2.1. Schematic figure to explain 1D, 2D, 1D-1D and 1D-2D model concepts.

Abstract-TH-2793_156104035

2.2.1 One Dimensional Models (1D)

Most of the 1D models focus on hydraulic channel routing through drainage networks than surface flow routing. In one dimensional model, the drainage network is composed of conduits links such as pipes or channels (closed or open – rectangular, trapezoidal) and junctions as manholes [Abdullah et al., 2012; Seyoum, 2013]. The 1D modeling approach can also be used to interlink between closed conduits with open channel flow (the streets) and stagnant flood accumulation zones [Mark et al., 2004]. The detailed list of available models and their applications is given in Table 2.1.

2.2.2 Two Dimensional Models (2D)

The development and application of two-dimensional models are rare in urban flood modeling. The developed 2D models are mostly research-oriented models such as modified LISFLOOD- FP model for urban flood studies developed by Bates et al. [2010], FloodMap model developed by Yu & Lane [2006a], and FloodMap-HydroInundation2D model developed by Yu & Coulthard [2015]. In these models, the drainage is considered a mass loss to the system and applied at each cell level or uniform value over the complete study area. The detailed list of available models and their applications is provided in Table 2.1.

2.2.3 1D – 1D Models

In recent years, a new approach referred to as the "dual drainage model" [Djordjević et al., 2005] evolved by coupling two different dimensionality models. In this approach, major systems (natural and man-made ground flow pathways such as streets) and minor systems (drainage network with manholes and inlets) interact with each other through the weir or orifice type objects. In this modeling system, continuity and 1D Saint Venant equations are solved to estimate the flow depths, velocities, and flow discharge in the form of hydrographs at junctional nodes. The detailed list of available 1D – 1D models and their applications are given in Table 2.1. This modeling approach handles urban flooding with and without floodwater entry into houses [Mark et al., 2004]. These models are economic in computational time and input datasets, also robust alternative to 1D-2D models [Spry & Zang, 2006]. However, these modeling approaches are insufficient during flash floods [Mark et al., 2004] and when the flat areas have existed in the watershed.

Abstract-TH-2793_156104035

2.2.4 1D – 2D Models

In 1D – 2D coupled models, the 1D channel or pipe flow models are coupled with the surface flood flow model either loosely or tightly. This model treats the urban surface runoff as a two-dimension flow domain [Vojinovic & Tutulic, 2009; Price, 2011; Abdullah et al., 2012; Seyoum, 2013]. In this model, domains are coupled at the cell level by overlying drainage network paths as a point on overland grid cells [Vojinovic & Van Teeffelen, 2007; Price, 2011]. Phillips et al. [2005] simulated the flow using XP-SWMM2D, which is a coupling of 1D XP-SWMM (for minor systems) with a 2D TUFLOW (for major systems). Carr & Smith [2006] used a MIKE STORM (1D) – MIKE 21 (2D) model. The authors concluded that the model predicted better time series. Chen et al. [2007] linked the 1D SIPON solves continuity and Saint-Venant equations [Djordjević et al., 2005] with 2D UIM diffusive over-land flow model solves non-inertial flow equations. The authors concluded that SIPN/UIM model simulated complex flow processes over urban areas more effectively than the 1D models. This 1D – 2D modeling approach is complex and computationally expensive due to complex numerical solving schemes adopted in these models. The detailed list of available models and their applications is provided in Table 2.1.

Abstract-TH-2793_156104035

Table 2.1. Modeling approaches developed for urban flood simulation for small city scale applications (part of this taken from Salvador et al. [2015]).

Model	Dimensionality	Spatial scale	Temporal scale	Study Area (km^2)	Reference
SWMM* SWMM + Inundation model	1D	Semi-distribution, 120 *m*	5 *min*, 2 *min*, 1 *min*, 10 *min*, 15 *min*, 1 *hr*.	0.0581, 0.6, 0.7, 1.3, 2.3, 10.5, 250	Hsu et al. [2000]; Lee & Heaney [2003]; Gironás et al. [2010]; Petrucci & Bonhomme [2014]; Krebs et al. [2014]
PCSWMM[$]	1D	Semi-distribution	15 *min* – 12 *hr*.	6.8×10^{-2}	Rosenberger et al. [2021]
XP-SWMM[$]	1D	Semi-distribution	-	1.44×10^{-4}	Van et al. [2014]
XP-SWMM 2D[$] (1D XP-SWMM + 2D TUFLOW)	2D	< 10 *m*	-	1.65×10^{-4}	Phillips et al. [2005]
Urban residential model®	1D	UHE	1 *hr*.	1.4×10^{-3}	Xiao et al. [2007]
SURF®	2D	5 *m*	1 *hr*.	0.047, 0.134, 0.16	Bellal et al. [1996]; Rodriguez et al. [2000]
MUSIC[$]	1D	Semi-distributed, lumped	6 *min*	0.105, 0.28, 0.38, 0.89, 1.06, 40	Dotto et al. [2011]; Hamel & Fletcher [2013]
KAREN®	1D	lumped	6 *min*	0.105, 0.28, 0.38, 0.89, 1.06	Kleidorfer et al. [2009]; Dotto et al. [2011]

Abstract-TH-2793_156104035

Conceptual model®	2D	Semi-distributed	1 *min*	0.128	Aronica & Cannarozzo [2000]
URBS – UH®	1D	UHE	1 *min*, 2 *min*, 5 *min*	0.18, 0.6, 0.6, 1.8	Rodriguez et al. [2003]
URBS – MO®	1D	UHE	1 *min*, 2 *min*, 5 *min*	0.18, 0.6, 0.6, 1.8	Rodriguez et al. [2008]
SUES*	1D	UHE	≥ 1 *hr*, 5 *min*	0.21, 30	Grimmond & Oke [1991]; Mitchell et al. [2008]
UHE Model®	2D	UHE	1 *hr*.	0.47	Berthier et al. [2004]
Hyperbolic model®	2D	5 m	3 *min*	0.82	Aronica & Lanza [2005]
MOUSE$	1D	-	-	-	DHI Group [2009a]; Apirumanekul [2001];
MOUSE + FORM$	1D – 1D	Semi distributed	1 *min*	0.87	Thorndahl & Willems [2008]
GUFIM (GIS-based Urban Flood Inundation Model)®	2D	10 *m*	15 *min*	1.5	Chen et al. [2009]
Distributed Urban Drainage model®	2D	10 *m*, 200 *m*	1 *s*	2, 100	Pan et al. [2012]

REVIEW OF LITERATURE

Abstract-TH-2793_156104035

DRAINS	1D	-	-	-	O'Loughlin & Seneviratne [2006]
SIPSON + UIM	1D – 2D	2 *m*	0.5 – 5 *s*	1.5	Chen et al. [2007]
XP – SWMM + DRAINS	1D – 1D	-	-	-	Spry & Zhang [2006]
INFOWORKS CS (MWHSoft)[$]	1D – 1D	-	15 *min*, 30 *min*, 45 *min*, 60 *min*	-	Vaes et al. [2004]; Rubinato et al. [2013]
MIKE STOM + MIKE 21	1D – 2D	0.5 *m*	-	2.1×10^{-4}	Carr & Smith [2006]
MOUSE + MIKE 21	1D – 2D	1 *m*	1 *s*, 1 *hr.*	-	Vojinovic & Tutulic [2009]
TOPURBAN	1D	Semi distribution	1 *hr.*	8	Valeo & Moin [2000]

UHE: Urban Hydrological Element

*Open-Source / Free

[$]Commercial

[®]Research oriented

Institute of Technology Gu

Abstract-TH-2793_156104035

REVIEW OF LITERATURE

2.3 WEATHER RADAR RAINFALL

The Quantitative Precipitation Estimation (QPE) of rainfall using weather radar is essential for urban flood studies, especially for flash flood forecasting. The urban drainage flood modeling requires the rainfall resolution of < 1 *km* spatially and 1-5 *min* temporally [Ocha-Rodriguez et al., 2015, 2019]. A weather radar is a powerful tool that satisfies the above requirement, measures rainfall at high Spatio-temporal resolution (< 300 *m*, 1-10 *min*). A weather radar transmits the electromagnetic pulses through the transmitter at microwave frequencies by the antenna into the atmosphere. A part of the transmitted energy is absorbed by the material (such as water droplets) in the atmosphere. A fraction of scattered energy returns (backscattered) to the radar antenna and receives through the receiver. The backscattered energy is termed "Reflectivity", a measure of the target's efficiency, and it depends on the physical properties of the target such as shape, size, orientation, and composition. The reflectivity value measure in dBZ (decibel logarithmic scale) shows higher values for stronger targets such as convective storms or hails in the cloud and lower values for weaker targets such as stratiform clouds and drizzle. The dBZ measurement is related to the number of raindrops per unit volume and the sixth power of their diameter. Doppler weather radar scans rainfall from low angle to highest angle by rotating 360°, at each scan sends pulses and receive any backscattering from raindrops. Generally, the backscattered energy from clouds is displayed in three formats, namely PPI (Plan Position Indicator), CAPPI (Constant Altitude PPI), and RHI (Range Height Indicator). The typical plot of the radar PPI format is shown in Figure 2.2.

Weather Radars not measure rainfall directly; and instead, it measures backscattered energy in reflectivity factor. The earlier studies identified that both rainfall rate and reflectivity are a function of raindrop size distribution. Precipitation can be measured by using an empirical power law which is also called as Z – R relationship. The standard rainfall rate and reflectivity relationship is in the form of empirical power law [Marshall & Palmer, 1948; Battan, 1973] can be expressed as:

$$Z = A\,R^{b}$$

Where Z is the measured radar reflectivity factor (mm^6/m^3), R is the rainfall rate (mm/h), and A and b are coefficients to be determined.

Abstract-TH-2793_156104035

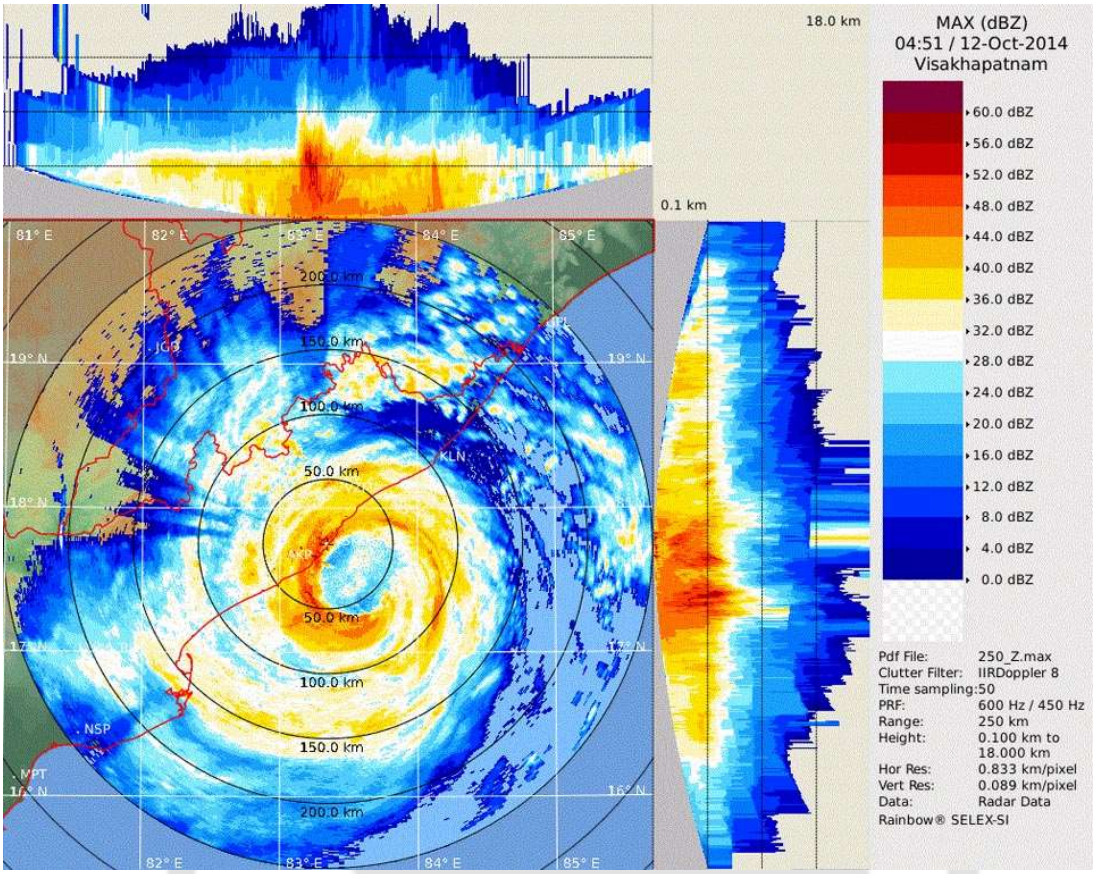

Figure 2.2. PPI and RHI of Vishakapatnam, India during Hudhud tropical cyclone (Source: India Meteorological Department)

Table 2.2. Various Radar Reflectivity (Z) – Rainfall Rate (R) ($Z = AR^b$) relationships for different storm types (taken from Kim et al. [2021]).

Storm (Rainfall) Type	A	b	Reference
Stratiform	200	1.6	Marshall & Palmer [1948]
Convective	300	1.4	Fulton et al. [1998]
Tropical	32	1.65	Gochis et al. [2015]
Orographic	31	1.71	Blanchard [1953]
Warm	230	1.25	Rosenfeld et al. [1993]
Hurricane	300	1.35	Jorgensen & Willis [1982]
Snow	2000	2.0	Carlson [1970]
Snow at the surface	75	2.0	Zhang et al. [2011]
Thunderstorm	486	1.37	Jones [1956]
German weather Service	254	1.42	Brommundt & B´ardossy [2007]

Abstract-TH-2793_156104035

Table 2.3. Radar Reflectivity Rainfall Rate relationships developed for various regions (Part of it taken form Pattani [2010]).

A	b	Region	Country	Type of storm	Reference
200	1.6			All types	Marshall & Palmer [1948]
100	1.2	Chennai	India	north east monsoon	Raghavan & Sivaramakrishnan [1982]
100	1.3	Chennai	India	south west monsoon	
267	1.35	Chennai	India	All types	Chennai radar [IMD]
214	1.15	SHAR	India	Stratiform	Devajyoti Dutta et al. [2012]
42	1.79	SHAR	India	Stratiform	
50	1.5	Darwin	Australia	Convective	Steiner & Houze [1993]
150	1.5	Darwin	Australia	Non - Convective	
650	1.36	Bauru	Brazil	All rain for Near range	
230	1.25	GATE			Hudlow & Arkell [1978]
185	1.22	GATE		Climatological Z – R relation	Atlas et al. [1990]
300	1.4			US WSR – 88D	Fulton et al. [1998]
82	1.47	Darwin	Australia	Convective	Steiner et al. [1995]
143	1.5	Darwin	Australia	Stratiform	Steiner et al. [1995]
178	1.51	National MST radar facility Gandaki	India	Convective	Rao et al. [2001]
162	1.44	National MST radar facility Gandaki	India	Transition	
251	1.48	National MST radar facility Gandaki	India	Stratiform	
155	1.39	National MST radar facility Gandaki	India	Northeast Monsoon	
407	1.32	National MST radar facility Gandaki	India	Southwest Monsoon	
334	1.19	Kapingamarangi		Convective	Atlas et al. [1999]
230	1.4	Massachusetts	USA	Ordinary rain	Austin [1987]
400	1.3	Massachusetts	USA	Intense Convective Cells	
100	1.4	Massachusetts	USA	Non-Cellular rain	

Abstract-TH-2793_156104035

Many researchers have carried out to determine the coefficients to establish the relationship. The detailed literature to establish the Z-R relationship is provided in chapter 3. The coefficients depend on the type of rainfall, type of storms, region, and difference in climatology, such as ecological zones. The meteorologists developed different relationships for different storm types and regions, listed in Table 2.2 and Table 2.3.

Table 2.4. Major algorithms/techniques developed to track convective cells and Nowcast the high intensity of convective rainfall.

Model	Name	Reference
TREC	Tracing of Radar Echoes by Correlation	Rinehart & Garvey [1978]; Smythe & Zrnic [1983]; Tuttle & Foote [1990]
COTREC	Continuity of TREC vectors	Li et al. [1995]; Schmid et al. [2000]; Novak et al. [2009]
MAPLE	McGill Algorithm for Precipitation Nowcasting by Lagrangian Extrapolation	Bellon & Austin [1978]; Germann & Zawadzki [2002, 2004]; Turner et al. [2004]
S-PROG	Spectral Prognosis	Seed [2003]
STEPS	Short Term Ensemble Prediction System	Bowler et al. [2006]; Seed et al. [2013]
TITAN	Thunderstorm Identification, Tracking, Analysis, and Nowcast	Dixon & Wiener [1993]
SCIT	Storm Cell Identification and Tracking	Johnson et al. [1998]
TRACE3D	Tracking Algorithm	Handwerker [2002]
CELLTRACK	Convective Cell Tracking	Kyznarová, & Novák [2009]
CAPS	Center for Analysis and Prediction of Storms	Kong et al. [2011]

The weather radar is a powerful tool and is extensively used for nowcasting short-term high-intensity storm events, where traditional methods and satellite measurement of rainfall lack. A weather radar is only the tool that is useful to nowcast/forecast the localized mesoscale convective generated high intensity of rainfall. Many researches have been carried out to develop nowcasting models by incorporating weather radar reflectivity, which comprises from optical flow techniques [Gibson, 1950; Germann & Zawadzki, 2002; Bowler et al., 2004; Liu et al., 2015] to

Abstract-TH-2793_156104035

recent advanced neural network techniques [Shi et al., 2015; Han et al., 2017; Yu et al., 2017; Han et al., 2019; Yao et al., 2020]. The detailed literature survey and its drawbacks are discussed in chapter 4. Some of the significant nowcasting techniques or models are listed below, given in Table 2.4.

2.4 TOPOGRAPHIC DATA FOR URBAN FLOODS

Topographic data is one of the most significant datasets needed to set up the flood modeling and prepare the inundation maps. The topography is a driving variable that drives surface flow and represents the storage hotspots at depressions in urban flood modeling [Wechsler, 2007]. The advanced technologies enabled the generation of high-resolution accurate topographical maps over urban landscapes relatively short of time compared to traditional surveying techniques. The high-resolution topographic datasets such as LiDAR (Light Detection and Ranging) and IfSAR (Interferometric Synthetic Aperture Radar Sensor) are available in most of the developed countries [Wechsler, 2007]. Urban hydrologists believe that high-resolution DEM such as LiDAR can solve the problems associated with critical small-scale features and poor representation of surface elevations towards urban flood modeling [Seyoum, 2013]. However, acquiring and maintaining a high-resolution dataset such as LiDAR is challenging for most developed and developing nations due to its acquiring cost and difficulties in processing the data [Sanders, 2007].

Moreover, the required resolution of topographic data varies based on its application area. It depends on many factors such as study area size, complexity of the model, type of model selected, and purpose of urban flood modeling [Seyoum, 2013]. For example, the FloodMap-HydroInundation2D model developed by Yu & Coulthard [2015] identified that the model is insensitive to spatial resolution of topographic data and resolution not affected much on flood depths and inundation area [Yu et al., 2016]. It revealed that the medium resolution DEMs ($<50\ m$) are also helpful for urban flood modeling, making the potentiality of open-source DEMs, mostly available at a spatial resolution of $< 30\ m$, applicable in urban flood modeling inundation mapping. The popularly known and available medium resolution digital elevation models, characteristics, and applications are provided below-given Table 2.5. The detailed literature survey on the application of DEMs in urban flood modeling is discussed in chapter 5.

Abstract-TH-2793_156104035

Table 2.5. Summary characteristics on major open-source and commercial DEMs available in the world.

Dataset (Acquisition)	Imaging Sensors	Spatial Resolution	Spectral Range	b/H ratio	Horizontal accuracy	Vertical accuracy	Popular application	Product Coverage	Reference
ALOS AW3D	Optical	[$$]5 *m*, 30 *m*	0.52-0.77 *μm*	1	5 *m* (RMSE)	5 *m* (RMSE)	Rockslide studies, Glacier debris studies, Fluvial landscapes,	Global	Grohmann [2018]; Zaho et al. [2019]; Huang et al. [2018], Rounce et al. [2018], Boulton & Stokes [2018],
ALOS PALSAR	SAR-L band	12.5 *m*	24 *cm*	-	NA	NA	Permafrost movement, drainage extraction, Morphometric analysis,	Global	Wang et al. [2017], Niipele & Chen [2019], Nitheshnirmal et al. [2019],
ASTER	Optical and Infra-Red	30 *m*, 90 *m*	0.78 -0.86 *μm*	0.6	30 *m* (CE95)	20 *m* (LE95)	Morphometric analysis, Coastal studies, Glacier studies	Global	Grohmann [2018], Sujatha et al. [2015], Wang et al. [2018], Tielidze [2016], Jarihani et al. [2015]
CARTOSAT	Optical and Infra-Red	[$$]5 *m*, 30 *m*	0.50-0.85 *μm*	0.63	< 15 *m* (CE90)	< 8 *m* (LE90)	Landslide study, Morphometric analysis, **Urban**, Timber volume estimation,	India, Europe[$$]	Muralikrishnan et al. [2013], Martha et al. [2010], Yadav et al. [2014], Wurm [2014], Straub et al. [2013],
NED	Merging of	1/9 *s*, 10 *m*, 30 *m*	NA	-	3 *m*, 10 *m*, 30 *m*	< 0.5 *m*, < 7 *m*, < 15 *m* (RMSE)	Hydrologic applications, Glacier studies, Snow cover	Contiguous USA and	Sanders [2007], Chaney et al. [2016], Le Bris & Paul [2015],

Abstract-TH-2793_156104035

	different datasets						mapping, **Urban**, River hydraulic study	other surroundigs	Selkowitz & Forster [2016], Bhaskar et al. [2015], Saksena & Merwade [2015]
SRTM	SIR-C/X-SAR band	30 *m*, 90 *m*	5.66 *cm*/3.1 *cm*	-	< 20 *m* (CE90)	< 16 *m* < 10 *m* (LE90)	Hydrological modeling, River flood plain mapping, change and artifact detection, Coastal studies	Global	Rodriquez et al. [2006], Farr et al. [2007], Grohmann [2018], Hirt [2018], Kulp & Strauss [2018], Jarihani et al. [2015]
TanDEM-X	SAR-X band	#12 *m*, #30 *m*, 90 *m*	3.1 *cm*	-	< 10 *m* (CE90)	< 10 *m* (LE90)	Change detection, Flood study, **Urban**,	Global	Grohmann [2018], Karila et al. [2019], Mason et al. [2016], Archer et al. [2018], Kent et al. [2019],
Geoeye-1[$$]	Optical and Infra-Red	0.5 *m*, 1 *m*	0.45-0.92 *μm*	Variable (0.54-0.83)	4 *m*, 15 *m* (CE90)	6 *m*, 22 *m* (LE90)	Flood mapping, Mining studies, Hydraulic studies, Glacier debris studies, Fault studies, Geomorphometric analysis,	Global	Deilami & Hashim [2011], Tsanis et al. [2014], Paradella et al. [2015], Vozinaki et al. [2017], Rounce et al. [2018], Bi et al. [2018], Barbarella et al. [2017],
IKNOS[$$]	Optical and Infra-Red	1 *m*	0.445-0.853 *μm*	0.54-0.83	6.2 *m* (CE90)	10.1 *m* (LE90)	Forest growth studies, Canopy height model, Highway model construction	Global	Elaksher [2009], Deilami & Hashim [2011], Neigh et al. [2016], Neigh et al. [2014], Shaker et al. [2011],

REVIEW OF LITERATURE

Abstract-TH-2793_156104035

SPOT-5[$$]	Optical	5 *m*, 10 *m*, 20 *m*	0.48-1.75 *μm*	Variable ~ 0.8	15 – 30 *m* (CE90)	10 – 20 *m* (LE90) and *5 – 11 *m* (LE90)	Glacier studies, Forest Mapping, Gully erosion,	Global	SPOT Image [2004], *Toutin [2006], Berthier et al. [2007], Wallerman et al. [2010], Maerker et al. [2015],
Worldview-1[$$]	Optical and Infra-Red	0.5 *m*	0.4 – 0.9 *μm*	Variable	4 *m* (CE90)	3.7 *m* (LE90)	Sub glacier lake studies,	Global	Digital Globe [2016], Shean et al. [2016], Willis et al. [2015],
Worldview-2[$$]	Optical and Infra-Red	0.5 *m*, 2 *m*	0.4 – 1.04 *μm*	Variable	3.5 *m* (CE90)	3.6 *m* (LE90)	Glacier debris studies, Glacier studies, Timber volume estimation,	Global	Digital Globe [2016], Shean et al. [2016], Rounce et al. [2018], Fieber et al. [2018], Straub et al. [2013],
KOMPSAT-2[$$,@]				Variable	< 25.4 *m* (CE90)	< 22.4 *m* (LE90)			Deilami & Hashim [2011]

a. LExx and CExx indicates Linear Error and Circular Error at xx% of Confidence level
b. $$ - Commercially available
c. @ - Army/Military purposes
d. # - Available by accepting project proposal with nominal charges

Abstract-TH-2793_156104035

2.5 SUMMARY

The state-of-the-art literature discussed above highlights the potentiality of advanced geo-spatial technologies such as weather radar rainfall and high and medium resolution topographic models for urban flood modeling. The literature review on urban hydrological modeling revealed that most models or studies focused on 1D, 1D-1D, and 1D-2D approaches that work at small spatial scales. The 1D, 1D-1D models, are insufficient to simulate surface water flow over the urban landscapes. The 1D-2D models are complex and require large datasets, including drainage networks, which is impossible for most developing nations. All these models work at local scales insufficient to simulate flood at city scale. The 2D models with an assumption of drainage as a mass loss to the system work fine and show its potentiality over city-scale urban landscapes. However, there are only a few studies that investigate by taking complete hydrological processes into the model. Also, the incorporation of radar rainfall, medium resolution DEMs, imperviousness at cell level with less drainage data was not studied elaborately. These approaches yet to be studied for urban flash flood forecasting. The literature on rainfall retravel for radar reflectivity revealed that the relationships are regional and seasonal dependent. For Indian conditions, these relationships are yet to be developed. The existing approaches are not sufficient to establish a relationship for tropical countries where the pattern of rainfall changes rapidly. The literature on nowcasting techniques revealed that the existing methods are tracking the storm effectivity. However, they still lack in the estimation of storm growth and dissipation quantitatively. State of the art on applying topographic models to floods highlights most of the studies carried out for fluvial flooding even in urban landscapes. None of the studies carried out the suitability of open-source or medium resolution DEMs for urban flooding in data scare regions. It reveals the necessity of understanding the application of open-source or medium resolution DEMs for urban flood modeling and inundation mapping, which can be easily accessible to most of the developing nations.

Abstract-TH-2793_156104035

This Page Intentionally Left Blank

Abstract-TH-2793_156104035

3

RADAR REFLECTIVITY RAINFALL RATE RELATIONSHIP

(Establishing the Relationship to Retrieve the Rainfall Rate from Weather Radar Reflectivity)

Abstract-TH-2793_156104035

3.1 INTRODUCTION

Precipitation events that are highly influenced by a wide range of surface processes make equilibrium in a non-equilibrium state, which may occur in a different condition (number, type, size, intensity, and duration) and contribute significant variation in the total amount of precipitation over a region, especially in heterogeneous urban landscapes. Information about the high spatial-temporal heterogeneity of precipitation is vital for flood early warning system design and management. This high spatial-temporal heterogeneity of precipitation is always not possible to capture totally using conventional precipitation measurements (rain gauges), even though they provide relatively accurate point rainfall at the ground surface [Ocha-Rodriguez et al., 2019]. Moreover, it is a challenging task to forecast precipitation with longer lead time based on single point measured rain gauge data only [Simões et al., 2011; Looper & Vieux, 2012].

In recent decades, weather radar data is extensively used for developing real-time precipitation forecasting and early warning systems to forecast floods especially flash floods. The weather radar extensively covers and captures the heterogeneous precipitation with high spatial and temporal resolutions. The application of weather radars extends from small spatial scales such as urban regions [Sempere-Torres et al., 1999; Thorndahl et al., 2013] to large scale river basins [Dolciné et al., 2001; Teague et al., 2013]. Instead of measuring rainfall directly by weather radars, the rainfall is being derived indirectly from backscattered radar reflectivity. Traditionally, the rainfall rate (R) was retrieved from radar reflectivity (Z) by applying a simple parametric power law equation named as Z-R relationship [Marshall & Palmer, 1948; Spilhaus, 1948; Wilson & Brandes, 1979; Fulton et al., 1998]. The Z-R relationship is defined as follows:

$$Z = AR^{B} \qquad \text{(eq.3.1)}$$

Where, Z, is the radar reflectivity factor (mm^6/m^3); R, is rainfall rate (mm/h); and A and B, are power law function parameters [Marshall & Palmer, 1948]. The Z-R relationship is dependent on the distribution of raindrop sizes [Battan, 1973]. A range of Z-R relationships were developed depending on storm type, power of the radar (wavelength type), season, and regions (Table 2.2 and Table 2.3). Till to date, the Z-R relationship proposed by Marshall and Palmer [1948] with parameters (A = 200, B = 1.6) has been

Abstract-TH-2793_156104035

used in most of the radars all over the world for an entire year overall seasons, even though such type of fixed relationship is problematic where the relationship varies spatially, temporally and for storm type throughout a region [Kim et al., 2021]. However, in extreme rainfall events, the accuracy of radar measurements and conversion of rainfall using the Marshall-Palmer equation is insufficient [Einfalt et al., 2004; Einfalt et al., 2005; Marra & Morin, 2015; Bárdossy & Pegram, 2017].

Several studies have attempted to establish the Z – R relationship based on different methods to improve the estimation of radar-derived rainfall rates. The methods include parametric regression traditional matching by synchronizing the reflectivity and rainfall rate measured at point gauge [Calheiros & Zawadzki, 1987; Rosenfeld et al., 1990; Baldanado, 1996], based on raindrop size distribution data [Marshall et al., 1947; Marshall & Palmer, 1948; Stout et al, 1968; Ulbrich & Atlas, 1977], by considering climatic parameters (rainy days, humidity, precipitable water) into parametric power-law equation [Cataneo, 1969; Cataneo & Vercellino, 1972; Ulbrich & Atlas, 1977], nonparametric probability based matching by synchronizing the pairs where the synchronizing is unachievable by traditionally, Probability Matching Method [Calheiros & Zawadzki, 1987; Atlas et al., 1990; Rosenfeld et al., 1993; Crosson et al., 1996], Window Probability Matching Method [Rosenfeld et al., 1994], correlation based methods [Piman et al., 2007], Artificial Neural Network based methods [Basile et al., 1993]. However, the synchronization of reflectivity and rainfall rate pairs still a challenging task for radar meteorologists. Several bias correction techniques are developed to overcome uncertainty subjected to multiple sources of errors instead of focusing on reflectivity rainfall pair synchronization. Along with error correction techniques, the advanced techniques are developed in radars, including more recent advances based on dual-polarization radar measurements [Bringi & Chandrasekar, 2001; Sugier & Tabary, 2006; Rico-Ramirez & Cluckie, 2008; Bringi et al., 2011; Chandrasekar et al., 2013; Hall et al., 2015].

This study attempted to synchronize the radar reflectivity pairs by adopting the novel Gravity – Turbulence physical based principle proposed here. The proposed method identifies the appropriate radar pixel over a point rain gauge to accurately synchronize the pairs. The method selects an appropriate radar pixel where gravity force overcomes the turbulence or shear force (low spectral width variable) acting on

Abstract-TH-2793_156104035

a raindrop. This chapter begins with describing the selected study area where weather radar is operating, data obtained, and its analysis. Then Section 3 introduces the developed methodology along with existing parametric and nonparametric methods. Section 4 includes the results, discussion, and evaluation of the method. Finally, section 5 summarizes the main conclusions.

3.2 STUDY AREA, DATA COLLECTION, AND ANALYSIS

3.2.1 Study Area Description

The study area, Delhi NCR (National Capital Region), and its surrounding regions are located in the north part of India were considered for the present study (Fig.3.1).

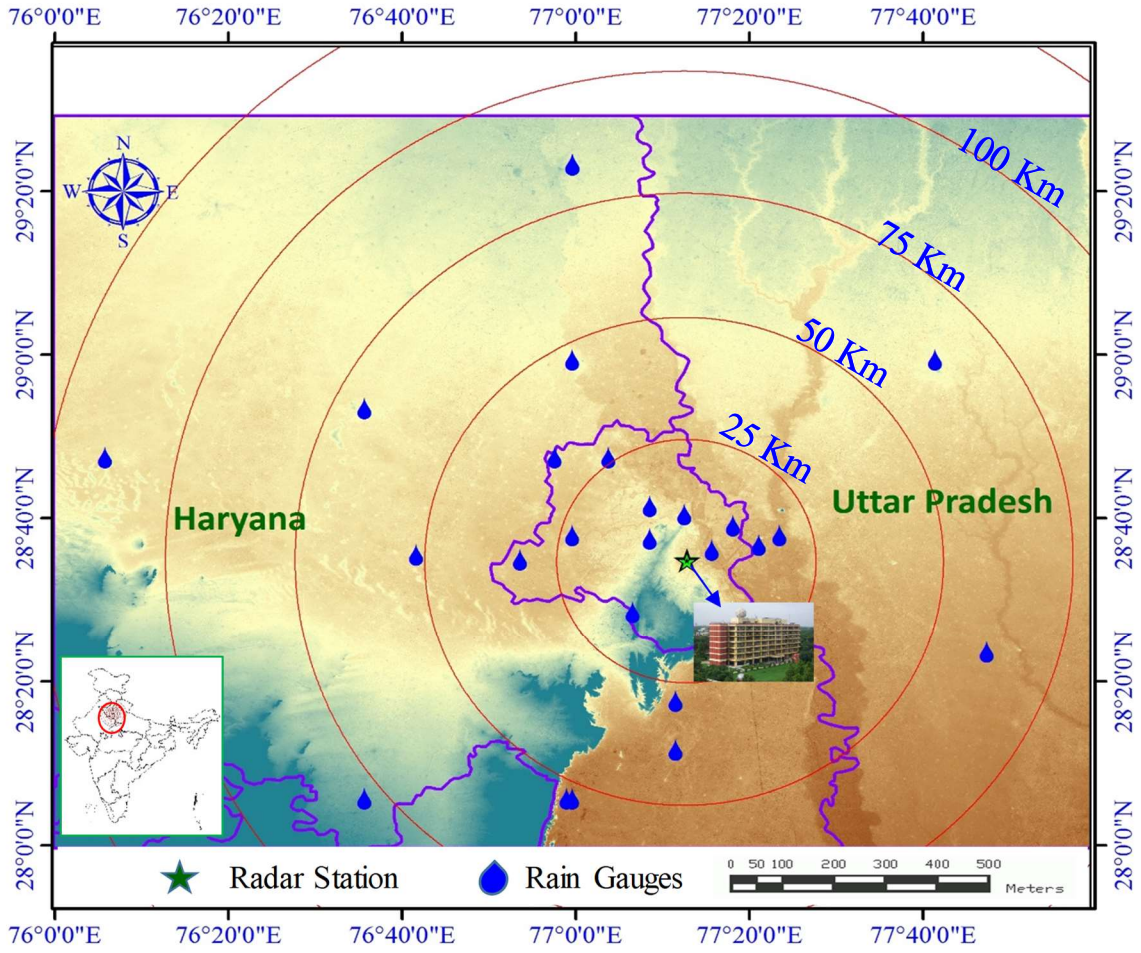

Figure 3.1: Selected study site with a radar coverage over the region, and Automatic Weather Stations with in study region maintained by IMD Mausam Bhawan, New Delhi, with a topography.

It has two eco-climatological zones, monsoon-influenced humid subtropical (Köppen climate type, *Cwa*) and semi-arid (Köppen climate type, *BSh*), surrounded by Aravalli Mountains in its south-west, Eastern Himalayas in the north-east, desert land in north-west, and Yamuna River passing through the city. Every year, two wind branches, namely the Arabian sea and the Bay of Bengal branch, meet and form monsoon troughs over the study area. The average annual rainfall of the study area is approximately 714mm; the majority of contribution is from the Indian monsoon season. The minimum elevation of the study area is around 27m, and highest point is around 607m above the mean sea level.

3.2.2 Weather Radar Data and Processing

The Doppler weather radar data provided by India Meteorological Department (IMD) was used to investigate and establish the Radar reflectivity – Rainfall rate relationship. IMD operates C-band Doppler Weather Radar (DWR) for routine meteorological observations. The radar is located at IMD, New Delhi (28°35′23.28″ N, 77°13′18.84″ E, 253m height above the mean sea level and 36m height above ground level). The general characteristics of DWR are provided in Table 3.1.

Table 3.1: General Characteristics of C-band Doppler Weather Radar considered for the study.

Characteristic	
Wavelength	5.33 cm
Beam Width	0.95°
Pulse Duration	2 μsec
Azimuth speed	10.1788 degrees/sec
Band Width	619 Hz
PRF	600 Hz
Radial Resolution	0.3 km
Azimuthal Resolution	1°
Repetitive	10 min
Vertical Extent	0.5° - 21°
Clear Air mode Scan	500 km
Precipitation mode Scan	250 km

The radar reflectivity data during 2012 and 2013 were collected. The details of the collected data period, number of days, and time are provided in Table 3.2.

Table 3.2: Weather radar reflectivity data collected periods to establish relationship and for validation.

Year	Month	No. of days	Time	Purpose
2013	July	6	00:00 hr. - 18:00 hr.	For relation
	August	12	00:00 hr. - 18:00 hr.	
	September	2	00:00 hr. - 18:00 hr.	
2012	July	3	00:00 hr. - 24:00 hr.	For validation
	August	5	00:00 hr. - 24:00 hr.	

In this study, the radar data and AWS stations within 100*km* radar coverage were considered due to unreliable in radar data beyond 100*km* [Wessels, 1990] and its under-estimation at longer range [Holleman, 2006]. The Constant Altitude Plan Position Indicator (CAPPI) scan was considered at 1500*m* height from the ground. This level is free from ground clutter which is below the melting layer (observed at 3.5*km* from the ground in the study area), and also, the concentration of raindrops sufficiently exists at this level [Wessels, 1990]. The reflectivity values, which are less than 15dBZ in the radar scans were removed. The rainfall rate relates empirically in power-law form with reflectivity value [Marshall and Palmer, 1948; Marshall et al., 1955], which indicates reflectivity less than 15dBZ in a control volume are most likely either non-precipitable or very light precipitation. The sample Plan Position Indicator (PPI) plot with and without (post-processing) considering below 15dBZ reflectivity values for 20th July, 2013 were given in Appendix A1.

3.2.3 Rain Gauge Measured Rainfall Data

Rainfall data for this study was obtained from a network of 24 Automatic Weather Stations (AWS) deployed within the Radar reliable measuring field 100*km* (Fig.3.1, Appendix A2). The AWS network is maintained by the India Meteorological Department (IMD), Delhi. The gauges are evenly distributed, varying from radar station to a most distance of 112*km* (Fig.3.1 and Appendix A2).

Abstract-TH-2793_156104035

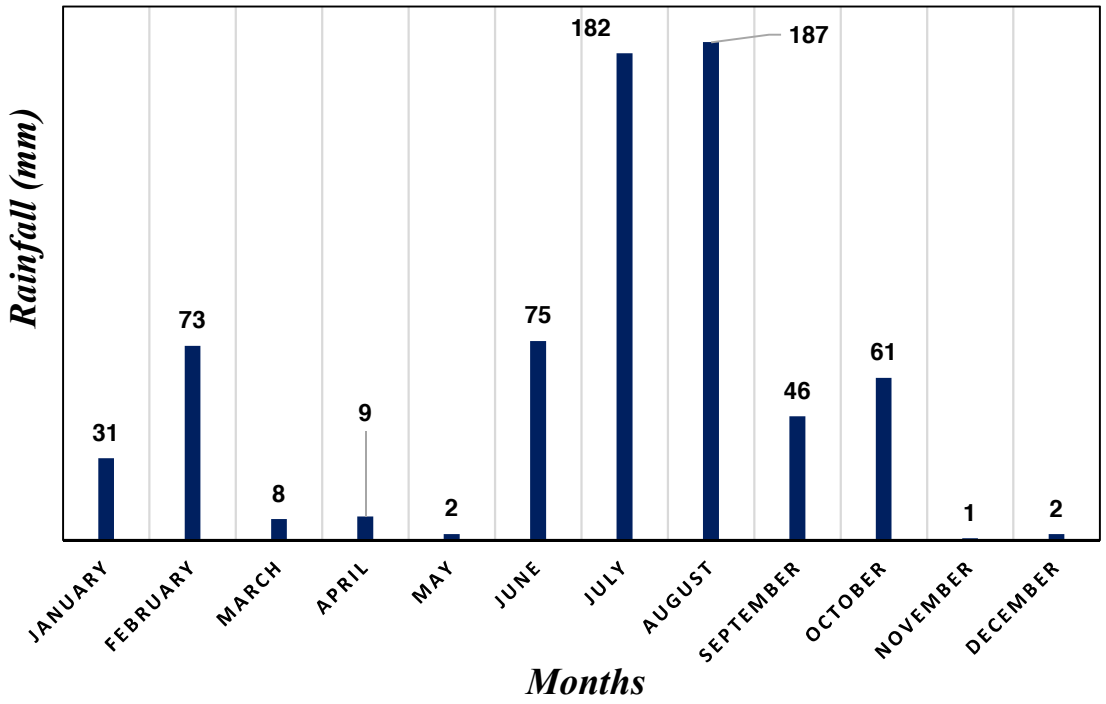

Figure 3.2: Monthly rainfall observed during the year 2013 over a study area with in the radar coverage of 100km.

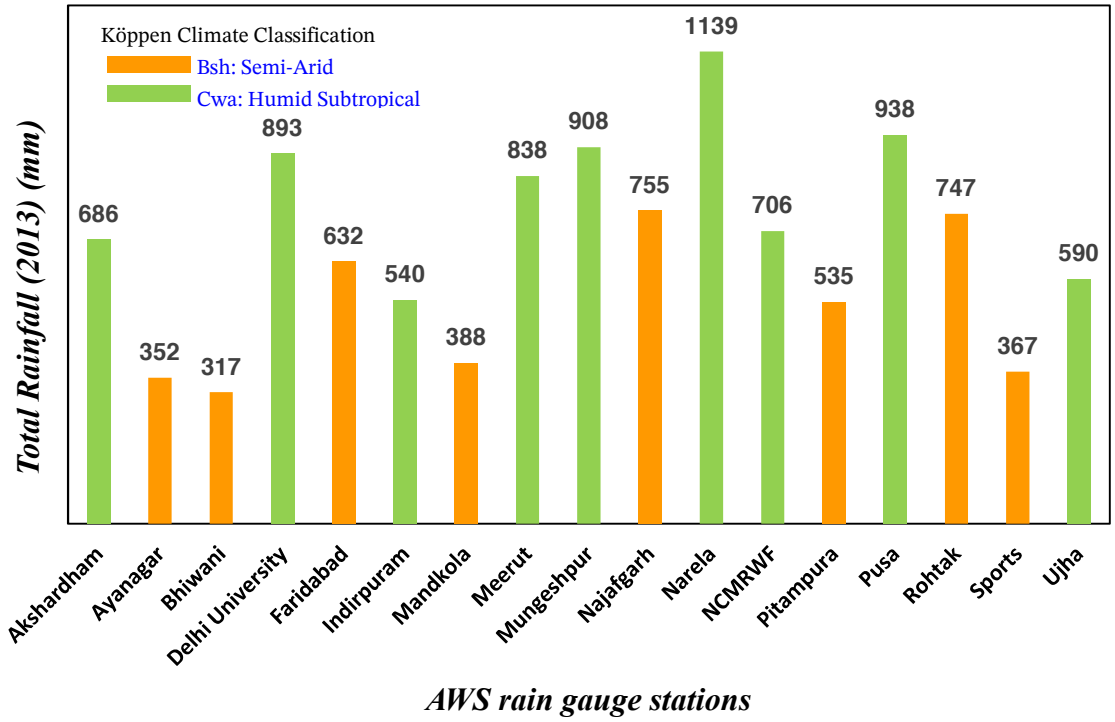

Figure 3.3: Total rainfall amount at all AWS stations observed during the year of 2013, based climate zones.

Abstract-TH-2793_156104035

The AWS gauges record rainfall at every one-hour interval. The monthly rainfall observed in the data collection period is depicted in Figure 3.2. The total amount of rainfall observed during the period 2013 at each station is shown in Figure 3.3.

3.3 METHODOLOGY

Here it described the proposed Gravity – Turbulence based method to establish the parametric Z-R relationship along with existing parametric Marshall-Palmer, TMM, and nonparametric PMM and WPMM methods. The relations were established based on two climatic zones comprised in the study area. Figure 3.4 illustrates the methodology adopted to establish the relationship and validate the proposed method. The detailed description of parametric such as Marshall – Palmer, Traditional Matching Method, and proposed approach empirical power-law equations along with nonparametric methods such as Probability Matching Method and Window Probability Matching Method are given below.

Abstract-TH-2793_156104035

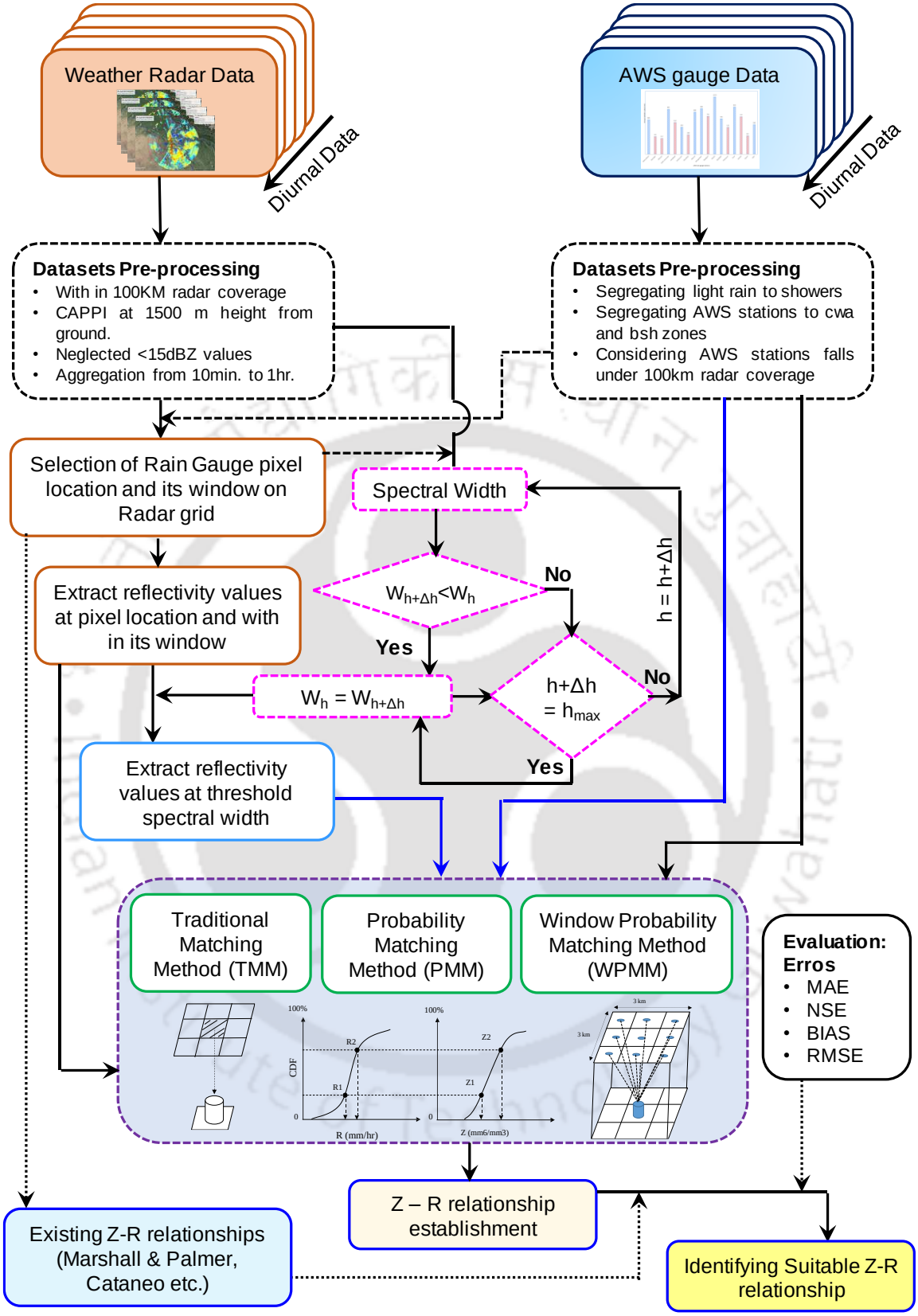

Figure 3.4: The methodological flow chart adopted to establish radar reflectivity – rainfall rate relationship and its validation.

Abstract-TH-2793_156104035

3.3.1 Parametric Z-R Relationship (Traditional Matching Method, TMM)

The reflectivity is the amount of energy backscattered by the raindrops to the weather radar antenna (receiver). The radar reflectivity factor Z, is proportional to the 6th moment of the diameter of the raindrop distribution (Rayleigh Approximation) per unit volume (Sample volume). The drop size is usually measured in mm, and volume is usually expressed in cubic meters. The radar reflectivity factor has units of mm^6/m^3.

$$Z = \int_0^\infty N(D)D^6 dD \qquad \text{(eq. 3.2)}$$

$$dBZ = 10\log_{10}^{(\frac{Z}{mm^6/m^3})} \qquad \text{(eq.3.3)}$$

Where N(D), is number of raindrops per unit volume; D, is diameter of raindrop; Z, is reflectivity factor; dBZ, is reflectivity in decibel (on logarithmic scale).

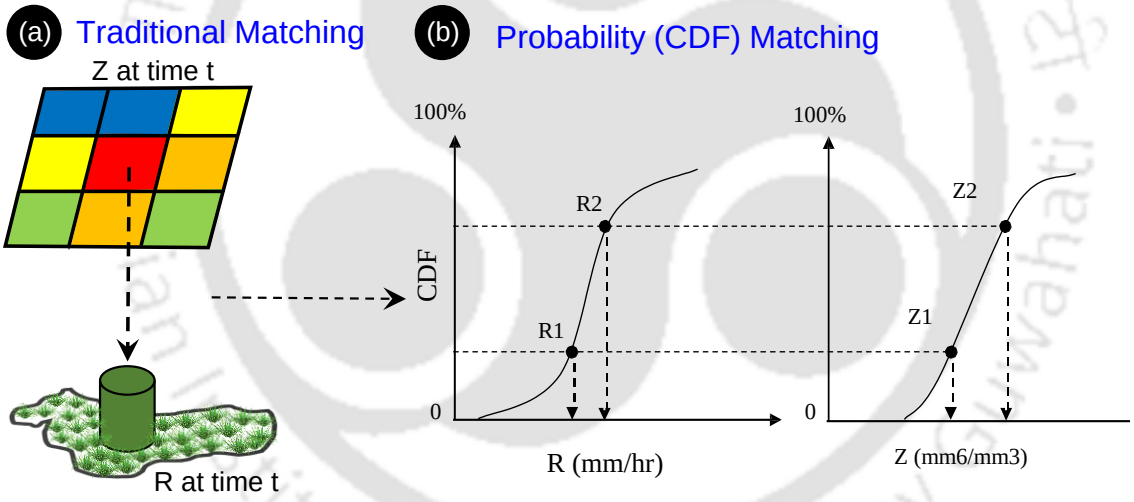

Figure 3.5: (a) Traditional one to one matching of rain gauge to radar pixel to establish parametric power-law relation; (b) probability cumulative distribution wise matching for a particular rain gauge – radar pixel extracted values to establish nonparametric relationship.

Then the reflectivity factor is transformed into the rainfall rate by using the Z-R relationship. With an assumption that the backscattered radar echo has a known distribution of raindrops (precipitation particles) will enable one to convert the reflectivity to rainfall rate, which named as the Z-R relationship [Marshall and Palmer, 1948; Blanchard, 1953; Jones, 1956; Carlson, 1970; Jorgensen and Willis, 1982; Rosenfeld et al., 1993; Fulton et al., 1998; Brommundt & B´ardossy, 2007;

Goudenhoofdt & Delobbe, 2009; Mapiam et al., 2009; Zhang et al., 2011; Looper & Vieux, 2012; Wang et al., 2012; Hasan et al., 2014; Gochis et al., 2015; Kim et al., 2021]. The Z-R relationship is a simple empirical power-law, which is commonly assumed as provided in equation 3.1. The Marshall-Palmer equation has been a widely adopted parametric equation (A = 200 and B = 1.6) worldwide, which was developed based on disdrometer drop size distribution (DSD) data. Here, the Marshall-Palmer equation is also used to compare the present proposed method. Traditionally, the parametric Z-R relationship was developed by applying one-to-one power-law regression between rain gauge measured rainfall to reflectivity value extracted from the radar control volume considered over the rain gauge (Fig.3.5a), which was also used to compare the established relationship using the proposed method.

3.3.2 Gravity-Turbulence Based Proposed Approach (Parametric Relation)

3.3.2.1 *Physical Principle*

Doppler Weather Radar measures the Spectrum Width (W), Velocity (V), and other parameters along with Reflectivity (Z). Spectrum Width (W) measures the dispersion of velocities within the radar scanned control volume. In a situation where shear and turbulence are small within a control volume, the spectrum width will be small vice versa. A technical way of defining spectrum width is the standard deviation of the velocity distribution within a considered control volume. In the atmosphere, during the condensation, the tiny droplets grow and impact with their neighbors as they are carried by shear and turbulent air motion until they become large enough so that the force of gravity overcomes that of shear friction (turbulence force), and they begin to fall. As aforementioned, it can be inferred that there is a more probability of occurrence of rainfall at lower spectral width (lower shear/turbulence) values. So, it is assumed that the cloud cell is matured and ready to give rainfall where the spectral width (turbulence) is optimum. So, the reflectivity – rainfall relationship can be established by considering reflectivity values at a control volume (pixel) where the spectral width values are minimum or designed thresholds. The detailed physical process that acts around raindrop during the coalescence process within radar pixel control volume is shown in Figure 3.6.

Abstract-TH-2793_156104035

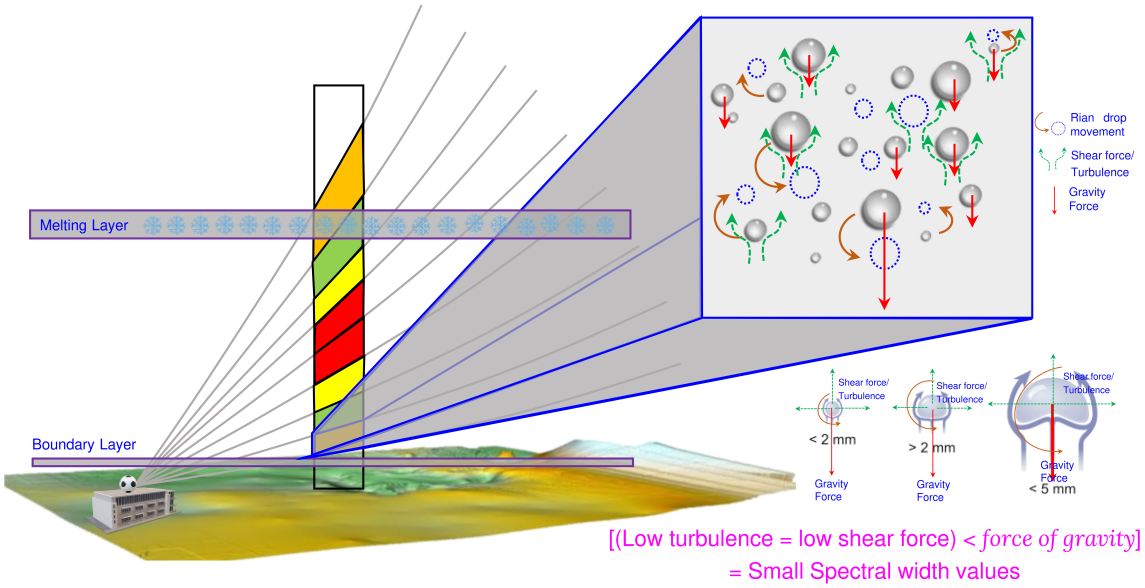

Figure 3.6: Conceptual sketch of Gravity-Turbulence based proposed approach and gravity – Turbulence forces acting on a raindrop within control volume.

3.3.2.2 *Gravity –Turbulence based approach application*

The significant deviation between the accurate point measurement device like rain gauge rainfall and radar pixel over the rain gauge can be detected due to the represented radar pixel rainfall occurring over a particular time, space [Rabiei & Haberlandt, 2015] and unknowing of exact time of contribution of radar pixel towards the earth. The deviation in time and space was addressed previously using PMM and WPMM methods. The uncertainty in identifying the radar pixel that will contribute as a rainfall towards the point measured rain gauge on the earth is still unresolved. Here, the Gravity – Turbulence based on the spectral width thresholds mentioned above is used to establish the Z – R relationship. The detailed flow work to identify the threshold spectral width values and identify the appropriate radar pixel that contributes rainfall towards the point measured rain gauge is shown in Figure 3.4.

Initially, the minimum spectral width values were identified within the vertical structure of radar scanning (from ground clutter free height to melting layer height, Fig.3.6). Then, the reflectivity values were taken where (pixel) the threshold or minimum spectral width criteria satisfied (Fig.3.6). Finally, the power-law regression equation was fitted between extracted reflectivity value and rainfall rate recorded at the rain gauge. The same procedure was adopted for two ecological zones separately.

3.3.3 Nonparametric Z-R Relationship (Probability Matching Method, PMM)

The Probability Matching Method was developed to overcome time deviation and collocation difficulties in TMM [Calheiros & Zawadzki, 1987; Atlas et al., 1997; Rosenfeld et al., 1990]. Here, it is assumed that both reflectivity and rainfall rate follow similar distributions [Rosenfeld et al., 1993; Atlas et al., 1997]. In this method, the synchronized pairs of reflectivity and rainfall rate were derived by matching the CDF curves of both reflectivity and rainfall rate (Fig.3.5b). The matching of both variables at CDF level is shown in Figure 3.5(b), and the equation is given in equation 3.4.

$$\int_{R_i}^{\infty} P(R)dR = \int_{Z_i}^{\infty} P(Z)dZ \qquad \text{(eq. 3.4)}$$

Where, P(R), is the probability density function of gauge measured rainfall intensities; P(Z), is the probability density function of reflectivity; R_i, is the minimum threshold value of rainfall rate (here 1 mm/hr); Z_i, is the minimum threshold value of reflectivity (here 15dBZ).

3.3.4 Nonparametric (Window Probability Matching Method, WPMM)

The window probability matching method was developed to overcome the geometrical mismatch and synchronization difficulties in PMM [Rosenfeld et al., 1994].

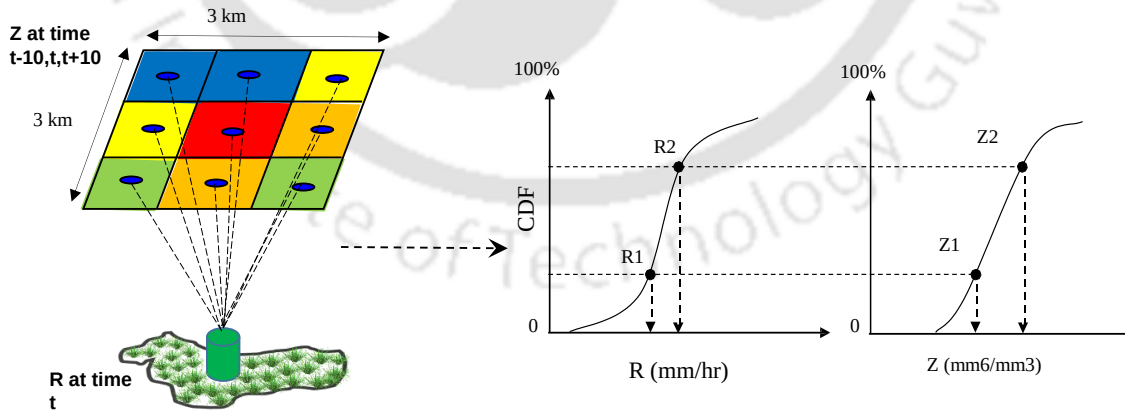

Figure 3.7: The concept of window probability matching method by cumulative distribution wise matching for a particular rain gauge at $3km \times 3km$ window radar pixel extracted values to establish nonparametric relationship.

Abstract-TH-2793_156104035

Here the spatial widow was considered instead of selecting a single radar pixel (Fig.3.7). Then the PMM was followed by taking reflectivity and rainfall rate at space and time window respectively, to match at the same percentile level using CDFs. Here, a $3km \times 3km$ window of radar scan over the point measured rain gauge and one rainfall intensity value of 1hr time window were used for this study (Fig.3.7).

3.3.5 Performance Evaluation

The proposed method was evaluated by quantifying the error metrics. Mean Absolute Percentage Error and Root Mean Square Error are expressed below. The evaluation was done for the 2012 datasets.

$$\mathrm{MAPE} = \frac{Abs\left(R_{metho} - R_{gauge}\right) \times 100}{N \times R_{gauge}} \quad \text{(eq.3.5)}$$

$$RMSE = \sqrt{\frac{1}{n}\sum_{t=1}^{n}\left(R_{meth} - R_{gauge}\right)^2} \quad \text{(eq.3.6)}$$

The proposed method was also compared with the existing Marshall-Palmer, Traditional Matching Method, Probability Matching Method, and Window Probability Matching Method using the above error metrics.

3.4 RESULTS and DISCUSSION

The Z-R relationships were established with the proposed Gravity – Turbulence threshold spectral width method and evaluated using MAPE and RMSE error metrics, compared with the existing Marshall – Palmer parametric power-law equation, nonparametric PMM, and WPMM methods. All parameters and synchronization pairs obtained and computed error metrics are discussed in the sections given below.

3.4.1 Gravity – Turbulence based Z – R Relationships

Six different scenarios were investigated using this method to match Z – R pairs and establish the Z – R relationship. Here, the method was tested for some particular, extreme events only. Two extreme rainfall event days, namely 20 July 2013 and 16 August 2013, were considered for the study. The six scenarios TMM with and without

Abstract-TH-2793_156104035

considering threshold spectral widths for the humid subtropical region, Semi-Arid region, and all stations.

It was observed that the overall minimum spectral width identified by the C-band weather radar is 0.031 *m/s*; the other spectral width values are its multipliers. The overall maximum spectral width value identified by the C-band weather radar was observed as 0.62 *m/s*, which is 20 times greater than the minimum spectral width. The minimum and maximum spectral width values depend on the local weather conditions and vary for each storm and in each vertical column of radar scan over a rain gauge. Initially, it was assumed that the regression fit between two variables, Z and R, must be given at minimum spectral width value. Interestingly, it was found that the best regression fit was observed at the second minimum spectral width value for every event and every station. The weighted reflectivity was then calculated by giving the weightage of minimum and second minimum spectral widths within the vertical column (in between boundary layer to melting layer) over each rain gauge station during the considered period.

The power-law regression equations were obtained for above-considered scenarios. The parameters A and B in the power-law equation were estimated for different scenarios and the results are presented in Table 3.3, and fitted curves are shown in Figures 3.8.

Table 3.3: Parameters A and B in radar reflectivity and rainfall rate relationship (eq.3.1) for different scenarios considered based on two ecological zones.

Scenario	Parameters		Correlation Coefficient
	A	B	R^2
TMM	561	1.2	0.62
TMM with SW	544	1.2	0.70
TMM at *Cwa*	563	1.3	0.67
TMM at *Cwa* with SW	543	1.3	0.77
TMM at *Bsh*	849	0.95	0.49
TMM at *Bsh* with SW	685	1.04	0.55

*TMM: Traditional Matching Method; SW: Spectral Width; *Cwa*: Humid Subtropical climate; *Bsh*: Semi-Arid climate

Abstract-TH-2793_156104035

The parameter B did not vary for with and without considering spectral width thresholds. The parameter A also not vary much. However, the correlation coefficient increased after applying threshold spectral width criteria. Here, it was tested for only two events, by taking a large number sample might have indicated the impact of considering reflectivity value at threshold spectral width.

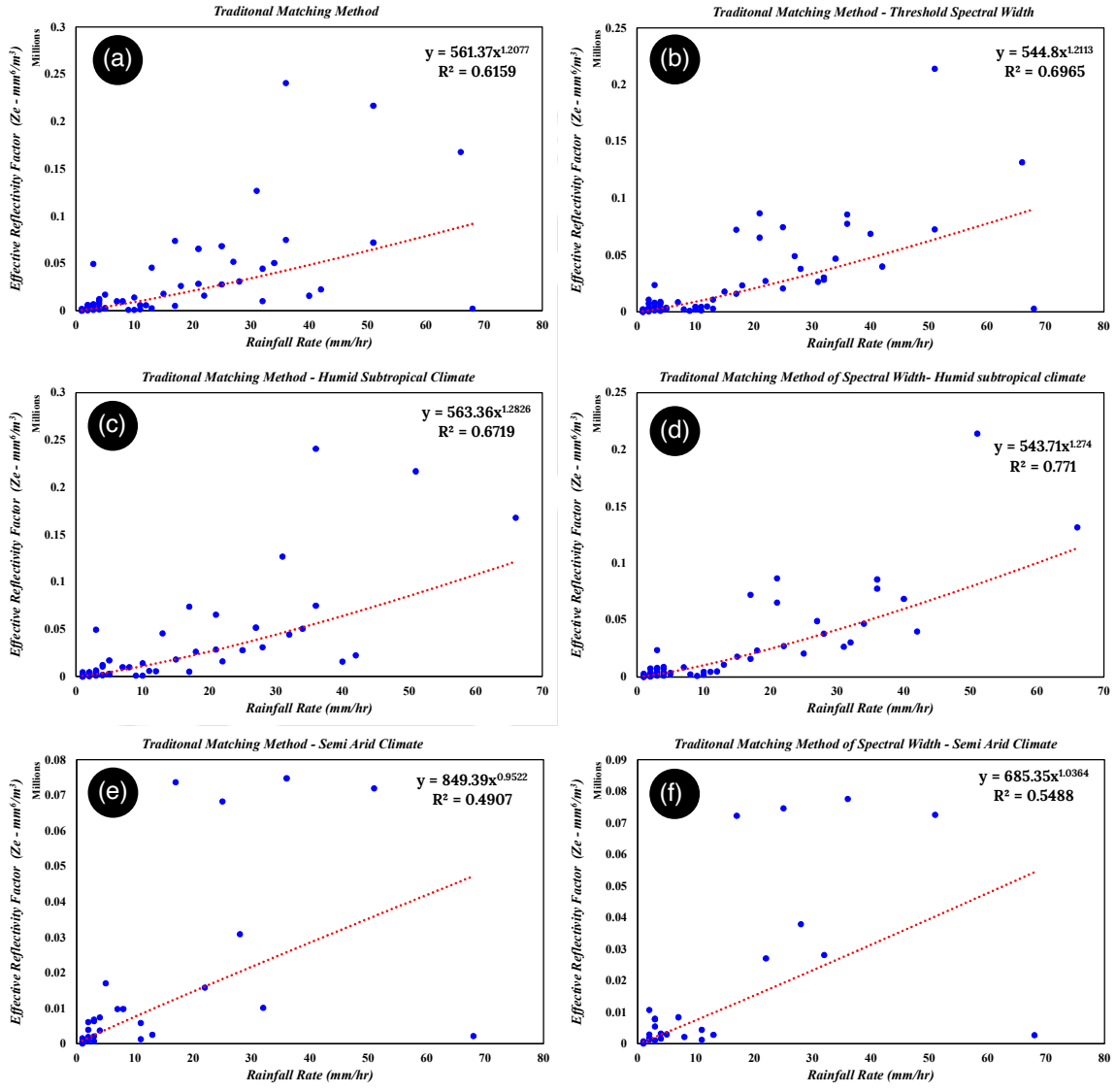

Figure 3.8: Scatterplots and power-law regression fits of radar reflectivity – rainfall rate relationship for formulated scenarios: a) Traditional Matching Method; b) Traditional Matching Method considering spectral width threshold; c) Traditional Matching Method in humid subtropical climate zone; d) Traditional Matching Method considering spectral width threshold in humid subtropical climate zone; e) Traditional Matching Method in semi-arid climate zone; f) Traditional Matching Method considering spectral width threshold in semi-arid climate zone.

Abstract-TH-2793_156104035

The parametric relationship with TMM was established by considering all rainfall events on all AWS stations (Table 3.2). The established general power-law parametric equation with enormous data shown poor regression fit with a coefficient of determination 0.27 (Fig.3.9). The power-law parameters A and B were estimated as 203 and 0.34, respectively. The parameter A nearly matching with Marshall – Palmer parameter A (200), but a significant variation was observed in parameter B, which is 1.64 in Marshall – Palmer equation.

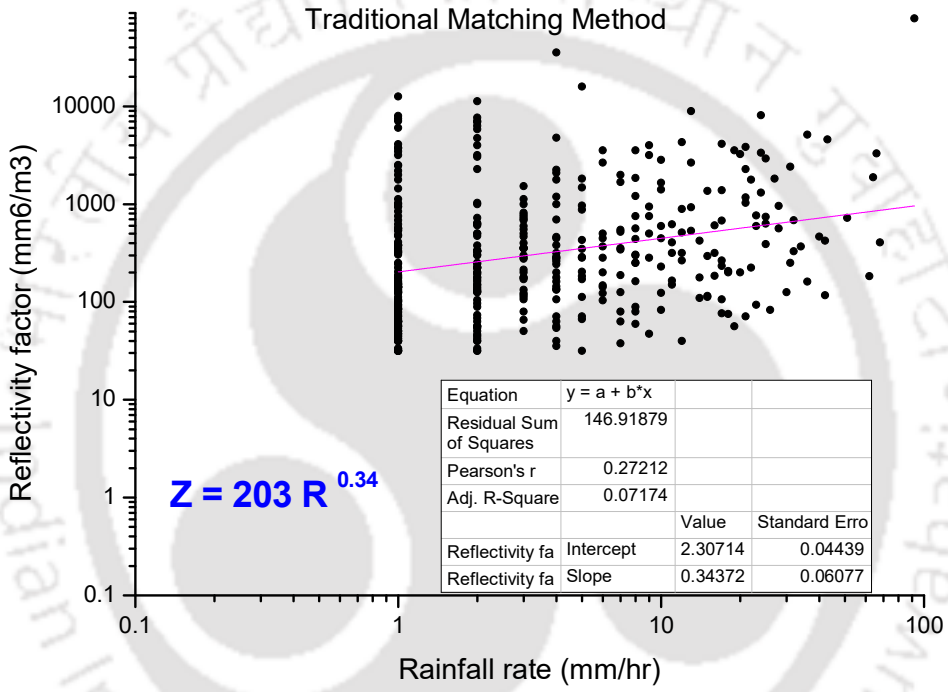

Figure 3.9: Scatterplots and power-law regression fits of radar reflectivity – rainfall rate relationship by Traditional Matching Method by considering all rainfall event days (Table 3.2).

3.4.2 Probability Matching Method based synchronized pairs

The probability synchronized pairs between rainfall and reflectivity were developed with the probability percentiles or cumulative distribution function (Fig.3.10). The parametric Z – R relationship was established with generated pairs to represent and to compare developed pairs with TMM and developed methodology (Fig.3.11). Here, the power-law regression equation was established by dividing the rainfall into two broad categories (Stratiform and Convective) and three subcategories (<30dBZ, 30-40dBZ, and >40dBZ) based on reflectivity values (Fig.3.11). The

Abstract-TH-2793_156104035

computed parameters A and B from nonparametric synchronized pairs are represented in Table 3.4. The degree of fit of the relationship based on PMM was measured in terms of correlation coefficient and presented in Table 3.5.

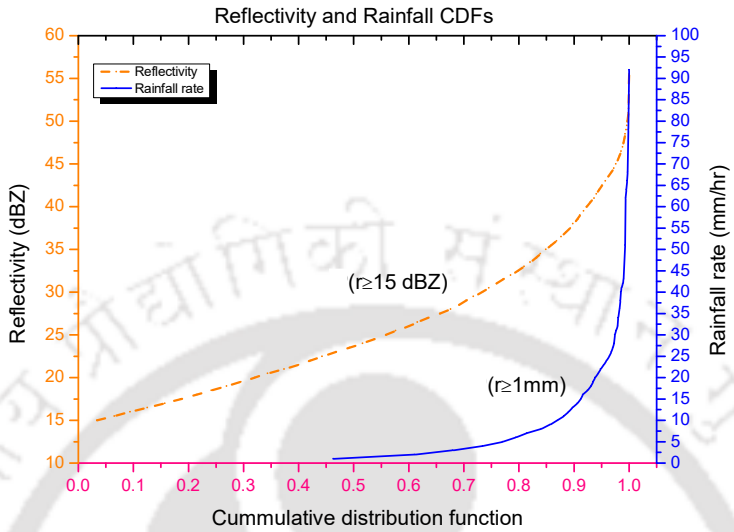

Figure 3.10: The probability pairs (cumulative distribution functions) generated for both rainfall rate (threshold 1 *mm/hr.*) and reflectivity (threshold 15dBZ) at point rain gauge to single radar pixel for probability matching method by considering all rainfall event days.

Table 3.4: Parameters A and B in reflectivity and rainfall rate relationship (eq.3.1) computed from nonparametric synchronized pairs for different storm types by PMM and WPMM.

Storm Category	PMM		WPMM	
	A	B	A	B
< 30dBZ (stratiform)	182	1.19	254	0.82
30-40dBZ (convective)	100	1.62	94	1.37
>40dBZ (convective)	45	1.92	40	1.62

Table 3.5: Pearson's r of Z – R pairs for different storm categories for PMM and WPMM methods.

Storm Category	PMM	WPMM
< 30dBZ (stratiform)	0.9972	0.9971
30-40dBZ (convective)	0.9983	0.9938
>40dBZ (convective)	0.9905	0.9642

Abstract-TH-2793_156104035

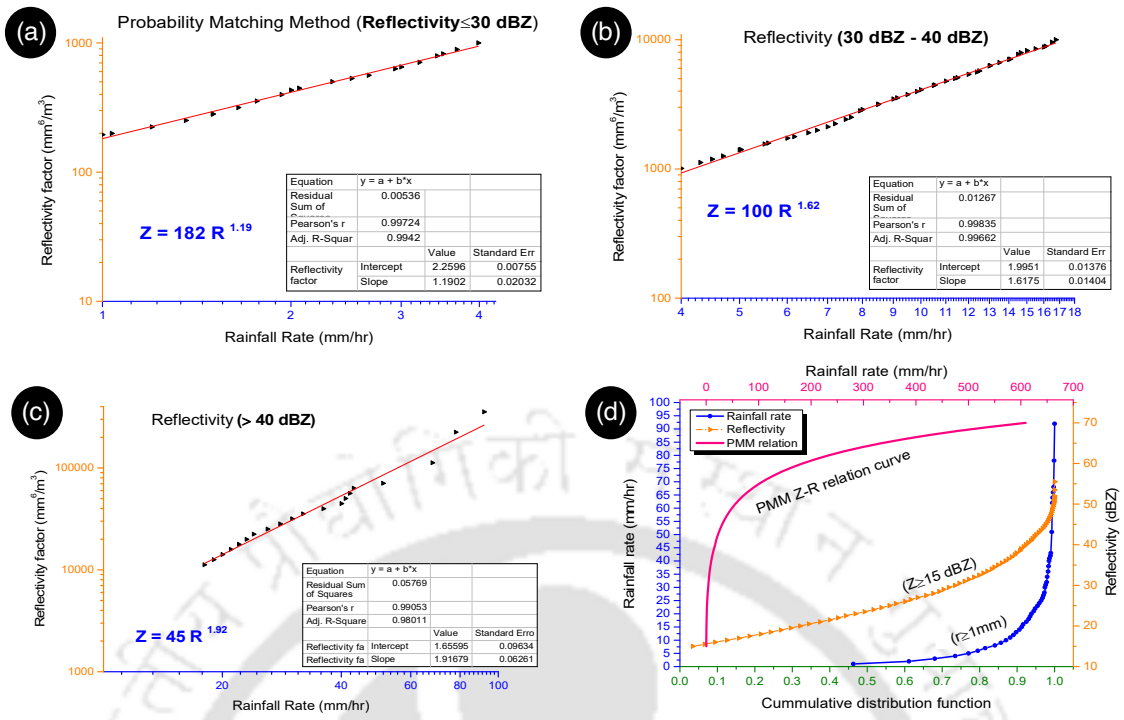

Figure 3.11: Power-law regression fits of radar reflectivity – rainfall rate relationship established with a value extracted from PMM probability percentiles: a) For < 30dBZ (stratiform); b) 30-40dBZ (convective); c) >40dBZ (convective); d) Synchronized pair curve established with PMM method.

Table 3.4 for PMM indicates that with an increase in reflectivity (stratiform to convective), the value of parameter 'A' decreased whereas the value of parameter 'B' increased. However, parameter 'B' is not much varied as compared to parameter A.

3.4.3 Window Probability Matching Method based synchronized pairs

The probability synchronized pairs between rainfall and reflectivity were developed with the probability percentiles or cumulative distribution function (Fig.3.12) by taking reflectivity values from a $3km \times 3km$ window. The parametric Z – R relationship was established with generated pairs to represent and to compare developed pairs with TMM and developed methodology (Fig.3.13). Here, the power-law regression equation was established by dividing the rainfall into two broad categories (Stratiform and Convective) and three subcategories (<30dBZ, 30-40dBZ, and >40dBZ) based on reflectivity values (Fig.3.13). The computed parameters A and B from nonparametric synchronized pairs are represented in Table 3.4. The degree of fit of the relationship based on PMM was measured in terms of correlation coefficient and presented in Table 3.5.

Abstract-TH-2793_156104035

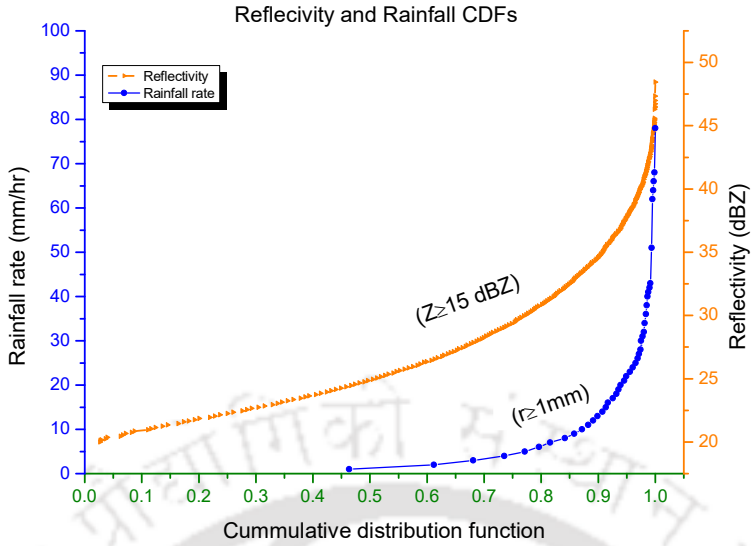

Figure 3.12: The probability pairs (cumulative distribution functions) generated for both rainfall rate (threshold 1 *mm/hr.*) and reflectivity (threshold 15dBZ) at point rain gauge to single radar pixel for window probability matching method by considering all rainfall event days.

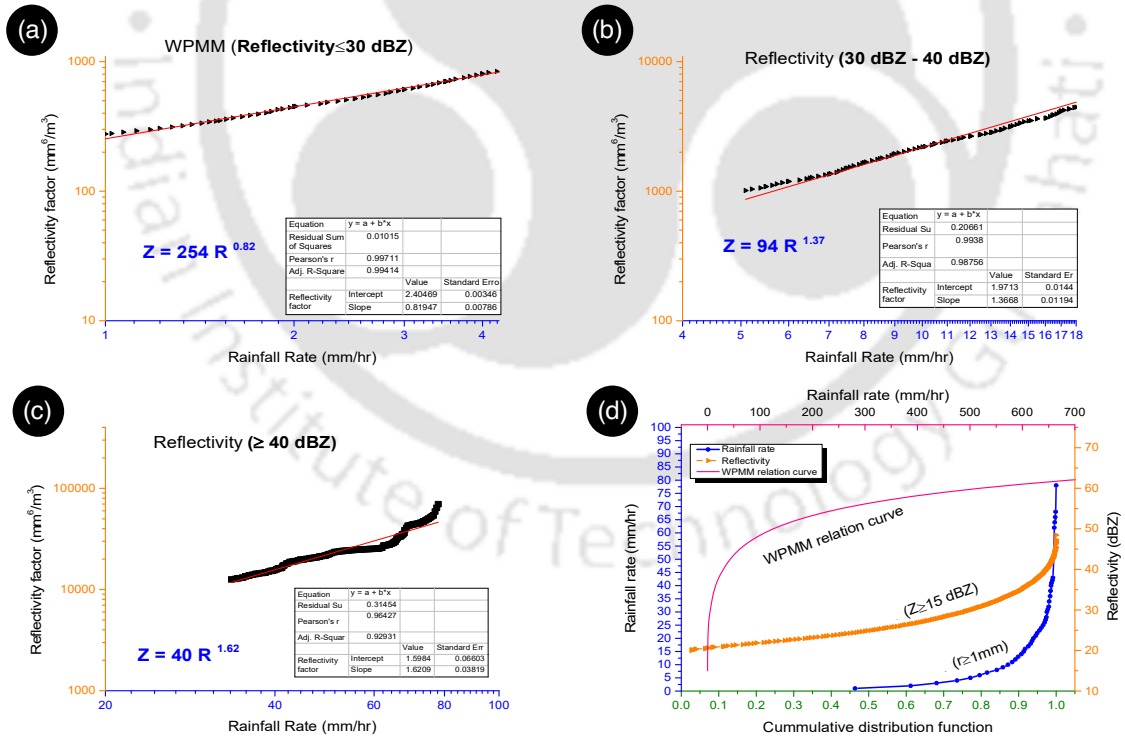

Figure 3.13: Power-law regression fits of radar reflectivity – rainfall rate relationship established with a value extracted from WPMM probability percentiles: a) For < 30dBZ (stratiform); b) 30-40dBZ (convective); c) >40dBZ (convective); d) Synchronized pair curve established with PMM method.

Table 3.4 for WPMM indicates that with an increase in reflectivity (stratiform to convective), the value of parameter 'A' decreased, whereas the value of parameter 'B' increased. However, parameter 'B' is not much varied as compared to parameter A.

3.4.4 Accuracy Assessment (Evaluation) and Comparison

The Z – R established from the proposed Gravity – Turbulence based method is compared with those existing parametric Marshall – Palmer and TMM method equations and with nonparametric PMM and WPMM methods using error metrics MAPE and RMSE. The error metrics computed for all methods for different storm categories are presented in Table 3.6 and Table 3.7.

Table 3.6: Error metrics Mean Absolute Percentage Error (MAPE) computed for each method.

MAPE (%)	TMM	PMM	WPMM	Proposed Method	Marshall-Palmer $Z = 200\ R^{1.6}$
Average overall error	640.61	≈ 26	≈ 48	≈ 16	≈ 28
< 30dBZ (stratiform)	78.68	≈ 18	≈ 32	≈ 12	≈ 13
30-40dBZ (convective)	1019.77	≈ 28	≈ 57	≈ 18	≈ 33
>40dBZ (convective)	No data in 2012	No data in 2012	No data in 2012	No data in 2012	No data in 2012

Table 3.7: Error metrics Root Mean Square Error (RMSE) computed for each method.

RMSE (mm/hr)	TMM	PMM	WPMM	Proposed Method	Marshall-Palmer $Z = 200\ R^{1.6}$
Average overall error	-	21.59	30.97	16.21	22.58
< 30dBZ (stratiform)	-	0.70	0.85	0.55	0.62
30-40dBZ (convective)	-	22.87	34.69	18.55	24.76
>40dBZ (convective)	No data in 2012	No data in 2012	No data in 2012	No data in 2012	No data in 2012

The proposed method is estimating rainfall rate with minor errors than other methods. It has shown 16% overprediction for all storms combined, while other

Abstract-TH-2793_156104035

methods overpredicted with an error of more than 25%. The estimated Z – R relationship using TMM has given the largest MAPE of 640. All methods performed well with an error of RMSE < 0.8 *mm/hr* for the stratiform precipitation. There was not much difference found between proposed and Marshall-Palmer equations for stratiform storms. It indicates that the Marshall-Palmer equation is well suited for stratiform precipitation. Moreover, all methods showed high error for convective storm with RMSE > 19 *mm/hr*. However, the proposed method has given minor errors comparative to other methods for the convective type of precipitation.

3.5 CONCLUSIONS

In recent decades, weather radars have become an essential tool to design flood early warning systems, especially for flash floods in both urban and mountainous regions, where the density and in-advance quantitative estimation of point gauge measurements are insufficient. The errors in quantitative estimation of rainfall using radars due to difficulties in converting radar received signal measurements to rainfall rates. Even though numerous Z – R relationships were developed based on region and season, numerous bias correction techniques also evolved; it is still quite challenging to retrieve rainfall rates from radar reflectivity. It is due to the highly dynamic nature of raindrop size distribution even within a single storm event [Ulbrich, 1993; Smith et al., 2009]. In recent years, dual-polarization radars have a capability to identify the dynamic nature of raindrop size distribution by collecting additional information on raindrops. However, the advanced technologies have not changed the existence of inherent limitations in converting reflectivity to rainfall rate due to indirect measurement of rainfall and well above the ground with the radar [Ochoa-Rodriguez et al., 2019]. In this study, a Gravity – Turbulence-based method was developed to reduce the error in converting reflectivity to rainfall by selecting appropriate radar pixel, which will contribute rainfall towards the ground. This method is dependent on the identified thresholds of spectral width values. The parametric Z-R relationship was established with the proposed method for two different ecological zones. The relationship was compared with the existing parametric relationships such as Marshall-Palmer, TMM method, and nonparametric methods PMM and WPMM. The proposed method has shown better performance than all other methods with an error of 16% for overall storms, 12% for stratiform storms, and 18% for convective storms.

Abstract-TH-2793_156104035

The method was applied with limited data due to the unavailability of large datasets at present. This method was applied on the single-polarization radar due to the unavailability of dual-polarization radar data. In the future, the method has to be applied over large datasets and for dual-polarization radars. It might increase the accuracy of the rainfall estimation from radar reflectivity.

भारतीय प्रौद्योगिकी संस्थान गुवाहाटी • Indian Institute of Technology Guwahati •

Abstract-TH-2793_156104035

This Page Intentionally Left Blank

Abstract-TH-2793_156104035

4

REFLECTIVITY HYETOGRAPH PREDICTION

(Hierarchical Supervised Machine Learning based Stochastic Generation and Prediction of High Intensity Rainfall Hyetograph)

Abstract-TH-2793_156104035

4.1 INTRODUCTION

The severely localized high-intensity rainfall events in a short time usually trigger unprecedented natural disasters such as flash floods resulting in severe losses of life and property [Moon et al., 2019]. The flash flood induced by high-intensity rainfall can also cause significant disruption to the day-to-day human activities and traffic in heterogeneous urban landscapes. The probability of such flash flood events across the world shown in an increasing tendency [Karl et al., 1998; Easterling et al., 2000; Manton et al., 2001; Pattanaik & Rajeevan, 2010]. The local scale convective systems are most responsible for producing such type of extreme rainfall induced flash floods [Leon et al., 2016]. Even medium intensity rainfall produced due to the short-term mesoscale convective system can create flash flood scenarios over heterogeneous urban landscapes. It is of utmost importance to predict these localized short-term extreme rainfall events in advance so that decision makers can take action to protect life, property and prosperity.

A short-term rainfall forecasting within the next 0-6 *hours* is often referred as Nowcasting [WMO, 2019] which is widely used as part of the flash flood forecasting and early warning to be issued in an extreme event [Yu et al., 2017]. Nowcasting of localized mesoscale convective precipitation has long been an important problem in the field of weather prediction, and it has emerged as a burning research topic in the weather forecast community [Shi et al., 2015]. The Nowcasting of short-term convective precipitation is still a challenging task for the metrological community even though much progress has happened over the past several decades [Han et al., 2017]. Unlike short-range and long-range forecasting, Numerical Weather Prediction (NWP) models with satellite and ground observed variables are not much useful in nowcasting of localized short-term convective events due to their fast growth and dissipation over a small area. The weather radars can provide an extensive measurement of such events more precisely due to their high spatial and temporal resolutions. There is uncertainty in its estimation using weather radar mode [Zhang et al., 2016]. However, it is the only measurement mode that detects less than the meso-beta scale short term events. Therefore, various radar-based nowcasting algorithms have been developed to assist nowcasters in severe weather warning [Joe et al., 2004; Han et al., 2019]. The existing Nowcasting methods can be classified into several categories: radar image and eco extrapolation, statistical methods, NWP models, blend of NWP with extrapolation

Abstract-TH-2793_156104035

techniques and newly emerged machine learning models [Wilson et al., 1998, 2010; Sun et al., 2014; Han et al., 2017].

Extrapolation of radar imagery [Todini et al., 2005] includes optical flow technique [Gibson, 1950; Germann & Zawadzki, 2002; Bowler et al., 2004; Liu et al., 2015], linear regression including probabilistic information [Antolik, 2000; Appleqist et al., 2002; Sokol, 2006], logistic regression technique [Appleqist et al., 2002] with the ensemble mean [Hamil et al., 2004], quantile regression statistical method enhancing the Numerical Weather Prediction (NWP) model outputs [Bermnes, 2004] and, similar quantile regression technique used for statistical downscaling of extreme precipitation [Friederichs and Hense, 2007]. Some statistical forecasting techniques are based on Bayesian approaches [Sloughter et al., 2007], and other stochastic schemes [Andersson & Ivarsson, 1991; Schmid et al., 2000; Seed et al., 2013; Atencia & Zawadzki, 2014; Foresti et al., 2015]. NWP based models include NWP outputs with radar data [Cluckie et al., 2006], analog prediction to effectively process the ensemble forecasts by NWP models [Wu & Lin, 2017]. The blend of the NWP model with other methods includes NWP results blended with the probabilistic method [Kober et al., 2012]. However, the NWP models have significant limitations for Nowcasting, with high computational cost, in the spatial domain, in temporal resolution, its frequency, amount of ensemble members, its sensitive to the initial condition, assimilation data, and spin-up problem [Golding, 1998; Mecklenburg et al., 2000; Zahraei et al., 2013]. These may cause the low accuracy in the prediction of localized short-term convective events. The success of the optical flow technique is also limited due to its separation of flow estimation step and radar echo step, which made it complex to determine the model parameters [Shi et al., 2015]. The aforementioned techniques are also lacking in predicting growth and dissipation with the time of occurrence of peak of a local scale convective storm. The radar echo extrapolation techniques allow to nowcast convective storm with its growth and dissipation. It made them superior to other conventional methods and is widely used by weather forecasters.

These methods mainly work on the principle of field advection of radar echoes and several extrapolation schemes. The deterministic nowcast postprocessing, analogue approach and stochastic approaches are the main category of models. The TREC (Tracing of Radar Echoes by Correlation) based on cross correlation method [Rinehart & Garvey, 1978; Smythe & Zrnic, 1983; Tuttle & Foote, 1990], COTREC

Abstract-TH-2793_156104035

(Continuity of TREC vectors) [Li et al., 1995; Schmid et al., 2000; Novak et al., 2009], Eulerian and lagrangian persistence [Dixon & Wiener, 1993; Germann & Zawadzki, 2002] for advection and MAPLE (McGill Algorithm for Precipitation Nowcasting by Lagrangian Extrapolation) [Bellon & Austin, 1978; Germann & Zawadzki, 2002, 2004; Turner et al., 2004] are some of the deterministic approaches. These are the area based algorithms based on field advection of radar echoes with extrapolation scheme. The S-PROG (Spectral Prognosis) [Seed, 2003] and STEPS (Short Term Ensemble Prediction System) [Bowler et al., 2006; Seed et al., 2013] are stochastic ensemble approaches. These approaches are mainly dependent on advection assimilated with spectral decomposition. These stochastic approaches temporal evolution and which blends with the downscaled NWP model outputs mainly STEPS [Bowler et al., 2006; Seed et al., 2013]. Some of other models such as TITAN [Dixon & Wiener, 1993] and SCIT (Storm Cell Identification and Tracking) [Johnson et al., 1998] which identifies and tracks individual storms and produces nowcasts based on tracking information and its extrapolation [Han et al., 2017; Han et al., 2019]. Other models like TRACE3D [Handwerker, 2002], CELLTRACK [Kyznarová, & Novák, 2009] and CAPS [Kong et al., 2011] have also been developed. In convective storm condition, cell tracking algorithms show higher skill than the area based tracking algorithms, as the convective cloud motion often differs from the surrounding cloud motion [Wilson et al., 2004; Pierce et al., 2005; Kyznarová, & Novák, 2009]. The evolution in precipitation quantity during its growth and dissipation of convective cloud also differs from the surrounding clouds. The area and cell based algorithms which smoothens the local scale clouds by considering as noise while performing overall scene. However, in recent times STEPS is implemented in most parts of the world and is the mostly used model [Shakti et al., 2015; Foresti et al., 2016]. The performance of these traditional nowcasting methods is limited by their underlying physical assumptions and they partially represent the true atmospheric state. These extrapolation techniques are not able to forecast convective storm initiation, and have limited growth and decay identification of convective storm [Dixon & Wiener, 1993; Wilson et al., 2010].

In recent years, the application of machine learning and deep learning approaches in nowcasting are emerged to predict short-term convective events without making any assumptions of physical atmospheric state. These approaches have great flexibility in demonstrating nonlinear processes and are computationally inexpensive

Abstract-TH-2793_156104035

[Yu et al., 2017]. The machine learning approaches such as Random Forest, SVM [Han et al., 2017; Yu et al., 2017], Convolutional LSTM [Shi et al., 2015], CNN [Han et al., 2019] are greatly used to nowcast the convective precipitation. However, the existing machine learning methods are not accurate at very close steps compared to traditional methods [Yao et al., 2020] and these approaches neglect the physical state of atmospheric conditions. These approaches still need further improvements in many aspects. Moreover, we also observed the existing traditional echo extrapolation and newly emerged machine learning models lack in prediction of accurate quantitative precipitation (predictors) even though they nowcast accurately with position, size and speed (classifiers). It can be noticed that the quantitative prediction of localized mesoscale convective rainfall is more important for forecasting of devastated flash flood especially in heterogeneous urban landscapes. The fusion of atmospheric physical processes into machine learning model may help to improve the predictions of local weather quantitatively and accurately.

In this research, we focused on quantitative prediction than its tracking, where other methods lacks. The developed approach works at storm hyetograph level instead at radar imagery level. This study was performed keeping in view the needs of both meteorologists for weather nowcast and hydrologists for management and design purposes. The stochastic synthesis and prediction of storm hyetograph satisfies the both present and future needs of hydrologists and meteorologists. As of now, the storm hyetograph synthesis and its approximation are usually developed and performed at ground observed rain gauge station level. Here we developed and performed at atmospheric level with weather radars. So, the objective of this study is to provide effective real-time high intensity rainfall to forecast flash floods and to synthesis the storm hyetographs to develop “design storms” used for flood risk assessment. For this purpose, we proposed a hierarchical machine learning based stochastic approach with Maxwell approximation at hyetograph level by separating convective baby rain cells for nowcasting of real-time radar derived storm hyetograph. The rest part of this chapter is organized as follows. The second section presents the methodology and the development of real-time radar-derived rainfall hyetograph prediction. Section 3 describes the study area, datasets, pre-processing and extraction of datasets. Section 4 includes results, discussion, evaluation, and prediction performance of model. Finally, section 5 summarizes the main conclusions and limitation of the work.

Abstract-TH-2793_156104035

4.2 METHODOLOGY

4.2.1 Hierarchical Machine Learning Approach

Here, the hierarchical machine learning can be treated as a supervised machine learning problem. The Figure 4.1 shows detailed work flow of hierarchical machine learning approach for synthesis and prediction of convective storm hyetograph. In the hierarchical branching the primary task engagement is designed for hyetograph synthesis which can be used for training the data during prediction of extreme storm hyetograph. The secondary task engagement is used for prediction purpose during real time events. In the first hierarchical branching of primary task segment the convective baby cells were separated with image processing techniques (detailed explanation in next sections). In next hierarchy the hyetographs (time vs reflectivity) were prepared and then approximated with Maxwell approximation. The detailed explanation of synthesis of hyetograph (primary task engagement of hierarchical) is explained in subsequent sections.

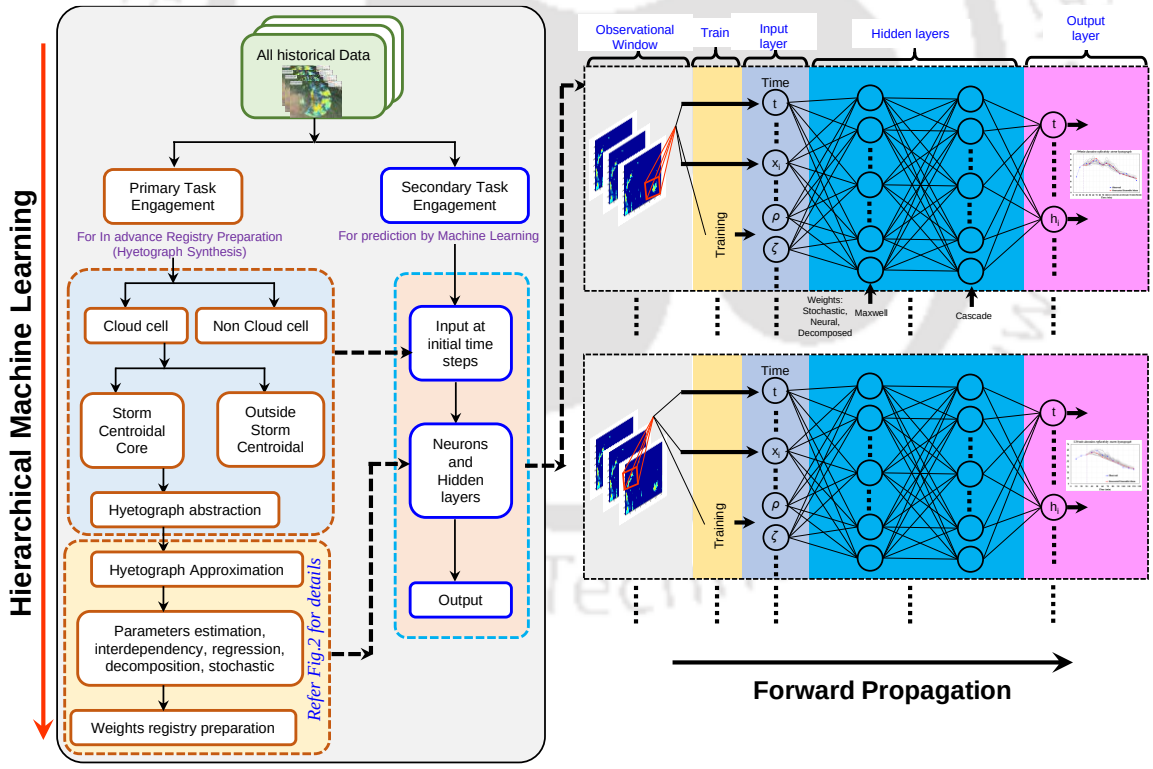

Figure 4.1. Architecture of proposed hierarchical machine learning approach to synthesis and predict high intensity storm hyetograph.

In the secondary task engagement of our hierarchical model, we solve the problem using synthesized parameters and stochastic nature of random variables. Our

Abstract-TH-2793_156104035

developed machine learning approach is child of general “Random Forest” machine learning approach. In this Random Forest child machine learning approach, the ensembles were generated by approximating the hyetographs with Maxwell equation and with random variables by creating weightages from the training of observed data at initial time steps. In this approach only, forward propagation was considered due to availability of less training datasets. The subsequent subsections provided the detailed explanation of hyetograph synthesis and evaluation procedure of developed model (Fig.4.3).

4.2.2 Storm Reflectivity Hyetograph Analysis

The central core of the storm cell specifies the high volume of precipitable water ultimately which displays the high reflectivity values in weather radar data. The futuristic estimation of this reflectivity core (RCs) of a storm cell can be helpful in Nowcast of precipitation which causes flash floods. The centroidal reflectivity core (RCs) of a storm cell fluctuates with time for a particular storm. In this study, the time series of the Centroidal radar reflectivity core (RCs) value is coined as “Reflectivity Hyetograph”. This study introduces a new approach to Nowcast the high intensity of precipitation by predicting the extended path of Reflectivity Hyetograph. The typical Reflectivity Hyetograph shown in Figure 4.2 is observed from extracted data of C-band weather radar.

Several fluctuations were noticed in the Reflectivity Hyetograph spectrum as shown in Figure 4.2. Similar patterns in Reflectivity Hyetograph were observed for all collected storms over an area and time. The possible primary cause for these fluctuations may be the turbulence and coalescence process happen inside the clouds. The condensation and aggregation of cloud droplets can increase the reflectivity value in a control volume and downpour of water droplets to the ground or disaggregation in droplets can decrease the back-scatter energy in a considered control volume. We state that this particular condensation-disaggregation-evaporation-downpour cycles might have caused fluctuations in reflectivity hyetograph. In this study, we broke down the reflectivity hyetograph into two wave spectrums and coined the terms “Atmospheric” and “Turbulent” waves (Fig.4.2) to each component.

Abstract-TH-2793_156104035

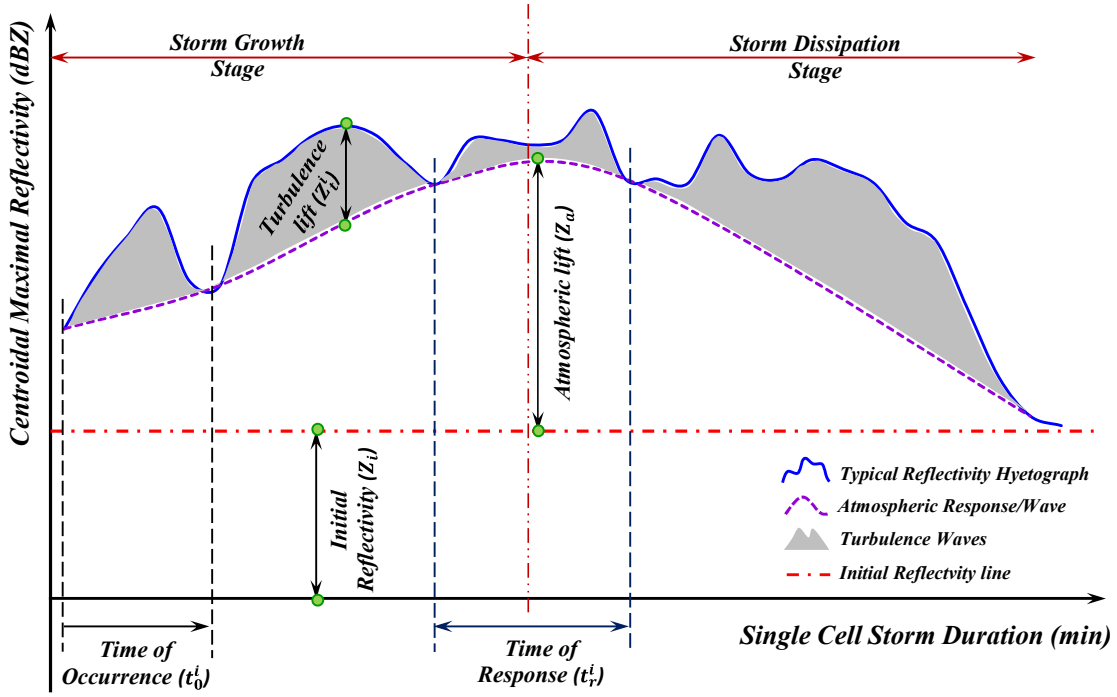

Figure 4.2. Typical storm reflectivity hyetograph comprising atmospheric response and turbulence fluctuations.

Here, the "Atmospheric Wave" component is a portion of mean response in growing and receding stages of a cloud cell which ultimately depends on atmospheric parameters such as temperature, pressure, humidity etc. The other component "Turbulent Wave" is aggregation of multiple caps (fluctuations) over mean atmospheric response, which are the fast responses over a time due to turbulent processes in clouds. Then these components were approximated as given below.

4.2.3 Storm Reflectivity Hyetograph Approximation

This section elaborates the comprehensive analysis of reflectivity hyetograph, its approximation and prediction (Fig. 4.3). The duration of storm varies for each event and it comprises of growing to receding stage. To establish universality in collected reflectivity hyetograph, the duration of storm was normalized to unit duration [Koutsoyiannis & Foufoula-Georgiou, 1993] and it is expressed as:

$$t_D^o = \frac{t}{D} \qquad \text{when} \quad 0 \le t \le D \qquad \text{(eq. 4.1)}$$

Here t_D^0 is the dimensionless time (normalized unit duration), t, the base time of a storm and D, duration of a storm event (life period of storm).

Abstract-TH-2793_156104035

Initially, the atmospheric wave was approximated using the function suggested by Maxwell [Maxwell, 1960], which is extensively used in the field of hydrology and geomorphology. It better approximates any natural time-frequency series with good association of peak values to its length ratio [Karmaker & Dutta, 2010; Howard, 1990].

The Maxwell approximation function used for atmospheric wave, is expressed as:

$$Z_a(t) = Z_i + Z_a \left[\frac{t_D^o}{k_a} \exp\left(1 - \frac{t_D^o}{k_a}\right) \right]^{r_a} \qquad \text{(eq. 4.2)}$$

Here, t_D^0 is the base time in unit duration; $Z_a(t)$, height of atmospheric wave at a time t_D^0; Z_i, the initial reflectivity (it considered as 15 dBZ); Z_a, the lift of atmospheric response (atmospheric lift); k_a and r_a, model fitted parameters which depends on the time to peak and duration of the storm respectively.

Similarly, the turbulence waves are approximated. For a single turbulence wave, the characteristics are defined by using Maxwell approximation:

$$Z^i(t) = Z_t^i \left[\frac{t_D^{o,i}}{k_t^i} \exp\left(1 - \frac{t_D^{o,i}}{k_t^i}\right) \right]^{r_t^i} \quad \text{when} \quad t_o^i \le t_D^{o,i} \le (t_o^i + t_r^i) \qquad \text{(eq. 4.3)}$$

Here, $Z^i(t)$, is the height of ith turbulence wave (fluctuation) at a time $t_D^{0,i}$; Z_t^i , an amplitude of the ith turbulence wave; k_t^i and r_t^i , model fitted parameters; t_r^i and t_o^i , time of response and time of occurrence of ith wave respectively (Fig. 4.2).

By cascading the atmospheric wave with the n number of turbulence fluctuations the function is expressed as:

$$Z(t) = Z_i + Z_a \left[\frac{t_D^o}{k_a} \exp\left(1 - \frac{t_D^o}{k_a}\right) \right]^{r_a} + \sum_{i=1}^{n} Z_t^i \left[\frac{t_D^{o,i}}{k_t^i} \exp\left(1 - \frac{t_D^{o,i}}{k_t^i}\right) \right]^{r_t^i}$$

$$\text{where } n = f(D) \qquad \text{(eq. 4.4)}$$

The several distribution parameters adopted in above expressions are described briefly in Table 4.1.

Abstract-TH-2793_156104035

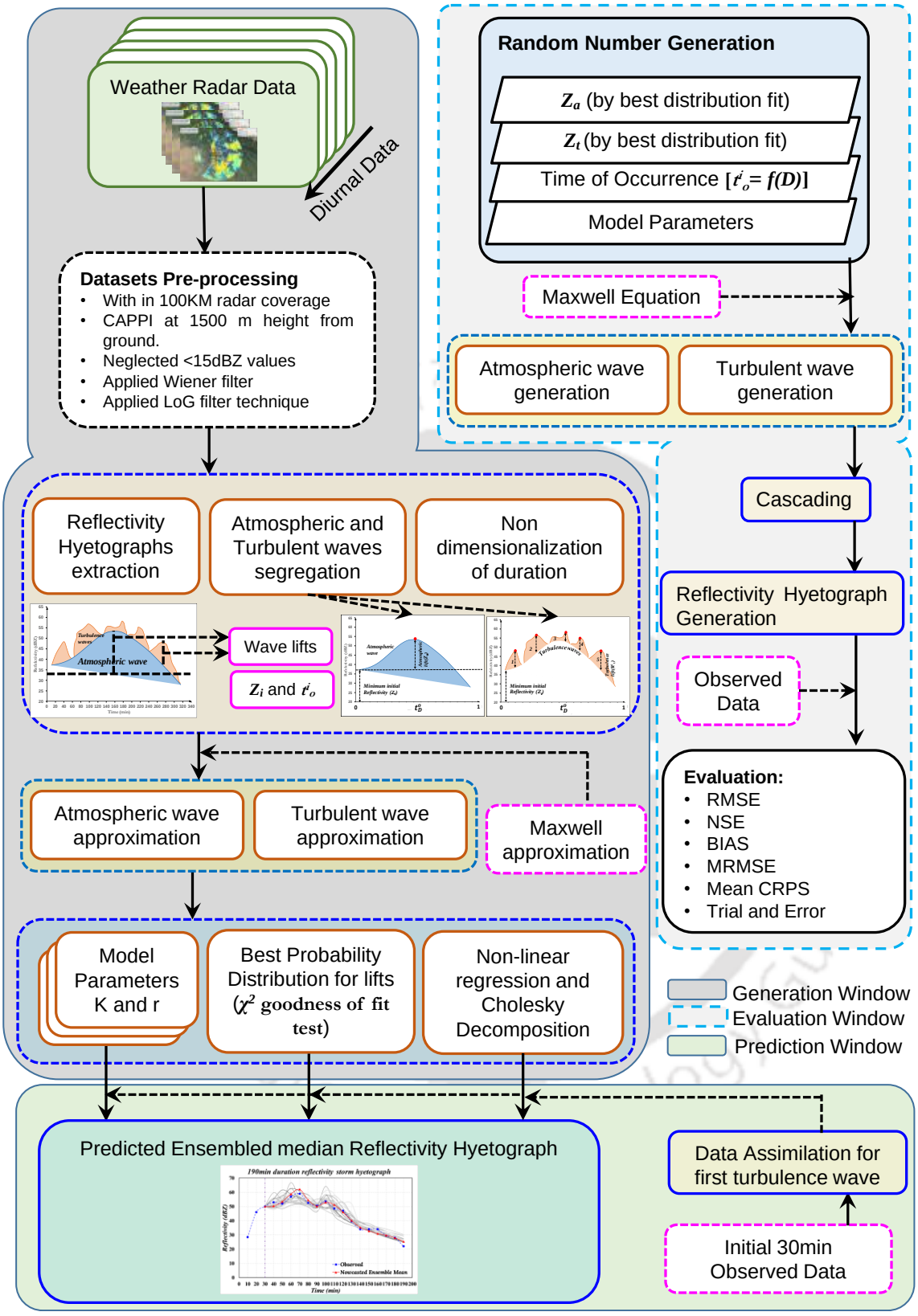

Figure 4.3. Conceptual illustration of data preprocessing, analysis, approximation, generation and prediction of reflectivity hyetograph.

Abstract-TH-2793_156104035

Table 4.1. Brief description of considered variables and model parameters in the Maxwell approximation for storm hyetographs

Variables	Computation (or) approximation	Generation procedure for prediction	Nature
Initial reflectivity (Z_i)	Determined from minimum reflectivity after pre-processing the observed data	Here it is considered the minimum reflectivity with 15dBZ	Deterministic
Atmospheric lift (Z_a)	Probability density function is fitted for the observed atmospheric wave amplitudes with goodness of fit test	Based on their probability density function	Stochastic
k_a and r_a	Model fitted parameters of Maxwell approximation for atmospheric wave	Generated based on regression fits or Cholesky decomposition	Stochastic (and) Deterministic
Subsequent amplitudes of turbulence waves ($\boldsymbol{Z_t^i}$)	Probability density function is fitted for the observed turbulence wave amplitudes with goodness of fit test	Approximated based on their probability density function	Stochastic
Number of turbulence waves (n)	The number of turbulence waves depends on the storm duration, which is observed from data. It is a function of base period of the storm	Generated based on the considered storm duration	Deterministic
Time of occurrence of turbulence waves (t_o^i)	It is observed that t_o^i is a function of storm duration	Generated based on the function of storm duration	Deterministic
k_t^i and r_t^i	Model fitted parameters of Maxwell approximation for different turbulence waves	Generated based on regression fits or Cholesky decomposition	Stochastic (and) Deterministic
Storm duration (D)	Observed from the data, it is an initialization variable for prediction of storm hyetograph	It is generated based on the first turbulence wave time of response and Cholesky decomposition	Deterministic
Time of response (t_r^i)	It is base period of the turbulence waves	Approximated using time of occurrence turbulence waves	Deterministic

Abstract-TH-2793_156104035

4.2.4 Model Parameters and Variables

The Chi-square (χ^2) goodness of fitting test was performed to identify the best probability fit for random variables listed in Table 4.1. Linear and nonlinear regressions between variables and model parameters were also approximated by identifying the hotspots in the correlation and covariance matrix. The remaining variables which failed to obey linear combination were decomposed with Cholesky decomposition [Huynh et al., 2008; Press et al., 2007] (Appendix B.2).

4.2.5 Performance Evaluation

Generally, the performance of nowcasting techniques is evaluated at spatial and temporal scales based on predicted events with respect to occurrence of events. In this study, the quantitative nowcasting technique is developed in terms of storm reflectivity hyetograph prediction. So, the performance evaluation of developed technique was done by considering the nowcasted storm hyetograph as a time series.

The prediction reliability of generated storm hyetographs with respect to its bias and deviation is the most important aspect of the developed methodology, as it describes the capability of real-time prediction. The reliability of hyetograph generation is quantified using the Root Mean Square Error (RMSE), Nash-Sutcliffe Efficiency (NSE) metrics, mean error (BIAS), mean continuous ranked probability score (CRPS) and temporal mean of ensemble root mean squared error (MRMSE), which are defined in Appendix B (Eq. B1-Eq. B13). The ratio between MRMSE and RMSE is calculated at different sample sizes of generated hyetographs. The ratio above one indicates the generated ensemble spreads are overestimated vice-versa.

4.3 STUDY SITE, DATA DESCRIPTION, AND PROCESSING

4.3.1 Regional Setting

Doppler weather radar data provided by India Meteorological Department (IMD) was used to investigate storm characteristics and analyze the historical storms. IMD operates C-band Doppler Weather Radar (DWR) for routine meteorological observations. The radar is located at IMD, New Delhi (28°35′23.28″ N, 77°13′18.84″ E, 253 m height above the mean sea level and 36m height above ground level). Rainfall in this area is influenced by the western disturbances around the year and two branches

Abstract-TH-2793_156104035

of (from the Arabian sea and the Bay of Bengal) of South-West winds from June to September. The climate overlaps between monsoon-influenced humid subtropical (Köppen climate type, *Cwa*) and semi-arid (Köppen climate type, *BSh*). Figure 4.4 shows the locations of operational radar network in India, the radar station which is considered for present study and its areal coverage.

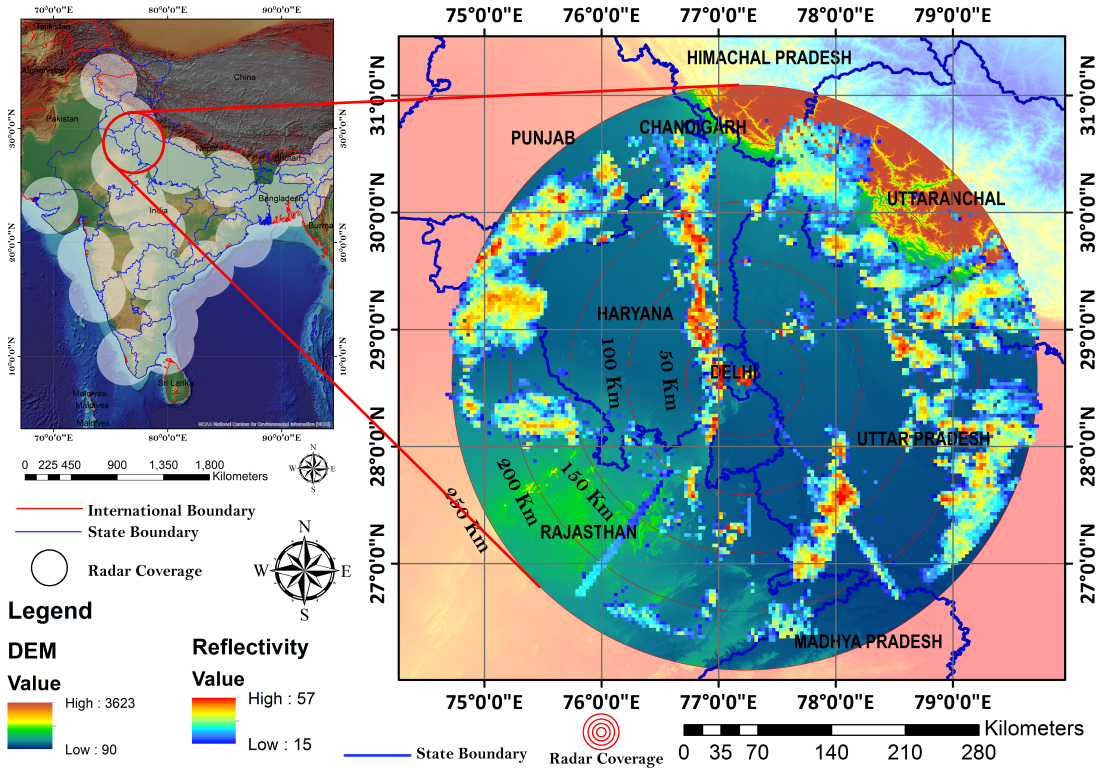

Figure 4.4. Radar coverage over the India region by IMD operational radar network, the location and coverage (250 *km*) of radar over Mausam Bhawan, New Delhi, with topography.

4.3.2 Data Description

The operating wavelength of considered DWR is 5.33 *cm*, and radial resolution is 0.3*km* having a 1˚azimuthal resolution. Radar records the precipitation in terms of reflectivity (dBZ) at every ten minutes with the antenna scanning through ten Plan Position Indicator (PPI) scans at a different elevation angles ranging from 0.5˚-21˚ to cover the vertical extent of detectable precipitation. The radial coverage is 500*km* and 250*km* radius in clear air mode and in precipitation mode respectively. The radar reflectivity data during the period of 2012 – 2016 were collected and analyzed. The local convective storms (or meso-beta scale events) were considered for the study, which causes flash flood events in cities. However, only ninety-two storm events were

Abstract-TH-2793_156104035

extracted from the data based on the high Centroidal reflectivity core (RCs) which were directly related to the high intensity of rainfall.

4.3.3 Data Pre-Processing

In this study, storm cells that travel within 100*km* radar coverage were considered due to unreliable in radar data beyond 100*km* [Wessels, 1990] and its under-estimation at longer range [Holleman, 2006]. The Constant Altitude Plan Position Indicator (CAPPI) scan was considered at 1500*m* height from the ground. This level is free from ground clutter and which is below the melting layer (observed at 3.5*km* from ground in the study area), and also the concentration of raindrops sufficiently exists at this level [Wessels, 1990]. The reflectivity values which are less than 15dBZ in the radar scans were removed (Fig.4.5(b)). The rainfall rate relates empirically in power law form with reflectivity value [Marshall & Palmer, 1948; Marshall et al., 1955], which indicates reflectivity less than 15dBZ in a control volume are most likely either non-precipitable or very light precipitation. The wiener filter [Lim, 1990] was applied over a scan to remove noise (Fig. 4.5(c)). Then Log of Gaussian [Lindeberg, 1998] filtering technique was used to detect the storm cell boundaries [Daliakopoulos & Tsanis, 2012] (Fig. 4.5(d)). This step is useful to differentiate the storm cells and track them separately and to extract reflectivity core values within the storm cell.

4.3.4 Reflectivity Hyetographs Abstraction

The RCs of storms were extracted manually after identification of storm cell boundary. The reflectivity hyetographs (Fig.4.2) were prepared and plotted with RC value at every 10min time interval of radar sweep. In a total, 92 events were abstracted at different storm durations ranging from 50 *min* to 370 *min* for the 2012 to 2016, five-year period. 65 storm hyetographs out of 92 were used for approximation and remaining for performance evaluation.

Abstract-TH-2793_156104035

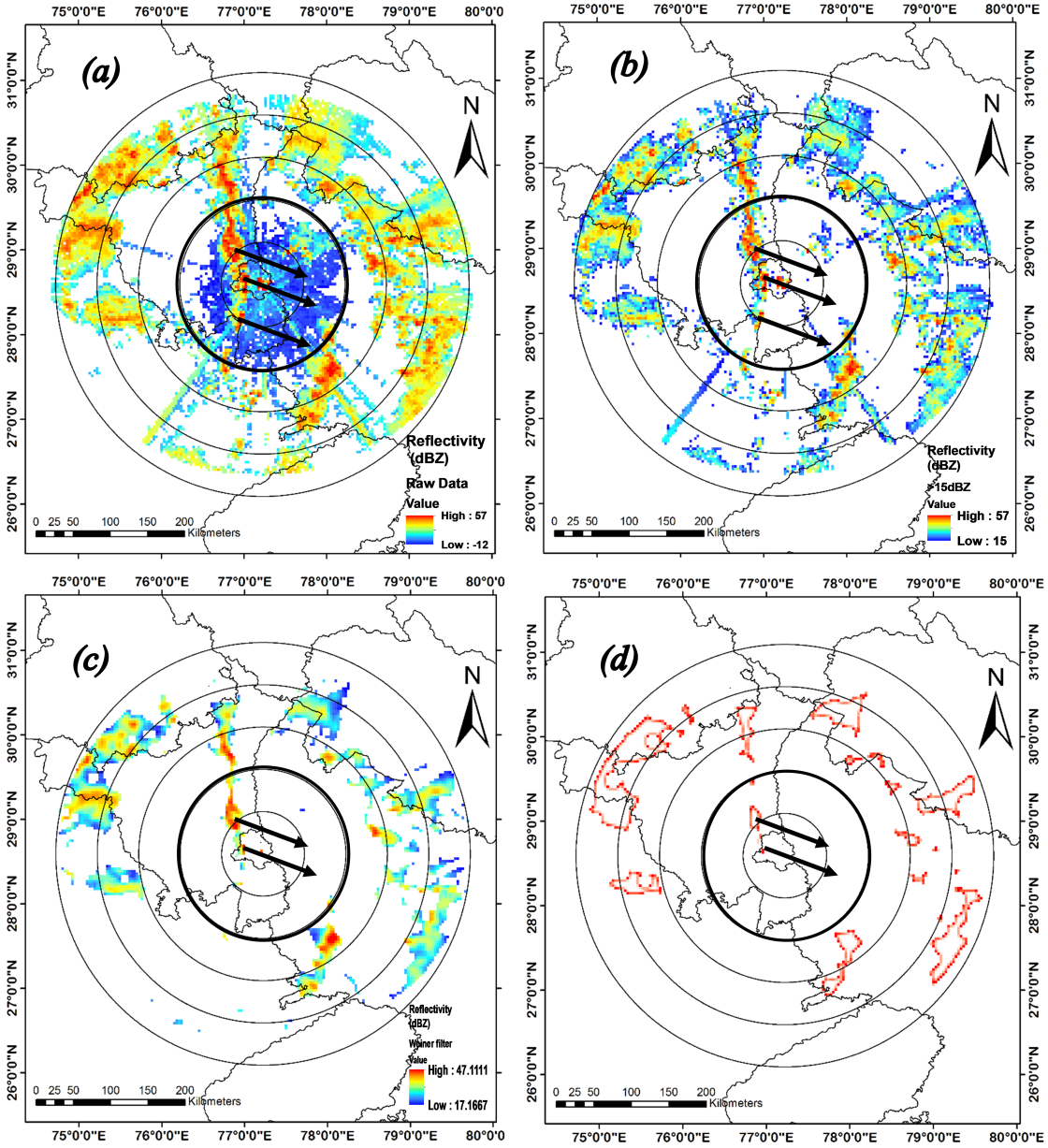

Figure 4.5. Radar data preprocessing (a) Raw data, (b) after removing less than 15dBZ reflectivity values, (c) Wiener filter application, processed with a 3×3-pixel Wiener filter and (d) storm cell boundary detection using Log of Gaussian (LoG) technique.

Abstract-TH-2793_156104035

4.4 RESULTS AND DISCUSSION

4.4.1 Analysis of Reflectivity Hyetograph Parameters

The model variables such as lifts, durations, number of fluctuations, its occurrences were extracted then the model fitted parameters such as *k* and *r* were approximated with Maxwell approximation function. The average of three to five turbulence fluctuations were observed in extracted reflectivity hyetographs, which are dependent on the duration of storm (Fig.4.6). It was also noticed that the time of occurrence of each turbulence wave depended on storm duration (Table 4.2).

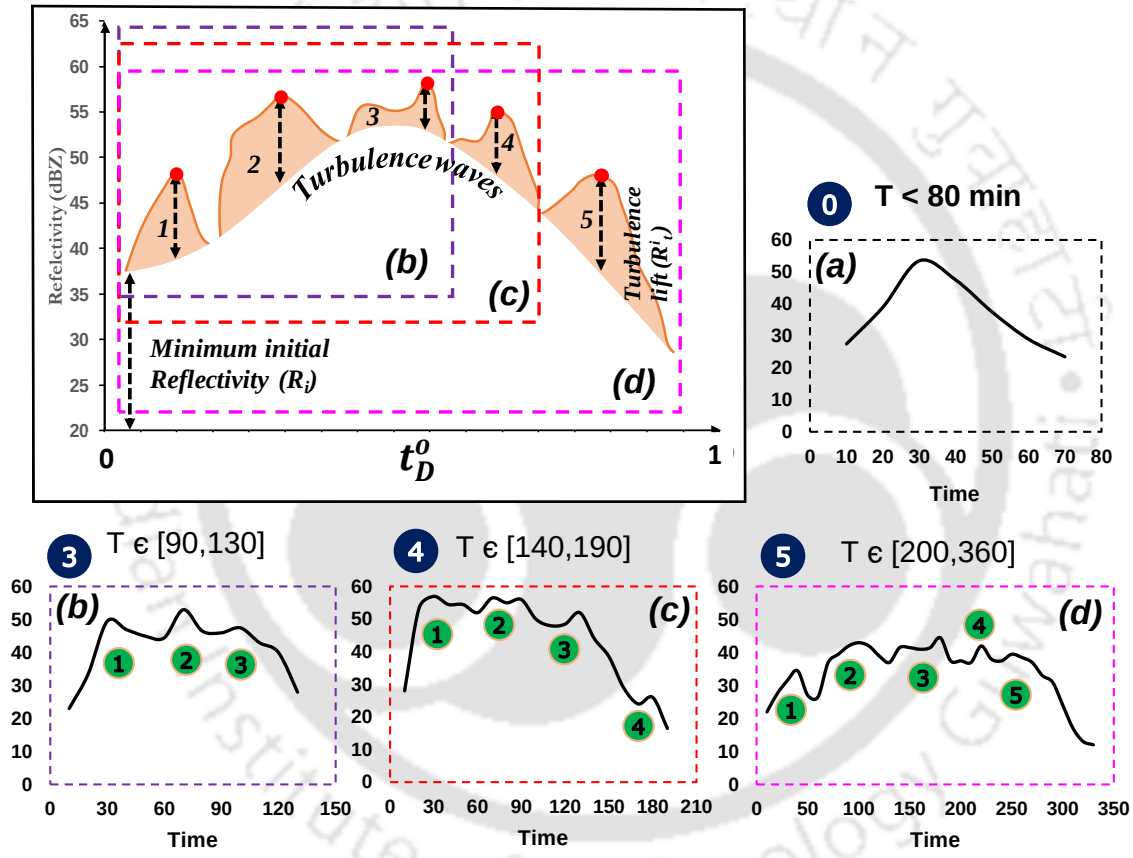

Figure 4.6. Turbulence wave fluctuations in a reflectivity hyetograph depends on storm duration; (a) no waves if duration less than 80 *min*, (b) 3 waves if duration is in between 90 *min* and 130 *min*, (c) 4 waves if duration is in between 140 *min* and 190 *min*, and (d) 5 waves if duration is in between 200 *min* and 360 *min*.

Abstract-TH-2793_156104035

Table 4.2. Range of parameters for Turbulence waves and atmospheric response (wave)

Duration (min)	No. of Turbulence waves	wave1	wave2	wave3	wave4	wave5
		Time of Occurrence (*min*)				
50-80	0					
90-130	3	10	40	60		
140-190	4	10	40	80	110	
200-310	5	10	50	100	160	210
Parameters	**Statistical parameters**	**wave1**	**wave2**	**wave3**	**wave4**	**wave5**
Z_t	Range	0.84-35.84	0.52-26.46	1.62-24.21	1.71-18.28	1.61-25.29
	Average	8.81	8.23	10.30	10.15	11.38
	Standard deviation	6.60	4.68	4.73	4.61	7.39
	Median	6.69	7.60	9.35	9.90	10.96
k_t	Range	0.02-4.37	0.19-0.75	0.27-0.89	0.43-0.98	0.58-0.95
	Average	0.23	0.44	0.62	0.72	0.80
	Standard deviation	0.58	0.16	0.14	0.12	0.09
	Median	0.14	0.40	0.62	0.73	0.81
r_t	Range	0.78-257	11.81-1418	9.16-3384	30.35-819	48.95-3385
	Average	23.51	95.84	166.47	226.85	656.07
	Standard deviation	38.44	196.30	488.89	204.18	874.92
	Median	11.02	49.34	63.96	127.14	376.54
	Quartiles					
		Q1, Q2 (+ve Skewed)		**Q3, Q4 (-ve Skewed)**		
Z_a	Range	23-46		19-45		
	Average	35.93		33.97		
	Standard deviation	5.20		7.17		
	Median	36.75		34.50		
k_a	Range	0.07-0.45		0.19-0.46		
	Average	0.33		0.31		
	Standard deviation	0.10		0.08		
	Median	0.31		0.29		
r_a	Range	0.05-5.63		0.30-0.54		
	Average	1.52		0.43		
	Standard deviation	1.41		0.05		
	Median	1.13		0.43		

Abstract-TH-2793_156104035

It was also observed that the maximum and the median of the atmospheric lift is decreasing with storm duration, as 46dBZ and 41.25dBZ for 50-80*min* storm duration, 45dBZ and 39dBZ for 90-130*min*, 41dBZ and 37dBZ for 140-190*min*, 39.5dBZ and 36dBZ for 200-310*min*. Table 4.2 summarizes the ranges of the lifts and model fitted parameters of reflectivity hyetograph.

The sample average of turbulence lift was increased from first wave to last wave (Table 4.2). It shows that the growth of the fluctuation at receding stage of the storm is more. It means more moisture entering into the central core of the storm was from its surroundings though the moisture lifting from earth surface has stopped. The turbulence model parameter k_t also increased from first to last turbulence wave, which shows indirect representation of peak increment. The model parameter rt also increased from first to last fluctuation, which represents the base spread of the wave. The lifts, k_t and r_t increment in turbulent waves represent the fluctuations that were formed with low base and lifts at initial stage of storm than at receding stage of storm where storm fluctuations were formed with large base and lift.

4.4.2 Decomposition of Random Variables and Parameters

4.4.2.1 *Interdependency between random variables*

In order to identify interdependency between all variables and model fitted parameters, the coefficient of determination of Pearson Correlation Coefficient (linear interdependency) and Spearman Rank Correlation Coefficient (non-linear) were estimated between each variable. Visualizing the dominant interdependency between all 24 random variables with coefficient of determination would be challenging, so here the problem is resorted by Circos diagrams for visualization of higher dimensional data (Fig.4.7).

The coefficient of determination between each variable was plotted in separate chord diagrams for both Pearson and Spearman created by the Ciros tool which is developed by Krzywinski et al. [2009]. Circos uses a circular ideogram layout to simplify the display of relationships between a pair of random variables represented by the use of ribbons or chords with its size (thickness), orientation and position.

Abstract-TH-2793_156104035

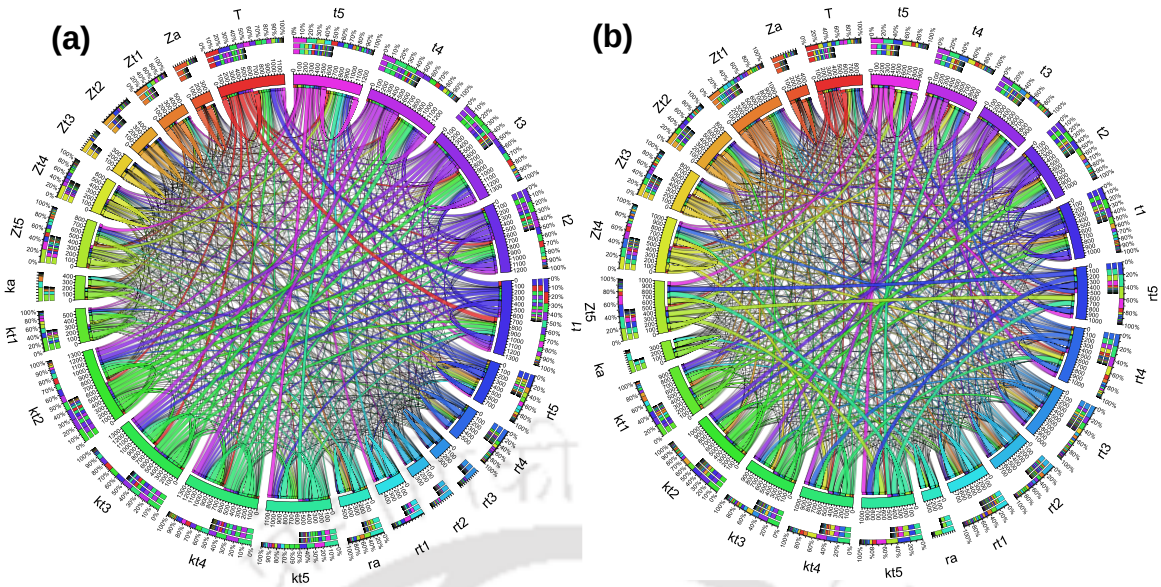

Figure 4.7. Circos plots to visualize dominant interdependency between each random variable with; a) Pearson rank coefficient of determination (linear); b) Spearman rank coefficient of determination (Non-linear).

Here, in the Circos diagram, the values on the outer periphery of the circles represents the fraction of overall percentage of dependence of particular variable on other variables. On the inner periphery of the circles represents the color assigned for each variable and two-way flow between the variables. The color strips inside the circle represent the order of splits obtained from Pearson Correlation Coefficient (Fig.4.7(a)) and Spearman Rank Coefficient (Fig.4.7(b)). The Ciros were drawn mainly to show the liner and non-liner interdependency between random variables. Here, it was observed more ribbons were exposed in non-linear dependency (Fig.4.7(b)) than in the linear dependency Circos (Fig.4.7(a)). It also observed the thickness of color strips are same in size in non-linear Circos plot while linear Circos plot highlighted some are thicker and some are less thick strips. It clearly indicated that there is an equal interdependency between each random variable but mostly non-linear and it also suggested that the interdependency between variables can be stored to generate future random variables.

4.4.2.2 *Probability distribution function for lifts*

It was observed that the Atmospheric lift (Z_a) and Turbulence wave lifts (Z^i_t) are stochastic in nature, which have not shown any interdependency with other variables

Abstract-TH-2793_156104035

(Fig.4.9(a,c), Appendix Fig.B1). Here, the lifts were fitted with best probability distribution function using Chi-square (χ^2) goodness of fit (*gof*) statistic [Chow et al., 1988] test. The probability distribution function for which the null hypothesis of an adequate fit was not rejected at the 5% (lower limit) and 95% (upper limit) significance levels were selected for future random variable generation (Fig.4.8). The Chi-square goodness of fit test showed extreme value distribution in atmospheric and fifth turbulence lift, Gamma distribution in first and third turbulence fluctuations, and Weibull distribution in second and forth turbulence fluctuations (Fig.4.8).

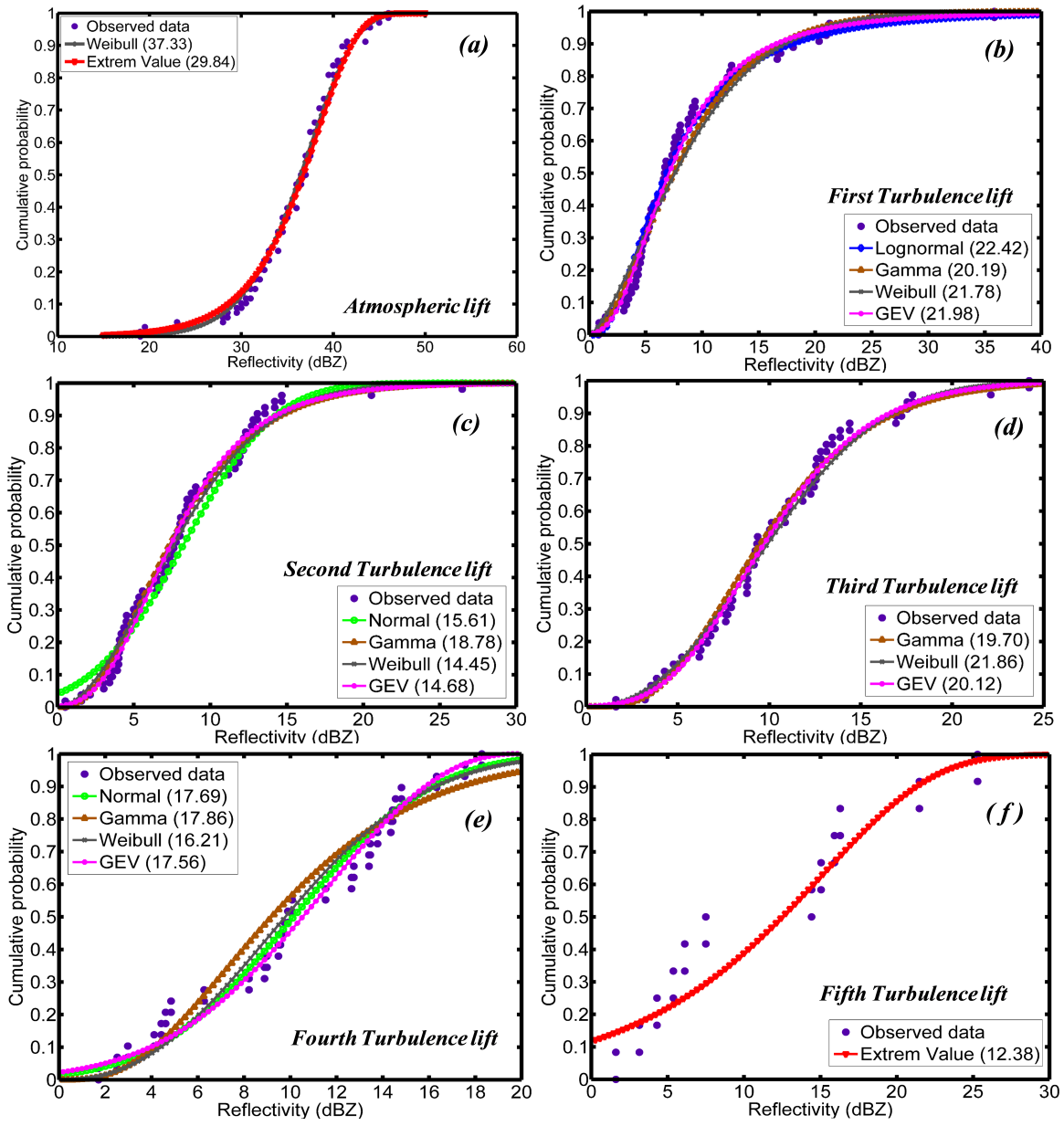

Figure 4.8. cumulative Probability distribution functions for: (a) for atmospheric lift; (b) First turbulence wave lift; (c) Second turbulence wave lift; (d) Third turbulence wave lift; (e) Fourth turbulence wave lift; and (f) Fifth turbulence wave lift (numerical values within the brackets indicates Chi-square statistic value, significant at $p<0.05$ and $p>0.95$).

Abstract-TH-2793_156104035

4.4.2.3 *Regression between depended variables*

There are some variables which showed high linear interdependency, as thick ribbons in Circos plot (Fig.4.7) and hot spots in correlation matrices (Fig.4.9 and Appendix Fig.B1). The linear and some nonlinear regression equations were developed by selecting the combination of variables which exhibited high coefficient of determination and the equations are presented in Table 4.3. The regression curves with 95% confidence bands are presented in Appendix Fig.B2-B9.

Table 4.3. Linear regression equations between highly interdependent variables.

Variables	Best fit – equation (Linear - Polynomial)	r^2	*RMSE*	*SSE*
K_a *vs.* r_a	$y = 11.085\ x^{2.014}$	0.76^{**}	0.156	1.508
t_o^2 *vs.* t_o^3	$y = 1.389\ x^{0.805}$	0.73^{**}	0.070	0.217
t_o^3 *vs.* t_o^4	$y = 637.84\ x^5 - 1531.78\ x^4 + 1415.22\ x^3 - 625.93\ x^2 + 132.79\ x - 10.27$	0.72^{**}	0.070	0.119
t_o^3 *vs.* k_t^2	$y = -13.93\ x^4 + 23.88\ x^3 - 14.41\ x^2 + 4.54\ x - 0.377$	0.90^{**}	0.043	0.073
t_o^3 *vs.* k_t^3	$y = -123.23\ x^5 + 337.03\ x^4 - 359.21\ x^3 + 185.84\ x^2 - 45.67\ x + 4.704$	0.77^{**}	0.067	0.179
t_o^4 *vs.* k_t^3	$y = -479.17\ x^5 + 1558.78\ x^4 - 2004.90\ x^3 + 1274.27\ x^2 - 399.34\ x + 49.69$	0.85^{**}	0.043	0.045
t_o^4 *vs.* k_t^4	$y = -3389.86\ x^6 + 13795.02\ x^5 - 23093\ x^4 + 20345\ x^3 - 9943\ x^2 + 2335.9\ x - 269.4$	0.94^{**}	0.032	0.021
t_o^5 *vs.* k_t^5	$y = -2279\ x^5 + 11136\ x^4 - 20203\ x^3 + 17478.74\ x^2 - 7311.25\ x + 1193.23$	0.94^{**}	0.025	0.003

** *Represents significant at 0.01 level of two tails*

4.4.2.4 *Decomposition of Non-linear interdependent random variables*

The non-linear interdependent random variables were decomposed without restoring the noise with the Cholesky decomposition [Tarpanelli et al., 2012; Huynh et al., 2008; Press et al., 2007]. The algorithm and form of Cholesky decomposition is provided in Appendix B.2. The Cholesky factorization matrix developed with Spearman Rank Coefficient and Covariance matrix are shown in Figure 4.9.

Abstract-TH-2793_156104035

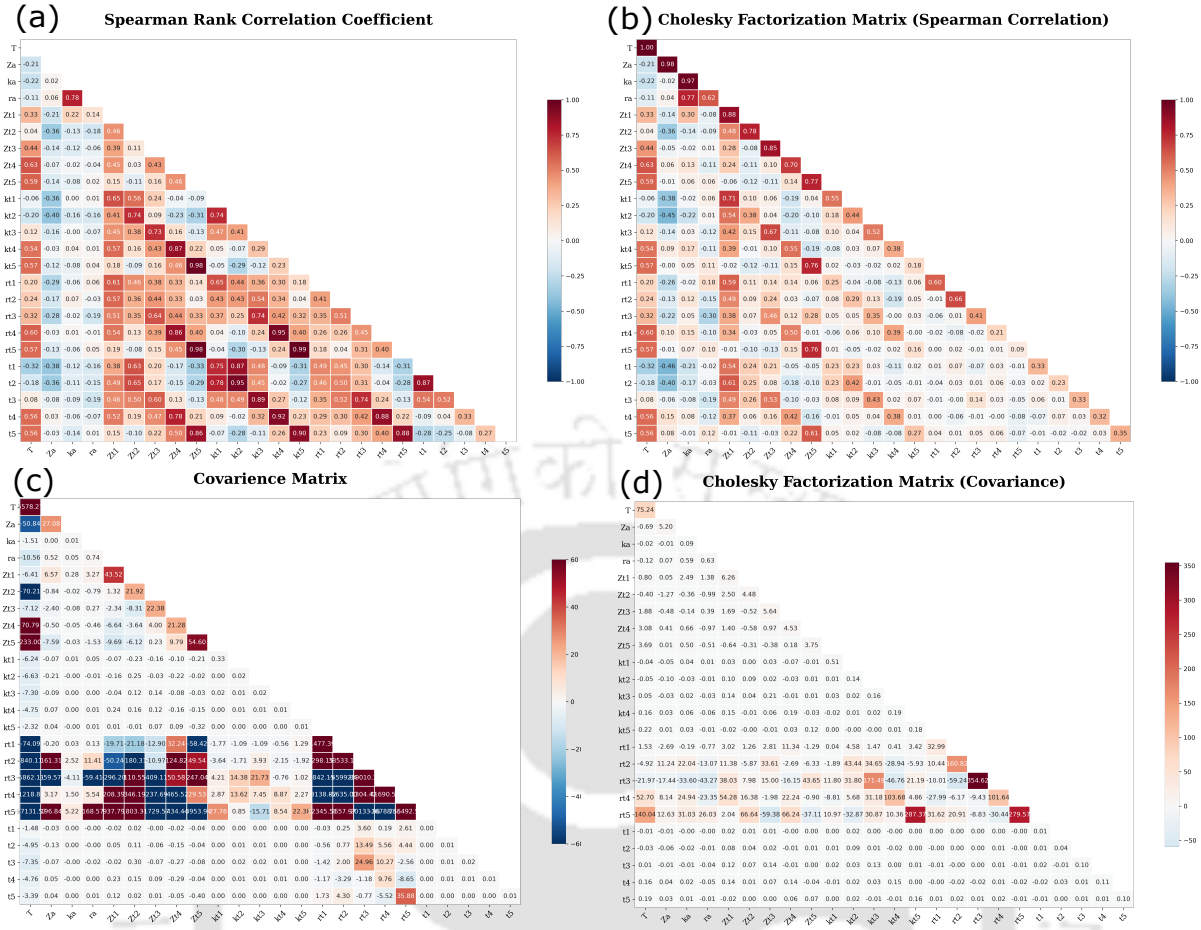

Figure 4.9. Lower triangular matrices for: (a) Spearman Rank Correlation Coefficient; (b) Cholesky factorization matrix for Spearman correlation; (c) Covariance matrix; (d) Cholesky factorization matrix with covariance matrix.

4.4.3 Performance Evaluation of Generated Hyetographs

The different sample sizes of hyetograph ensembles were generated by computing atmospheric and turbulence responses separately with the use of probability fits and decomposed matrices and then cascading of both the waves. The four hyetographs were chosen for evaluation purpose, which falls within four different duration clusters (50-80, 90-130, 140-190 and 200-310*min*) (Fig.4.5). Here, the error metrics such as RMSE, NSE, BIAS, Mean CRPS, and MRMSE were used to evaluate generated ensembles with observed hyetographs. Table 4.4 summarizes the average statistical error metrics computed for selected sample sizes of generated ensembles with observed hyetograph. The error metrics at all different sample sizes are provided in Appendix Table B1.

Abstract-TH-2793_156104035

Table 4.4. Statistical error metrics to evaluate performance of generated hyetographs (the detailed table provided in Appendix Table B1).

Sample Size	Statistical Verification Score	Storm Duration (*min*)			
		70	***120***	***190***	***310***
m = 2	RMSE (mean) dBZ	6.06 (2.42)	5.03 (3.11)	6.64 (4.66)	7.07 (6.52)
	NSE (mean)	0.63 (0.75)	0.79 (0.79)	0.63 (0.71)	0.66 (0.71)
	BIAS (mean) dBZ	1.07	-3.71	1.58	-1.78
	Mean CRPS dBZ	2.09	4.11	4.81	3.17
	MRMSE dBZ	5.59	4.32	5.84	6.64
m = 5	RMSE (mean) dBZ	4.35 (1.48)	5.35 (2.65)	6.17 (2.73)	7.42 (5.81)
	NSE (mean)	0.81 (0.91)	0.75 (0.85)	0.67 (0.90)	0.61 (0.77)
	BIAS (mean) dBZ	-0.32	-0.24	-1.12	-1.41
	Mean CRPS dBZ	1.55	2.76	2.36	4.08
	MRMSE dBZ	4.10	4.87	5.61	6.90
m = 10	RMSE (mean) dBZ	5.23 (1.28)	3.84 (1.90)	5.74 (2.33)	7.01 (4.60)
	NSE (mean)	0.72 (0.93)	0.87 (0.92)	0.71 (0.93)	0.65 (0.86)
	BIAS (mean) dBZ	-1.24	0.05	1.83	-1.90
	Mean CRPS dBZ	1.75	2.17	2.13	2.66
	MRMSE dBZ	5.21	3.21	5.41	6.69
m = 20	RMSE (mean) dBZ	5.59 (1.11)	6.06 (1.74)	6.83 (2.19)	6.72 (3.96)
	NSE (mean)	0.68 (0.95)	0.67 (0.93)	0.60 (0.94)	0.68 (0.89)
	BIAS (mean) dBZ	-1.08	0.46	1.99	-1.30
	Mean CRPS dBZ	1.79	2.24	1.99	2.82
	MRMSE dBZ	5.68	6.01	6.85	6.49

**average values are given; **The value given in bracket is the 5% confidence value for RMSE and 95% confidence value for NSE*

The results show good performance of method and the performance declined with increment in storm duration. The average statistical indicators such as RMSE, mean CRPS and MRMSE showed ~26%, ~51%, and ~18% of error increment with an increment in duration of hyetograph. At all sample sizes the RMSE errors at 5% confidence level were slightly higher for longer duration events (~3-7dBZ) than shorter duration events (~1-3dBZ). The bias also showed more error at larger duration events and it indicated the model slightly under-predicted the hyetograph values at all

Abstract-TH-2793_156104035

duration of storm events. However, the NSE values at 95% confidence level are lay within acceptable ranges (0.71-0.89).

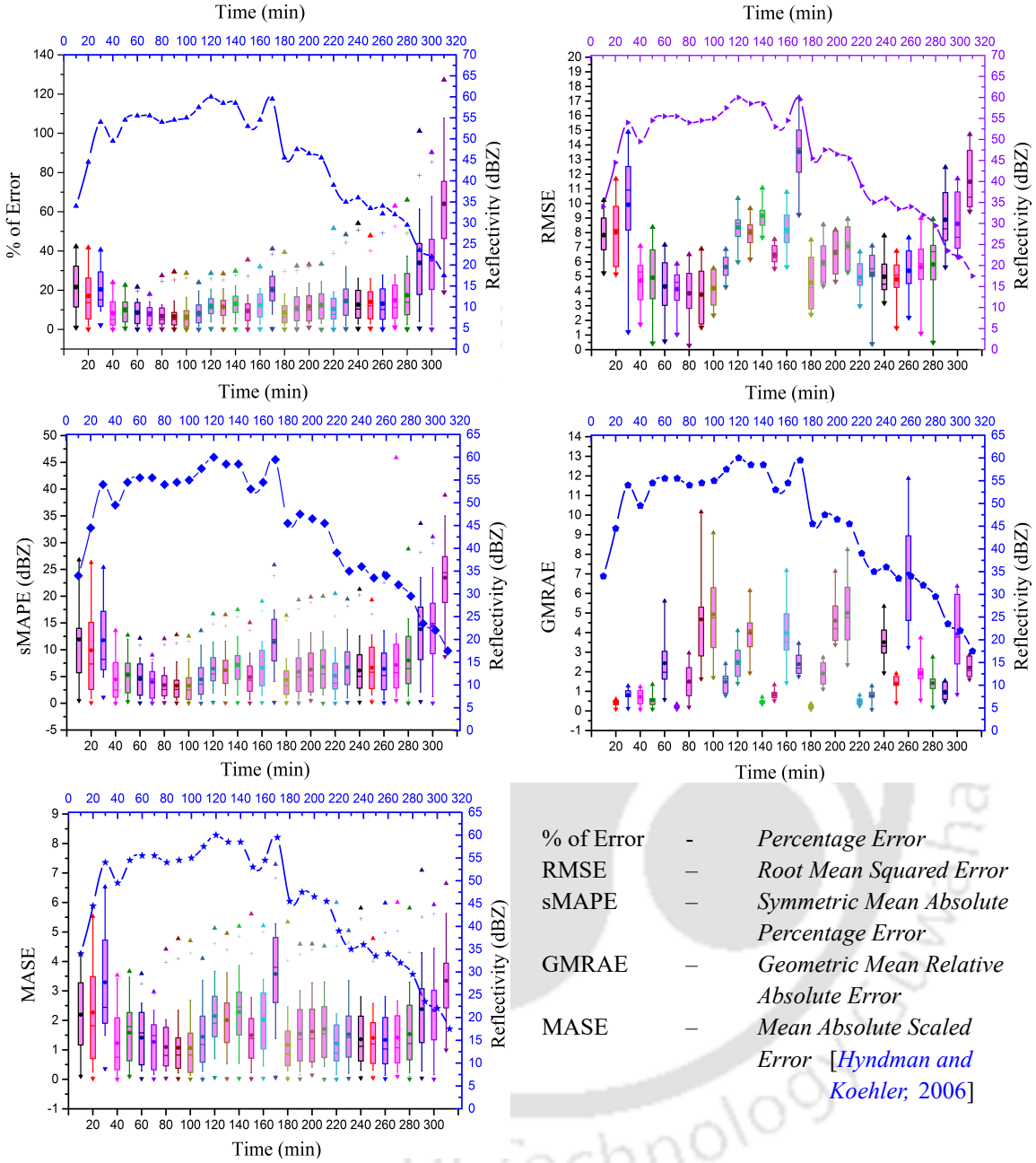

Figure 4.10. Error Analysis of hyetograph tail ends at each time step using percentage, squared, absolute, relative and scaled accuracy measures for 310*min* storm hyetographs (for other storm durations provided in Appendix B5).

The error metrics decreased (RMSE ~7%, mean CRPS ~32% and, MRMSE ~5%) with increment in size of generated ensembles at all storm durations. The threshold sample size was observed at m=5 then thereafter no significant change was found in error metrics. The ratio between MRMSE and RMSE was observed between 0.84 - 1.02 at all sample sizes and event durations. In ideal condition the ratio should be 1, any

Abstract-TH-2793_156104035

significant deviations from ideal value indicates that generated sample spread is less reliable. However, the average ratio 0.99 and 0.92 were observed at generated sample sizes m = 20 and m = 5 respectively. It indicates that the developed model is reliable but it has slightly under-predicted.

The average RMSE and MRMSE of ~5dBZ was observed at all storm events and generated sample sizes. This error is negligible at lower reflectivity values (tails of hyetograph) but this error is more significant and unreliable at higher reflectivity values (peak of hyetograph) due to the logarithmic nature of reflectivity value. The tail end error analysis was performed to check the reliability of model at tails and peaks. The tail end error analysis was performed with the statistical errors such as %error, RMSE (squared error), sMAPE (symmetric error), GMRAE (relative error), and, MASE (scaled error). Figure 4.10 summarizes the computed error statistical metrics at 310 min storm duration hyetograph (error plots at other durations provided in Appendix Fig. B10). The overall indicators of error metrics showing the variability of error were more at rising and recession limbs (tails) instead of at the peaks of the hyetograph (Fig.4.10). The peak values are more important than tail end values while predicting high intensity of rainfall. With these error metrics analyses, it can be stated that, the model predicted satisfactorily at hyetograph peaks and in trend, but it was slightly under-predicted in the reflectivity values.

4.4.4 Prediction of Storm Hyetograph

Here, the hyetographs were predicted with an initial 30*min* observed data assimilation window as a training data by machine learning approach mentioned in aforementioned section. Form the results it was observed that the time of response of the first turbulence wave varies with in 30-40*min*, due to this the first 30min observation was considered as data assimilation window. The characteristics of first 30*min* of hyetograph were interpreted then the samples were trained by generating the random variables using best probability fits and decomposed relations. Then the random forest ensembles were generated with the trained parameters and variables. Here, four events were considered to test the hyetograph prediction efficiency of the model. The events, which occurred on 6 August 2013 (70*min*), 5 August 2015 (120*min*), 20 August 2012 (190*min*) and, 22 July 2013 (310*min*) were considered for the prediction. 25 number of ensembles were predicted with proposed hierarchical child

Abstract-TH-2793_156104035

of random forest machine learning approach and it was compared with observed hyetograph (Fig. 4.11).

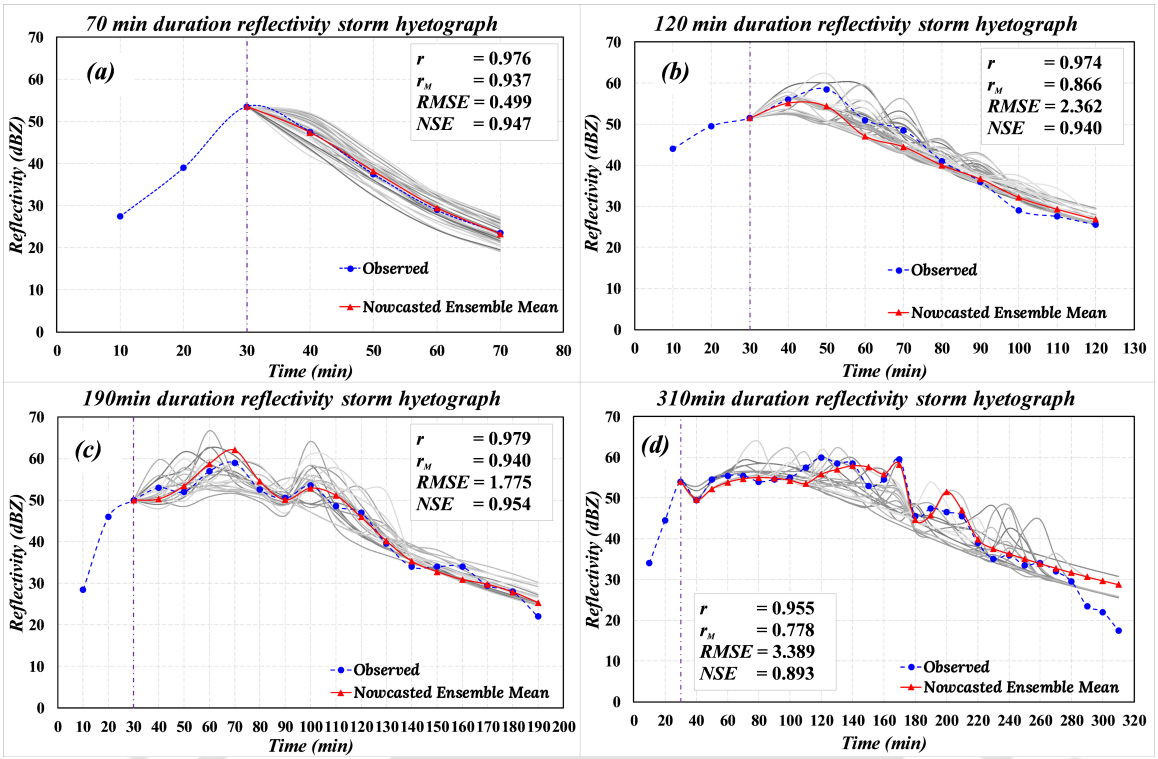

Figure 4.11. Predicted storm hyetograph at different storm duration (a) 6 August 2013(70*min*), (b) 5 August 2015(120*min*), (c) 20 August 2012(120*min*) and (d) 22 July 2013(310*min*) [line with triangles represents the predicted ensemble median storm hyetograph].

Here, prediction efficiency of the model was tested with the Pearson Correlation Coefficient (PCC(r)), NSE and RMSE instead of forecast skill parameters where the comparison was performed at hyetograph level. The PCC index is inadequate to compare two time series (hyetograph) datasets, due to its insensitiveness to identify difference between the size, shape and dispersion of two time series curves. Here, along with PCC the modified correlation index (r_M) was used to evaluate the prediction performance [MuCuen & Snyder, 1975]. The results show the dispersion of both predicted and observed hyetographs were almost identical (Fig.4.11a and 4.11c). Thus, the modified index, r_M (0.937 and 0.940) was very close to Pearson's r (0.976 and 0.979) for 70min and 190min storm durations respectively. The predicted and observed hyetographs in Figure 8(d), the modified index, r_M (0.778) was much lesser than Pearson's r (0.955), which indicates the shape and dispersion of predicted and observed hyetographs are different even though their trend is same. The results also showed modified index value approaches nearly to Pearson's r for shorter storm duration,

which indicates similarity in hyetograph dispersion and pattern between observed and predicted at short duration storms.

4.5 CONCLUSIONS

A new hierarchical machine learning approach to the generation and prediction of synthetic reflectivity-rainfall hyetograph is proposed by splitting storm hyetograph into different responses and then approximating with Maxwell function, decomposing random variables and model fitted parameters. Here, it was observed that the extracted hyetograph comprises of the harmonic fluctuations at certain time intervals. The similar patterns of radar reflectivity and power time series were plotted by Marshall et al. [1955]. The extracted hyetograph fluctuations exhibited similar trends in its number and occurrence with the duration of storm event. The extracted hyetographs were separated and grouped into four quartiles depending on its time to peak evolution to check behavior of storm hyetographs. Interestingly, it was noticed that the reflectivity hyetographs agreed with rainfall hyetographs plotted by Huff [1967] for the gauge recorded rainfall in the USA. Here, the extracted hyetograph was broken down into two sub-patterns and then coined into new terms as “Atmospheric” and “Turbulence” waves. The patterns were approximated with Maxwell function and fitted parameters, other variables were decomposed with Cholesky factorization matrix. The atmospheric and turbulence lifts showed non-dependency with other variables. They were fitted with best probability distribution function selected by Chi-square static test. Results showed that the statistical properties of random variables such as duration of event, time of occurrence of fluctuations, model fitted parameters, wave lifts and its extreme values were preserved satisfactorily by the proposed procedure. The good performance of the proposed approach in generating the accurate hyetograph similar to observed hyetograph and prediction capacity of model along with its simplicity, make it a valuable tool for the synthetic generation and prediction of storm hyetographs for extreme events which causes flash flood situation in urban regions. Furthermore, it should be noted that the proposed approach could be also applied to the rain gauge observed hyetographs due the similar tendency observed between reflectivity hyetographs observed here and rain gauge observed hyetographs by Huff [1967]. Here, it is tested for limited year datasets. It would be of considerable

Abstract-TH-2793_156104035

interest to extend the analysis to several year datasets and other urban regions for further investigations of return period rainfall events.

The proposed approach can be readily implemented in conjunction with a distributed urban hydrological model in order to estimate nuisance floods to flash floods. This approach by applying over long period datasets can also be implemented to estimate design flood peak over study region every time the rainfall field has to be properly reproduced.

Finally, based on the achieved results it is evident that the model slightly under-predicted and the results are limited to particular time period, as well as their sensitivity to different parameters was limited due to limited year data availability. Still the model remains to be explored in detail with the large number of data periods during monsoon and pre-monsoon storm events and other aspects which were not considered in this study, to prove its operational capabilities further.

Abstract-TH-2793_156104035

5

ASSESSMENT OF OPEN-SOURCE DEMS

(Assessment Framework to Select Open-Source DEMs for Urban Flooding)

Abstract-TH-2793_156104035

5.1 INTRODUCTION

Throughout our civilization, urban areas with waterfront access, exposure, and leisure amenities, etc., have always been attractive zones for societies to live in [Buch et al., 2014; Carlino & Saiz, 2019]. The reports say that 55% of the world's population live in urban regions and is projected to 68% by 2050 [UNDESA, 2019]. This increment leads to more development in the urban ecosystem, which could cause significant changes in urban landscapes. Any modification in urban landscape affects each component of meteorological and hydrological processes [Miller et al., 2014; Akkimi et al., 2019]. The affected topographical, meteorological, and hydrological components lead towards increase exposure to all types of flooding in urban regions [Kelleher & McPhillips, 2020]. Strategies and mitigations to reduce exposure and cope with nuisance floods to flash floods rely to some extent upon the prediction of floods.

The urban hydrologists consider that impervious land cover in urban regions is the sensitive parameter for floods [Smith et al., 2005; Ogden et al., 2011; Miller et al., 2014; Barnes et al., 2018]. Although it is a primitive reason for urban floods, the modifications in urban topography also worsen the situation due to altering its slopes and storage capacity. The topography is a primary control in flood movement and its inundation extent in urban landscapes [Jencso & McGlynn, 2011; Kelleher & McPhillips, 2020]. The urban region needs high gridded resolution and high vertical and horizontal accurate topography data for all sorts of studies. In this regard, new technologies such as LiDAR can satisfy high resolution and accuracy needs [Liu, 2008]. However, acquisition of such datasets is not possible for most developing countries and some parts of developed nations too due to its cost expensive and not feasible in given time constraint [Sanders, 2007; Hawker et al., 2018; Zhang et al., 2019]. It created an interest for researchers to learn what can be accomplished using open-source Digital Elevation Models and how feasible these models are for flood studies [Sanders, 2007; Schumann et al., 2014; Archer et al., 2018]. Some popular open-source and commercially available DEMs with their respective properties, accuracies, and application are listed in Table 2.5.

Although much research on the application of on-line available DEMs is focused on fluvial, flood plains, forest, large river basin scale studies, and morphometric analysis (Table 2.5) than urban studies. In urban regions, these

Abstract-TH-2793_156104035

topographic models are likely to less attractive due to their medium to coarse spatial resolution and incorporation of surface features (Digital Surface Model, DSM) rather than its bare earth elevations (Digital Terrain Model, DTM) [Gorokhovich & Voustianiouk, 2006; Avtar et al., 2015]. On the other hand, most urban hydrologists model urban flooding by focusing more on drainage networks such as natural, engineered channels and sewers than natural surface topography [Mark et al., 2004; Schmitt et al., 2004]. However, in recent years, a growing body of literature demonstrates the importance of and use of open-source DEMs in urban flood studies (Table 2.5). Nevertheless, the question that arises to the urban hydrologist community is whether these online DEMs (mostly they are DSMs) satisfy the needs. Many studies or researchers say "no" and confirms that urban flood studies need high-resolution datasets such as LiDAR [Gamba et al., 2002; Rossi & Grenhardt, 2013]. Secondly, most middle- and low-income group nations can acquire these high-resolution datasets. To date, only some countries like some parts of the USA, Europe, Canada, and Australia are able to acquire these datasets [Zhang et al., 2019]. Lack of LiDAR data products worldwide made the dependence on open-source DEMs in most of the world, where data is scarce [Schumann et al., 2014; Sampson et al., 2016]. Many researchers examined the different open-source DEMs at different gridded resolutions using statistics such as RMSE, STDE, LE90, and with storage-elevation functions and with different 1D/2D hydrodynamic models. Are these assessment techniques adequate to assess DEM accuracy towards urban flood modeling [Fereshtehpour & Karamouz, 2018], or any new framework should be developed to assess the DEMs for urban flooding? Over the past years, to accommodate global DEMs to societies, many researchers have studied the production of high-resolution bare-earth products from global DEMs by removing all surface features which obstruct the flow movement and misidentify the watershed boundaries [Werner, 2001; Gorokhovich & Voustianiouk, 2006; Ettritch et al., 2018]. The bare-earth product can only be sufficient for urban flooding modeling, or some surface features need to be preserved.

To this date, much attention has not been given to these issues. Therefore, in this chapter, we tried to address the above raised questions. One is whether online global DEMs (mostly DSM) satisfy urban flood modeling and inundation mapping needs; if yes, then which one is better in data-scare regions. Second, only a bare-earth topographic model will be sufficient to predict flood characteristics and their extent in

Abstract-TH-2793_156104035

the urban region. Another main contribution of this chapter is introducing a novel technique based on storage-elevation curves (zero-dimension hydrological model) with its normalized parameters to identify the watershed characteristics and assess the DEMs in complex urban terrain for flood modeling and inundation mapping. It also proposed a new assessment framework as a guided setup while selecting an appropriate topographic model for urban flooding. The proposed novel technique easily identifies the suitable DEM, which performs well during nuisance floods, regular floods, and flash floods. This chapter begins with describing selected six different study sites in order to answer the above-raised questions. The rest of the chapter is organized as follows. Section 2 provides the details of datasets selected and it's pre-processing. Section 3 introduces the developed assessment framework with a novel storage-elevation curve assessment approach. The section 4 includes the results, discussion, and limitations. Finally, section 5 summarizes the main conclusions.

Abstract-TH-2793_156104035

5.2 STUDY AREA AND DATA DESCRIPTION

5.2.1 Study Areas

Six urban settings were chosen for analysis, including the different urban features, the density of high raised infrastructure (Obstructions for the flood movement), and varying drainage area (Table 5.1). The shaded relief images of all study areas with ALOS AW3D (30m) DEM are shown in Fig.5.1.

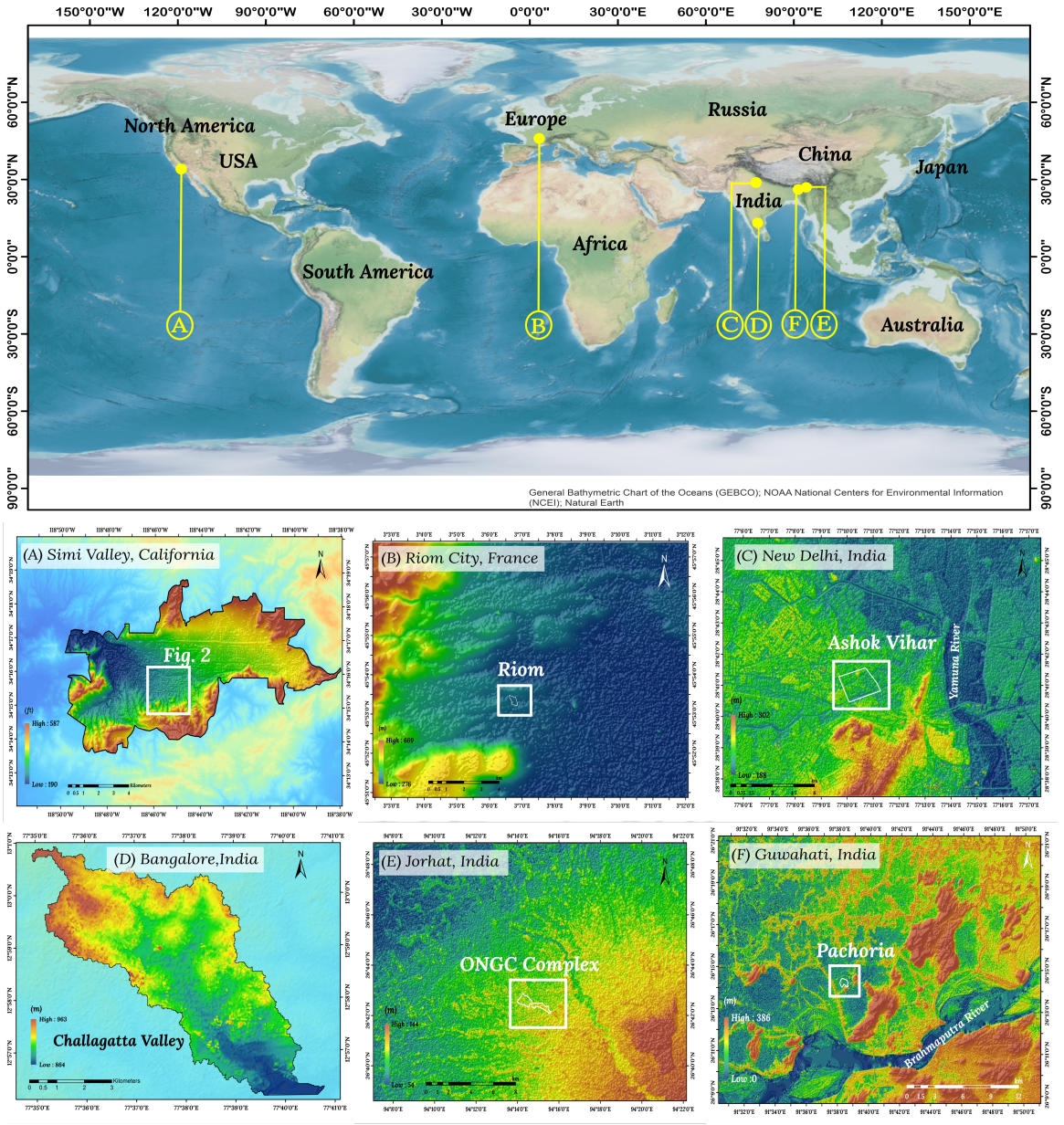

Figure 5.1. Shaded relief images of study areas with indication of places considered (Shaded relief illumination prepared with ALOS AW3D 30 data, at 315˚N, 20˚ above the origin)

Abstract-TH-2793_156104035

Table 5.1. Selected study areas and their characteristics

Station Name	Drainage Area (sq.km)	Watershed Length (km)	Watershed Width (km)	Characteristics of Study Area (or) Land use/Landform	Land use / Land cover changes since 2000	% Density of high-rise infrastructure (% of Impervious)	Methods followed to collect base data	Data spatial resolution	Collected Agency
Simi Valley, California, USA	6.90	2.57	2.68	Partially impervious with large parking yards	Slightly changed (0.1%)	3.35 (22)	LIDAR	1 *ft.*	CHI Water
Riom, France	0.09	0.42	0.24	Fully impervious with buildings, roads and surrounded by tall trees	No changes	23.56	LIDAR	1 *m*	CHI Water
Ashok Vihar, New Delhi, India	3.15	1.62	1.94	Partially impervious with buildings, roads, park with large tusk trees and metro bridge	Slightly changed (1%)	4.64	-	5 *m*	IIT Delhi
Challagatta Valley, Bangalore, India	37.07	13.45	4.85	Fully urbanized with high raised infrastructure, commercial complexes, large bridges, large lakes and roads.	Slightly changed (2% -3%)	39.63 (63)	Total Station Surveyed	Only storm sewer and drains data collected	IISc Bangalore
Pachoria, Guwahati, India	0.45	0.90	0.80	Fully pervious with ponds and wetlands, agriculture lands stored with water	It changes every year	1.1 (1.1)	Total Station surveyed	0.9 *m*	IIT Guwahati
Jorhat, India	0.03	0.27	0.99	Fully impervious with roads and buildings	No changes	31.14 (94)	Total Station Surveyed	0.9 *m*	IIT Guwahati

Abstract-TH-2793_156104035

An inset of Simi Valley watershed (Fig.5.2) shaded relief images highlights the level of urban features resolved by different DEMs. The shaded relief images for other selected DEMs at all study areas are presented in Appendix C11.

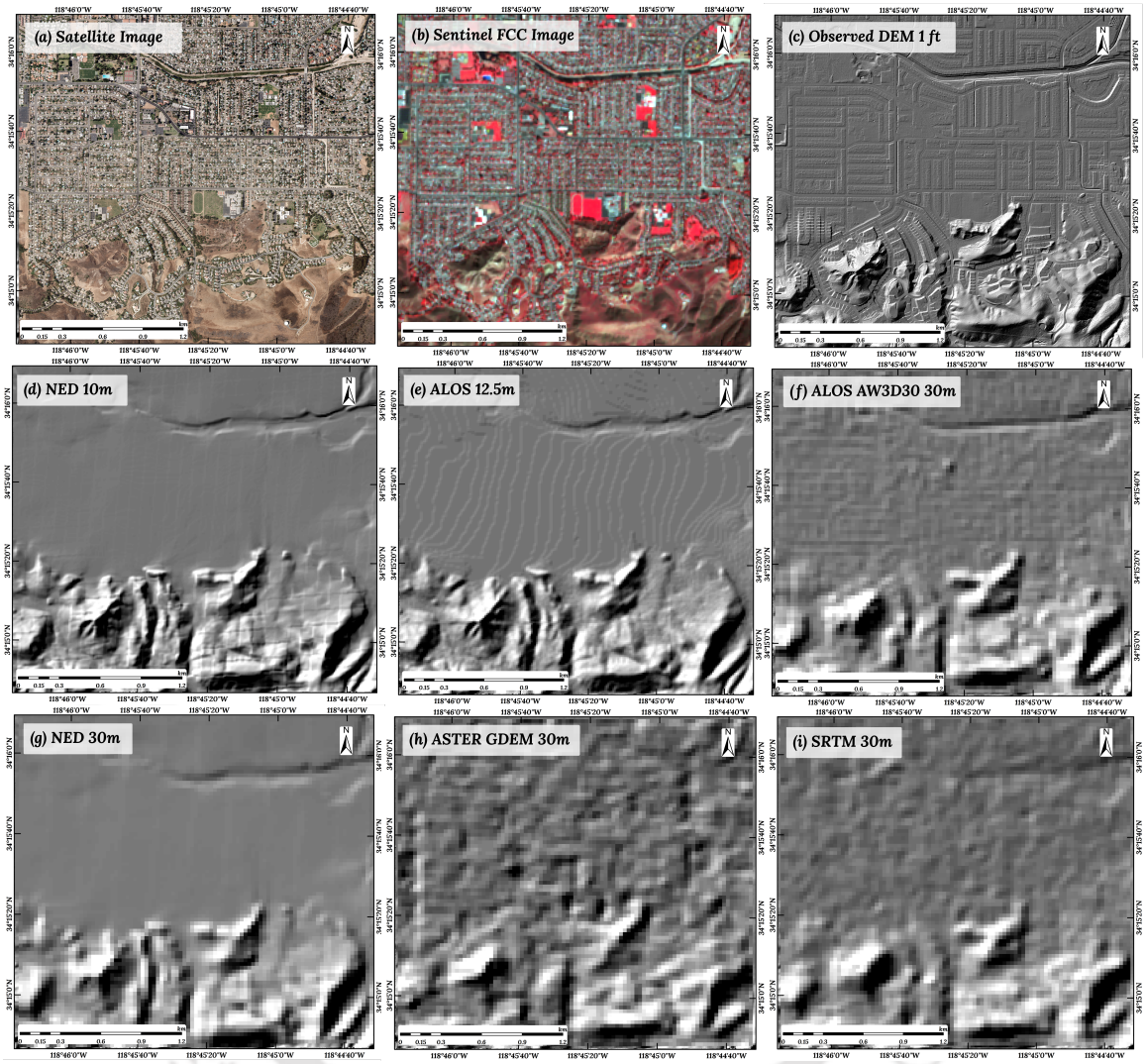

Figure 5.2. Shaded relief images of the Simi Valley urban settings (Fig.5.1A), the level of features depicted by A) Airborne image; B) Sentinel-2A image; C) LIDAR (1ft); D) NED (10m); E) ALOS (12.5m); F) ALOS AW3D (30m); G) NED (30m); H) ASTER (30m); I) SRTM (30m).

5.2.2 Datasets Description

The Digital Elevation Models, namely ALOS AW3D, ALOS PALSAR, ASTER, CARTOSAT vR3.1, NED, EU-DEM, and SRTM, were used to evaluate against surveyed topography depending on the availability of DEMs at selected study sites. A detailed description of selected DEMs is provided in Appendix C1. The commercial (IKNOS, WorldView, etc.) and recently released TanDEM-X were not used here due to its non-availability for general users. The characteristics, imaging system, accuracy,

Abstract-TH-2793_156104035

applications of DEMs used in this study are listed in Table 2.5. The surveyed datasets were acquired from the total station survey in some areas and LiDAR data (Air-borne survey) in other areas. The details of the acquisition of surveyed datasets are provided in Table 5.1.

5.2.3 Software and Data Availability

The GIS tools such as GRASS-GIS version 7.4.2 [Neteler et al., 2012; Neteler & Mitasova, 2013; Development team GRASS, 2018] and Arc-GIS v.10.6.1 were used to process the large size datasets and to develop the slope, contour, DoD maps etc. Matlab 2018b was used to calculate DEM statistics.

The surveyed datasets were acquired from multisource like total station survey and airborne LIDAR. The details of surveyed datasets are provided in Table 5.1. All DEMs less than 30m and freely available were only considered for the study. ALOS AW3D ($30m$) data was accessed from the Japanese organization JAXA Earth Observed Resource Center (https://www.eorc.jaxa.jp/ALOS/en/aw3d30/index.htm). ALOS PALASAR ($12.5m$) high-resolution terrain data was obtained from Alaska Satellite Facility (https://www.asf.alaska. edu/sar-data/palsar/). CRTOSAT v.3R1 ($30m$) was downloaded from the National Remote Sensing Centre open Earth Observation archive Bhuvan (https://bhuvan-app3.nrsc.gov.in/data/download/index.php). EU-DEM ($25m$) of two versions for Europe was obtained from the Copernicus Land Monitoring Service (https://land.copernicus.eu/imagery-in-situ/eu-dem/eu-dem-v1.1). NED ($10m$, $30m$) data for the Continental United States was accessed from USGS National Geospatial Program TNM (The National Map Viewer-https://viewer.nationalmap.gov/advanced-viewer/), which was updated in July 2018. The SRTM ($30m$) and ASTER ($30m$) Global DEM were downloaded from the USGS Land Processes Distributed Active Archive Center – LP DAAC (https://gdex.cr.usgs.gov/gdex/).

5.2.4 Data Pre-Processing

The downloaded DEMs are void free datasets except ALOS PALSAR $12.5m$ at Pachoria, Guwahati, India. The voids were filled by using Inverse Distance Weightage technique provided in Arc-GIS v10.6.1. The water surfaces were not masked even though which creates noisy surface in DEMs generated using interferometric principle

Abstract-TH-2793_156104035

[Wendleder et al., 2012]. The water bodies act as sinks or storage bodies during floods, mainly in urban areas. Some of the DEM elevations are with respect to ellipsoidal heights referenced to the WGS84, ALOS PALSAR 12.5m, and CARTOSAT 30m [Das et al., 2015; Muralikrishnan et al., 2013]. Some global DEMs such as ALOS AW3D, ASTER, and SRTM are referred to as the geoid vertical datum [Tachikawa et al., 2011; Farr et al. 2007]. While regional DEMs like NED, EU-DEM are referred to local vertical datum. All ellipsoidal referenced DEMs and local datum DEMs were converted into orthometric height (H) using addition of geoid undulation (N) to ellipsoidal height (h) (h = H+N). The geoid undulation or separation obtained from NGA provided EGM96 (https://earth-info.nga.mil/GandG/update/index.php).

5.3 METHODOLOGY

The assessment was done by two approaches: (i) comparison of datasets by descriptive statistics; and (ii) comparison of datasets by zero-dimensional flood simulation model. A flowchart of the DEMs assessment routine and approach to select the suitable DEM is presented in Figure 5.3. The stages underlined in the assessment approaches are discussed below.

5.3.1 Descriptive Statistics Assessment Approach

To address the first approach of assessment of DEMs, the data sets were compared based on: a) descriptive statistics of elevation values; b) descriptive statistics of land slopes; c) contour lines and length analysis: and d) analysis of DEMs of differences (DoD) between surveyed data (high resolution) and each selected DEM.

The first stage, elevations of the study area are discussed in terms of its descriptive statistics such as the values of minimum, maximum, range, mean, median, standard deviation, skewness, kurtosis, 25th and 75th percentiles, and histograms of elevation for each study area. The second stage, descriptive statistics of slopes are also presented as histograms, its statistical matrices and plots of mean slope at each elevation and slope contour maps. In the third stage, number of contour lines and their lengths at each study site are derived from considered DEMs, and then assessment was carried out. Finally, the DoDs are derived between surveyed and selected DEMs and then analyzed by their statistical matrices, histograms, and maps. The raster algebra

Abstract-TH-2793_156104035

suggested by Shapiro & Westervelt [1994] was used to calculate DoDs by subtracting each DEM from the surveyed dataset. The positive values in DoDs indicate that the surveyed topographic dataset has higher elevations than the other selected DEM and vice versa. The selected DEMs were resampled to field survey one for each study site with a bicubic interpolation scheme to perform DoD operation.

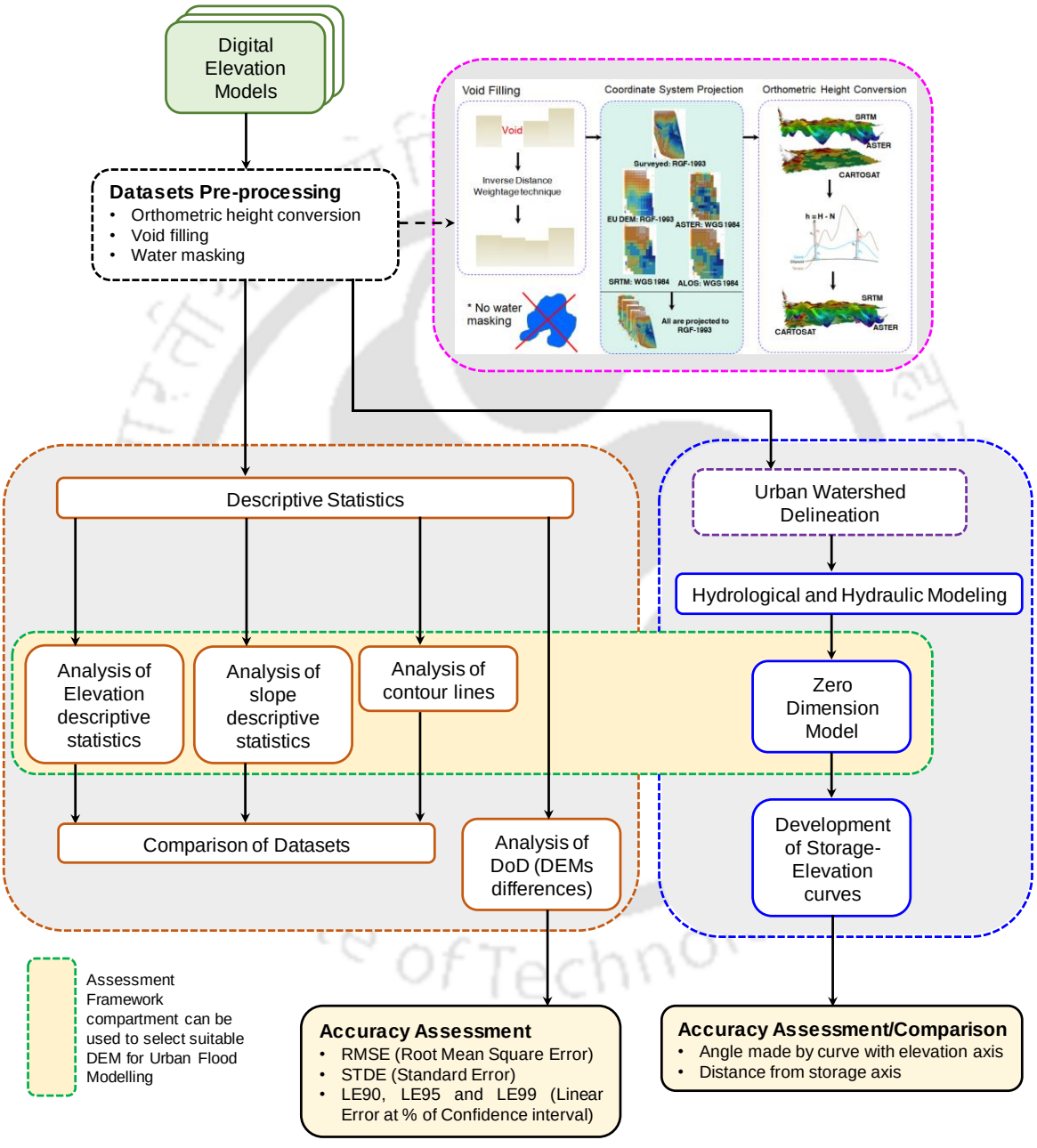

Figure 5.3. Framework followed for assessment of digital elevation models and selection criteria of suitable DEM for urban flood modeling.

Abstract-TH-2793_156104035

The vertical accuracy of datasets was quantified by some of selected metrics [Wessel et al., 2018; Grohmann, 2018] such as Mean Error (ME) [Wessel et al., 2018; Zhang et al., 2019], Root Mean Square Error (RMSE) most commonly used metrics in many fields [Nikolakopoulos et al., 2006; Stage et al., 2016], Standard Deviation Error (STDE), and Linear Errors (LE) at 90%, 95% and 99.73% confidence levels. The Linear Errors are proportional to STDE with an assumption of vertical errors are normally distributed [Greenwalt & Shultz, 1962; Congalton & Green, 2019]. The quantile distribution proposed by Höhle and Höhle [2009] was also used to quantify the appropriate linear error when vertical errors not follows the standard normal distribution.

$$ME = \frac{1}{n}\sum_{i=1}^{n}\left(Z_{ref,i} - Z_{DEM,i}\right)$$

$$RMSE = \sqrt{\frac{1}{n}\sum_{i=1}^{n}\left[\left(Z_{ref,i} - Z_{DEM,i}\right)^2\right]}$$

$$STDE = \sqrt{\frac{1}{n-1}\sum_{i=1}^{n}\left[\left(Z_{ref,i} - Z_{DEM,i}\right) - ME\right]^2} = \sqrt{\frac{1}{n-1}\sum_{i=1}^{n}\left(Z_{ref,i} - \overline{Z_{DEM}}\right)^2}$$

Linear errors by assuming the vertical errors are normally distributed.

$$LE90 = 1.65 \times STDE$$

$$LE95 = 1.90 \times STDE$$

$$LE3\sigma = 3.00 \times STDE$$

Linear errors by taking quantile distributions.

$$LE90 = \hat{Q}_{|\Delta h|}(0.90)$$

$$LE95 = \hat{Q}_{|\Delta h|}(0.95)$$

$$LE99 = \hat{Q}_{|\Delta h|}(0.99)$$

Where Z_{ref}, is the elevation of reference (survey) dataset; Z_{DEM}, is the elevation in each DEM (resampled to survey one); $\overline{Z_{DEM}}$, is arithmetic mean of Z_{DEM}; and n is the total number of valid pixels or points. These metrics were calculated from differences

Abstract-TH-2793_156104035

between the selected DEMs and with surveyed one as an independent source or reference of higher accuracy [Wechsler, 2007; Baade & Schmullius, 2016].

5.3.2 Flood Inundation Assessment Approach

For the second approach of the assessment, flood inundation modeling was accomplished with a Zero-dimension model consisting of storage-elevation curves. The zero-dimension hydrological model is a simplistic flood simulation model. It does not use any real-time data such as precipitation, imperviousness, infiltration, evapotranspiration, and it does not take into the account of overland flow and channel flow. Here, the assessment of DEMs was discussed with a zero-dimension model by the analysis of storage-elevation curves. These curves were generated for each DEM at all study areas.

The curves were plotted by considering the lowest point of a watershed as a reference elevation (Figure 5.4), and basin storage was calculated at regular elevations until the highest point (elevation) of the watershed. Then the curves were non-dimensionalized with respect to their maximum values of elevation and watershed storage, respectively. The curve makes an angle (α) with elevation (horizontal) axis and the distances at 25, 50, 75 percentiles (h_{25}, h_{50}, *and* h_{75}) from storage (vertical) axis were calculated. The characteristics of urban watershed were identified and DEMs were compared using angle (α) and distances (h_{25}, h_{50}, *and* h_{75}). Figure 5.4 shows a conceptual framework of curve generation, its non-dimensionalization, and its analysis.

Abstract-TH-2793_156104035

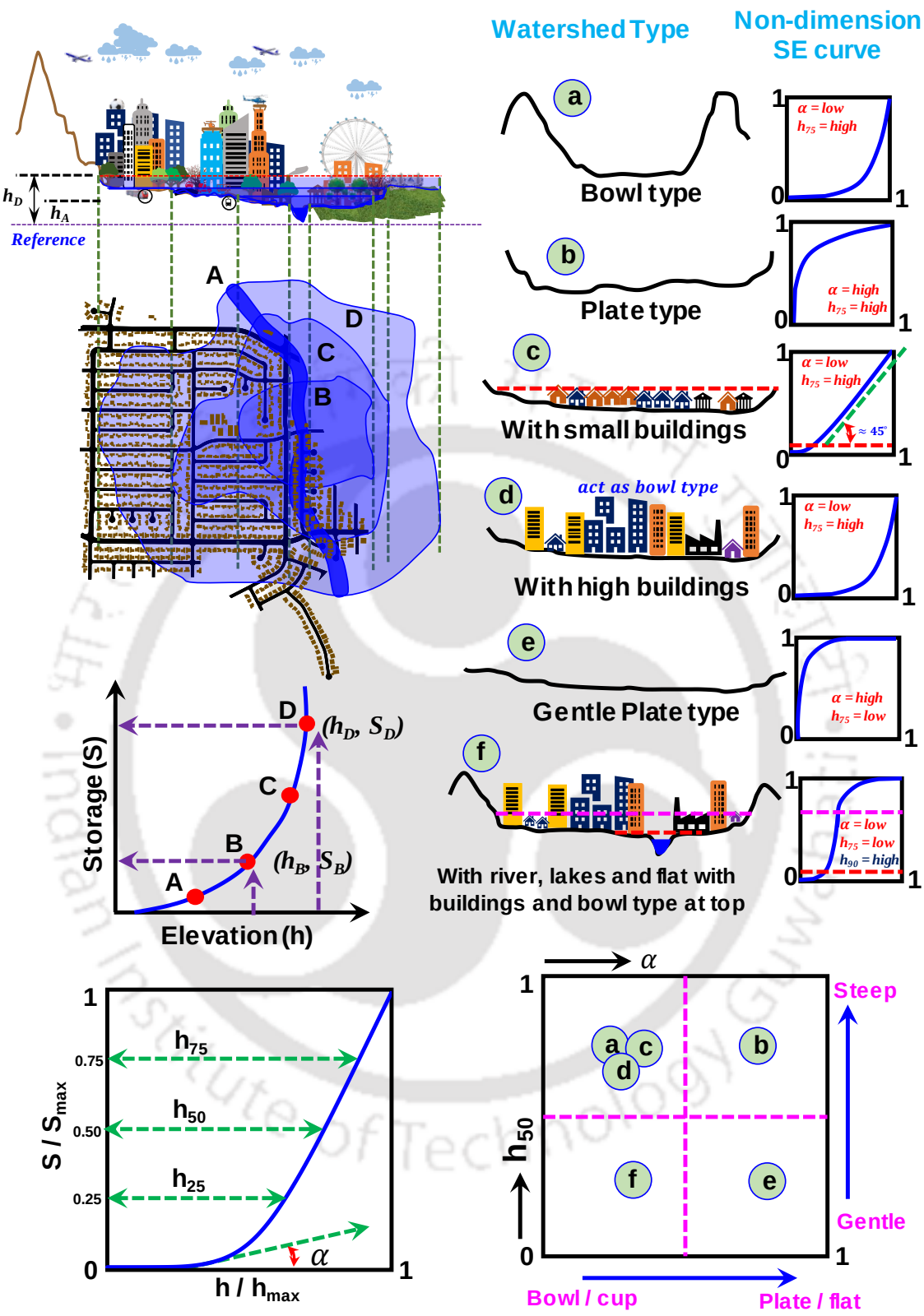

Figure 5.4. Conceptual sketch which depicts the hypothetical urban catchments, their storage-elevation curves, normalized angle-percentile distance parameters and catchment classification graph.

Abstract-TH-2793_156104035

5.4 RESULTS and DISCUSSION

5.4.1 Descriptive Statistics of Elevation Values

The frequency distribution of elevations extracted from all DEMs at selected study areas is depicted as histograms (Fig.5.5), while the statistics are provided in Appendix C2. The trends in all histograms show similar patterns, with slight shifts in distribution curves, the local difference in peaks position and shape of the histogram.

In the Simi Valley watershed (Fig.5.4A), all histograms except ASTER showed asymmetrical nature with a bimodal distribution. In contrast, ASTER was shown trimodal distribution with slightly shifted towards lower elevations (left of other data). A major peak was observed in bimodal distribution around 800-900*ft* in the valley, and the secondary peak is at 1000*ft* in hilly terrain accounted for by artifact patches. The focus of frequency fluctuations in the major peak around 800-900*ft* (at 815*ft*, 835*ft*, 867*ft*, and 880*ft*) in the histogram of NED data is well matched with the surveyed data, while ALOS AW3D and SRTM were not shown any peak at 815*ft*. The high spatial resolution of NED data (10*m*) and its compilation with other existing high-precision datasets in the USA are capable of capturing general topography such as low land area, cemetery, parking lots, ponds, swimming pool, and the channel pattern, while ALOS AW3D and SRTM were shown higher elevations than the mean surveyed elevations at these features. However, the NED was shown absence of urban artifacts in their datasets. ALOS AW3D and SRTM were exhibited similar peaks in histogram around 800-900*ft* interval except at 815*ft*. It may be due to the response of optical and C/X band sensors is comparable over an area where buildings at moderate height and mixed land cover presence. This might have resulted in similarity in ALOS AW3D (optical) and SRTM (C band) histogram distribution despite variability in elevations (Optical vs. Radar, Appendix C9).

In the Ashok Vihar, New Delhi watershed, all histograms exhibited trimodal distributions except ALOS PALSAR and ASTER, which were shown unimodal distribution (Fig.5.4B). In this watershed, the surveyed topography is a digital terrain model rather than a digital surface model. The data is free from man-made artifacts except the metro line passing through the study area (Appendix CF6). It could have accounted for the slight left shift of the second and third spikes at 212 and 214*m* in a surveyed histogram, while same spikes lie around 215-220*m* for other datasets. The

Abstract-TH-2793_156104035

ALOS AW3D and CARTOSAT DEMs have shown first peak (represents stream) clearly, while this response was unidentified in other DEMs.

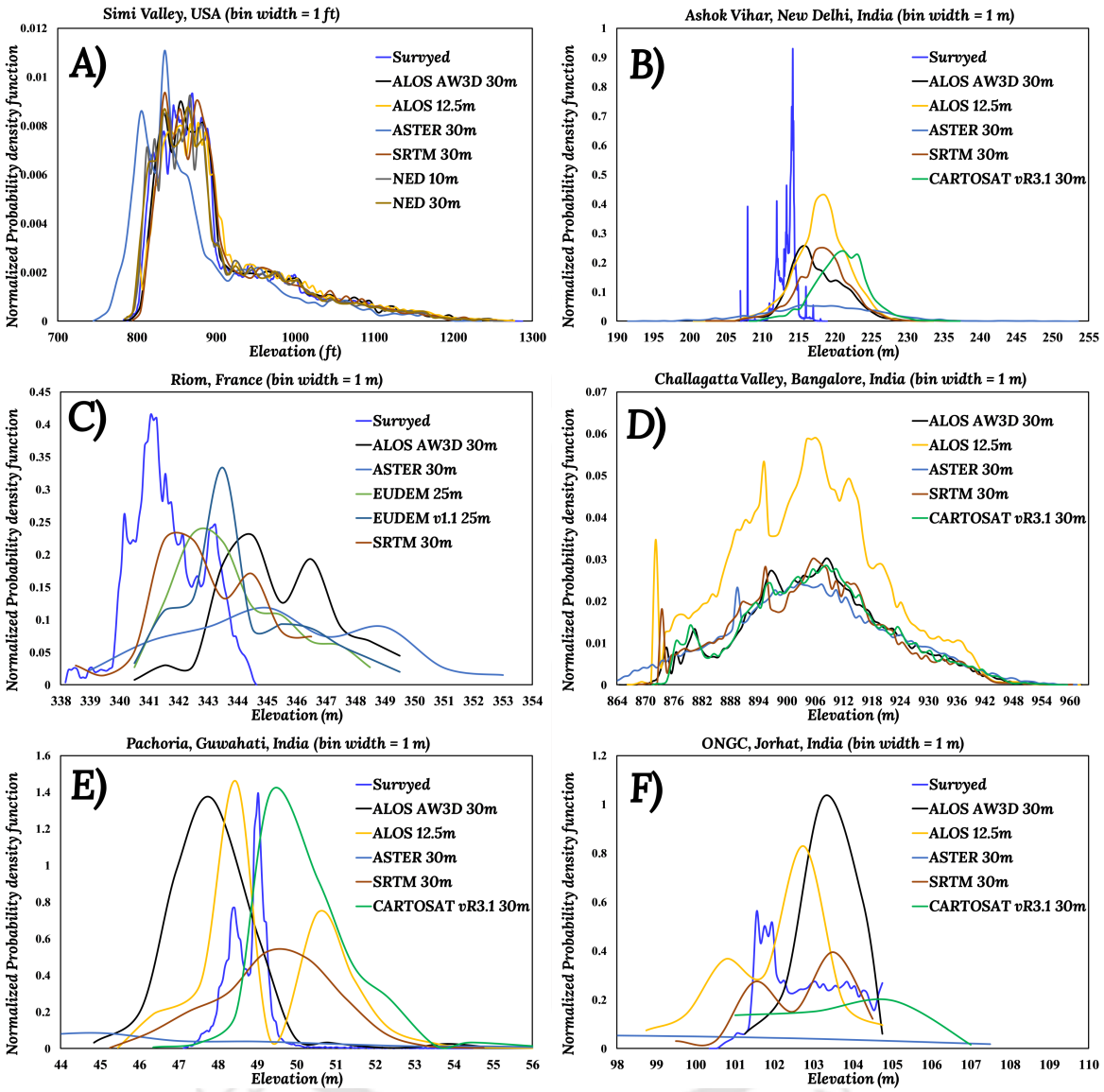

Figure 5.5. Frequency distributions of all selected DEMs at A) Simi Valley; B) New Delhi; C) Riom; D) Bangalore; E) Guwahati and F) Jorhat.

In the case of ALOS AW3D (PRISM) and CARTOSAT, the original data was acquired at 5*m* and 2.5*m* spatial resolution, which could have captured the stream in these datasets even after resampling to medium resolution. The buildings surrounded by open vegetation could have accounted for the second spike in the SRTM data, while it was shifted towards higher elevations for other datasets. It indicates that the captured elevation values in SRTM data are closer to bare ground values observed in the surveyed data. The deeper penetration of the C-band radar signal in leaf foliage, open vegetation areas, along with shadowing, layover effect (Optical vs. Radar, Appendix

Abstract-TH-2793_156104035

C9), might have resulted in the SRTM elevations closer to surveyed data (bare ground values).

The Pachoria, Guwahati watershed is a plain land comprise of small ponds and wetlands. Here, the elevation histogram of total station data was shown bimodal distribution while other datasets were exhibited unimodal distribution with peaks at different elevations (Fig.5.4E). The surveyed data was acquired in May 2014, which falls between the pre-monsoon and post-westerlies season, while other datasets were acquired during the years 2000-2009 with a fusion of different seasoned images. In this area, cloud coverage is also dominated most of the seasons, which could have accounted for the voids, which resulted in irregular responses in histogram shapes and peaks for all DEMs. However, all histograms are shown a similar tendency to surveyed with a hidden first spike in the curves around 45-48m (Fig.5.4E).

In the Jorhat watershed, total station surveyed data, ALOS PALSAR and SRTM elevation histogram were shown bimodal curves with peaks at ~101.5m and ~103.5m, while others were shown unimodal distribution around ~103-105m. The size of considered area is small and comprises with buildings and roads only, there could be a chance of horizontal shift in the datasets. The horizontal shift of one pixel in DEM data costs heavily on elevations for 30m and 12.5m spatial resolution datasets at small study areas.

5.4.2 Descriptive Statistics of Land Slopes

Figure 5.6 represents the frequency distribution of slopes as a histogram for all study areas. The maps of slopes and tables of statistical metrics were given in Appendix C3. The mean slopes at elevation were also computed (Appendix C13), which reveals the response of DEM to its local variations in topography, which is helpful to compare the response of DEMs in an effective way [Guth, 2006; Grohmann, 2018].

In general, a strong disagreement is found between the shapes of the slope histograms derived from considered DEMs at all study areas. The surveyed datasets have steeper slopes where the density of urban infrastructure is high (Simi Valley, Jorhat, Riom) (Fig.5.6A, C, and F). It also showed a high frequency of lower slopes where an area is a plane such as Pachoria, Guwahati (Fig.5.6E). At the same time, other open-source DEMs represented medium-range and moderate frequency of slopes.

Abstract-TH-2793_156104035

However, the histogram peaks of all DEMs showed strong agreement with surveyed data (Fig.5.6). The high spatial resolution of surveyed datasets was accounted for steeper slopes than coarser-resolution datasets. The steepness in slopes was decreased as DEM resolution became coarser [Chow & Hodgson, 2009; Chen & Zhou, 2013, Grohmann, 2018].

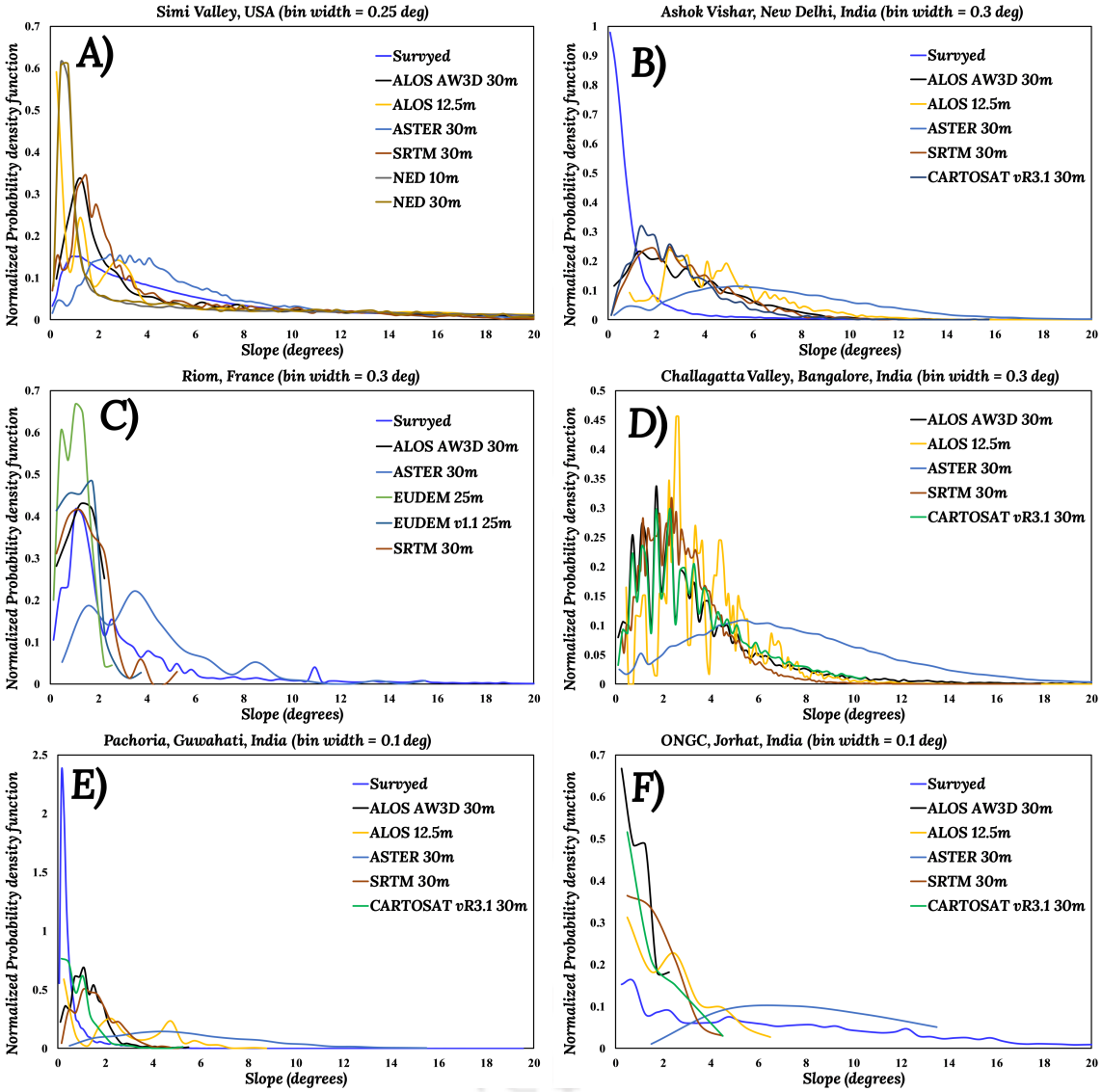

Figure 5.6. Frequency distributions of all selected DEM slopes at A) Simi Valley; B) New Delhi; C) Riom; D) Bangalore; E) Guwahati and F) Jorhat.

The ALOS AW3D has approximately depicted the slopes of streams, roads, grounds, and at foothills as similar as surveyed data even though it is a coarser resolution DEM. The NED 10*m* DEM has poorly depicted the slopes at buildings and roads, but it was depicted well at hills, streams, and plain lands (Fig.5.7a-c). The

smoothness (Digital Terrain Model) in the NED product might have accounted for the undetermined slopes at urban features.

In a plain area such as Pachoria, where the landscape is dominated by agriculture and wetlands, the spike in surveyed data differs from other DEMs. However, the mean slope value of CARTOSAT DEM agreed with the field surveyed data (Fig.5.6 and Appendix tableC6). The peak amplitude between ALOS AW3D and CARTOSAT was shown strong agreement (kurtosis 9.50 and 9.24). Similar behavior between ALOS AW3D and CARTOSAT was observed in other selected areas and also agreed in mean slope per elevation. In the highly impervious area, such as Challagatta Valley, dominated by high-rise commercial and residential buildings, ALOS AW3D has shown steeper slopes than other DEMs even though it is coarser than ALOS PALSAR (12m). ALOS AW3D was shown approximately similar behavior as the surveyed in terms of mean slope per elevation (Appendix C13) and better statistical metrics than other DEMs. The NED products in the Simi Valley, ALOS PALSAR in all areas, EU-DEM in Riom, and field surveyed data in New Delhi have shown higher amplitude at lower slopes than other datasets. It reveals that these datasets exhibit smooth topography and less evidence of artificial artifacts. At all study areas, ASTER data has shown evidence of more noise and artifacts introduced while processing the optical datasets (Optical vs. Radar, Appendix C9) [Reuter et al., 2009b; Miliaresis & Paraschou, 2011].

5.4.3 Analysis of Contour Lines and Lengths

The count of contour lines and lengths reveals the ability of DEMs to respond over a similar landscape. Grohmann [2018] stated that noisy DEMs produce a larger number of contour lines and the total length, while a smoothed DEM results in shorter lines at the same number of counts. In general, the artifacts in the form of buildings introduced to the DEMs considers as noise. However, this form of noise is essential in urban flood modeling due to the effect of buildings on flood inundation and its movement in cities. The finer DEMs accurately represent more urban features that produce the higher count and length of contours than coarser resolution DEMs. The ratio between length to count was calculated, which was used to evaluate the performance of different DEMs. Similar datasets would result similar in length to count ratio of contours.

Abstract-TH-2793_156104035

Contours were produced for each DEM at all study areas, with a vertical interval depending on the study area's size. 2*ft* at Simi Valley; 0.5*m* vertical interval at Riom, New Delhi, Challagatta Valley, and Guwahati; and 0.1*m* at Jorhat. The contour count and length values presented in Appendix C4 show the total length, count, and ratio for each DEM at all study areas. The plots of the cumulative sum of lengths and counts are shown in Appendix C14-15.

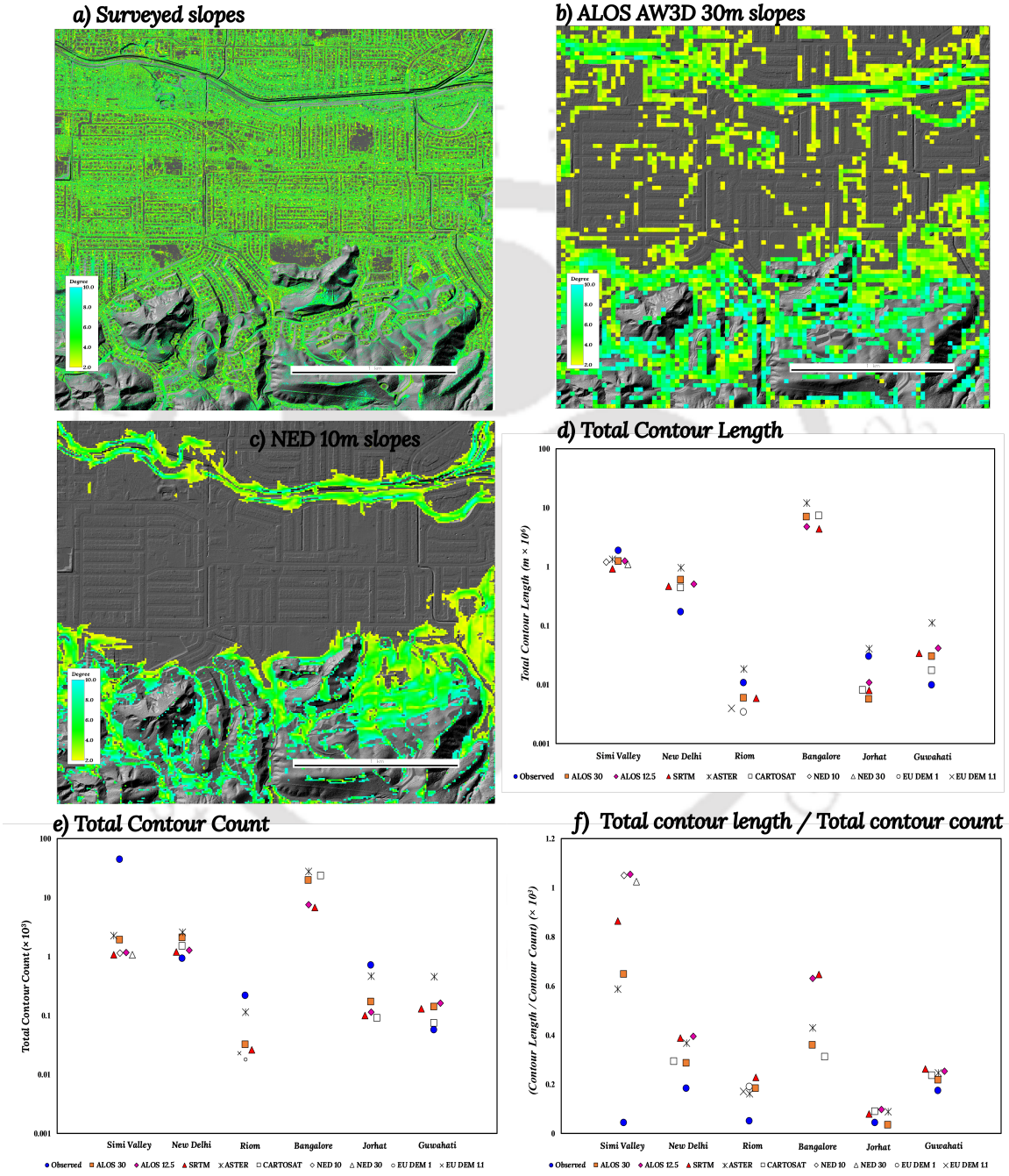

Figure 5.7. Slope values at Simi Valley corresponding to building edges or stream traces for a) surveyed data; b) ALOS AW3D; c) NED 10 m and contour characteristics at all study areas d) cumulative total of contour lengths; e) cumulative total of contour count; f) ratio between cumulative contour length to contour count.

Abstract-TH-2793_156104035

In Figure 5.6(d-e), the surveyed datasets with their high resolution have shown a higher total count and total length of contours at all study areas except New Delhi and Guwahati. As aforementioned in previous sections, the surveyed data at New Delhi is a terrain model instead of a surface model. Guwahati is also a plane area with wetlands, which could have accounted for lower values in count and lengths than other datasets in both study areas. Apart from surveyed data, ASTER has also shown higher values than other DEMs. However, as discussed in earlier sections, the ASTER has exhibited more noise in urban settings. The ALOS AW3D and SRTM showed similar contour lengths in all areas. However, the difference in contour count with higher values in ALOS AW3D DEM reveals that SRTM misses some urban features. In ALOS AW3D DEM, more levels of features were captured at 5m resolution of its original dataset. In Riom, EU-DEM has lower total length and counts than other products due to smoothness in those DEMs.

In Figure 5.6f, the contour length to count ratio of ALOS AW3D is nearer to the surveyed than other DEMs at all study areas. The CARTOSAT showed similar values to ALOS AW3D in all areas. The SRTM and ALOS PALSAR were shown similar values except at Simi Valley. In Simi Valley, finer resolution datasets such as ALOS PALSAR and NED products have shown similar ratios but away from surveyed data.

5.4.4 Analysis of DEMs of Difference (DoDs)

DEMs of differences (DoDs) provides several insights, such as issues built-in during the process of DEMs production [Grohmann, 2018], change detection or anthropogenic interaction in any landscape, process and forms in morphodynamics such as morphological sediment budgets [Wheaton et al., 2010] and intercomparing of survey techniques [Bangen et al., 2014]. The DoDs are also helpful in evaluating quantitatively how accurate DEMs represent the vertical elevations for the same landscape.

Figure 5.8(D) shows calculated statistical matrices of elevation differences for all datasets at each study area by considering surveyed data as a reference. The maps of DoDs and histograms are shown in Appendix C16 and Appendix C17, respectively. The descriptive statistics of DoDs are given in Appendix C5.

Abstract-TH-2793_156104035

In Simi Valley, the larger errors have shown at the edges of buildings and steep slopes of the hills in all datasets (Fig.5.8A, B). It reveals the problem in acquiring elevations at the building edges due to its coarse resolution and shadow effect in photogrammetry (ALOS AW3D, ASTER), or shadowing and overlay effect to the radar sensor in interferometry (SRTM, ALOS PALSAR) (Optical vs. Radar, Appendix C9). The topographic profile (Fig.5.8C) plotted from NE to SE covers the stream feature (Fig.5.8C(a)), hill characteristics (Fig.5.8C(c)), and urban features (Fig.5.8C(b)).

The topographic profile (Fig.5.8C) reveals that ALOS AW3D and surveyed one followed a similar pattern at all considered features. However, it has slightly shifted towards the left, which could have accounted for the positive difference (red) in NE (aspect ~45˚) – SW (aspect ~225˚) slope direction and negative differences (blue) in SW-NE slope directions (Fig.5.9A-B). This horizontal shift resulted in a horizontal error in ALOS AW3D DEM could have affected the vertical accuracy. ASTER was shown intense noise with values lower than surveyed data (Fig.5.8C). It reveals ASTER might have encountered with offset issue during its production process. The finer resolution datasets such as ALOS PALSAR and NED have strong asymmetrical histograms of DoD with a mean error of -0.33m and -0.11m, respectively (Fig.5.8B; Fig.5.8D, Appendix C6). Moreover, NED has shown ~0m DoDs at plane areas such as roads and playgrounds (Fig.7B-C). SRTM was shown clear tendency of negative difference (blue) for eastern aspects (N-S: ~ 0˚→ 180˚) and positive differences (red) for western aspects (S-N: ~ 180˚→ 360˚) (Fig.5.9C-D), a similar tendency was observed at Challagatta valley. However, it would not be observed in ALOS PALSAR, which was also developed by microwave interferometry. The thick blue patches in ALOS AW3D and thick red patches in SRTM exhibited around the urban settings in the Simi Valley watershed indicated localized anthropogenic land use changes such as modification of land to the playground, cemetery purpose, and non-anthropogenic variations such as change in vegetation cover from 2000 (SRTM acquisition), 2006 (ALOS AW3D) to 2014 (Surveyed dataset). These changes can be seen in Figure 5.9E, collected from archive historical imageries from the Google Earth platform (https://www.google.com/intl/en_in/earth/).

Abstract-TH-2793_156104035

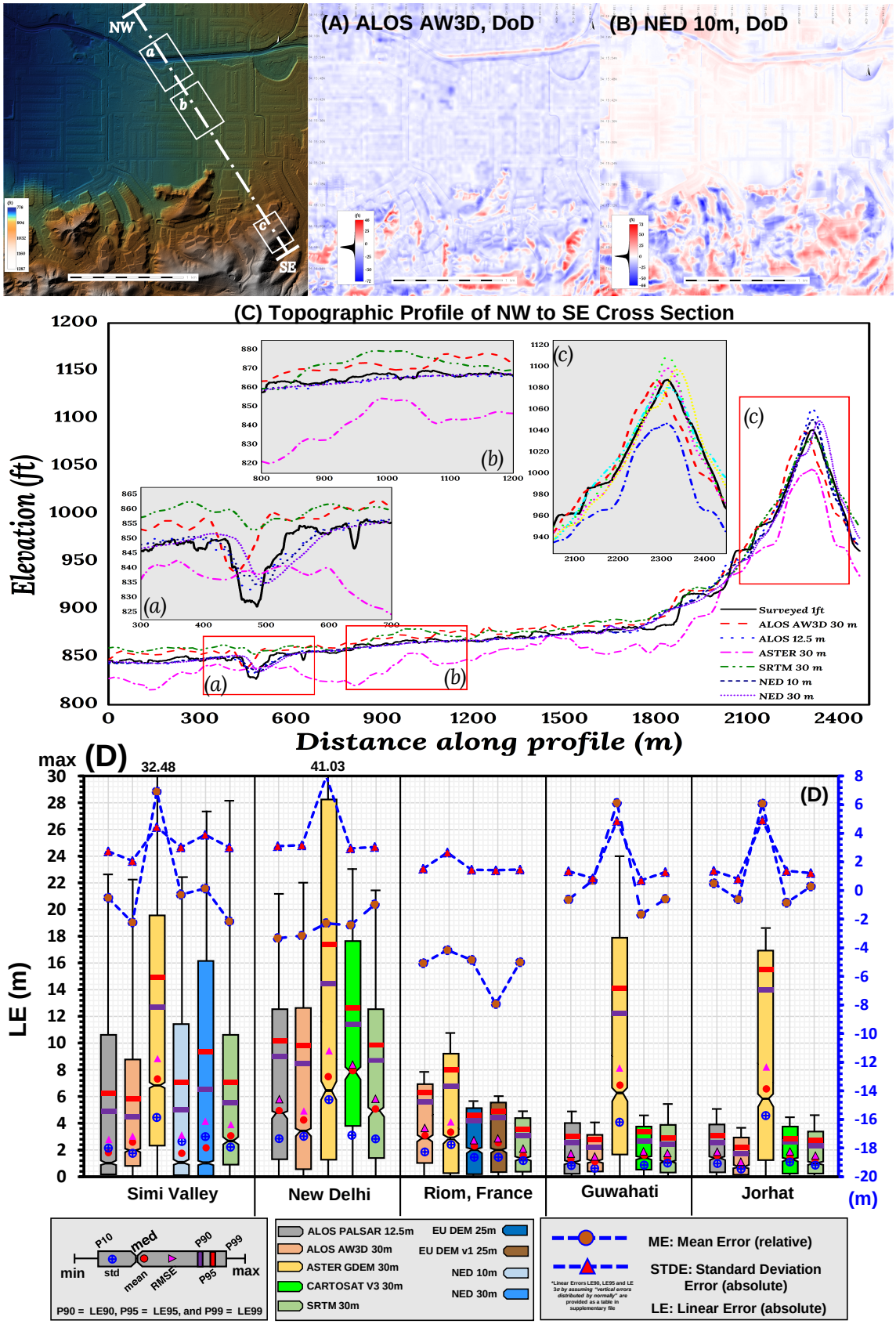

Figure 5.8. Difference between surveyed and other DEMs their errors. A) DEM of Differences (Surveyed–ALOS AW3D); B) DEM of Differences (Surveyed–NED10*m*); C) Topographic profile from NW to SE; D) Errors/ accuracy metrics at all study areas for all DEMs.

Similar patterns of blue and red patches in DoDs were observed between photogrammetry-based DEMs at New Delhi, even though the datasets are acquired on different time periods (Fig.5.10A-B). Similar patches were also observed between interferometry-based DEMs at this study area (Fig.5.10C-D). It can be noted that the surveyed dataset at the New Delhi watershed is a DTM which represents the bare ground of the study area. The large white patches (~0*m* differences) over the open area were observed in ALOS AW3D and CARTOSAT DEMs (Fig.5.10A and B), which implies the optical DEMs were closely approximated to the field surveyed elevations at open areas. Several red patches were observed along the stream and extreme right side of the area (Fig.5.10). These patches are the results of the anthropogenic changes in wetlands filling up to prepare cricket ground and non-anthropogenic changes such as vegetation growth along the stream from the year 2000 (SRTM), the year 2006 (ALOS) to the year 2014 (Surveyed). These changes can be seen in Figure 5.10E, collected from archive historical imageries from Google Earth platform (https://www.google.com/intl/en_in/earth/). These red patches in ALOS AW3D, SRTM, and ALOS PALSAR DEMs could have accounted the larger LE90 than CARTOSAT DEM.

The minimum and maximum LE90 and RMSE errors obtained for each DEM were provided in Table 5.2. The all other statistical error is shown in Figure 5.8D, and the complete error metrics tables with and without considering the normal distribution of error were provided in Appendix C7.

Table 5.2. Error Metrics (Vertical Accuracy) compared to field surveyed data including at all urban settings. LE90: Linear error at 90%; RMSE: Root Mean Square Error (Detailed Error Metrics provided in Appendix C).

DEM	LE90 (m)		RMSE (m)	
	Minimum	Maximum	Minimum	Maximum
ALOS AW3D 30m	1.73	8.61	1.07	5.18
ALOS PALSAR 12.5m	2.63	9.01	1.59	5.87
ASTER 30m	6.82	14.58	4.09	9.36
CARTOSAT vR3.1 30m	2.77	11.46	1.69	8.32
NED 10m	-	5.29	-	3.19
NED 30m	-	6.55	-	4.07
SRTM 30m	2.41	8.82	1.48	5.77

Abstract-TH-2793_156104035

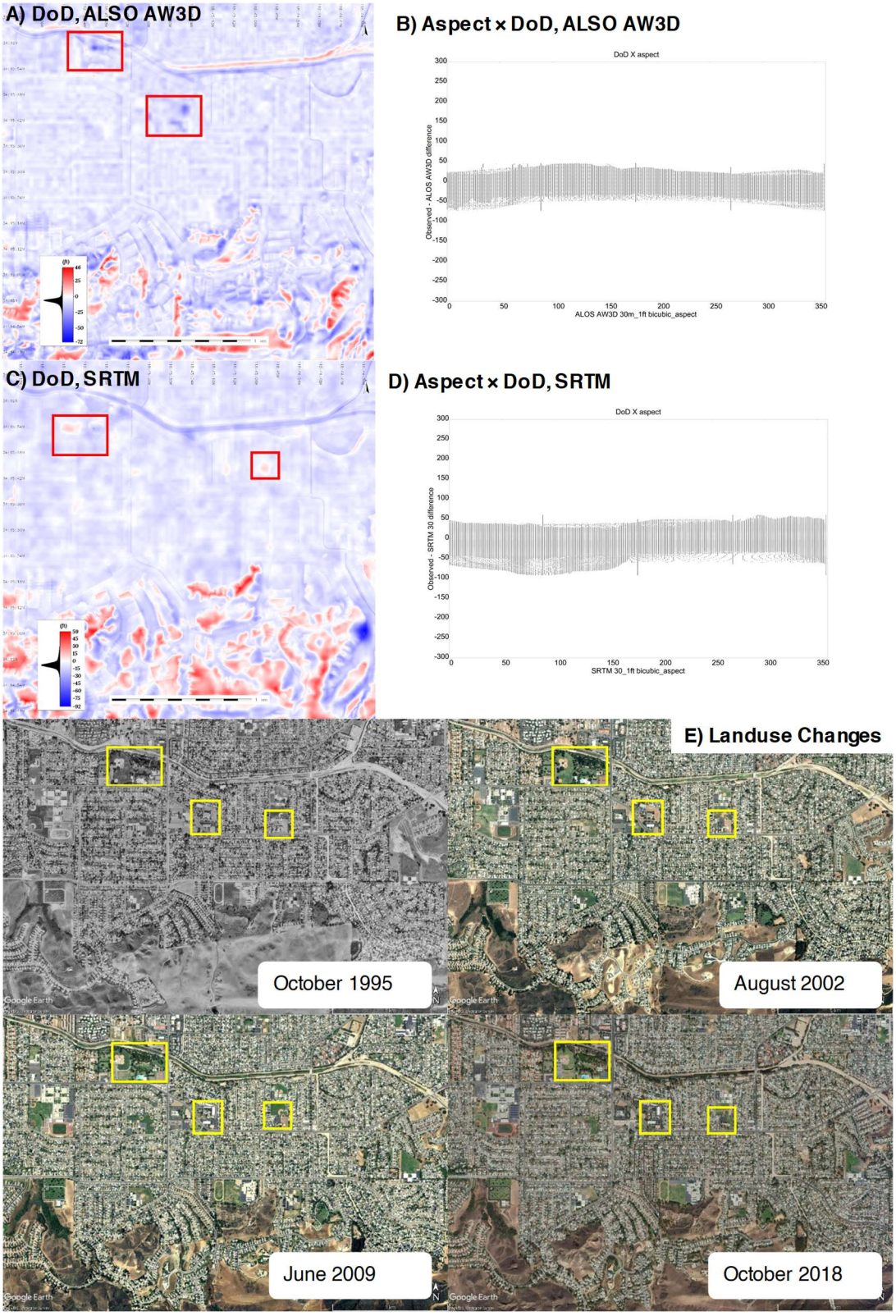

Figure 5.9. At Simi Valley watershed, A) DEMs of Differences (Surveyed–ALOS AW3D); B) scatterplot of ALOS AW3D 30*m* aspect *versus* deviations from field surveyed; C) DEMs of Differences (Surveyed–SRTM); D) scatterplot of SRTM 30*m* aspect *versus* deviations from field surveyed; E) Landsat images of October 1995, August 2002, June 2009, October 2018, satellite imagery ©Landsat/Copernicus powered by Google Earth.

Abstract-TH-2793_156104035

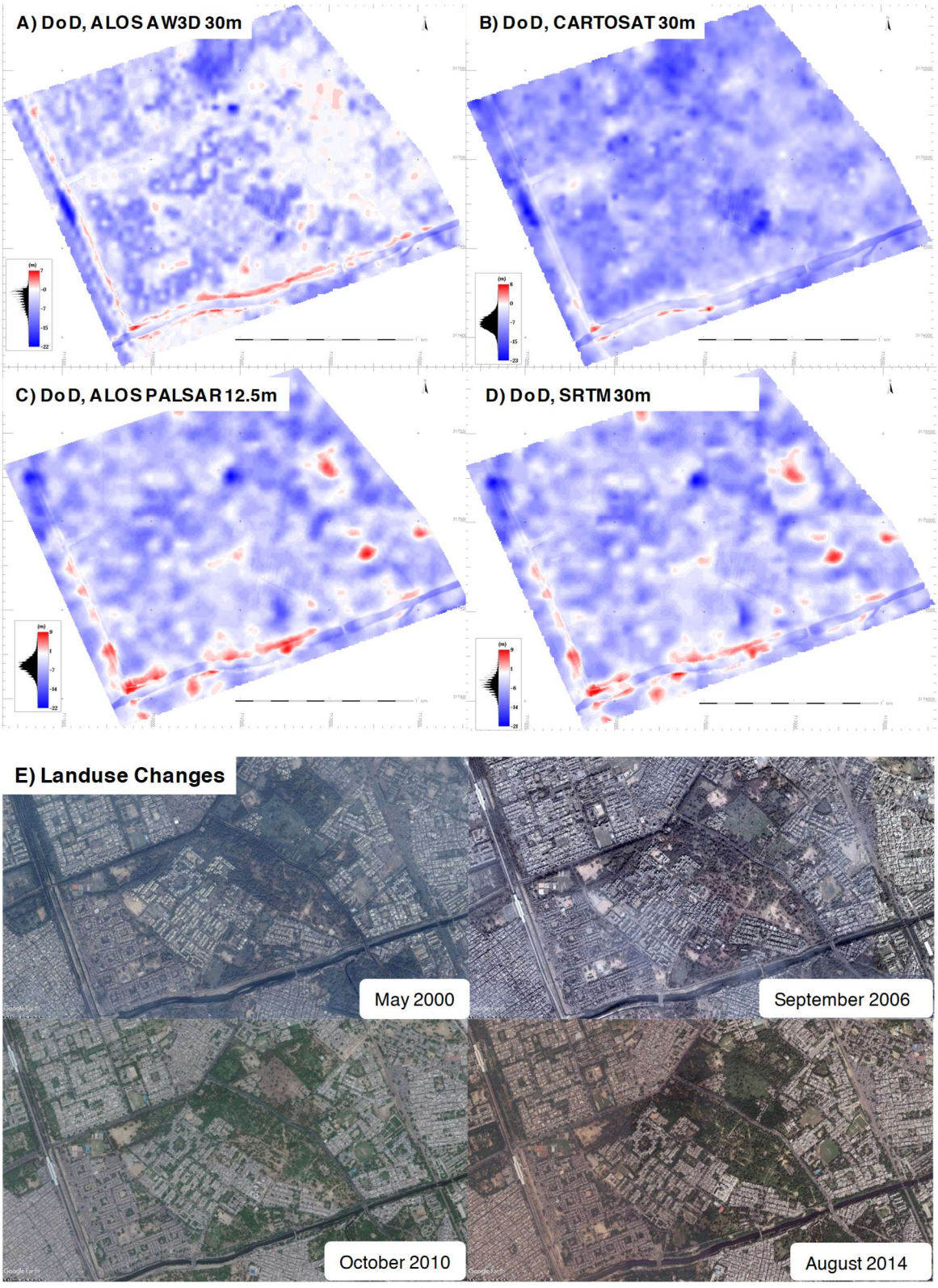

Figure 5.10. At Ashok Vihar, New Delhi watershed, A) DEMs of Differences (Surveyed–ALOS AW3D); B) DEMs of Differences (Surveyed–CARTOSAT); C) DEMs of Differences (Surveyed–ALOS PALSAR); D) DEMs of Differences (Surveyed–SRTM); E) Landsat images of May 2000, September 2006, October 2010, August 2014, satellite imagery ©Landsat/Copernicus powered by Google Earth.

Abstract-TH-2793_156104035

5.4.5 Zero Dimension Hydrological Model

The relationship between flood elevations and their respective inundation volumes (storage-elevation functions) were calculated for each DEM for all study areas. The graphs of storage-elevation curves were plotted and presented in Appendix C20. Figure 5.11(A-B) shows the storage-elevation curve and its non-dimensionalization at the Simi Valley watershed for each DEM. The curve making an angle (α) with its elevation axis and the distances at 25, 50, 75 percentiles (h_{25}, h_{50}, and h_{75}) from the storage axis (y-axis) were calculated for each DEM for all study areas and presented in Figure 5.11(C-E).

The Storage-Elevation curve presented in Figure 5.11A illustrates the volume of flood inundation with respect to the watershed elevation of Simi Valley. The lower land elevation or minimum level of a watershed is considered as a reference (zero). The three zones of upper land (Fig.5.11A(a)), midland (Fig.5.11A(b)), and lower land (Fig.5.11A(c)) of the watershed were considered to illustrate and evaluate quantitatively how accurate DEM predicts the storage with respect to surveyed data. Figure 5.11A(a) shows ALOS AW3D is closely following the path of surveyed data, the other DEMs NED and ALOS PALSAR exhibits apparent differences with surveyed and SRTM lies in between smooth (NED; ALOS PALSAR) and rough (ALOS AW3D; ASTER) DEMs. In the midland part (Fig.5.11A(b)), all DEMs shown a little difference with surveyed data but in the higher land part (Fig.5.11A(c)), the surveyed data slightly shifted towards smooth DEMs and fairly matched with SRTM DEM.

In general, the SE curves for all DEMs at any study area show similar trends with slight deviation due to large ranges in its storage values, making it challenging to analyze the results. In this study, the results are interpreted using normalized angle-percentile distances α and h_{25}, h_{50}, and h_{75}, respectively. These parameters provide several insights such as watershed characteristics, whether flat type of cup type, a gentle slope, or steep slope, and valuable to evaluate quantitatively how accurate the representation level of DEMs for the same landscape. The relation between α and height percentile at h_{25} has shown more scatter, while h_{75} has shown a close horizontal band. It highlights the influence of DEM type on flood inundation at lower inundation depths and can be negligible at higher inundation depths. The relation between α and h_{50} (median of elevations) has taken to analyze and assess the performance of DEMs.

Abstract-TH-2793_156104035

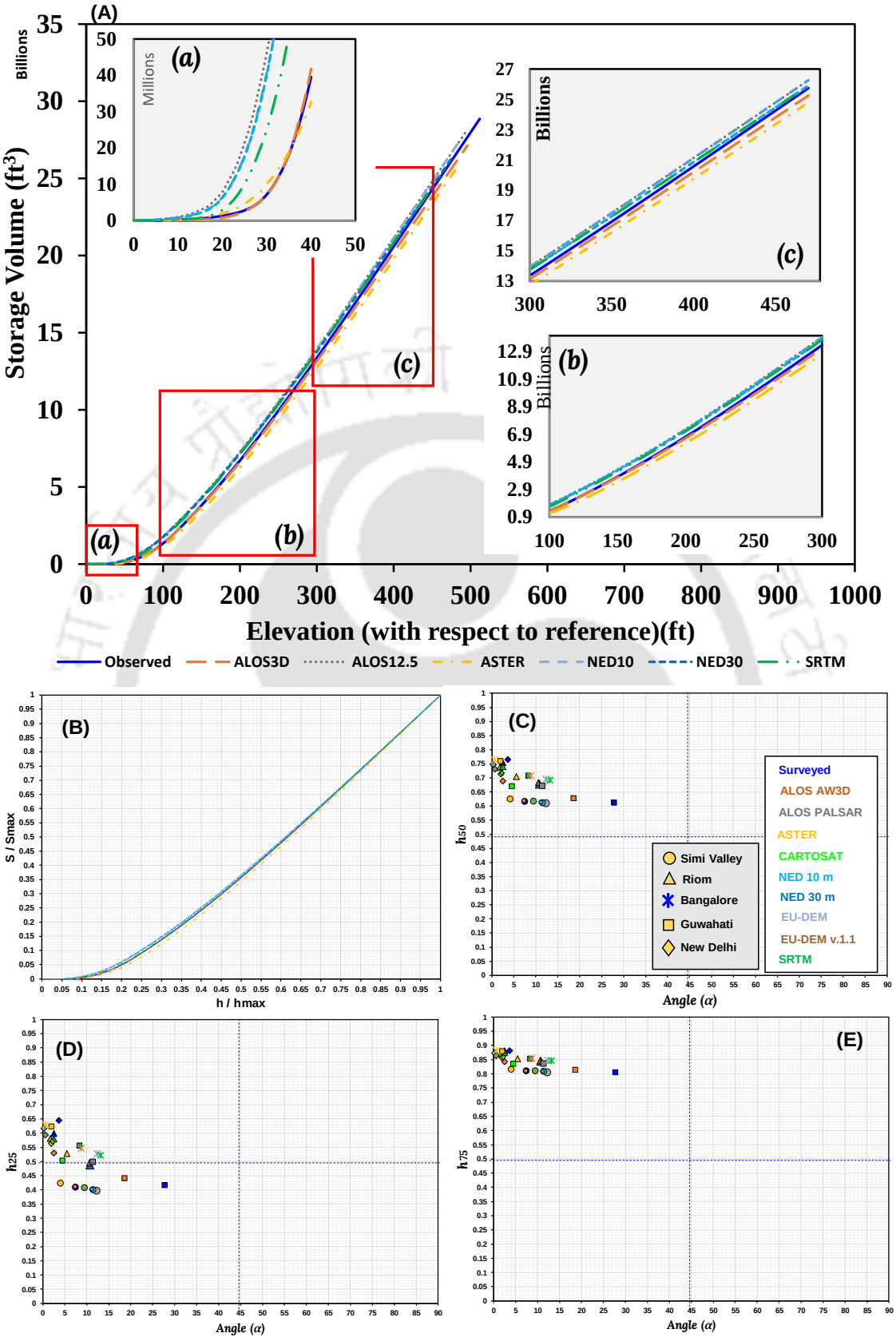

Figure 5.11. The results of angle and percentile distance parameters estimated from storage-elevation curves: A) S-E curve at Simi Valley; B) Normalized SE curve; C) scatter plot between angle and h

Abstract-TH-2793_156104035

The surveyed data at Guwahati falls towards the right extreme of α-h_{50} graph (Fig.5.11C), which indicates the watershed is plate type with a gentle slope with respect to other areas. It can also be noticed by visual inspection of DEM, satellite image, and statistics explained in previous sections. For the Simi Valley watershed, there was a slight difference in h_{50}, but more difference was observed in angle, which indicates all DEMs represent the same steepness but differ in watershed type (refer Fig.5.4 and Fig.5.11). The ASTER has shown as more rugged or cup type than others. The ALOS AW3D overlapped with the surveyed one, while NED and ALOS PALSAR have shown close relation, but SRTM has fallen in between surveyed and NED DEMs. For Riom, ALOS AW3D and SRTM were closed to surveyed data and shown steeper and bowl type than EU DEM. For New Delhi, the field surveyed data was shown flatter and steeper than other DEMs. The DEMs developed by interferometry techniques such as SRTM and ALOS PALSAR have shown close relation with each other, steeper and bowl type than other DEMs

In contrast, CARTOSAT, ASTER, and ALOS AW3D were shown close relation with each other at the New Delhi site. In the Bangalore watershed also, interferometry DEMs showed close relation, but less steep and flatter than ALOS AW3D and ASTER. Interestingly, CARTOSAT (photogrammetry) predicted similar storage inundation to SRTM (interferometry) in Challaghatta (Bangalore) watershed. The graph (Fig.5.11) that ASTER has shown steeper and cup type watershed in all areas than other datasets, while ALOS AW3D has shown close relation to the surveyed data.

5.4.6 Overall Assessment and Limitations

The results mentioned above show the remarkable value of medium resolution gridded DEMs for urban flood modeling that can be accessed online. The elimination and selection of perfect DEM are quite challenging due to their feature identification capability of the topographic model. The cognizable capacity of the DEMs table was prepared to assess and presented in Table 5.3. This table gives the overall rating by assigning a 0-5 rating system at each study area based on its visual and quantitative comparing capability at a particular feature. The individual ratings were given for each model were presented in table Appendix C8.

Consistently for all visual and quantitative metrics, ALOS AW3D has shown higher dominance than all other DEMs. It showed higher dominance than other DEMs

Abstract-TH-2793_156104035

except for NED in comparison to surveyed datasets for these key reasons: (i) vertical accuracy, (ii) acquisition date, (iii) acquisition grid resolution ($5m$ - later it resampled to higher grid resolutions – $30m$), and (iv) acquisition process which is effective in urban regions than riverine planes and other types of land covers. Identifying man-made artifacts such as buildings, roads, drains, and bridges are essential for flood modeling in urban regions to prepare accurate inundation maps. The identification of natural streams without obstructed by human-made artifacts also crucial for flood routing in urban settings. It indicates that bare-earth with some induced man-made artifacts DEM product should be needed for the urban flood modeling. The ALOS AW3D shown balance between these two features (DSM and DTM), which is still required to remove unwanted surface artifacts such as vegetation, aligning with surveyed data in urban hydrological modeling. Earlier studies stated that ALOS AW3D is comparable to recently acquired high-resolution TanDEM-X [Grohmann, 2018] even though it is a medium resolution dataset. ALOS AW3D by removing surface artifacts such as trees and bridges except building footprints could further enhance the capability of ALOS AW3D for urban flood modeling purposes.

The ALOS AW3D and SRTM DEMs may appear quite attractive in developing countries where the acquisition of high-resolution surveys such as LiDAR is quite expensive and a challenging task. Several limitations should be considered when using medium resolution online available DEMs for urban flood modeling. Firstly, no topographic model can identify the cross-section of drainage channels and small streams. Secondly, the suitability of a DEM for urban flood modeling may depend on the type, size of the area, and flood frequency. The high-resolution DEMs should be required for frequent flood event simulations than rare flood events [Sanders, 2007]. The infrequent flood events produce higher flood depths and larger storage volumes. The initial results of the zero-dimension model have shown that the influence of DEM resolution at higher depths (h_{75}) is negligible. So, the medium resolution open-source DEM will be suitable to simulate the infrequent flood events.

Abstract-TH-2793_156104035

Table 5.3. Cognizable capacity of DEMs towards urban flood modeling (all are relative to field surveyed data). (Detailed rating scores are provided in Appendix C).

DEM	Features by Visual Identification					Statistical Analysis			Elevation Differences (DoDs)	Storage Holding Capacity	Overall Performance
	Buildings	Water bodies	Roads	Channel Network	Vegetation	Elevations	Slopes	Contours			
ALOS PALSAR (12 m)											
ALOS AW3D (30 m)											
ASTER GDEM (30 m)											
CARTOSAT (30m)											
EU DEM (~25 m)		---									
EU DEM V1 (~25 m)		---									
NED (10 m)											
NED (30 m)											
SRTM (30 m)											



Abstract-TH-2793_156104035

Taking all these together, we suggest that the open-source DEMs have shown their capability towards urban flood modeling. It is also suggested that the user has to be understood the topographical characteristics of the urban or peri-urban study area, its size, and at which flood frequency modeling is going to set up. The framework proposed acts as a guiding step while selecting the appropriate DEM for urban flood inundation modeling in data-scarce regions. The most recent studies have identified that the TanDEM-X has the potential capability to map urban features [Rossi & Gernhardt, 2013]. The authors hope it may be beneficial for urban flood modeling in the future, but now it is not available for general users.

5.5 CONCLUSIONS

It is widely accepted that high-resolution DEMs are suitable for urban studies due to their accurate representation of topography with high horizontal-vertical accuracy and their ability to detect building footprints, vegetation, bare earth, and other features. Most developing and developed nations cannot acquire high-resolution datasets such as LiDAR due to its acquisition cost and post-processing complexities. This chapter aimed to identify the appropriate online available DEM that can be used to set up the 1D/2D urban hydrological flood model. A novel technique based on normalized angle and percentile distances of the Storage-Elevation curve was introduced in this study to identify the best performed DEM for urban flood modeling. This technique also identifies the characteristics and type of watershed. An assessment framework was also designed with descriptive statistics such as elevation histograms, slopes, and contours analysis to identify the suitable online DEM for urban flood modeling and mapping. Here, the statistics mentioned above were analyzed to assess the open-source DEMs for urban flood mapping. Among the sources we used, available online DEMs such as ALOS AW3D, ALOS PALSAR, CARTOSAT, EU-DEM, NED, and SRTM were assessed with field surveyed data as a reference over six urban settings.

This thorough study observed that ASTER global DEM infuse with complete noise and significant elevation differences to other datasets in urban settings. So, the ASTER global DEM can be eliminated for any studies in urban settings. The high-resolution DEMs such as ALOS PALSAR global model, 1/3 s NED and medium resolution 1s NED available for the USA depict the good ground elevations, which effectively stripped away the building and other artificial artifacts. These models

Abstract-TH-2793_156104035

represent DTM rather than DSM, and these DEMs may work fine in riverine flood plains but not in urban settings. The high-resolution DEMs (ALOS PALSAR and NED) represented a flat type of watershed with gentle slopes. It creates overprediction in flood extent and underprediction in flood depths and creates low flow velocity zones. These models also produced vertical accuracy around 6m (LE90) while ALOS AW3D shown around 4m (LE90). The ALOS PALSAR has shown a large area of voids over the entire globe. The EU-DEM performed well over Riom than any other DEM, but it can be comparable to SRTM. The CARTOSAT regional product for India performed well than SRTM and comparable with ALOS AW3D in descriptive statistics, but it showed mixed satisfaction in the zero-dimension hydrological model. The ALOS AW3D showed consistent overall performance even though it is a medium resolution DEM. However, it has also shown a mismatch between adjacent pixels and large area voids in some places. The results showed that ALOS AW3D would not be helpful for small study areas due to a mismatch in adjacent pixels. The ALOS AW3D and CARTOSAT are the photogrammetry-based datasets; the cloud coverage in original images could have caused large voids in these datasets. Besides, the open-source DEMs were acquired a long way back in early 2000. The ALOS AW3D has shown potential capability in the urban region by giving an excellent overall performance. Removing unwanted noise such as vegetation cover, bridges, etc. could further enhance the ALOS AW3D DEM.

From this study, we hope for urban hydrologists to take away that when choosing a topography model in urban environments, there is no single topographic model that works fine everywhere and every time. So, from this research, it is advocated that researchers and hydrologists always go for the initial assessment of topographic model statistics before going to modeling. It is strongly recommended to perform the proposed framework with available DEMs for a particular urban region before using DEMs for urban hydrological modeling. It is also helpful to understand the characteristics of a watershed, which gives the idea of which DEM should be used to set up the hydrological model.

Abstract-TH-2793_156104035

6

INFLUENCE OF DEMs ON SWMM MODEL

(Assessing the Impact of Open-Source DEMs on SWMM Model Outputs)

Abstract-TH-2793_156104035

6.1 INTRODUCTION

The frequency and magnitude of urban flooding are increasing in many cities worldwide due to potential causes of climate change and the growing percentage of imperviousness in urban areas [Leitão et al., 2016; Kelleher & McPhillips, 2020]. The exposure to flooding has increased in many cities due to its local growth, population migration, and concentration [UNDESA, 2014]. There is also evidence that efforts are increasing to localized reductions in vulnerability by making preparedness and mitigating the floods [Jongman et al., 2015; Tanoue et al., 2016]. The prediction and mapping of flood inundation extent are essential to mitigate the floods and reduce their interaction with day-to-day human activity in urban areas. The topography has become an essential tool to map the flood inundation in urban areas, as overland flow is driven by gravity [Leitão & de Sousa, 2018]. Many earlier studies have also shown that a simplistic topographic-based urban routing model yielded similar results to a highly complex model and a physical-based model that incorporates engineering dense urban drainage networks [Lhomme et al., 2004; Kelleher & McPhillips, 2020].

In many urban hydrological models, the topography data has been used to identify the urban watershed boundary, extract the natural urban fluvial networks, overland flow network paths, rim elevation for natural and man-made urban drainage networks, and terrain depressions/ponds. These are essential inputs extracted from the topographic model to reliably model the pluvial flooding in urban areas using the 1D hydrological model [Leitão et al., 2013]. The evolution of remotely sensed topographic models such as Digital Elevation Models (DEM) has changed the current condition of hydrological models from 1D to 2D and its widespread usage [Bates, 2004, 2012; Schumann et al., 2007, 2009]. These DEMs have become the primary source of topographical data [Wilson & Gallant, 2000; Baghdadi et al., 2005]. The high spatial resolution DEMs acquired by airborne and vehicle-mounted such as LiDAR has given opportunities to explore simplistic high-end urban hydrological models.

Moreover, in urban hydrology, the extensive focus on DEMs' high resolution and quality is increased with the extensive use of 2D flood models [Peña & Nardi, 2018; Ogania et al., 2019; Muthusamy et al., 2021]. However, the acquisition of such high-resolution DEMs is always not possible for many nations in the world due to its financial and practical challenges and complexity in data processing [Sanders, 2007;

Abstract-TH-2793_156104035

Muthusamy et al., 2021]. This made urban hydrologists to explore the open-source medium resolution digital elevation models for urban flood modeling and mapping. These medium resolution open-source DEMs have an inherent source of uncertainties, which could be due to their spatial resolution and source of preparation of data, which can impact the outputs of urban flood models. Although much research is carried out to assess the impact of DEMs and their resolution towards fluvial floods and urban fluvial floods through river modeling [Saksena & Merwade, 2015; Muthusamy et al., 2021], very few studies have been attempted for the urban flood model [Fewtrell et al., 2008; Leitão et al., 2009].

This study attempted to assess the influence of medium resolution globally available DEMs on an urban hydrological model, which can be helpful where high-resolution topographic model data scarcity is there. Here, the influence of open-source medium resolution DEMs on the 1D hydrological model Storm Water Management Model (SWMM) was attempted instead of any 2D hydrological model. Even though the extensive use of 2D hydrological models is increased with its significant benefits towards overland flow flood simulation, the use of 1D models is still of interest and quite popular for many flooding simulation purposes, such as early flood warning [Leitão et al., 2010; Leitão et al., 2013] and emergency management. Moreover, the SWMM model is the most popular used one worldwide for urban flood prediction and design purposes than any other model. In this study, to compute the flood inundation extents and plot the maps, many drainage networks with a large number of nodes/junctions were generated manually over an area. It made the 1D SWMM model into some sort of 2D model characteristics, which helps compute the overland flow in the 1D SWMM model. The influence of the DEM source and its resolution on each output variable extracted from the SWMM model were analyzed. The model's sensitivity was identified towards the DEM for each variable, such as flood depths, peaks, and inundation areas. Here, it is also attempted to identify the suitable global DEMs for urban flood modeling. The rest of the chapter is organized as follows. The second section informs the selected study areas and datasets. Section 3 describes the methodology adopted for the present study. Section 4 includes the results and discussion and followed by fifth section on conclusions.

Abstract-TH-2793_156104035

6.2 STUDY AREA AND DATA DESCRIPTION

The five urban settings chosen for the study, the selected open-source digital elevation models, its description, and its pre-processing, the software used for this study are already provided in detail in Section 5.2.

6.3 METHODOLOGY

Figure 6.1 shows the methodological flow chart of the framework followed to assess the influence of open-source DEMs on the 1D urban hydrological model. The assessment of open-source DEMs effect on the urban hydrological model was done by 1D hydrological modeling simulation. For this purpose, Storm Water Management Model (SWMM) Tool was used, which is developed by the United States Environmental Protection Agency (US EPA), which is the most commonly used flood modeling and drainage design tool in urban regions. It has three compartments: Atmospheric, Surface flow, and Channel flow (Transportation). The other details, such as governing equations and numerical schemes, can be found in SWMM technical reference manuals (https://www.epa.gov/water-research/storm-water-management-model-swmm#tab-6).

The essential inputs for the SWMM model are drain data such as rim and invert elevations, drain network slopes and watershed slopes, watershed boundary, natural and artificial flow network paths, which can be extracted from the topographic data. The other inputs such as precipitation, imperviousness, channel lengths, and roughness also play a significant role. The topographic data is essential to assign rim elevations of natural and artificial drains in model setup, extract the urban watershed boundary, develop flood inundation extent maps, and calculate flood inundation areas where the field surveyed rim elevation is not available. In all study areas, the model was set up with drain rim elevations and slopes extracted from selected DEMs in this study, while the drain lengths, cross-sections, and roughness were given to the model collected during the field visit. Table 6.1 shows the detailed inputs used to simulate the 1D SWMM hydrological model in all study areas for all collected topographical models. In this study, to compute the flood inundation extents and plot the maps, many drainage networks with many nodes/junctions were generated manually over an area.

Abstract-TH-2793_156104035

It made the 1D SWMM model into some sort of 2D model characteristics helpful in computing the overland flow in the 1D SWMM model.

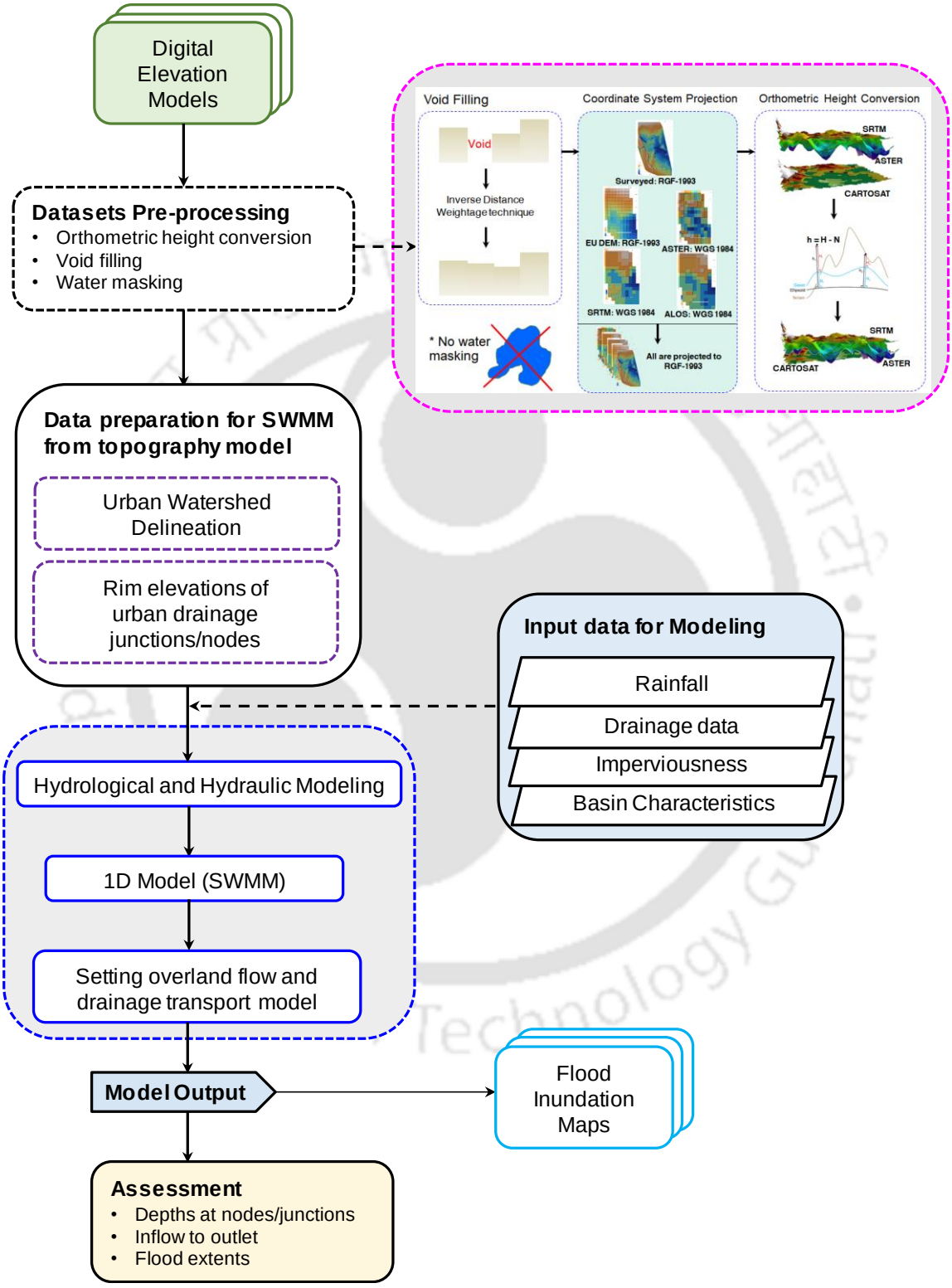

Figure 6.1. Flow outline followed to setup and simulate SWMM model for assessment of influence of DEMs on SWMM model.

Abstract-TH-2793_156104035

Table 6.1: Input datasets used for 1D urban hydrological model SWMM simulation

Study Area	Drain Sizes	Natural and Manmade - Drain Rim Elevations	Precipitation	Imperviousness	Watersheds, natural and man-made flow networks	U/S Conditions	D/S Conditions
Simi Valley, California, USA	Field survey	Respective topographical models*	--	Field survey	No sub-watersheds	Flow rate	Fixed outlet
Riom, France	Field survey	Respective topographical models*	--	Field survey	No sub-watersheds	Flow rate	Fixed outlet
Ashok Vihar, New Delhi, India	Field survey	Respective topographical models*	IDF Curve	Field survey	Delineated using respective DEMs	Surface runoff	Fixed outlet
Challagatta Valley, Bangalore, India	Field survey	Respective topographical models*	1969 event	Field survey	Delineated using respective DEMs	Surface runoff	Fixed outlet
Jorhat, India	Field survey	Respective topographical models*	IDF Curve	Field survey	Delineated using respective DEMs	Surface runoff	Fixed outlet

*Topographical models: Field Surveyed, ALOS AW3D, ALOS PALSAR, ASTER, CARTOSAT, NED, and SRTM Digital Elevation Models

Abstract-TH-2793_156104035

The simulated outputs, such as total inflow at the outlet, depths at nodal junctions, etc., were quantified and analyzed at all study areas. The flood inundation extent was calculated only at the Simi Valley watershed, and then the flood inundation maps were plotted by exporting outputs into the GIS tool such as Arc-GIS. The considered DEMs at all study areas were evaluated, and the sensitivity of the SWMM model towards DEMs source and resolution was assessed using calculated flood extents, its peak, flooded nodes, and total runoff generated at outfalls.

6.4 RESULTS and DISCUSSION

The hydrological behavior of the field surveyed and global DEMs were studied for the selected urban watershed flood response in terms of flood depths, and peak flows, inflow at the outlet, and flood extents using the SWMM model. The sensitivity of the flood estimation for these DEMs on the SWMM model was identified with its simulation outputs. The model simulations were carried out at different conditions (Table 6.1) for each study area, depending on its characteristics. The simulated hydrological responses were analyzed with reference to field surveyed data and presented below.

6.4.1 SWMM Simulated Flood Inundation Depths

Figure 6.2 shows box-and-whisker plots of flood inundation depths at all study areas for each selected topographic model (Tables in Appendix D1). Figure 6.3 shows the error diagram (scatter plot between RMSE and STDE) of flood inundation depths calculated for different DEMs with respect to field surveyed DEM simulated depths (Table in Appendix D1).

At Simi Valley watershed, in the Box-and-Whisker diagram of inundation depth (Fig.6.2a, Appendix DT1), the extreme deviations ranging from 0 to 9.47m. These are attributable to SRTM and ASTER DEMs. The median of all datasets matches clearly at 0.06m except for ASTER DEM. As expected, the ASTER predicted less accurate flood inundation depths, which can be seen in the box-and-whisker diagram of ASTER DEM in Figure 6.2(a). The inundation depths variation, its right and left tails of high-resolution datasets (ALOS PALSAR, NED) nearly match with field surveyed simulated

Abstract-TH-2793_156104035

depths. The NED 30*m* data showed similar values with NED 10*m* in Box plot and RMSE vs. STDE error plot (Fig.6.3).

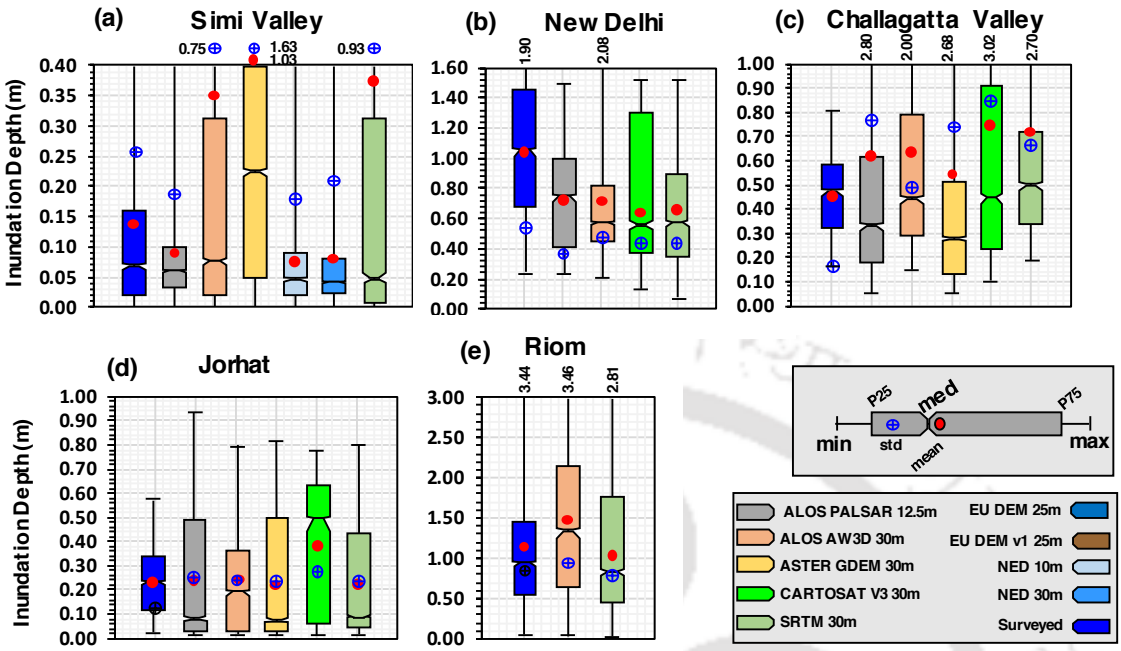

Figure 6.2: Box-and-Whisker plots of SWMM model simulated inundation depths at all study areas for different Digital Elevation Models.

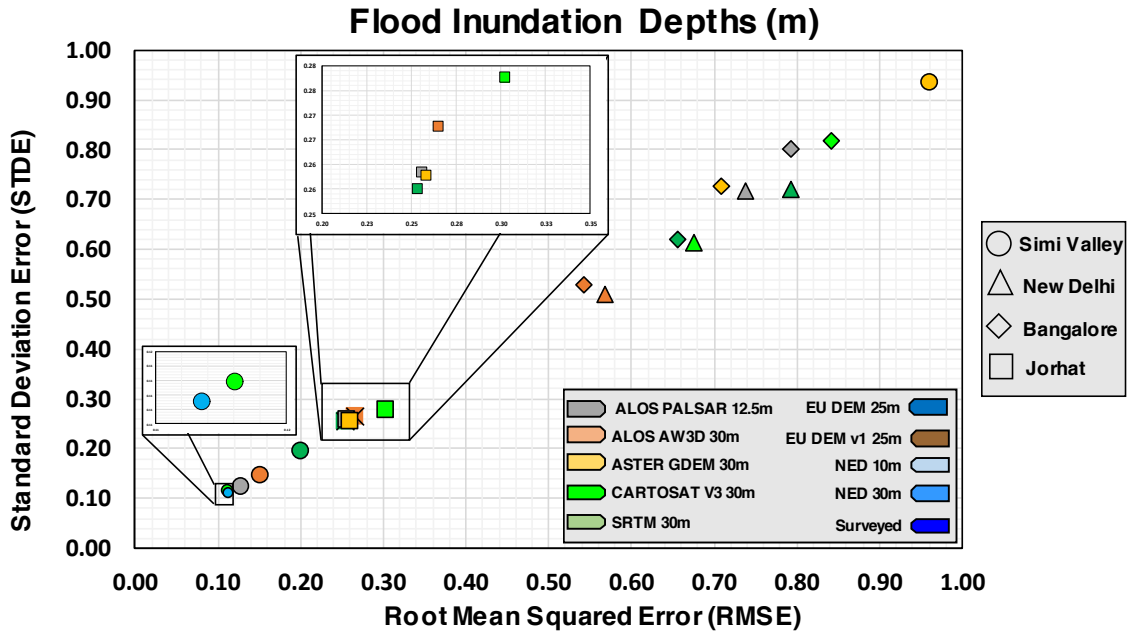

Figure 6.3: Error diagram (RMSE vs STDE) of SWMM model simulated inundation depths at all study areas for different Digital Elevation Models relative to field surveyed data.

Abstract-TH-2793_156104035

Similar results were observed between NED10*m* and NED30*m* in terms of peaks (Fig.6.4), hydrographs (Fig.6.6), and flood extents (Fig.6.7) of their binary metrics (Table 6.2) even though increment in its spatial resolution from 10*m* to 30*m*.

Not much difference in error was observed between high-resolution datasets (ALOS PALSAR, NED 10m) and medium resolution datasets (ALOS AW3D, SRTM) even though they show more variations Box-and-Whisker plot. In challagatta (Bangalore) and Jorhat watersheds, ALOS AW3D shown similar flood depth ranges to field surveyed data. While other DEMs showed large ranges in these areas. ALOS AW3D DEM was shown fewer errors comparatively other exact resolution DEMs except for Jorhat, where the watershed size is very small. The horizontal shift of pixel in ALOS AW3D DEM might have a reason for this. However, all DEMs showed less than 1m STDE and RMSE errors where the maximum depth is in the range of 3m, which are acceptable. However, the results showed that the model is sensitive to predicting the flood depths at nodal junctions.

6.4.2 SWMM Simulated Flood Peaks

Figure 6.4 represents the flood peaks simulated using SWMM and the Mean Error of peaks with respect to field surveyed data (Appendix D2). Figure 6.5 shows the error diagram (scatter plot between MAE and RMSE) of flood peaks calculated for different DEMs with respect to field surveyed DEM simulated peaks (Table in Appendix D2).

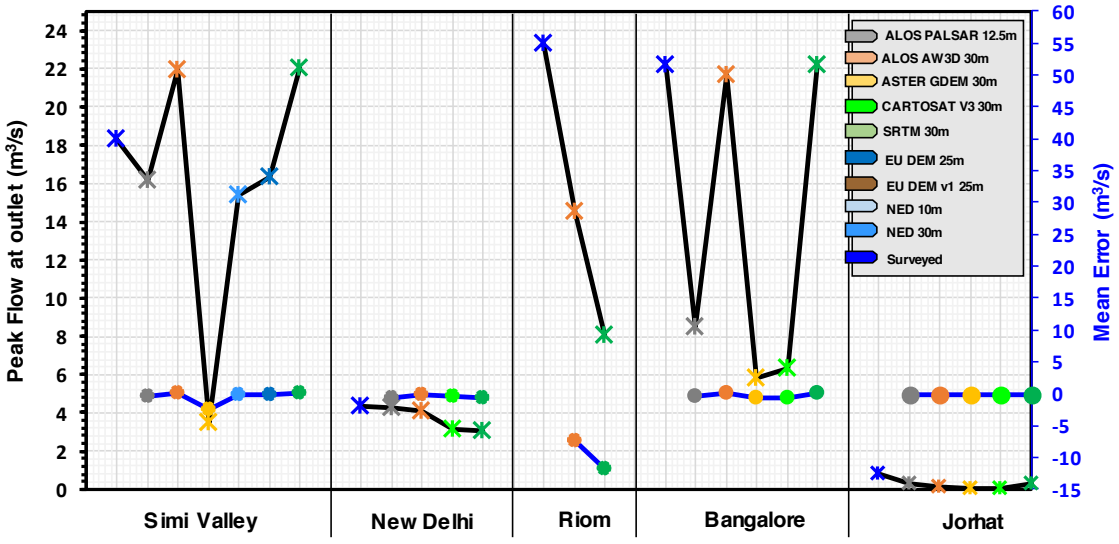

Figure 6.4: Peaks at outlet and Mean Error with respect to field surveyed data plots of SWMM model simulated outputs at all study areas for different Digital Elevation Models.

Abstract-TH-2793_156104035

The MAE vs. RMSE error diagram (Fig.6.5) shown clearly the ALOWS AW3D predicted flood peaks similar to field surveyed data than others. However, ALOS AW3D and SRTM were over-predicted the peaks than peak simulated with field surveyed data in the Simi Valley watershed. While in New Delhi and Bangalore watersheds, both DEMs ALOS AW3D and SRTM showed similar peaks to field surveyed peaks (Fig.6.4). However, the mean error of all DEMs falls nearer range except ASTER DEM even though the peaks were observed around ~20m^3/s. It indicates that the influence of DEMs on flood peaks is negligible whether DEM is high resolution or coarse resolution.

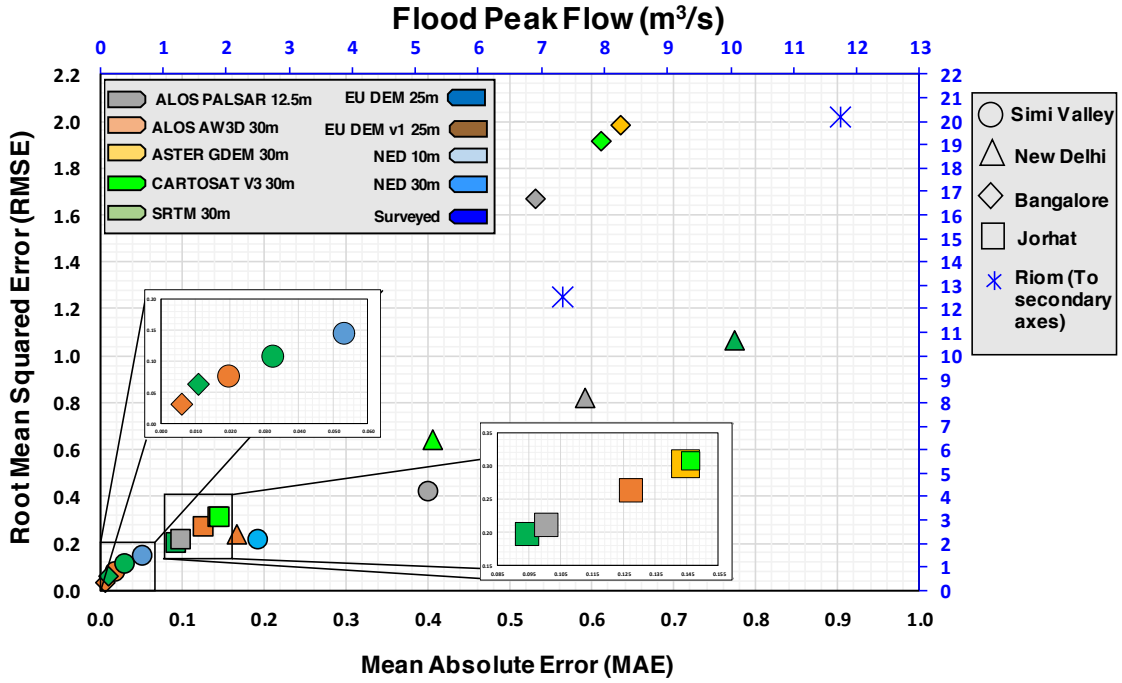

Figure 6.5: Error diagram (MAE vs RMSE) of SWMM model simulated flood peaks at all study areas for different Digital Elevation Models relative to field surveyed data

In Simi Valley, the high-resolution DEMs (ALOS PALSAR and NED) were under-predicted the peaks, while the medium resolution DEMs (ALOS AW3D and SRTM) were over-predicted. The high-resolution DEMs considered here are smooth ones (DTMs), while medium resolution DEMs are DSMs, which could have caused the less flood peak load at the outlet for high-resolution DEMs vice versa. It supports the underprediction of flood depths for high-resolution data (DTMs) and overprediction for medium resolution (DSMs) observed in the previous section (Fig.6.2). The smooth DEMs distribute the flood volume over an area due to the absence of urban artifacts in

Abstract-TH-2793_156104035

data, implying a decrease in flood depths and peaks in these datasets. The errors RMSE ($< 2.2\ m^3/s$) and MAE ($< 1\ m^3/s$) are in acceptable ranges (Fig.6.5).

6.4.3 SWMM Simulated Inflow at Outlet

The hydrograph computed at the outlet of Simi Valley watershed and its %error was plotted and shown in Figure 6.6.

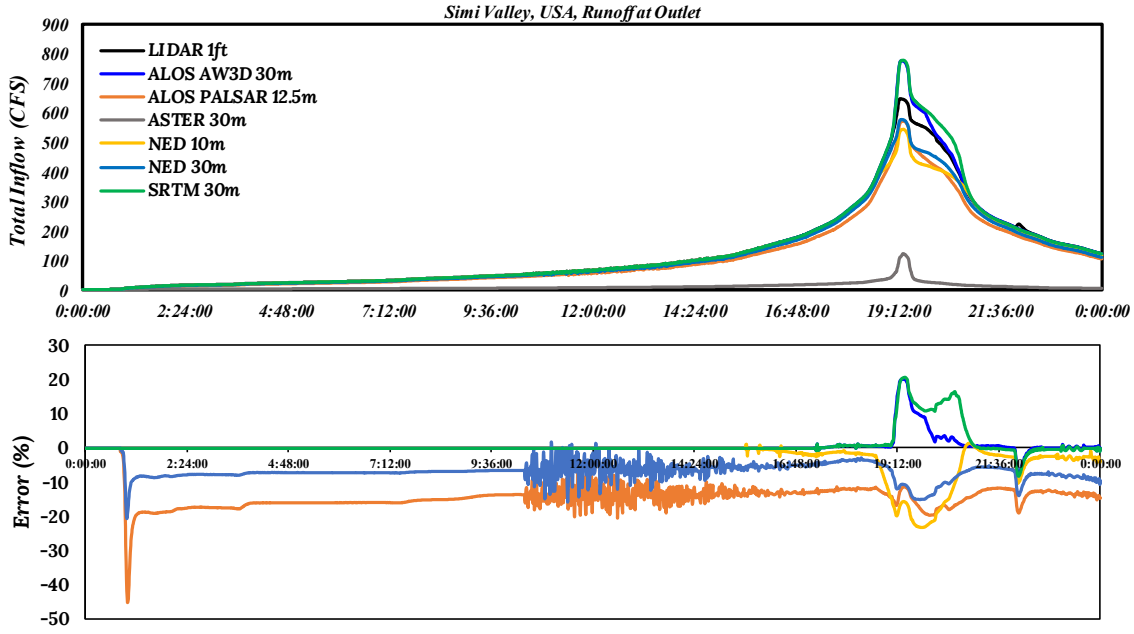

Figure 6.6: Inflow hydrograph its %error for each DEM with reference to field surveyed data at Simi Valley urban watershed.

It was observed that the total inflow hydrograph at the outlet is insensitive to the open-source DEM products except at hydrograph peaks (Fig.6.6). In rising limb of the hydrograph, the ALOS AW3D and SRTM have shown a similar pattern with negligible %error, while the high-resolution DEM (ALOS PALSAR, NED) curves were slightly lowered than the actual field surveyed data with ~-40% error at initial stages and ~-20% error at middle stages of the rising limb. In peak and recession limb of the hydrograph, the ALOS AW3D and SRTM have overpredicted with a 20% error, while ALOS PALSAR, NED 10m, and NED 30*m* were underpredicted with a -20% error. The results showed that the model is sensitive at peaks for all DEMs and insensitive at the rising limb of the hydrograph. However, the mean error at peaks was in the order of 4-6 m^3/s (Fig.6.4), and all DEM products have shown similar mean error, which indicates that the open-source digital elevation models can be attractive alternate sources for urban flood modeling with SWMM tool.

Abstract-TH-2793_156104035

6.4.4 Flood Inundation Extents

The flood inundated extents were plotted at Simi Valley watershed by exporting depths computed at junctional nodes (~15000 nodes) in SWMM all over the area into the GIS tool. Figure 6.7 shows the flood inundation extent maps plotted with maximum flood depths for all DEMs. The flood inundation areas were calculated for each DEM then the binary metrics (skill scores) were computed by overlapping flood inundation map generated by each DEM with field surveyed data map. The six binary metrics suggested by Stephens et al. [2014] were calculated to determine the sensitivity of DEM to SWMM model and to check the most successful topographic model. Table 6.2 provides the computed binary metrics (skill scores) of each DEM at the Simi Valley watershed. The Critical Success Index (CSI) score is to assess model skill, $F^{<3>}$ score to penalize under prediction, $F^{<4>}$ score to penalize over prediction, Bias is for balance between over and under prediction, Hit Rate is to show correctly predicted, and False Alarm Rate score is for incorrectly predicted areal cells between field surveyed and other DEMs.

Table 6.2: Binary metrics (Sill Scores) computed for each DEM at Simi Valley watershed.

Flood Extent Binary Metrics	CSI	$F^{<3>}$	$F^{<4>}$	BIAS	HR	FAR
ALOS AW3D 30m	0.15	-0.63	0.06	0.25	0.16	0.07
ALOS PALSAR 12.5m	0.45	0.40	-0.05	1.89	0.89	0.87
ASTER 30m	0.29	-0.27	0.13	0.52	0.34	0.16
NED 10m	0.41	0.31	-0.07	1.72	0.80	0.81
NED 30m	0.38	0.20	-0.07	1.47	0.68	0.70
SRTM 30m	0.14	-0.66	0.07	0.22	0.15	0.06

* CSI: Critical Success Index; HR: Hit Rate; FAR: False Alarm Rate;
$F^{<3>}$: score to penalize under prediction; $F^{<4>}$: score to penalize over prediction.

The high-resolution DEMs such as NED and ALOS PALSAR were outperformed than medium resolution DEMs such as ALOS AW3D and SRTM by flood inundation extent visual comparison and binary metric CSI score. The commonly used metrics such as CSI score and F score are alone not sufficient to understand the model over and under prediction performance.

Abstract-TH-2793_156104035

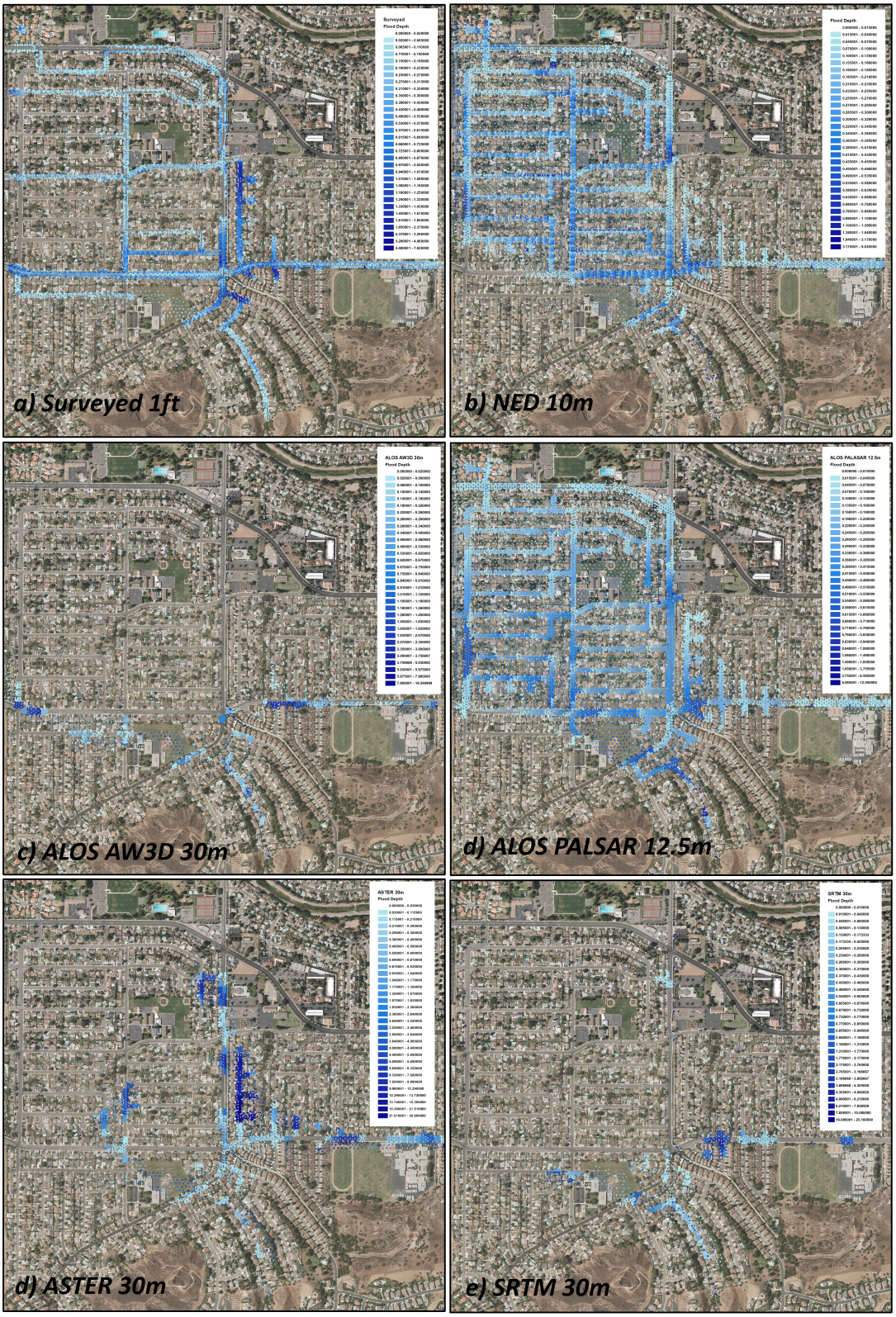

Figure 6.7: SWMM Modeled flood inundation extent maps at Simi Valley, USA for the DEMs, a) Surveyed; b) NED; c) ALOS AW3D; d) ALOS PALSAR; e) ASTER and f) SRTM.

Abstract-TH-2793_156104035

The CSI score for NED and ALOS PALSAR is higher than the ALOS AW3D and SRTM, while they strongly agreed with the $F^{<3>}$ score, which penalizes the underprediction but ALOS AW3D and SRTM were firmly disagreed. Due to the overprediction of flood extent by the high-resolution DEMs (ALOS PALSAR and NED). However, ALOS AW3D and SRTM were slightly agreed with $F^{<4>}$ score, penalizing overprediction, due to underprediction of flood inundation extent by these DEMs. It can be observed in the flood inundation extent maps shown in Figure 6.7, the NED and ALOS PALSAR DEMs were over predicted, while ALOS AW3D and SRTM were under predicted. The smoothness of these DEMs (DTM) could have caused the wide spreading of flood volume over an area, which also predicts low flood depths and peaks (Fig.6.2a). The Hit Rate for NED and ALOS PALSAR was higher than other DEMs, while the False Alarm Rate also much higher than other models. However, the ALOS AW3D and SRTM showed less Bias than NED and ALOS PALSAR, which balances the model over and under prediction capability. The success in predicting flood extent should not be misguided for locally accurate predictions of average water depths, peaks at junctions, and hydrograph shapes. The ALOS AW3D captured these variables well even though it fails to capture flood extents. The results showed that the SWMM is highly sensitive to DEM resolution and its type, whether DTM or DSM.

6.4.5 Overall Assessment

In the SWMM model simulation, 1s ALOS AW3D yielded flood peaks just 2%-19%, depths 0-0.34m, and 1s SRTM yielded flood peaks just 0-28%, depths 0.02-0.39m larger than field surveyed data. Whether or not this is a tolerable degree of uncertainty will indeed depend on the application. Another critical question is whether NED 30m (1s) is better for urban flood modeling than NED 10m (1/3 s), which gives more insight into the influence of grid resolution on SWMM urban flood modeling outputs. It was observed that 1s NED DEM (30m) yielded 0% in average inundation depths, 16% larger in maximum depths, 6% larger in peaks, and 16% larger in flood inundation zone than 1/3 s (10m) NED DEM. It shows that the impact of grid resolution on the SWMM model is significantly less, almost negligible. It contrasts with earlier studies done in riverine flood plain using hydrodynamic models, where the accuracy deteriorated with the decrease in DEM grid resolution, and inundation area also increased with grid resolution [Saksena & Merwade, 2015].

Abstract-TH-2793_156104035

Here, hydrological corrections for DEMs have not been performed before setup the urban hydrological SWMM model. The main target of the study to identify the influence of medium resolution DEMs on SWMM modeling for urban flood prediction, where building footprints, roads, and drains to be preserved and other artifacts such as trees should be removed. The corrections suggested in earlier studies may improve the model output results [Jarihani et al., 2015].

It can be stated that the open-source DEMs showed its capability towards urban flood modeling, even though they performed poorly at predicting flood extents. The results showed 1D SWMM model was insensitive to DEM resolution and its type except in flood inundation extent prediction and mapping. It was also observed that ASTER DEM has performed very poorly in flood depths, peaks, hydrographs, and flood inundation extent prediction and mapping at all areas. So, we suggest that ASTER DEM is not suitable for 1D/2D urban flood modeling. The most recent studies were identified that the TanDEM-X has the potential capability to map urban features [Rossi & Gernhardt, 2013]. We hope it may be beneficial for urban flood modeling in the future, but now it is not available for general users.

6.5 CONCLUSIONS

This chapter attempted to understand the impact of various open-source topographic models on the 1D SWMM urban hydrological model for urban flood modeling and mapping. It is also studied to identify the appropriate online available DEM to set up the 1D/2D urban hydrological flood model. Five urban watersheds, which comprises small to large areas, low to high development, and low raised to high raised buildings, were considered to assess the influence of DEM product and its resolution on 1D SWMM urban hydrological modeling. For this purpose, the best source of field surveyed datasets and the globally available open-source products such as ALOS AW3D (30m), ALOS PALSAR (12.5m), ASTER (30m), SRTM (30m), and nationally available products NED (10m), NED (30m), CARTOSAT vR3.1 (30m) were selected to conduct the series of simulations using SWMM model. The sensitivity of the SWMM model over selected DEM was studied, while simultaneously, the performance of globally open-source DEMs was evaluated for urban flood modeling.

The DEMs were utilized as topographic inputs into the 1D SWMM hydrological model, where the flood inundation depths, peaks, inflow hydrographs at the outlet,

Abstract-TH-2793_156104035

and flood inundation extents were analyzed. Topographic datasets were used for urban watershed identification and urban drain rim elevations as inputs into the SWMM model. It was observed that the SWMM model is insensitive to DEM product type and its resolution for flood depths, peaks, and hydrograph prediction, which showed a high sensitivity for flood inundation extent prediction and mapping. It was also observed that the global DEMs and national DEMs both failed to quantify the flood inundation area outputs in 1D SWMM simulation, which showed significant errors with poor skill score of CSI (<0.4) and other binary metrics (skill scores). The high-resolution DEMs (ALOS PALSAR and NED) showed overestimating flood inundation extent prediction and underestimating flood depths and peaks. These models represented a flat type of watershed with gentle slopes, which could have caused overprediction in flood extent and underprediction in flood depths and created low flow velocity zones. These models represent DTM rather than DSM, and these DEMs may work fine in riverine flood plains but not in urban settings. Overall, it was observed that the influence of DEM type and resolution was negligible over SWMM model outputs prediction. The ALOS AW3D performed better, and ASTER performed poorly in urban watersheds.

Abstract-TH-2793_156104035

7

DISTRIBUTED URBAN HYDROLOGICAL MODEL

(Development of **P**hysically based **U**rban **R**unoff **A**ccounting **H**ydrological **M**odel)

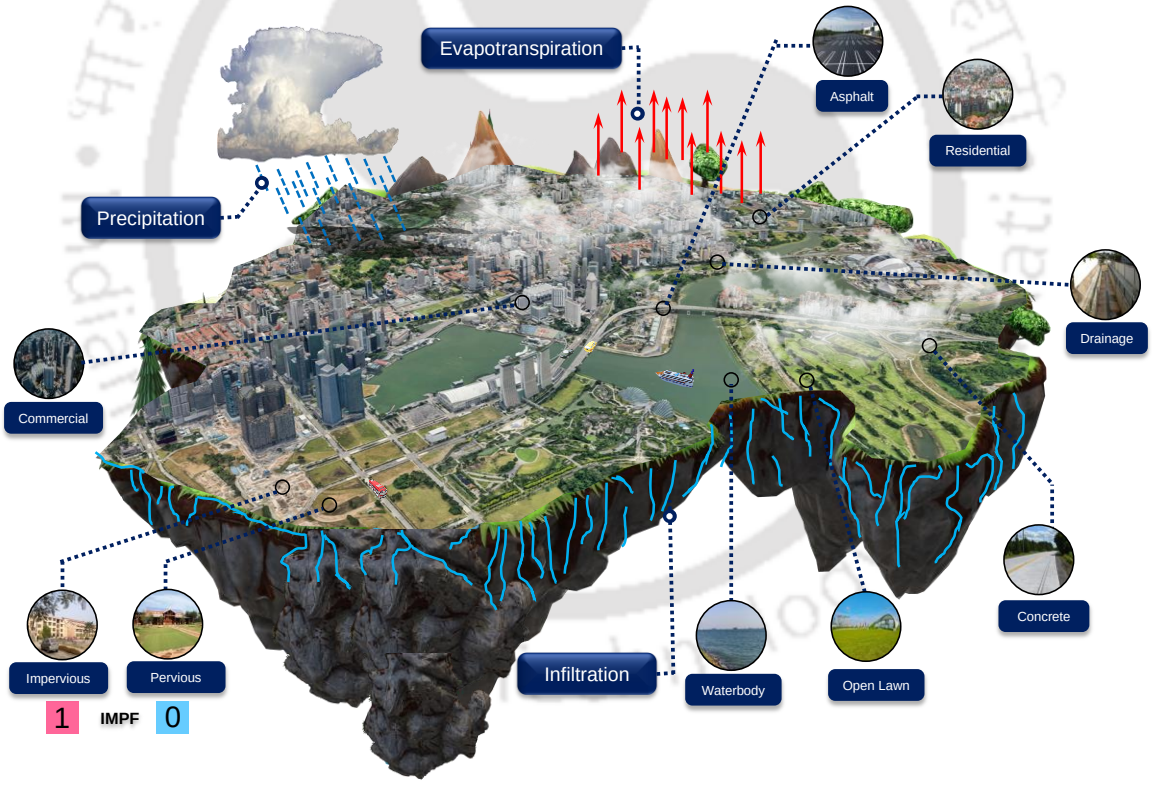

Abstract-TH-2793_156104035

7.1 INTRODUCTION

Surface water flooding is more responsible for flashing flood situations in urban areas during a high-intensity rainfall event. Surface water flooding occurred when the existed drainage system cannot drain the excess water generated from the surface when precipitation overwhelms the drainage capacity [Yu et al., 2016]. It is problematic for developing countries, where the drainage system is not appropriately designed or not existed at all, and in some places, the network systems are designed way back in 20-50 *years*. It disrupts human day-to-day life and traffic in urban areas, indirectly impacting loss of productivity and business opportunities. Urban hydrologists often face a tremendously challenging task to model these urban flash floods at street level to city-scale level due to the lack of availability of models that incorporate high spatial and temporal datasets such as weather radar precipitation and topography imperviousness. To design effective mitigation and adaptation strategies towards nuisance floods to low-frequency unexpected flash floods in urban regions, the distributed urban hydrological model with an early warning system, which uses an in-advance estimation of precipitation with weather radar rainfall needed.

In recent decades, the upsurge in the numerical modeling of surface water flooding in urban regions is observed due to the advent of computation methods for simulating surface and drain flows [Hsu et al., 2000; Ogden et al., 2000; Lee & Heaney, 2003; Zhang & Smith, 2003; Dong & Lu, 2009; Bates et al., 2010; Yu & Coulthard, 2015; Yu et al., 2016]. Urban hydrologists all over the world developed and adopted various modeling approaches which combine both surface and drain networks, including 1D surface flow routing with 1D storm drainage coupling (1D/1D) [Mark et al., 2004; Maksimović et al., 2009], 2D surface flow incorporated with 1D drainage routing (1D/2D) [Hsu et al., 2000; Schmitt et al., 2004], and only 2D surface flow (2D) [Fewtrell et al., 2011; Sampson et al., 2013; Bates et al., 2010; Yu & Coulthard, 2015; Yu et al., 2016]. In only the 2D surface routing model, storm sewer drainage is either neglected or simplified the interaction between surface runoff to drainage [Yu et al., 2016]. The 1D drainage with the 1D surface (1D/1D) and 1D drainage with 2D surface (1D/2D) coupling models often referred to as ‘dual drainage modeling’ [Djordjević et al., 1991; Schmitt et al., 2004; Smith, 2006]. In the ‘1D/1D’ model, the surface flow computation is oversimplified with lumped value and considers flood confined within the streets, creating difficulties when flood spreads laterally over an area. In contrast, the ‘1D/2D’

Abstract-TH-2793_156104035

coupled model considers two-dimensional surface flow, representing the surface flow in real condition by spreading over an area. In recent years, '1D drainage and 2D surface' coupled approach has been highly implemented either in loosely coupled (solves separately) or tightly coupled approach (solves simultaneously) at the street and city-scale level [Hsu et al., 2000; Schmitt et al., 2004; Leandro et al., 2009; Seyoum et al., 2012]. In both loosely and tightly coupled approaches, the surface runoff-induced flood is not considered but injected into the 1D drainage model as an input [Yu et al., 2016].

It is also quite challenging to apply this concept in developing countries due to the unavailability of the drainage network, unavailability of topographic datasets with the representation of urban features, etc. Moreover, these modeling approaches consider flood accumulation only at drains and collect total runoff at a single inlet rather than considering flood over the entire surface. However, in most of the flash flood situations in urban areas, the direct runoff produced due to the high intensity of precipitation is more significant than the drain surcharge. The direct surface runoff generated due to the high intensity of rainfall cannot enter into the drains; rather, it overpasses the drain entries and creates the ponding over surface depressions [Aronica & Lanza, 2005]. Sampson et al. [2013] and Bates et al. [2010] are modeled using a modified LISFLOOD-FP surface inundation model for urban flood simulation, but hydrological processes are not considered in their simulations. Yu & Coulthard [2015] and Yu et al. [2016] are incorporated hydrological processes into the model, but they are not considered extensive surface parameters (Impervious factor and Surface roughness) and infiltration processes. The other existing 2D model, such as MIKE 21, MIKE SHE, and MIKE Flood, works at local scales ($< 1km^2$), which are not applicable at city scale flood simulation, which is necessary during flash flood events occurs due to the high intensity of rainfall.

In this study, the distributed urban hydrological model (PURAHM) is developed by taking surface flow routing structure from Bates et al. [2010] and incorporating the hydrological processes with extensive surface roughness, soil infiltration, and soil infiltration and impervious factor parameters. This chapter begins with the description of model development with its compartments and used parameters in section 2. Then section 3 describes the case study, input datasets, and

Abstract-TH-2793_156104035

parameters. Section 4 includes the results, sensitivity analysis of the model, and its evaluation. Finally, section 5 summarizes the main conclusions and future scope.

7.2 MODEL DESCRIPTION

The Physically based Urban Runoff Accounting Hydrological Model (PURAHM) is developed by following the identical surface flow routing structure as the inertial model of Bates et al. [2010]. The developed model is a distributed local inertial-based flood inundation model designed for heterogeneous urban landscapes. It integrated with hydrological processes such as evapotranspiration and infiltration along with surface flow routing processes. Figure 7.1 depicts the processes that the PURAHM model adopted and the interlinkages between the compartments.

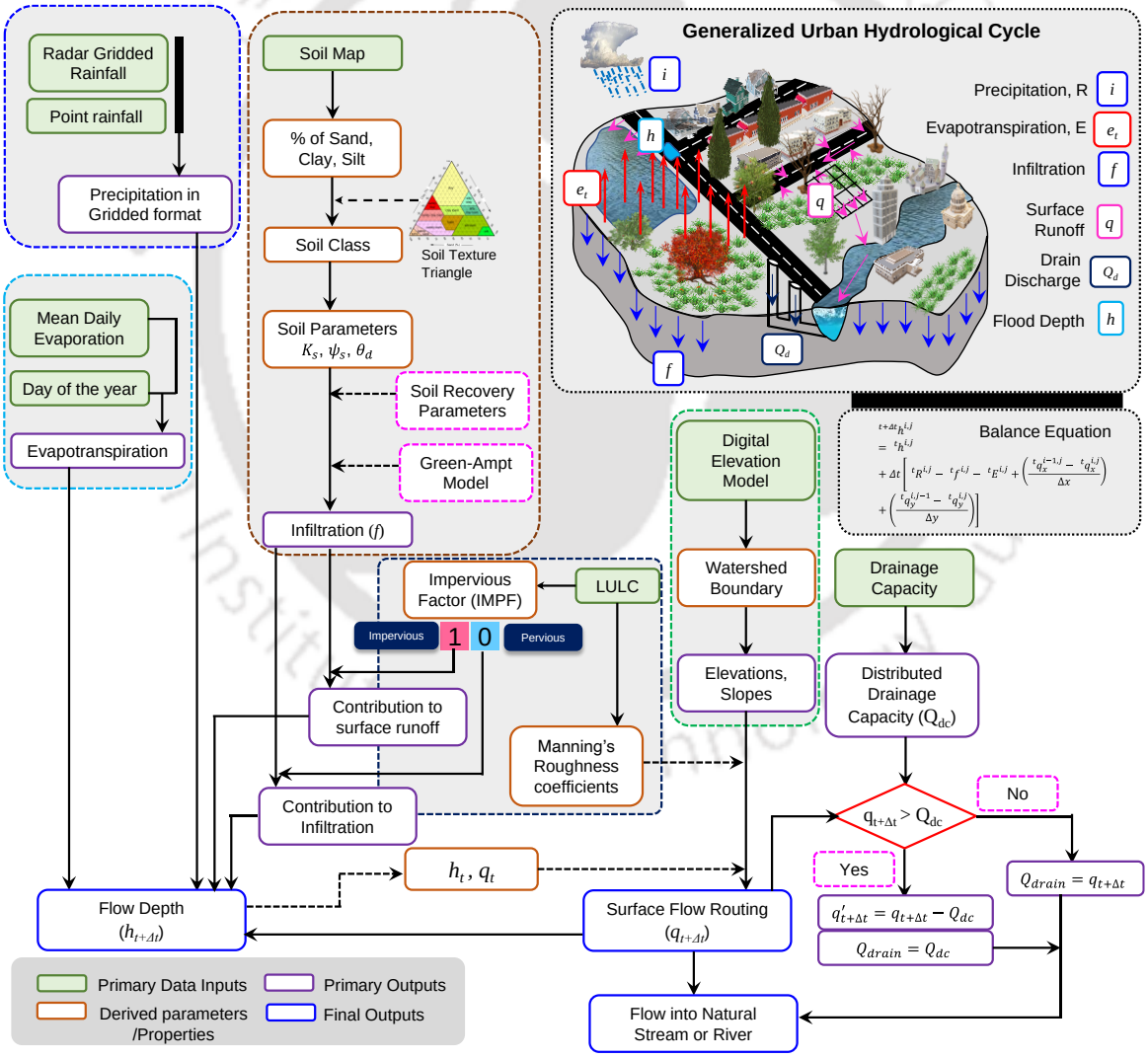

Figure 7.1. Generalized urban hydrological cycle and framework of the PURAHM model.

Abstract-TH-2793_156104035

The structure of the model, which includes hydrological processes precipitation, evapotranspiration, infiltration, surface flow routing, and characteristics of land surface soil properties, impervious, drainage are presented in subsequent sections.

7.2.1 Precipitation Model

Precipitation is the main driving force in the rainfall–runoff hydrological model simulation. Precipitation generates from the atmospheric compartment and deposits onto the land surface compartment. The surface runoff generated over a landscape is directly dependent on the time series of precipitation data (hyetograph). This hyetograph can be a single storm event or continuous-time period events such as multi-year series. In the model, the weather radar or multiple rain gauge objects are used to give the data in a gridded (distributed) format to represent the heterogeneity in the precipitation patterns over any landscape. Such representation is necessary for heterogeneous complex urban landscapes, where precipitation varies spatially and temporally at local scales. The model is designed to aid forecasting of a nuisance to the flash floods and storm water drainage design purposes. In this context, the model is designed to take single events such as return period events and continuous precipitation records of both weather radar data and rain gauge measured data.

7.2.2 Evapotranspiration Model

In this model, evapotranspiration is represented in two ways. It is approximated with a simple seasonal sine curve for daily potential evapotranspiration [Calder et al., 1983; Yu & Coulthard, 2015; Yu et al., 2016]. The user can also define evapotranspiration in time-series format. However, over urban landscapes during high-intensity events, the evapotranspiration is negligible compared to the precipitation amount. The simple seasonal sine curve is sufficient for such types of events. The simple sine curve equation adopted from Calder et al. [1983] is provided below.

$$E_p = \overline{E_p}\left[1 + \sin\left(\frac{360i}{365} - 90\right)\right] \qquad \text{(Eq.7.1)}$$

Where, $\overline{E_p}$ is the mean daily potential evapotranspiration and i is the day of the year.

Abstract-TH-2793_156104035

The amount of evapotranspiration over urban landscapes during the high-intensity precipitation conditions is in the order of 3-5*mm/day*, which is a small amount compared to other hydrological processes [Yu & Coulthard, 2015].

7.2.3 Infiltration Model

Infiltration is the process by which rainfall penetrates the ground surface and fills the pores of the underlying soil [Akan & Houghtalen, 2003]. In this model, infiltration over saturation and unsaturation are represented using the widely known Green-Ampt infiltration equation. The conceptualization of the infiltration process using Green-Ampt and its computational scheme for both saturated and unsaturated conditions were adopted from Environmental Protection Agency Storm Water Management Model (EPA SWMM, USA) model [Rossman & Huber, 2016] and Chow et al. [2010]. The Green-Ampt equation adopted in this model takes the following form:

$$f_p = K_s \left[1 + \frac{\psi_s \theta_d}{F}\right] \quad \text{(Eq.7.2)}$$

$$F_s = \frac{K_s \psi_s \theta_d}{i - K_s} \quad \text{(Eq.7.3)}$$

$$F = K_s + \psi_s \theta_d \, ln\left(1 + \frac{F}{\psi_s \theta_d}\right) \quad \text{(Eq.7.4)}$$

$$F_{t+\Delta t} = K_s \Delta t + F_t + \psi_s \theta_d \, ln(F_{t+\Delta t} + \psi_s \theta_d) - \psi_s \theta_d \, ln(F_t + \psi_s \theta_d) \quad \text{(Eq.7.5)}$$

Where K_s is the hydraulic conductivity of the soil (*cm/hr.*); ψ_s is the suction head at the wetting front (*cm*); θ_d is the soil moisture deficit at the start of the current rainfall event (initial); F is the cumulative infiltration depth (*cm*); f_p is the potential infiltration rate (*cm/hr*); F_t is the cumulative infiltration depth at current time step t; $F_{t+\Delta t}$ is the cumulative infiltration depth at next time step $t+\Delta t$.

The runoff generation in urban landscapes is sensitive to the infiltration process along with impervious areas. In most hydrological studies hydraulic conductivity often used as a calibration parameter [Yu & Coulthard, 2015].

Abstract-TH-2793_156104035

In the model, the Green – Ampt soil condition parameters such as hydraulic conductivity, suction head, initial soil moisture deficit are derived using soil texture triangle [Rawls et al., 1983] for user-defined soil types in the study area. The model also incorporates the experimental Green – Ampt soil parameters by defining in the model as inputs. The soil recovery parameter such as the thickness of the recovery layer (*cm*), recovery time (*hr.*), and recovery constant (hr^{-1}) can be computed in the model.

7.2.4 Surface Flow Routing

The derived continuity and quasi-linearized one-dimension Saint – Venant or Shallow water equations are adopted from Bates et al. [2010]. The equations derived to compute the surface flow at each grid are provided below:

The momentum equation:

$$\frac{\partial Q}{\partial t} + \frac{\partial}{\partial x}\left[\frac{Q^2}{A}\right] + gA\frac{\partial (h+z)}{\partial x} + \frac{gn^2Q^2}{R^{4/3}A} = 0 \qquad \text{(Eq.7.6)}$$

Where Q is the discharge [$L^3\ T^{-1}$]; A is the flow cross section area [L^2]; h is the flow depth [L]; z is the surface elevation [L]; R is the hydraulic radius [L]; g is the acceleration due to gravity [$L\ T^{-2}$]; and *n* is the Manning's roughness coefficient.

Here, the flow advection (convective acceleration) term is neglected due to its unimportance in many flood plain flows [Hunter et al., 2007]. After neglecting flow advection in Saint – Venant equation and assuming a rectangular cross section and divide through by a constant flow width, *w* [L], the momentum equation is in terms of flow per unit width q as given below.

$$\frac{\partial q}{\partial t} + \frac{gh\partial (h+z)}{\partial x} + \frac{gn^2q^2}{R^{4/3}h} = 0 \qquad \text{(Eq.7.7)}$$

Along the y-axis direction, a similar formulation can be produced to compute flow per unit width. Discretizing the above equation with respect to the time step Δt, and approximating the hydraulic radius R, with the flow depth, *h*, produces:

$$\frac{q_{t+\Delta t} - q_t}{\Delta t} + \frac{gh_t\partial (h_t+z)}{\partial x} + \frac{gn^2q^2}{h^{7/3}} = 0 \qquad \text{(Eq.7.8)}$$

After rearranging above equation to give an explicit form for flow per unit width *q* at time t+ Δt:

Abstract-TH-2793_156104035

$$q_{t+\Delta t} = q_t - gh_t\Delta t\left[\frac{\partial(h_t+z)}{\partial x} + \frac{n^2 q_t^2}{h_t^{10/3}}\right] = 0 \quad \text{(Eq.7.9)}$$

The above equation is modified further to reduce the instability arise at shallow depths due to large friction terms. The equation is modified by replacing q_t with $q_{t+\Delta t}$ in the friction term in equation 7.9. The improved implicit form of the equation is given below:

$$q_{t+\Delta t} = q_t - gh_t\Delta t\left[\frac{\partial(h_t+z)}{\partial x} + \frac{n^2 q_t q_{t+\Delta t}}{h_t^{10/3}}\right] = 0 \quad \text{(Eq.7.10)}$$

After rearranging above equation 7.10 in explicit form to calculate the flows at the next time step can be as:

$$q_{t+\Delta t} = \frac{q_t - gh_t\Delta t\left(\frac{\partial(h_t+z)}{\partial x}\right)}{\left(1+gh_t\Delta t n^2 \,{}^{q_t}/_{h^{10/3}}\right)} \quad \text{(Eq.7.11)}$$

In this model, the flow in the *x* and *y* directions is decoupled and taken the same form. The flow per unit width is computed at the cell, and flow depths are computed at the center of cells. The Courant-Freidrichs-Levy (CFL) condition is used to maintain the stability of the model.

$$C_r = \frac{V\Delta t}{\Delta x} \quad \text{(Eq.7.12)}$$

Where the non-dimensional Courant number should be less than 1 for stability and here V is a characteristic velocity [LT^{-1}].

The continuity equation is derived to compute the flow depths is given below:

$$\frac{{}^{t+\Delta t}h^{i,j} - {}^{t}h^{i,j}}{\Delta t} = \left[{}^{t}R^{i,j} - {}^{t}f^{i,j} - {}^{t}E^{i,j}\right] + \left(\frac{{}^{t}q_x^{i-1,j} - {}^{t}q_x^{i,j}}{\Delta x}\right) + \left(\frac{{}^{t}q_y^{i,j-1} - {}^{t}q_y^{i,j}}{\Delta y}\right) \quad \text{(Eq.7.13)}$$

$${}^{t+\Delta t}h^{i,j} = {}^{t}h^{i,j} + \Delta t\left[{}^{t}R^{i,j} - {}^{t}f^{i,j} - {}^{t}E^{i,j} + \left(\frac{{}^{t}q_x^{i-1,j} - {}^{t}q_x^{i,j}}{\Delta x}\right) + \left(\frac{{}^{t}q_y^{i,j-1} - {}^{t}q_y^{i,j}}{\Delta y}\right)\right] \quad \text{(Eq.7.14)}$$

Where *R* is the rainfall; *f* is the infiltration; and *E* is the evapotranspiration.

7.2.5 Impervious Area/ Impervious Factor (IMPF)

The model represents the impervious area as an impervious factor at each cell level instead of the effective impervious or total impervious area percentage. In the model, each cell connected with surrounding cells with pervious and impervious fractions. The impervious factor ranges from 0 to 1, dependent on the land use and land cover (LULC) classes. The broad categories of LULC classes and its assumed impervious factor is provided in Table 7.1. The model incorporates a large number of subclasses which can be observed in the urban landscapes. The subclasses and their impervious factors are provided in Appendix E1.

Table 7.1. The broad categories of perviousness of land use and land cover classes and its impervious factors incorporated in the model (detailed subclasses provided in Appendix E1)

LULC Class	Category	Impervious Factor
Asphalt	Impervious	1
Concrete	Impervious	1
Sparse Vegetation	Pervious	0
Moderate Vegetation	Pervious	0
Dense Vegetation	Pervious	0
Waterbody	Impervious	1
Wetland/Swamp	Pervious	0
Open Land	Pervious	0

7.2.6 Manning's Roughness Coefficient

In the model, Manning's roughness coefficients (n) are computed based on user defined land use and land cover classes. The user can also define the coefficients based on experimental or field observed values in the model. The Manning's roughness coefficients based on different classes are adopted from different works of literature [Table 7.2 and Appendix E]. Table 7.2 provides Manning's roughness coefficients incorporated in the model for broad LULC classes. In detail, coefficients taken in the model for each subclass are provided in Appendix E1.

Abstract-TH-2793_156104035

Table 7.2. The Manning's roughness values incorporated in PURAHM model for broad categories of land use and land cover classes (detailed subclasses provided in Appendix E1)

LULC Class	Manning's (n)	Range of n	Reference
Asphalt	0.011	-	MuCuen et al. [1996]
Concrete	0.013	-	MuCuen et al. [1996]
Sparse Vegetation	0.0585	0.032 – 0.071	Sarkar & Dutta [2008]
Moderate Vegetation	0.062	0.039 – 0.085	Sarkar & Dutta [2008]
Dense Vegetation	0.077	0.044 – 0.110	Sarkar & Dutta [2008]
Waterbody	0.035	-	Kalyanapu et al. [2009]; Shen et al. [2017]
Wetland/Swamp	0.27	-	Mtamba et al. [2015]
Open Land	0.001	-	-

7.2.7 Soil Properties

The user can define the soil classes directly or provide the %Sand, %Silt, and %Clay in the model. The model is incorporated to identify the soil class with sand, silt, and clay percentages using the soil texture triangle suggested by Rawls et al. [1983]. The user can also define the soil properties of the field and experimental values in the model.

7.2.8 Drainage Capacity

The drain system (Storm and Sewer) acts as a source of mass loss in urban landscapes for urban stormwater runoff. In the model, we assume that the existed storm conveyance system drains water away from the system at its maximum drainage design capacity. It is also assumed that there will be no loss of capacity due to surcharge. The maximum drainage design capacity usually corresponding to a particular return period rainfall event where the drains are designed at a particular location. The model allows users to define drainage capacity for cell by cell or uniform as a lump value over an area. The drainage capacity values can also be scaled to represent the drains' age, blockage, and malfunction effect. At each time step, the amount of mass loss to the drainage system is calculated by scaling the design capacity (LT^{-1}) for the time step and then compared with the computed flow per unit width q. The conditions for the computing drain loss to the drain system are provided below:

Abstract-TH-2793_156104035

$$q'_{t+\Delta t} = q_{t+\Delta t} - Q_{dc} \qquad if\ [q_{t+\Delta t} > Q_{dc}\ ] \qquad \text{(Eq.7.15)}$$

$$Q_{drain} = Q_{dc}$$

$$q'_{t+\Delta t} = 0 \qquad if\ [q_{t+\Delta t} < Q_{dc}\ ] \qquad \text{(Eq.7.16)}$$

$$Q_{drain} = q_{t+\Delta t}$$

However, the hydraulic processes in the drains and manholes were not represented explicitly in this model.

7.2.9 Boundary Conditions

The user can define the boundary conditions for the model. The Dirichlet boundary conditions for flow computation and Neumann boundary conditions for depth computation are used in the model. The conditions at outfall also user can select within the incorporated conditions in the model. The different types of outfalls are incorporated in model: free outfall, fixed outfall, time-series outfall, normal outfall and tidal outfall. The outfall categories adopted in the model are taken from SWMM model structure [Rossman & Huber, 2016].

7.3 MODEL APPLICATION: CASE STUDY AND DATASETS

7.3.1 Study Site

The model was tested in the Valley Stream watershed in New York, USA, one of the highly urbanized watersheds in New York and nearer to the coastal belt (Fig.7.2). The area of the selected watershed is $9km^2$. The minimum ground elevation of the watershed is around $1m$, and the maximum elevation is around $35m$ from mean sea level (Fig.7.2b). Watershed falls under the humid subtropical climate (Köppen climate type, *Cfa*) and it has an oceanic climate. The temperature varies around -10°C in winter and around 30°C in summer. The watershed receives rainfall annually around $1200mm$. Figure 7.2 describes the watershed boundary, its topography, and orthoimagery of the Valley Stream urban watershed.

Abstract-TH-2793_156104035

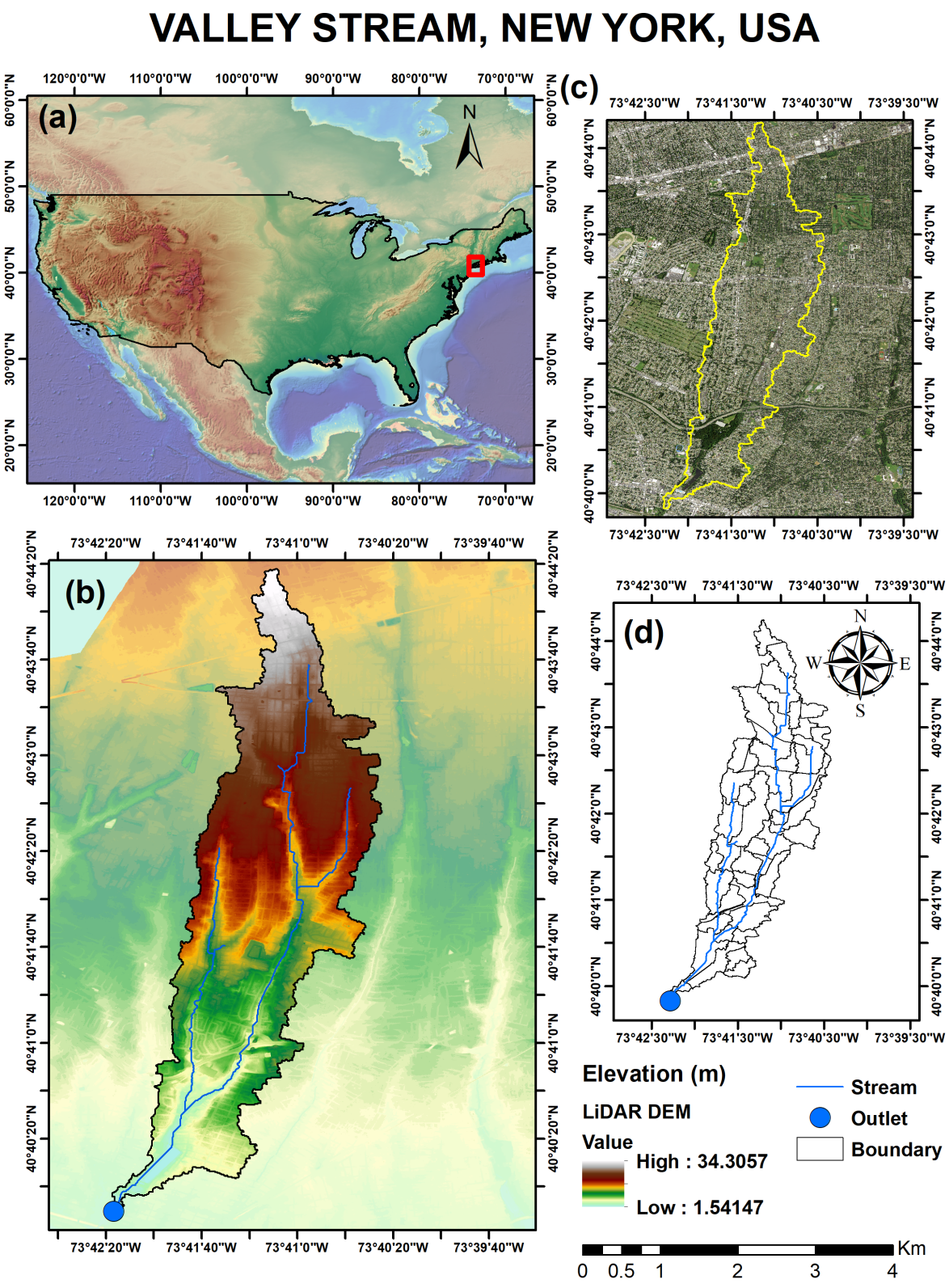

Figure 7.2. (a) Shaded relief images of the USA with identified study area; (b) Topography of the watershed (LiDAR $1m$); (c) Orthoimagery of the watershed ($0.6m$); and (d) watershed boundary with streams, sub watersheds and outlet (Discharge measuring site location).

Abstract-TH-2793_156104035

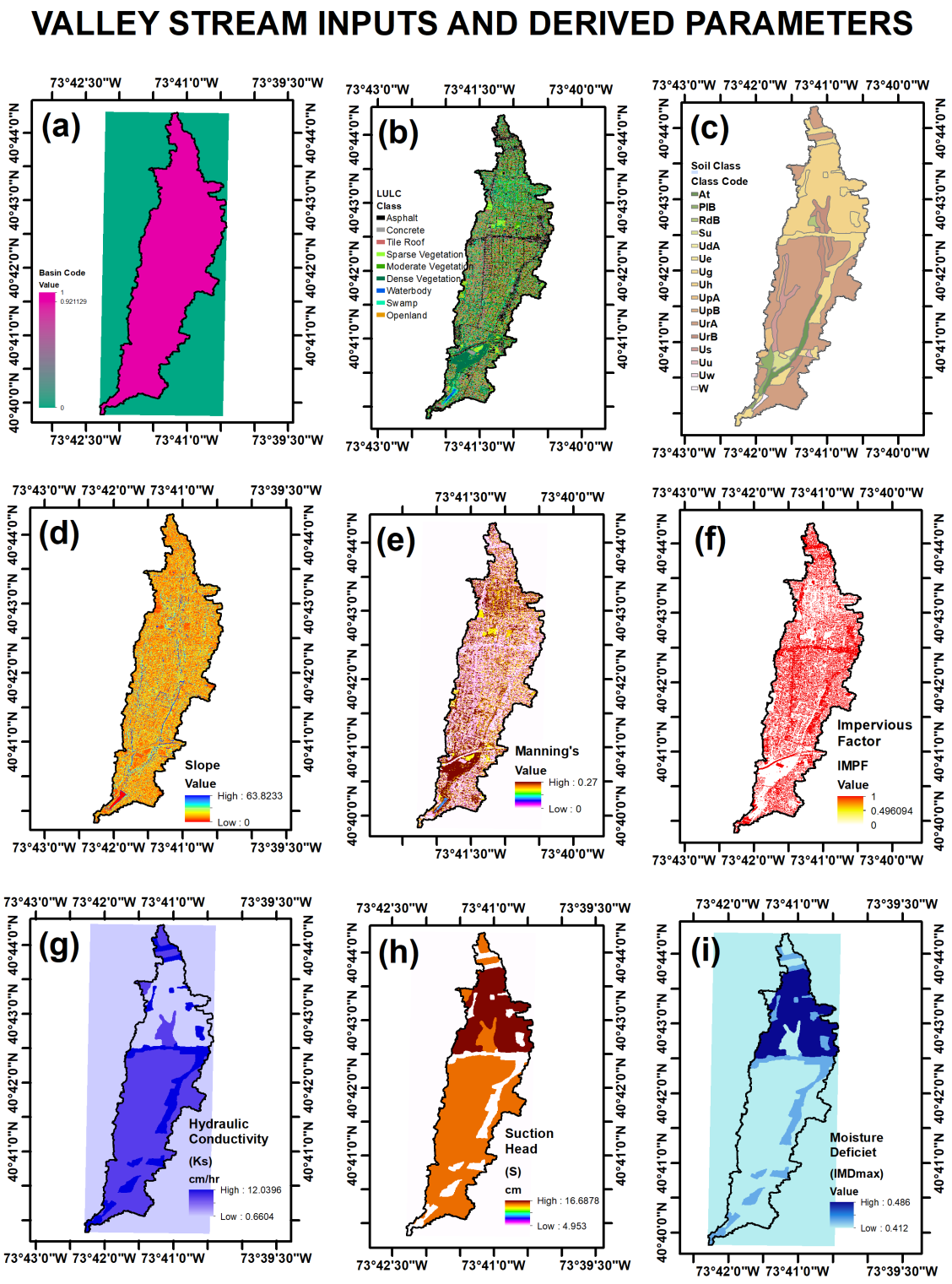

Figure 7.3. (a) Identification of cells falls inside boundary as 1 and outside boundary as 0; (b) LULC classes (0.6m); (c) Soil classes; (d) Slopes map (1m); (e) Manning's roughness, n (0.6m); (f) Impervious factor (0,1) (0.6m); (g) Hydraulic Conductivity (1m); (h) Suction Head (1m); and (i) Initial Soil Moisture deficit (1m).

Abstract-TH-2793_156104035

7.3.2 Datasets Description

The topography, precipitation, soil classes, orthoimagery datasets, and observed discharge at the outlet were collected from different sources. The other parameters such as Green-Ampt soil infiltration parameters, land use, and land cover classes, Manning's roughness coefficients, and impervious factors were derived from the collected input datasets. Figure 7.2–7.3 shows the detailed input datasets used in the model and parameters computed from the datasets to simulate the model. The details of datasets considered for the present study are elaborated below sections.

7.3.2.1 *Topography data*

The topographic data available at the New York city scale and selected watershed scale is a 1m LiDAR data (Fig.7.2b). The LiDAR Digital Elevation Model (DEM) data was acquired by U.S. Geological Survey during the period of 03 April, 2014 to 21 April, 2014. The LiDAR 1m DEM data can be accessed from USGS 3D Elevation Program (3DEP) National Map Viewer (https://apps.nationalmap.gov/viewer/) or NOAA data access viewer (https://coast.noaa.gov/dataviewer/#/lidar/search/). The LiDAR DEM data was processed to a 50m Digital Elevation Model to represent large scale urban watershed topography. The resolution of the DEM to the model was restricted to 50m due to the availability of discharge data at 15min time period interval and precipitation data at 1min time period interval to maintain the stability of the model. In the model, the time step is fixed to user defined step instead of the adaptive time step based on CFL stability criteria. So, the resolution of topography was restricted to 50m spatial resolution.

7.3.2.2 *Discharge data*

The flow data from the discharge and gauge measurement site located at the outfall of the watershed (40°39′49″ N, 73°42′16″ W) was collected to validate the model. U.S. Geological Survey maintains the gauge measurement site. The current station and other stations located in the USA can be accessed from the U.S. National Water Information System mapper (https://maps.waterdata.usgs.gov/mapper/index.html). The collected flow and gauge data are recorded at a time interval of 15min. The peak event that occurred from 12 August 2014 to 16 August 2014 over ten years period was selected to validate the model. Figure 7.4 shows the flow hydrograph and gauge height measured at gauge station for the period of 10-$years$ and the selected peak event.

Abstract-TH-2793_156104035

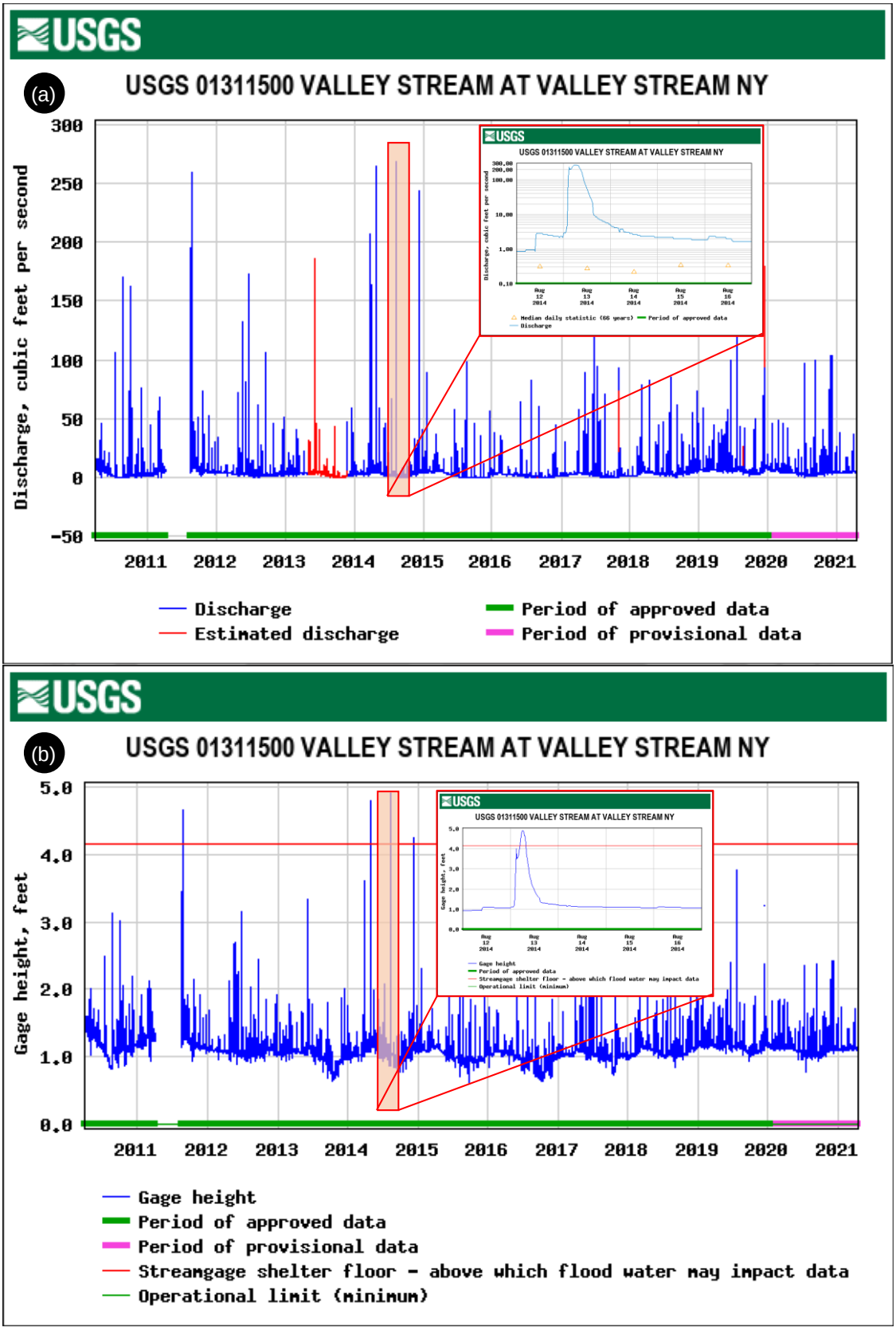

Figure 7.4. Flow hydrograph data observed at outlet by USGS, (a) Discharge of 10*year* records and selected peak event discharge during August 2014; and (b) Gauge height measured at outlet of last 10 *years* and selected peak event gauge height during August 2014.

Abstract-TH-2793_156104035

7.3.2.3 *Precipitation data*

The precipitation data as input to the model is typically derived based on an average of four rain gauge stations located outside the watershed. The rain gauge stations JFK Airport (40°34′48″N, 73°52′48″W), New York City (40°46′0.12″N, 73°58′59.88″W), LaGuardia (40°46′37.92″N, 73°52′23.16″W), and Farmingdale (40°43′43.61″N, 73°24′48.28″W) recorded rainfall data during the period of peak event were collected for the study. The rain gauges are operated and maintained by IOWA Environmental Mesonet, IOWA State University. The rain gauge measured rainfall data can be collected from IOWA Automated Surface Observing System (ASOS) archive datasets (https://mesonet.agron.iastate.edu/ASOS/). The collected rainfall data recorded at the interval of 1min. Figure 7.5 shows the peak rainfall event that occurred during the 13 August 2014 (EST time zone), which was used in this study to simulate and validate the model. The average of four stations' rainfall amount was incorporated uniform value over the watershed into the model.

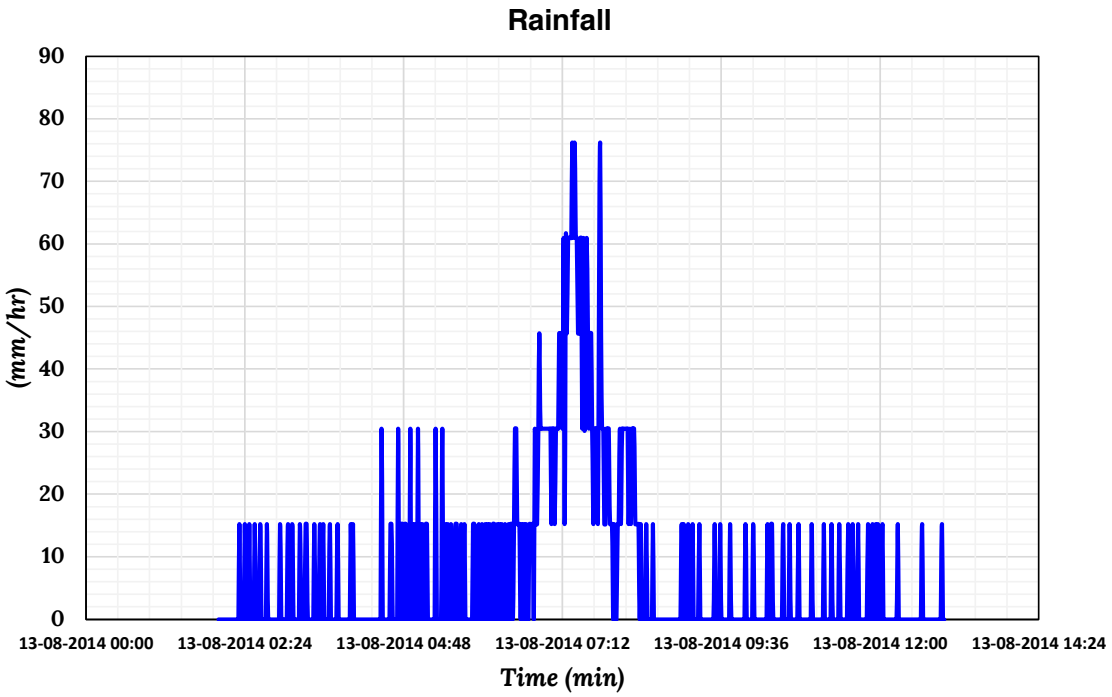

Figure 7.5. Rainfall hyetograph of average amount of four stations (JFK, NY city, Lagaurdia, and Farmingadale) during the period of 13 August, 2014 (EST time zone) used in the model.

Abstract-TH-2793_156104035

7.3.2.4 *Orthoimagery*

The high-resolution aerial survey (Ortho) images at 0.6*m* spatial resolution were collected to identify the land use and land cover classes in the Valley Stream watershed (Fig.7.2c). The orthoimageries were acquired by the U.S. Department of Agriculture (USDA) under the National Agriculture Imagery Program (NAIP) during 2019. The orthoimagery datasets for the Valley Stream urban watershed were collected from the USGS Earth Explorer (https://earthexplorer.usgs.gov/) under the Aerial imagery NAIP program.

7.3.2.5 *Soil data*

The soil data were obtained from the U.S. Department of Agriculture (USDA), Natural Resources Conservation Service (NRCS). The data was accessed from the USDA Natural Resources Conservation Service (NRCS) web soil survey map viewer (https://websoilsurvey.sc.egov.usda.gov/app/WebSoilSurvey.aspx).

Table 7.3. The Soil types its map units (Figure 7.3(c)), area and percentage of occupied area by soil class (detailed soil properties provided in Appendix E3-4)

MU Symbol	Map Unit (MU) Name	% slope	A (Acres)	Area (%)
At	Atsion loamy sand	-	57.6	2.7
PIB	Plymouth loamy sand	3 – 8	42.4	2.0
RdB	Riverhead sandy loam	3 – 8	9.9	0.5
Su	Sudbury sandy loam	-	25.2	1.2
UdA	Udipsamments	level	7.5	0.3
Ue	Udipsamments, wet substratum	-	3.8	0.2
Ug	Urban land	-	306.3	14.1
Uh	Urban land-Hempstead complex	-	523.7	24.1
UpA	Urban land-Plymouth complex	-	35.4	1.6
UpB	Urban land-Plymouth complex	0 – 3	16.9	0.8
UrA	Urban land-Riverhead complex	3 – 8	975.8	45.0
UrB	Urban land-Riverhead complex	0 – 3	95.0	4.4
Us	Urban land-Sudbury complex	3 – 8	58.9	2.7
Uu	Urban land-Udipsamments	-	4.1	0.2
Uw	Urban land-Udipsamments	-	0.0	0.0
W	Water	-	8.4	0.4

Abstract-TH-2793_156104035

Figure 7.3(c) shows the soil map and major soil types present in the Valley Stream urban watershed. The major types of soils observed in the watershed are provided in Table 7.3. The detailed map of soil types with orthoimage is given in Appendix E2.

7.3.2.6 *Drainage Capacity*

Uniform drainage capacity was used in the model for the Valley Stream watershed. The value was specified according to the design capacity of the storm drainage system of 30*mm/h* (http://ny-idf-projections.nrcc.cornell.edu/).

7.3.2.7 *Evapotranspiration*

The mean daily potential evapotranspiration was considered as 4*mm/day* from the U.S. Northeast Regional Climate Centre data archives provided by the Cornell University (http://www.nrcc.cornell.edu/wxstation/pet/pet.html).

7.3.3 Derived Parameters

The parameters such as Green-Ampt soil infiltration values: hydraulic conductivity, suction head, and initial soil moisture deficit were derived from the soil types acquired for this study. The land use and land cover classes, Manning's roughness coefficients and impervious factors were derived from the collected ortho imageries. The details of parameters (Fig.7.3) derived for the present study are elaborated below.

7.3.3.1 *Land Use and Land Cover classes*

The collected orthoimagery of the Valley Stream watershed was classified and obtained broad categories of LULC classes. The broad category of classes considered for the study to provide into the model is shown in Figure 7.3(b) and provided in Table 7.1. The percentage of classes occupied in the Valley Stream watershed are Asphalt (14.81%), Concrete (6.6%), Tile Roof (22.12%), Sparse Vegetation (7.22%), Moderate Vegetation (13.08%), Dense Vegetation (11.08%), Waterbody (0.27%), Swamp/Marshy (15.97%), and Open Land (8.85%). It was observed that in orthoimagery the buildings and roads were covered by the vegetation in many places, which might affect the approximation of impervious factor and Manning's n value in the study area, which might cause the error in flow and depth outputs simulated in the model.

Abstract-TH-2793_156104035

7.3.3.2 *Impervious Factor and Manning's n*

The Impervious Factors and Manning's roughness values were computed for each LULC classe at cell by cell level based on default pre-assigned values provided in Table 7.1 and Table 7.2. Figure 7.3(e) and Figure 7.4(f) shows the spatially distributed Manning's *n* values and Impervious Factors, respectively, over the Valley Stream watershed.

7.3.3.3 *Soil infiltration parameters*

The Green-Ampt infiltration parameters were computed in the model itself based on soil property at each cell in the watershed using a soil texture triangle. Figure 7.3(g-i) shows the hydraulic conductivity, suction head, and initial soil moisture deficit computed over a study area. The estimated soil class and computed soil parameters are provided in Table 7.4.

Table 7.4. Soil class based on map classes and assigned infiltration parameters by model.

MU Symbol	% Sand	% Silt	% Clay	Soil Class	Ks	S	IMD
At	60	30	10	Sandy Loam	1.09	10.99	0.41
PIB	60	30	10	Sandy Loam	1.09	10.99	0.41
RdB	60	30	10	Sandy Loam	1.09	10.99	0.41
Su	66.5	23.5	10	Sandy Loam	1.09	10.99	0.41
UdA	92.5	6.5	1	Sand	12.03	4.95	0.42
Ue	92.5	6.5	1	Sand	12.03	4.95	0.42
Ug	-	-	-	-	-	-	-
Uh	21.2	66.8	12	Silt Loam	0.66	16.69	0.49
UpA	60	30	10	Sandy Loam	1.09	10.99	0.41
UpB	60	30	10	Sandy Loam	1.09	10.99	0.41
UrA	60	30	10	Sandy Loam	1.09	10.99	0.41
UrB	60	30	10	Sandy Loam	1.09	10.99	0.41
Us	66.5	23.5	10	Sandy Loam	1.09	10.99	0.41
Uu	92.5	6.5	1	Sand	12.03	4.95	0.42
Uw	92.5	6.5	1	Sand	12.03	4.95	0.42
W	-	-	-	-	-	-	-

Abstract-TH-2793_156104035

7.3.4 Model Calibration, Sensitivity and Evaluation

7.3.4.1 *Sensitivity to roughness values*

The sensitivity analysis was undertaken to evaluate the sensitivity of the model response to variation of surface roughness. In the Valley Stream watershed, the Manning's roughness value varying from 0.001 to 0.27. A uniform Manning's roughness value (n) ranging from 0.001 to 0.25 at different intervals were given to the model for the sensitivity analysis.

7.3.4.2 *Sensitivity to hydraulic conductivity* (*Calibration*)

The calibration was done with hydraulic conductivity to evaluate the sensitivity of the model simulation to infiltration. The dominant type of soil type in the Valley Stream watershed is sandy loam of hydraulic conductivity (K_s) with 1.09*cm/h*. In the Valley Stream watershed, the hydraulic conductivity varied from 0.66 (Silt Loam) to 12.03 *cm/h* (Sand). A uniform hydraulic conductivity over a watershed ranging from minimum to maximum value at different intervals were undertaken to calibrate the model.

7.3.4.3 *Evaluation*

The model simulated flow at the outlet was evaluated with the gauge measured flow using error metrics Root Mean Squared Error (RMSE) and Nash-Sutcliffe Efficiency (NSE).

$$RMSE = \sqrt{\frac{\sum_{i=0}^{n}(Q_{s,i}-Q_{o,i})^2}{n}} \quad \text{(Eq.7.17)}$$

$$NSE = 1 - \frac{\sum_{i=1}^{n}(Q_{s,i}-Q_{o,i})^2}{\sum_{i=1}^{n}(Q_{o,i}-\overline{Q_o})^2} \quad \text{(Eq.7.18)}$$

Where, Q_s is the simulated/predicted output (depth/flow) and Q_o is the observed/referenced output (depth/flow) at outlet.

Abstract-TH-2793_156104035

7.4 RESULTS AND DISCUSSION

The model sensitivity to surface roughness and hydraulic conductivity of the soil was evaluated with error metric RMSE. The sensitivity of flood depths and discharge at the outlet to Manning's roughness were compared and evaluated at different n values by maintaining all other input datasets and parameters to field conditions. Also, the sensitivity of flow depths, discharge at the outlet, and cumulative infiltration depths to hydraulic conductivity were compared and evaluated at different Ks values. Model sensitivity to surface roughness values also evaluated at varying Manning's n values while keeping the hydraulic conductivity as a uniform value at $0.66 cm/h$. The model simulated outflow was compared and evaluated with the observed flow measured and gauge site using error metrics Coefficient of determination, RMSE, and NSE. A detailed description of sensitivity analysis and evaluation were provided in the below sections.

7.4.1 Sensitivity to Roughness Parameterisation

The model sensitivity to the surface roughness parameter was evaluated by varying Manning's roughness n value (0.001, 0.002, 0.003, 0.004, 0.005, 0.006, 0.007, 0.008, 0.009, 0.01, 0.02, 0.05, 0.1, 0.15, 0.2, and 0.25). Figure 7.6 shows the model response in terms of flood depths to the variation of n value. Figure 7.7 shows the model response to the variation of n value in terms of flow discharge at the outlet. Figure 7.8 shows the model response in terms of flood depths to the variation of n value while keeping uniform hydraulic conductivity at $0.66 cm/h$ over the watershed. Figure 7.7 shows the model response to the variation of n value in terms of flow discharge at the outlet while keeping uniform hydraulic conductivity at $0.66 cm/h$ over the watershed. The comparison of the percentage of difference in peaks and RMSE at each roughness value with reference to minimum roughness value 0.001 are provided in Table 7.5. Table 7.6 compares the % of peaks difference and error metric RMSE at each roughness with reference to n=0.001, while making hydraulic conductivity to its minimum value Ks = $0.66 cm/h$ uniformly over the considered watershed.

Abstract-TH-2793_156104035

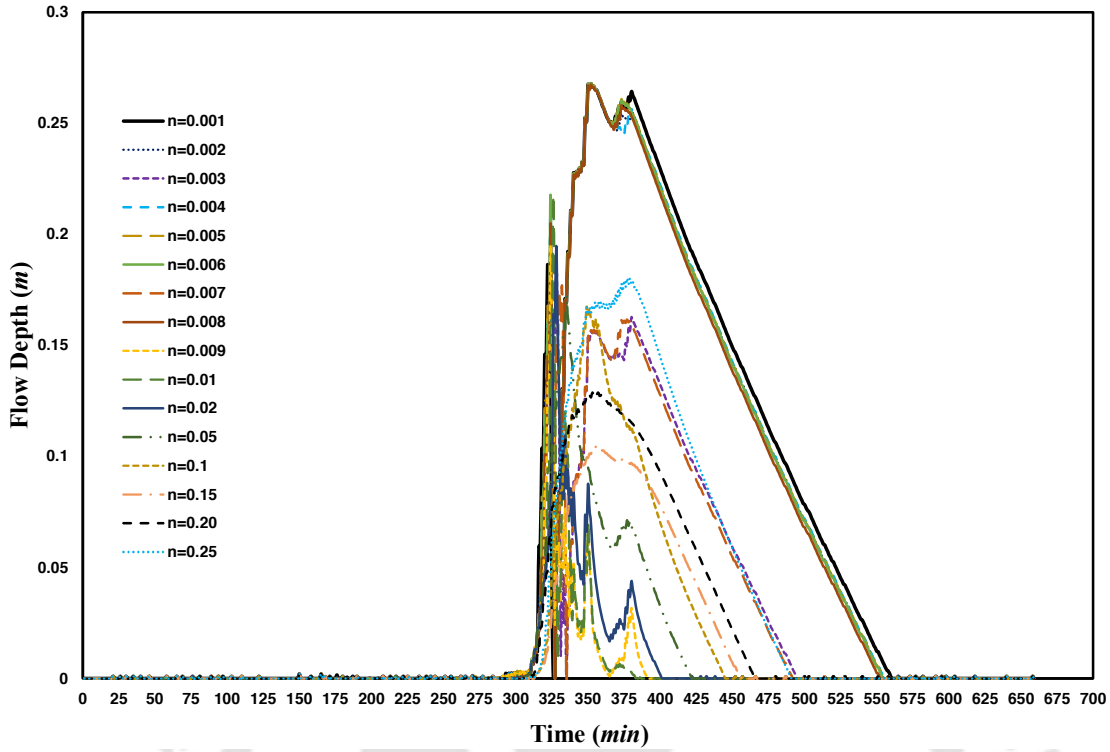

Figure 7.6. Sensitivity analysis of the model simulated flood depth to surface roughness Parameterisation.

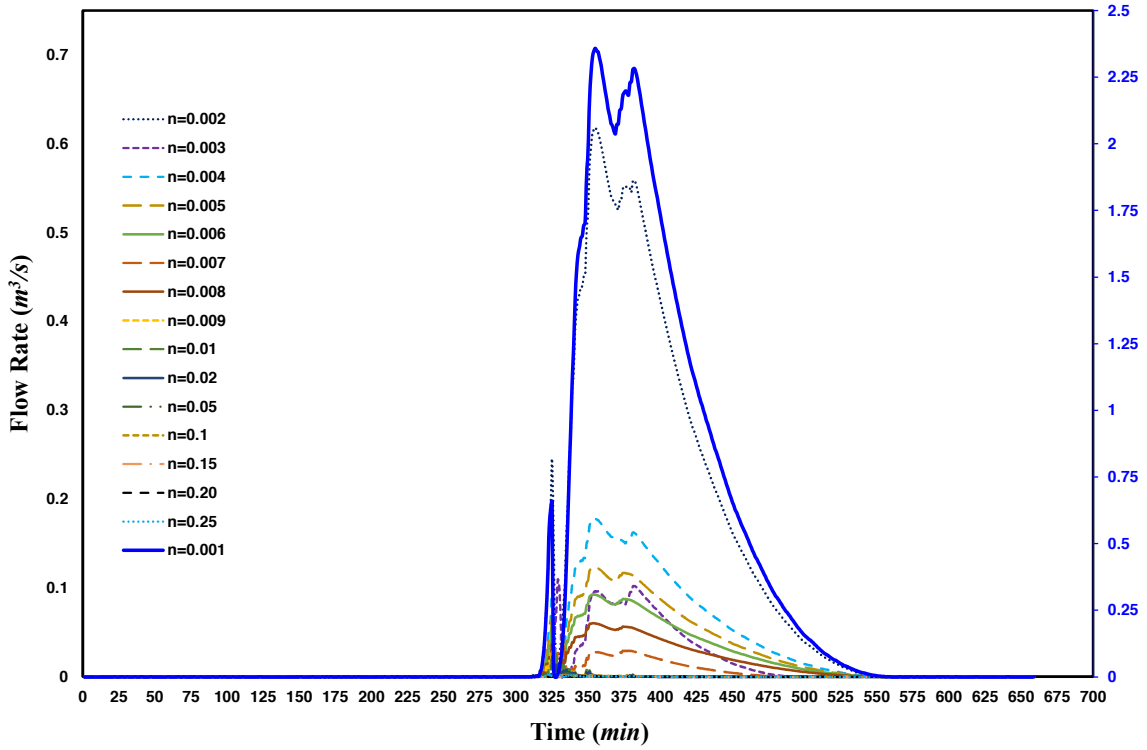

Figure 7.7. Sensitivity analysis of the model simulated runoff at outlet to surface roughness Parameterisation.

Abstract-TH-2793_156104035

Table 7.5. Percentage of difference between peaks and RMSE for varying surface roughness parameters in terms of flow depth (m) and flow rate (m^3/s) (reference to n = 0.001), while keeping all other parameters to field conditions.

Roughness n	Flow Depth (m)		Flow rate (m^3/s)	
	Diff. in peak (%)	RMSE	Diff. in peak (%)	RMSE
$n = 0.001$	-	-	-	-
$n = 0.002$	-0.02	0.0068	-73.79	0.5343
$n = 0.003$	-30.14	0.0546	-95.37	0.6888
$n = 0.004$	0.02	0.0070	-92.44	0.6620
$n = 0.005$	0.05	0.0071	-94.76	0.6778
$n = 0.006$	-0.01	0.0074	-96.06	0.6871
$n = 0.007$	-34.24	0.0548	-98.55	0.7077
$n = 0.008$	-0.19	0.0096	-97.43	0.6970
$n = 0.009$	-27.25	0.0966	-98.71	0.7153
$n = 0.01$	-18.94	0.0975	-98.65	0.7154
$n = 0.02$	-27.27	0.0929	-99.40	0.7154
$n = 0.05$	-35.55	0.0831	-99.81	0.7154
$n = 0.1$	-37.57	0.0701	-99.90	0.7154
$n = 0.15$	-61.02	0.0731	-99.91	0.7155
$n = 0.2$	-51.73	0.0653	-99.95	0.7155
$n = 0.25$	-32.75	0.0477	-99.82	0.7154

It was observed that the model is more sensitive to the surface roughness values, especially at lower roughness parameters (n = 0.001 – 0.008, open land) in terms of flow depth prediction. The model flow depth prediction at lower roughness values (n = 0.001 – 0.008) showed irregular %of peak difference from 0.02% to ~35% and RMSE values (Table 7.5 and Figure 7.6). The flow rate also increased from 73.79% to 95.37% in a difference of n value from 0.002 to 0.003 (Table 7.5). However, the flow depths and flow rates differ only marginally at higher roughness (n) values (n = 0.008 – 0.25, vegetation and urban cover) with RMSE for flow depth around 0.06 to 0.09m and for the flow rate is around 0.7155 m^3/s and difference depths peaks around 27% to 60% and difference in flow discharge peaks around 99%. The magnitude of RMSE was relatively small in flood depths (<0.09m) and flow measured at the outlet (<0.7m^3/s) with reference to the low surface roughness n=0.001 (open land). Suggesting that the model is relatively insensitive at higher surface roughness values (Vegetation to Urban cover) and the model is more sensitive to lower surface roughness parameters (Open Land).

Abstract-TH-2793_156104035

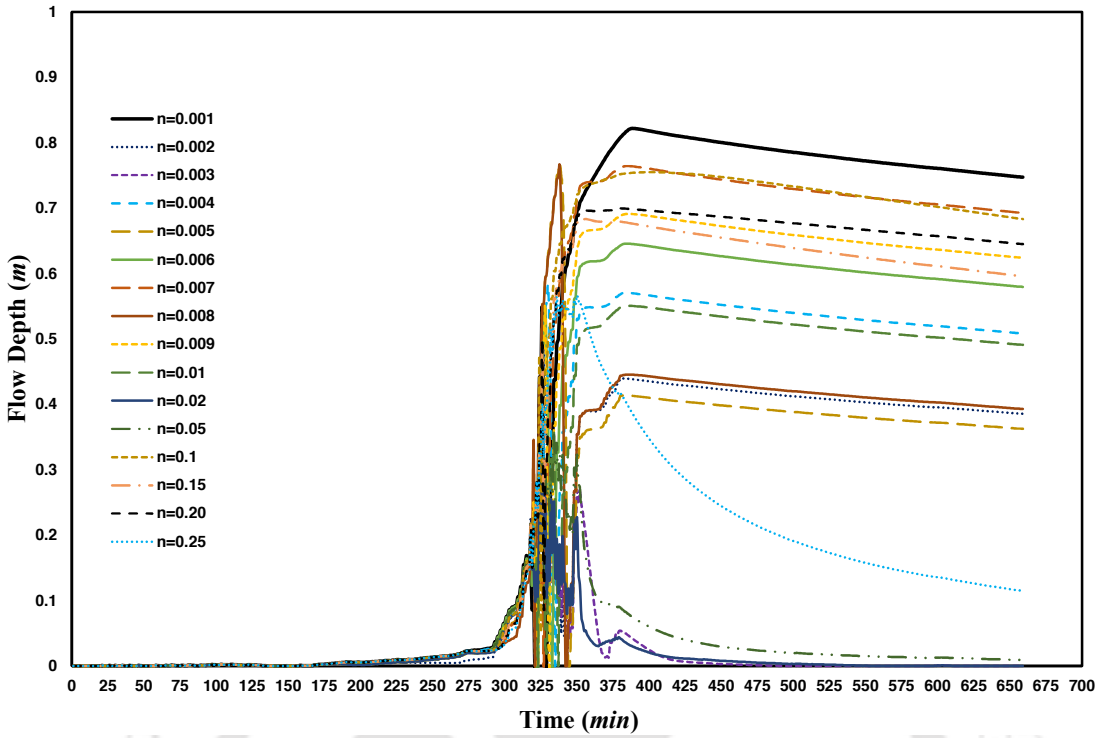

Figure 7.8. Sensitivity analysis of the model simulated flood depth to surface roughness Parameterisation, while keeping hydraulic conductivity (K_s) to 0.66 *cm/h*.

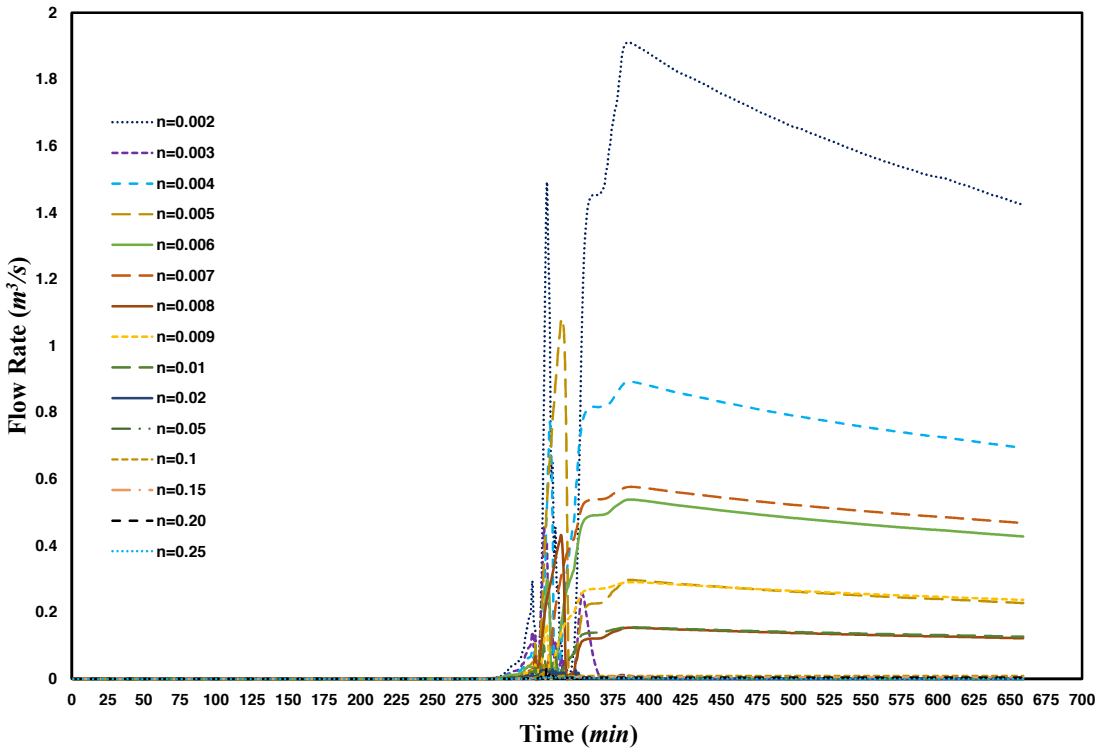

Figure 7.9. Sensitivity analysis of the model simulated runoff at outlet to surface roughness Parameterisation, while keeping hydraulic conductivity (K_s) to 0.66 *cm/h*.

Abstract-TH-2793_156104035

Table 7.6. Percentage of difference between peaks and RMSE for varying surface roughness parameters in terms of flow depth (m) and flow rate (m^3/s) (reference to n = 0.001), while keeping hydraulic conductivity $Ks = 0.66cm/h$ (*Note: Flow rate value at n = 0.001 is ~33* m^3/s).

Roughness n	Flow Depth (m)		Flow rate (m^3/s)	
	Diff. in peak (%)	RMSE	Diff. in peak (%)	RMSE
$n = 0.001$	-	-	-	-
$n = 0.002$	-32.71	0.2656	-94.08	18.600
$n = 0.003$	-46.27	0.5317	-98.59	19.706
$n = 0.004$	-29.29	0.1758	-97.23	19.169
$n = 0.005$	-6.40	0.2822	-96.65	19.531
$n = 0.006$	-21.45	0.1237	-98.33	19.379
$n = 0.007$	-7.01	0.0474	-98.21	19.351
$n = 0.008$	-6.92	0.2620	-98.66	19.617
$n = 0.009$	-15.92	0.0904	-99.10	19.529
$n = 0.01$	-33.02	0.1855	-99.52	19.615
$n = 0.02$	-61.54	0.5329	-99.90	19.711
$n = 0.05$	-57.09	0.5142	-99.96	19.710
$n = 0.1$	-8.15	0.0561	-99.87	19.705
$n = 0.15$	-16.84	0.1024	-99.95	19.707
$n = 0.2$	-14.88	0.0774	-99.90	19.708
$n = 0.25$	-31.08	0.3866	-99.98	19.710

In contrast, the model response is more sensitive to all roughness values for flow depths while taking uniform low hydraulic conductivity $Ks = 0.66cm/h$ (Silt Loam) over watershed by comparing with field observed soil hydraulic conductivity. Moreover, it was shown that RMSE relatively large (~0.5m) and irregularity in model prediction depths with varying roughness values at lower hydraulic conductivity (Table 7.6). However, the model predictions regarding of flow discharge at the outlet showed relatively insensitive to all roughness values for low hydraulic conductivity. The RMSE was observed same nearly 19m (the predicted value at reference roughness parameter n = 0.001 is ~33m^3/s) for varying roughness values, which is relatively large. Suggesting that the model is relatively insensitive to flow rate prediction at lower hydraulic conductivity (Silt Loam), but the model is more sensitive to flow depth prediction for lower Ks values at all varying roughness parameters.

Abstract-TH-2793_156104035

7.4.2 Sensitivity and Calibration to Hydraulic Conductivity

The soil hydraulic conductivity (K_s) was used as a calibration parameter and to check the sensitivity of the model due to uncertainty in the representation of rainfall, drainage, and storage capacity [Yu & Coulthard, 2015]. A set of *Ks* values, which are varying from 0.66 – 12*cm/h* (0.005, 0.01, 0.1, 0.5, 1, 2, 3, 4, 5, 6, 7, 8, 9, 10, 11, and 12 *cm/h*) in the Valley Stream watershed used to calibrate and to check the sensitivity of the model. Figure 7.10 shows the model response in terms of flood depths to the variation of *Ks* values. Figure 7.11 shows the model response to the variation of hydraulic conductivity values in terms of flow discharge at the outlet. Figure 7.12 shows the model response in terms of infiltration to the variation of *Ks* value. All other parameters were taken as model derived parameters with field observed and collected datasets. The comparison of flood depths, flow rates, and infiltration depths was done using computing error metric RMSE at each hydraulic conductivity value with reference to low hydraulic conductivity value 0.005*cm/h*. Table 7.7 compares the error metric RMSE at each hydraulic conductivity value with reference to Ks=0.005*cm/h*, while making all other parameters to model derived with observed datasets.

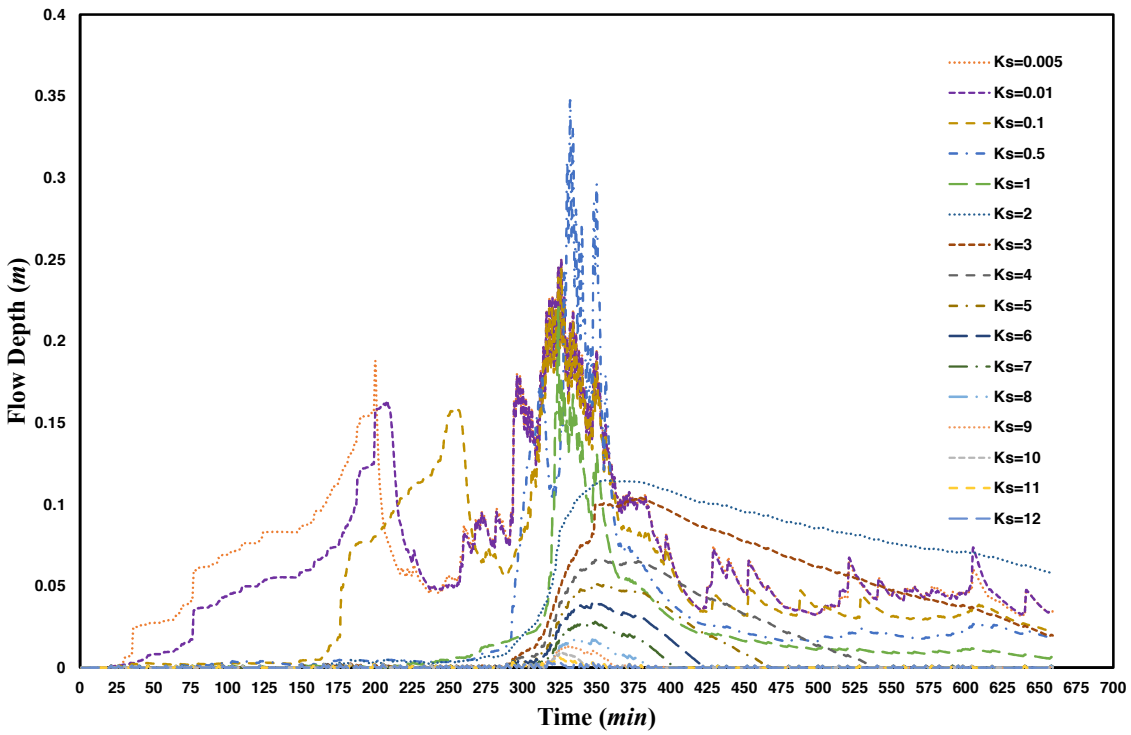

Figure 7.10. Sensitivity analysis of the model simulated flood depth to hydraulic conductivity.

Abstract-TH-2793_156104035

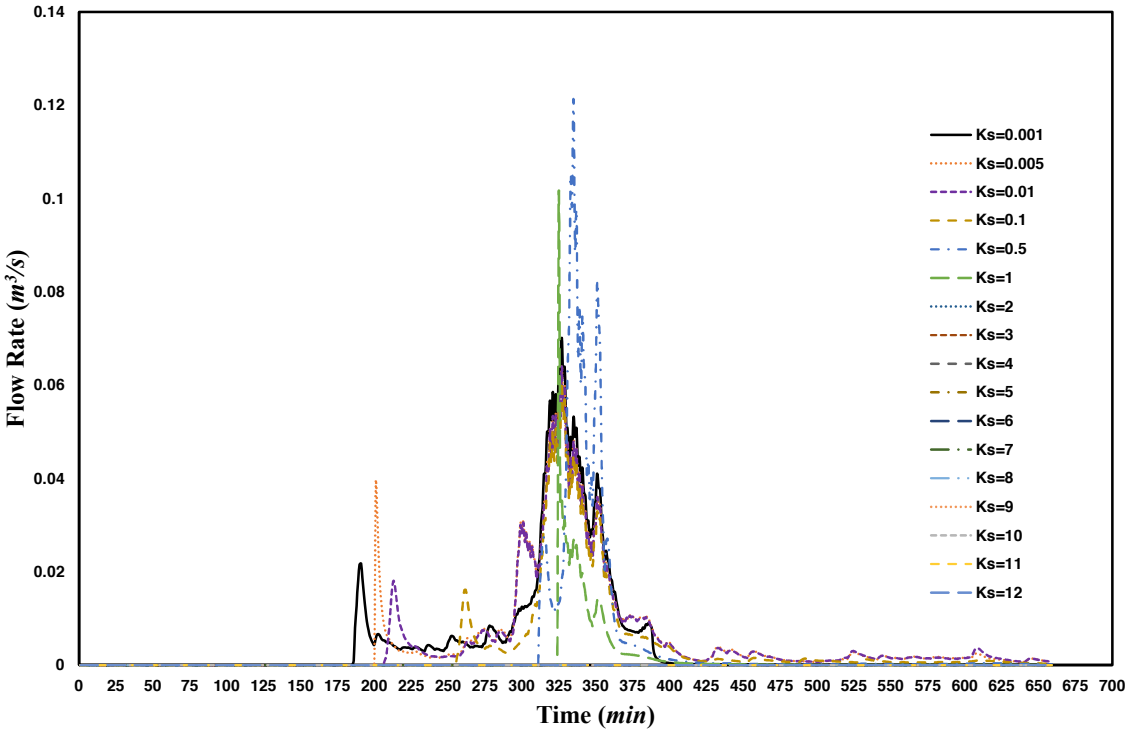

Figure 7.11. Sensitivity analysis of the model simulated runoff at outlet to hydraulic conductivity.

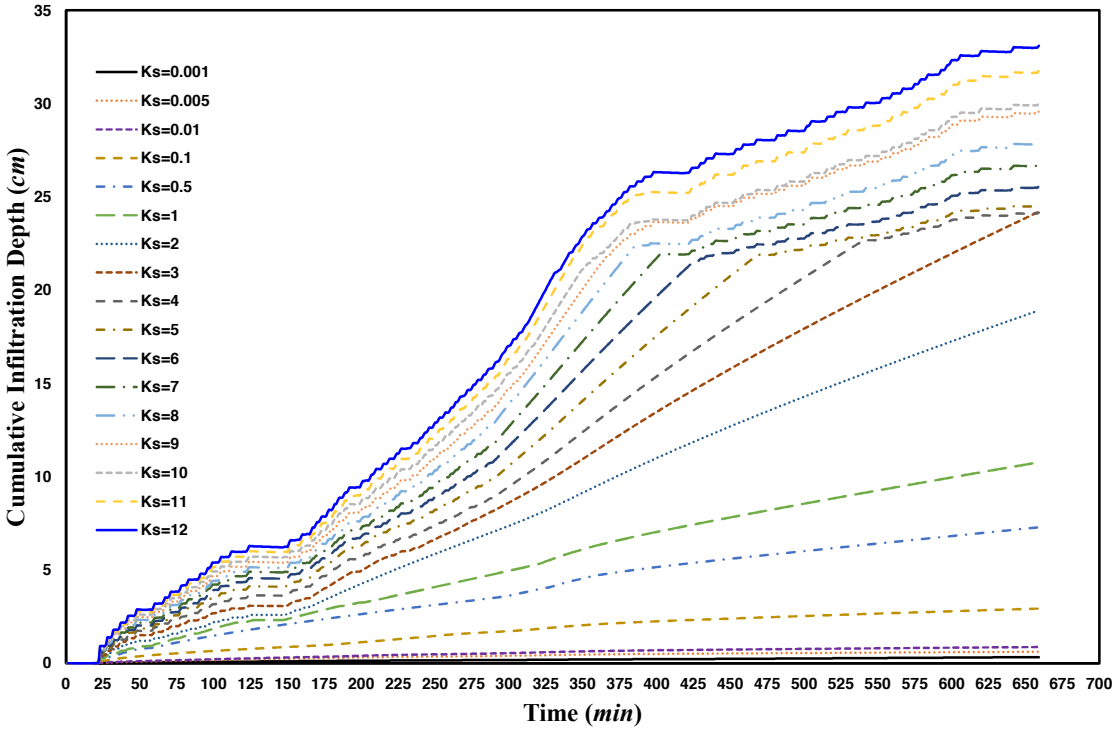

Figure 7.12. Sensitivity analysis of the model simulated infiltration depths to hydraulic conductivity.

Abstract-TH-2793_156104035

Table 7.7. Error metrics computed for model outputs at varying hydraulic conductivity values with reference to hydraulic conductivity $Ks = 0.005$, while keeping all parameters to field observed values.

Hydraulic Conductivity (K_s)	RMSE		
	Flow Depth (m)	Flow rate (m^3/s)	Infiltration Depth (cm)
$Ks = 0.005$	-	-	-
$Ks = 0.01$	0.114	0.0038	0.230
$Ks = 0.1$	0.116	0.0036	0.395
$Ks = 0.5$	0.127	0.0035	1.740
$Ks = 1$	0.138	0.0093	4.364
$Ks = 2$	0.146	0.0094	6.229
$Ks = 3$	0.114	0.0126	10.373
$Ks = 4$	0.131	0.0126	13.018
$Ks = 5$	0.151	0.0126	14.442
$Ks = 6$	0.156	0.0126	15.399
$Ks = 7$	0.158	0.0126	16.284
$Ks = 8$	0.159	0.0126	17.128
$Ks = 9$	0.160	0.0126	17.938
$Ks = 10$	0.160	0.0126	18.954
$Ks = 11$	0.161	0.0126	19.300
$Ks = 12$	0.161	0.0126	20.460

The model was found to be insensitive to the hydraulic conductivity in terms of flow depth and flow rate by viewing the RMSE value (Table 7.6). However, the model showed sensitive to hydraulic conductivity in terms of flow hydrographs and gauge height curves (Fig.7.10 and Fig.7.11). It was observed that till $Ks < 2cm/h$ model showed one trend, it showed a different trend after $Ks > 2cm/h$ values (Fig.7.10 and Fig.7.11). The error metric RMSE values for flow depth also showed increment from $Ks = 0.005$ to $2cm/h$ then the next increment in RMSE values showed form $Ks = 3$ to $12cm/h$ (Table 7.7). The model showed very sensitivity to the hydraulic conductivity in terms of infiltration depth. A small variation of Ks resulted a notable change in amount of infiltration depth (Fig.7.12 and Table 7.7). However, it was observed that the large variation in the infiltration depth was not affected much over depth and flow rate. Suggesting that model is relatively less sensitive to flow depth and flow rate prediction to hydraulic conductivity, but the model is more sensitive to infiltration depth.

Abstract-TH-2793_156104035

7.4.3 Evaluation of Model Prediction

The performance of the model was evaluated by comparing the model predicted runoff with the observed flow rate at the measuring station (outlet of considered Valley Stream watershed). The Pearson Coefficient of determination, RMSE, and NSE error metrics were used to evaluate the model's performance. The time series of the simulated and observed runoff is shown in Figure 7.13. In the model, the derived parameters obtained from observed datasets were used to simulate the model for the peak event observed during of 13 August 2014 (EST Time Zone), even though the calibration of the model performed using hydraulic conductivity.

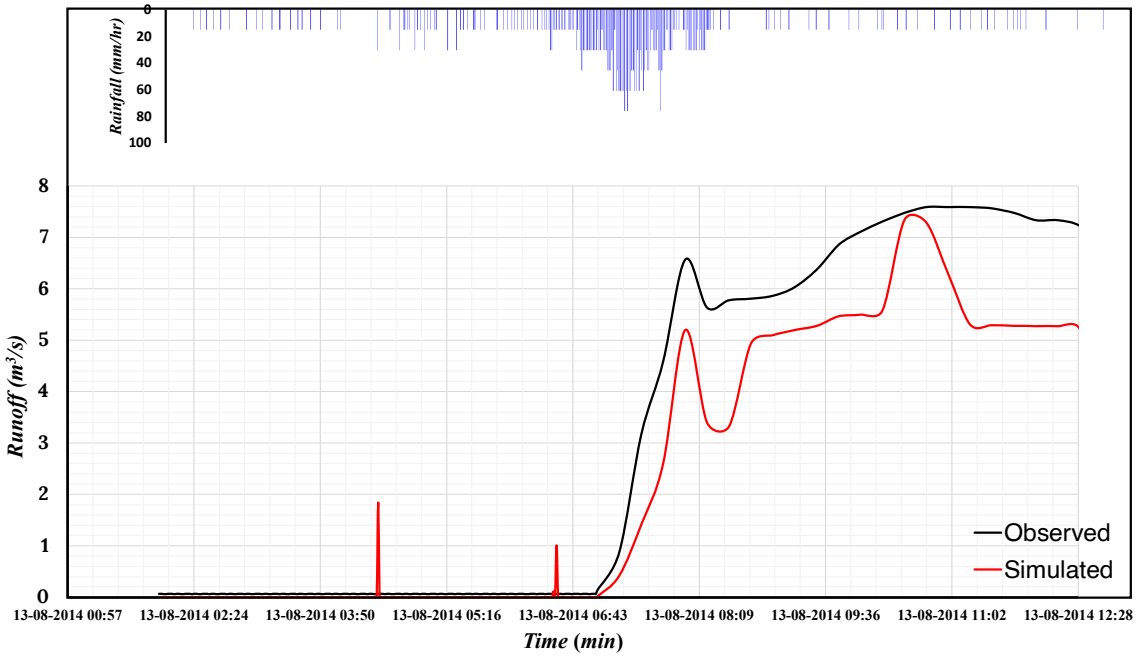

Figure 7.13. Comparison between the model simulated and observed flow discharge at outlet during the period of peak flood occurred on 13-08-2014 (EST Time zone).

Time series of flow rate demonstrated that the model was well captured the rising and peak phase of the runoff trend (Fig.7.13). Due to uncertainties in input datasets, the magnitude and pattern of the profiles might have differed from each other. However, it is observed that the general pattern of the response is agreed with the measured flow data. The scatter plot between simulated and observed also indicated model prediction was agreed with the observed one with R^2 of 0.8386, RMSE of 0.48 m^3/s, and NSE is 0.91 (Fig.7.14). However, it was observed that the model was slightly underpredicted (Fig.7.14).

Abstract-TH-2793_156104035

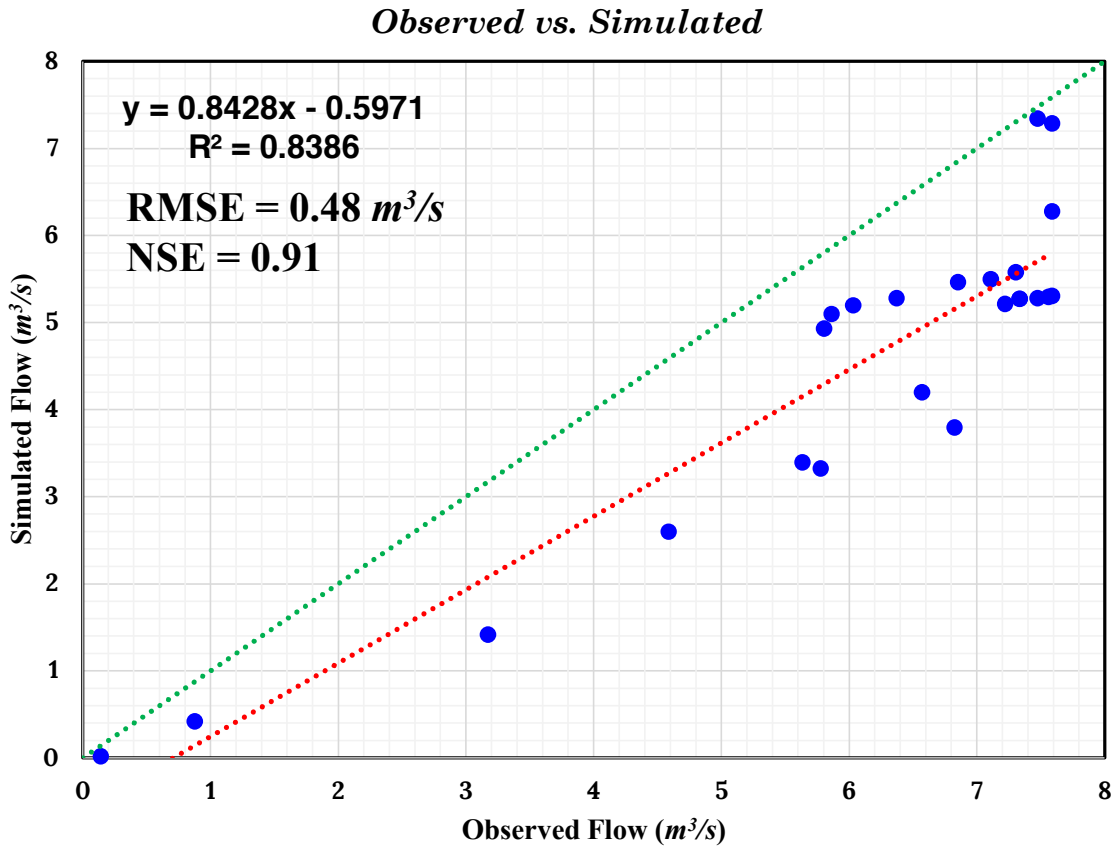

Figure 7.14. Performance Comparison of simulated flow with observed flow measured at outlet gauge station using error metrics RMSE, NSE and PCC during the period of peak flood occurred on 13-08-2014 (EST Time zone).

7.4.4 Time Series of Flow Depths

The simulated flow depths across the highly urbanized Valley Stream watershed at discrete time steps are shown in Figure 7.15. These time series plots demonstrated the evolution of the surface water flooding at the spatial and temporal scales during a high-intensity storm event that occurred on 13 August 2014 (EST Time Zone). The extensive flooding occurred around the stream corridors, at the South-East and East corners of the watershed (Fig.7.15). Extensive flooding occurred at the southeast corner of the watershed, where land is covered with swampy lands around 07:25 AM. The peak at the outlet occurred around 10:25 AM.

Abstract-TH-2793_156104035

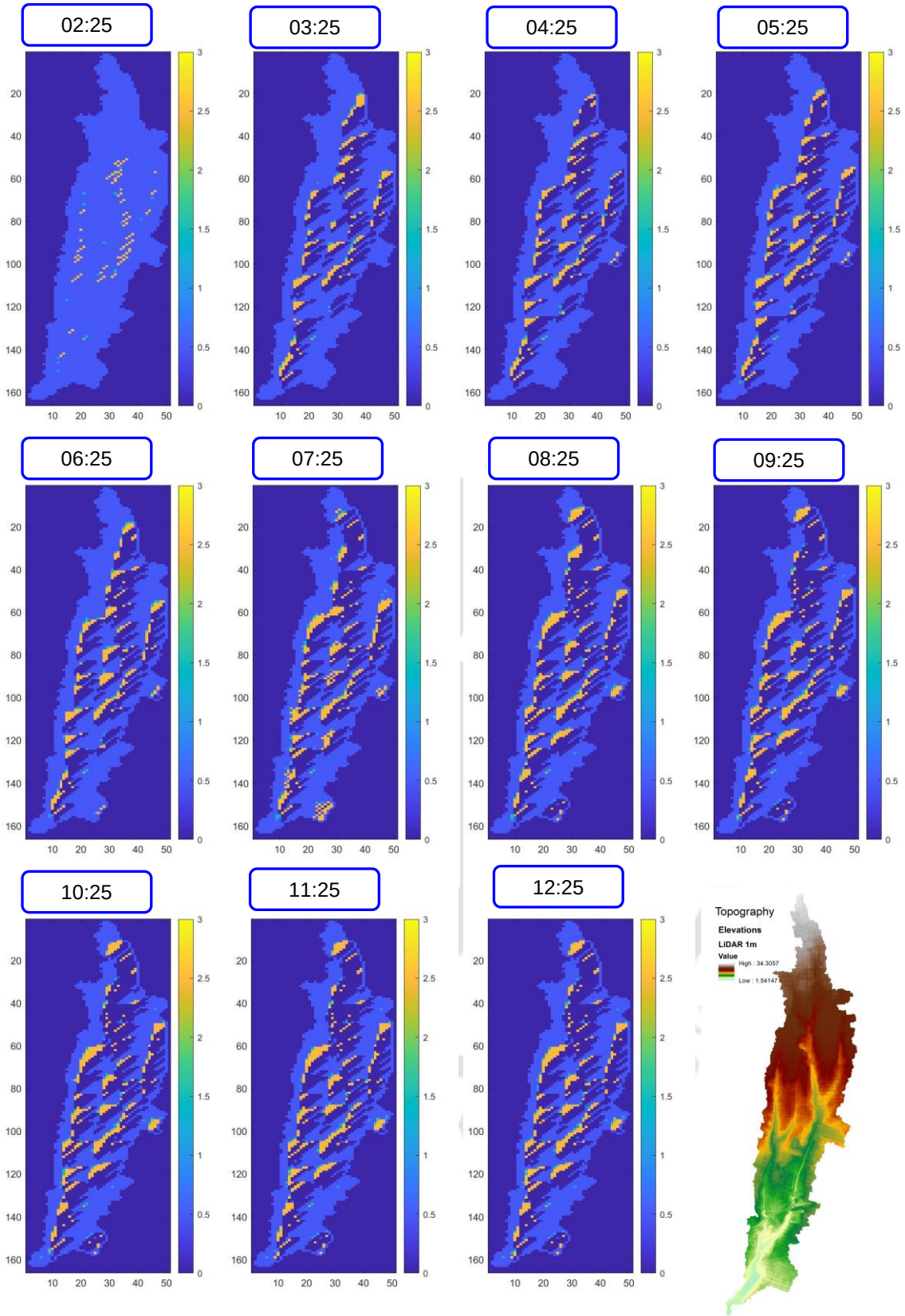

Figure 7.15. The predicted water depths in the Valley Stream watershed during the extreme storm event occurred on 13 August,2014 (EST Time zone).

Abstract-TH-2793_156104035

7.5 CONCLUSIONS

This chapter presents the development and application of a simple physically-based distributed urban hydrological flood inundation model, coupling with the hydrological processes within a surface flow routing structure taken from Bates et al. [2010]. The key hydrological processes such as infiltration and evapotranspiration, and surface hydraulic routing are represented in the model. Along with the processes, this study focused on incorporating impervious factors at the grid cell level instead of taking lumped impervious area percentage. The surface roughness in terms of Manning's roughness was also represented in the model. The linkage between the surface and drainage is simplified by assuming drain design capacity value and incorporating it at cell level or uniform over the city. In this model, the drainage from surface runoff to storm severs treated as mass loss to the system. Representing all hydrological and hydraulic processes at high spatial and temporal resolution made the model capable of applying at the city scale to derive the vulnerable areas to overland water flood risk during nuisance and flash flood. The key advantage of the model is the minimum requirement of drainage information and representation of impervious factors at the pixel level. Another key advantage of the model is that buildings or their footprints can be represented in the topographic model (DEM), which are the primary cause of the blockage to flood movement. This model works at city scale level as well as street level. In the model, green infrastructure as a low-impact development can also be incorporated.

The model was applied and tested to the extreme storm event that occurred on 13 August 2014 in the highly urbanized Valley Stream watershed, New York, USA. The sensitivity analysis was conducted to varying surface roughness parameters, and soil hydraulic conductivity values over the model simulated outputs such as flood depth and flow rate. The sensitivity analysis reveals that the model is sensitive to low surface values taken as Manning's roughness coefficients (Open Land) and insensitive to higher Manning's n values (Vegetation and Urban cover). The sensitive analysis also revealed that the model is highly sensitive to hydraulic conductivity regarding infiltration depths. However, which has not shown any impact on flow depths and runoff. The performance evaluation of the model also reveals that the model simulated values were well agreed with the observed flow rate values with NSE 0.91 and coefficient of determination 0.83.

Abstract-TH-2793_156104035

Future work should be directed towards analyzing the degree of sensitiveness to the mesh resolution and incorporating the adaptive time step instead of the constant time step to maintain the stability of the model at higher resolution datasets. The sensitivity analysis of any hydrological model depends on slope of the terrain, the sensitivity of sloped terrain likely to be magnified as compared to mild slope terrain [Yu & Coulthard, 2015]. The sensitivity analysis of the model to different terrain types of watersheds should also be performed in the future. The calibration of the model emphasizes the need for further improvement in the model. So, future work should be directed the extensive calibration to different parameters with high-resolution datasets.

Abstract-TH-2793_156104035

This Page Intentionally Left Blank

Abstract-TH-2793_156104035

8

SUMMARY AND FUTURE SCOPE

(Conclusions and Future Recommendations)

Abstract-TH-2793_156104035

8.1 SUMMARY

In the present research, a distributed urban hydrological model is developed to forecast the flash flood in heterogeneous urban landscapes. The model incorporates the in-advanced predicted high-intensity storm event rainfall and medium resolution to high-resolution topographic datasets. This study developed a novel gravity-turbulence based technique to retrieve rainfall rates from weather radar reflectivity. A new approach based on Maxwell approximation over reflectivity hyetograph is proposed to nowcast/predict the high intensity of rainfall using weather radars. This study also attempted to investigate the suitable open-source DEM for the urban flood modeling through the proposed new assessment technique based on angle-distance percentile storage-elevation curves, other statistical techniques, and hydrological modeling approach. Finally, the inertial-based hydro-inundated distributed hydrological model is developed, which applies at street scale to city-scale during the nuisance to flash flood situations. For this research, different study areas were considered depending on the work's objective and availability of high spatial and temporal resolution datasets. The following sub-sections presented a summary of the work done, the performance of proposed approaches, and observations made in the present research.

8.1.1 Radar Reflectivity Rainfall Rate Relationship

In recent decades, weather radars have become an essential tool to design flood early warning systems, especially for flash floods in both urban and mountainous regions, where the density and advanced quantitative estimation of point gauge measurements are insufficient. With weather radars, radar rainfall rates are derived indirectly from measured radar reflectivity instead of being direct measurement. The errors in quantitative estimation of rainfall using radars due to difficulties in converting radar received signal measurements to rainfall rates. Even though numerous Z – R relationships were developed based on region and season, numerous bias correction techniques also evolved; it is still quite challenging to retrieve rainfall rates from radar reflectivity. It is due to the highly dynamic nature of raindrop size distribution even within a single storm event [Ulbrich, 1993; Smith et al., 2009]. In recent years, dual-polarization radars have a capability to identify the dynamic nature of raindrop size distribution by collecting additional information of raindrops.

Abstract-TH-2793_156104035

However, the advanced technologies have not changed the existence of inherent limitations in converting reflectivity to rainfall rate due to indirect measurement of rainfall and well above the ground with the radar [Ochoa-Rodriguez et al., 2019]. In this study, a Gravity – Turbulence based method was developed to reduce the error in converting reflectivity to rainfall by selecting appropriate radar pixel, which will contribute rainfall towards the ground. This method is dependent on the identified thresholds of spectral width values. Spectral Width is an indirect measurement of turbulence/shear forces acting on raindrops within a single storm event. The parametric Z-R relationship was established with the proposed method for two different ecological zones. The established relationship was compared with the existing parametric relationships such as Marshall-Palmer, TMM method, and nonparametric methods PMM and WPMM. The proposed method showed better performance than all other methods, with an error of 16% for overall storms, 12% for stratiform storms, and 18% for convective storms. The method was applied with limited data due to the unavailability of large datasets at present. This study also identified that the basic Marshall-Palmer equation performed well for stratiform events than any other methods.

8.1.2 Reflectivity Hyetograph Prediction

In this objective, a new hierarchical machine learning approach to generating and predicting synthetic reflectivity-rainfall hyetograph is proposed by splitting storm hyetograph into different responses and then approximating with Maxwell function, decomposing random variables, and model fitted parameters. The data extracted in the study lead to the following observations.

- It was observed that the extracted hyetograph comprises the harmonic fluctuations at certain time intervals. Similar patterns of radar reflectivity and power time series were plotted by Marshall et al. [1955].
- The extracted hyetograph fluctuations exhibited similar trends in their number and occurrence with the duration of the storm event.
- The reflectivity hyetographs separated and grouped into four quartiles depending on its time to peak evolution were exhibited the same tendency of rainfall hyetographs plotted by Huff [1967] for the gauge recorded rainfall in the USA.

Abstract-TH-2793_156104035

The extracted hyetograph was broken down into two sub-patterns and then coined into new terms as “Atmospheric” and “Turbulence” waves. The patterns were approximated with Maxwell function and fitted parameters; other variables were decomposed with Cholesky factorization matrix. The derived variables and parameters in the study lead to the following interpretations.

- The atmospheric and turbulence lifts showed non-dependency with other variables. They were fitted with the best probability distribution function selected by the Chi-square static test.
- The statistical properties of random variables such as duration of the event, time of occurrence of fluctuations, model fitted parameters, wave lifts, and extreme values were preserved satisfactorily by the proposed procedure.
- The excellent performance of the proposed approach in generating the accurate hyetograph similar to the observed hyetograph and prediction capacity of the model and its simplicity makes it a valuable tool for the synthetic generation and prediction of storm hyetographs for extreme events which causes flash flood situation in urban regions.
- The proposed approach could also be applied to the rain gauge observed hyetographs due to the similar tendency observed between reflectivity hyetographs observed in this study and rain gauge observed hyetographs by Huff [1967].

The results of the study lead to the following conclusions.

- The proposed approach can be readily implemented in conjunction with a distributed urban hydrological model to estimate nuisance floods to flash floods.
- The model is slightly under-predicted, and the results are limited to a particular period, as well as their sensitivity to different parameters was limited due to limited year data availability.

8.1.3 Assessment of Open-Source DEMs

This objective aims to identify the appropriate online available open-source DEMs that can be used to set up the 1D/2D urban hydrological flood model. A novel technique based on normalized angle and percentile distances storage-Elevation based (zero-dimensional) hydrological model was introduced in this study to identify the best

Abstract-TH-2793_156104035

performed DEM for urban flood modeling. This technique also identifies the characteristics and type of watershed. Along with this technique, a new assessment framework was designed with descriptive statistics such as elevation histograms, slopes, and contours analysis to identify the suitable online available DEM for urban flood modeling and mapping. Here, the statistics mentioned above were analyzed to assess the open-source DEMs for urban flood mapping. Among the sources we used, online freely available DEMs such as ALOS AW3D, ALOS PALSAR, CARTOSAT, EU-DEM, NED, and SRTM were assessed with field surveyed datasets (reference dataset) over six urban settings. The results of the study lead to the following observations.

- The ASTER global DEM was infused with complete noise and showed significant elevation differences to other datasets in urban settings. So, the ASTER global DEM can be eliminated for any studies in urban settings.
- The high-resolution DEMs such as ALOS PALSAR global model, 1/3 s NED and medium resolution 1s NED available for the USA depicts the good ground elevations which effectively stripped away the building and other man-made artifacts. These models represent DTM rather than DSM, and these DEMs may work fine in riverine flood plains but not in urban settings. These models represented a flat type of watershed with gentle slopes, which creates overprediction in flood extent and underprediction in flood depths and creates low flow velocity zones. These models also produced vertical accuracy around 6m (LE90) while ALOS AW3D shown around 4m (LE90).
- The ALOS PALSAR showed a large area of voids over the entire globe.
- The EU-DEM performed well over Riom than any other DEM, but it can be comparable to SRTM.
- The CARTOSAT regional product for India performed well than SRTM and comparable with ALOS AW3D in descriptive statistics, but it showed mixed satisfaction in the zero-dimension hydrological model.
- The ALOS AW3D has shown consistent overall performance even though it is a medium resolution DEM, but it has also shown a mismatch between adjacent pixels and large area voids in some places. This indicates ALOS AW3D would not be useful for small study areas due to a mismatch in adjacent pixels.
- The ALOS AW3D and CARTOSAT are the photogrammetry based datasets; the cloud coverage in original images could have caused large voids in these

Abstract-TH-2793_156104035

datasets. Along with these, all DEM products are acquired a long way back in the early 2000.

- The ALOS AW3D showed potential capability in the urban region by giving an excellent overall performance. The removal of unwanted noise such as vegetation cover, bridges, etc., could further enhance the utility of ALOS AW3D.

The main point we hope urban hydrologists take away is that when choosing a topography model in urban environments, there is no single topographic model that works fine everywhere and every time. So, from this research, it is advocated to researchers, and hydrologists always go for the initial assessment of topographic model statistics before modeling. It is strongly recommended to perform the proposed framework with available DEMs for a particular urban region before using DEMs for urban hydrological modeling. It is helpful to understand the topographical and hydrological characteristics of the region and gives the idea of which DEM should be used to set up the hydrological model.

8.1.4 Influence of DEMs on SWMM Model

This objective attempted to understand the impact of various open-source topographic models on the 1D SWMM (Storm Water Management Model) urban hydrological model for urban flood modeling and mapping. It is also studied to identify the appropriate online available DEM that can be used to set up the 1D/2D urban hydrological flood model. Six urban watersheds comprising small to large areas, low to high development, low raised to high raised buildings, etc., were considered to assess the influence of DEM product and its resolution on 1D SWMM urban hydrological modeling. For this purpose, the best source of field surveyed datasets and the globally available open-source products such as ALOS AW3D ($30m$), ALOS PALSAR ($12.5m$), ASTER ($30m$), SRTM ($30m$), and nationally available products NED ($10m$), NED ($30m$), CARTOSAT vR3.1 ($30m$) were selected to conduct the series of simulations using SWMM model. The sensitivity of the SWMM model over selected DEM was studied, while simultaneously, the performance of globally open-source DEMs was evaluated for urban flood modeling.

The DEMs were utilized as a topographic input into the 1D SWMM hydrological model, where the flood inundation depths, peaks, inflow hydrographs at

Abstract-TH-2793_156104035

the outlet, and flood inundation extents were analyzed. Topographic datasets were used for urban watershed identification and urban drain rim elevations into the SWMM model. The results of the study lead to the following observations.

- It was observed that the SWMM model is insensitive to DEM product type and its resolution for flood depths, peaks, and hydrograph prediction, and it showed high sensitiveness for flood inundation extent prediction and mapping.
- Both global and national, medium resolution DEMs failed to quantify the flood inundation area outputs in the 1D SWMM simulation, which showed significant errors with poor skill score CSI (<0.4) and other binary metrics (skill scores).
- The high-resolution DEMs (ALOS PALSAR and NED) showed overestimating flood inundation extent prediction and underestimating flood depths and peaks. These models represented a flat type of watershed with gentle slopes, which could have caused overprediction in flood extent and underprediction in flood depths and created low flow velocity zones. These models represent DTM rather than DSM, and these DEMs may work fine in riverine flood plains but not in urban settings.
- The influence of DEM type and resolution was negligible over SWMM model outputs prediction. The ALOS AW3D was performed better, and ASTER was performed poorly in urban watersheds.

8.1.5 Distributed Urban Hydrological Model

This objective presents the development and application of a simple physically-based distributed urban hydrological flood inundation model, coupling with the hydrological processes within a surface flow routing, structure of model taken from Bates et al. [2010]. The key hydrological processes such as infiltration and evapotranspiration along with surface hydraulic routing are represented in the model. Along with the processes, this study focused on incorporating impervious factors at the cell level instead of taking the lumped percentage of impervious area. The surface roughness in terms of Manning's *n* value was also represented in the model. The linkage between the surface and drainage is simplified by assuming drain design capacity value and incorporating it at cell level or uniform over the city. In this model, the drainage from surface runoff to storm severs treated as mass loss to the system.

Abstract-TH-2793_156104035

Representing all hydrological and hydraulic processes at high spatial and temporal resolutions made the model capable of applying at the city scale to derive the vulnerable areas from surfacing water flood risk during nuisance and flash flood. The model's key advantage is the minimum requirement of drainage information and representation of impervious factors at the pixel level. Another key advantage of the model is that buildings or their footprints can be represented in the topographic model (DEM), which is the primary cause of the blockage to flood movement. This model works at city scale level as well as street level. In the model, green infrastructure as a low-impact development can also be incorporated.

The model was applied and tested to the extreme storm event that occurred during the period of 13 August 2014 in the highly urbanized Valley Stream watershed, New York, USA. The sensitivity analysis was conducted to varying surface roughness parameters, and soil hydraulic conductivity values over the model simulated outputs such as flood depth and flow rate. The results of the study lead to the following conclusions.

- The sensitivity analysis reveals that the model is sensitive to low surface values taken as Manning's roughness coefficients (Open Land) and insensitive to higher Manning's *n* values (Vegetation and Urban cover).
- The sensitive analysis also revealed that the model is highly sensitive to hydraulic conductivity regarding infiltration depths. However, which has not shown any impact on flow depths and runoff.
- The performance evaluation of the model revealed that the simulated model values were well agreed with the observed flow rate values with NSE 0.91 and coefficient of determination 0.83.

8.2 RECOMMENDATIONS FOR FUTURE RESEARCH

The present research developed and demonstrated the distributed urban hydrological model within the advanced prediction of precipitation and the importance of medium resolution topographic models in urban flash flood modeling. However, many other improvements have to be added to the proposed urban flood modeling framework, quantitative estimation, and rainfall prediction using weather radars. Also, many other essential aspects to be looked at in detail to retrieve accurate

Abstract-TH-2793_156104035

rainfall rates from radar data. Furthermore, for an understanding of topographic models used as inputs into the developed urban hydro-flood inundation model. The present research can be extended further with a prime focus on the following aspects and improvements.

- The proposed gravity-turbulence based rainfall retrieval from the radar reflectivity approach has to be applied for dual-polarization weather radar parameters to the long period observed datasets.
- The application of Maxwell approximated rainfall prediction technique can be tested for several year datasets and over other urban regions for further investigations of return period rainfall events and to make model real-time operational nowcasting.
- The proposed storage-elevation topography assessment methodology and statistical analysis can be performed on recently acquired TanDEM-X towards urban flood mapping.
- Analyzing the degree of sensitiveness to the mesh resolution of the model can be done in the future.
- In the model, the adaptive time step can be incorporated instead of the constant time step to maintain the stability of the model at higher resolution datasets, and its impacts on output can be analyzed.
- The sensitivity analysis of the model to different terrain types of watersheds should also be performed in the future.
- The extensive calibration to different parameters with high-resolution datasets can be performed to the developed urban flood model.

Abstract-TH-2793_156104035

This Page Intentionally Left Blank

Abstract-TH-2793_156104035

References

Abdullah, A. F., Vojinovic, Z., Price, R. K., & Aziz, N. A. A. (2012). A methodology for processing raw LiDAR data to support urban flood modelling framework. Journal of hydroinformatics, 14(1), 75-92.

Akan, A. O., & Houghtalen, R. J. (2003). Urban hydrology, hydraulics, and stormwater quality: engineering applications and computer modeling. John Wiley & Sons.

Akkimi, A., Dutta, S., & Ray, K. (2019). Flash Flood Generated Short Term Precipitation Forecast System in Heterogeneous Urban Landscape using Weather RADAR. Paper presented at American Geophysical Union Fall Meeting (AGUFM), 2019, San Francisco, USA, A53L-3067.

Andersson, T., & Ivarsson, K. I. (1991). A model for probability nowcasts of accumulated precipitation using radar. Journal of Applied Meteorology and Climatology, 30(1), 135-141.

Andjelkovic, I. (2001). Guidelines on non-structural measures in urban flood management. International Hydrological Programme (IHP), United Nations Educational, Scientific and Cultural Organization (UNESCO).

Antolik, M. S. (2000). An overview of the National Weather Service's centralized statistical quantitative precipitation forecasts. Journal of Hydrology, 239(1), 306-337.

Apirumanekul C. (2001). Modelling of Urban Flooding in Dhaka City. Master Thesis, No.WM 00-13, Asian Institute of Technology, Thailand

Applequist, S., Gahrs, G. E., Pfeffer, R. L., &Niu, X. F. (2002). Comparison of methodologies for probabilistic quantitative precipitation forecasting. Weather and Forecasting, 17(4), 783-799.

Archer, L., Neal, J. C., Bates, P. D., & House, J. I. (2018). Comparing TanDEM-X Data With Frequently Used DEMs for Flood Inundation Modeling. Water Resources Research, 54(12), 10-205.

Aronica, G., & Cannarozzo, M. (2000). Studying the hydrological response of urban catchments using a semi-distributed linear non-linear model. Journal of Hydrology, 238(1-2), 35-43.

Aronica, G. T., & Lanza, L. G. (2005). Drainage efficiency in urban areas: a case study. Hydrological Processes: An International Journal, 19(5), 1105-1119.

Atencia, A., & Zawadzki, I. (2014). A comparison of two techniques for generating nowcasting ensembles. Part I: Lagrangian ensemble technique. Monthly Weather Review, 142(11), 4036-4052.

Atlas, D., Rosenfeld, D., & Wolff, D. B. (1990). Climatologically tuned reflectivity-rain rate relations and links to area-time integrals. Journal of Applied Meteorology and Climatology, 29(11), 1120-1135.

Abstract-TH-2793_156104035

Atlas, D., Rosenfeld, D., & Jameson, A. R. (1997). Evolution of Radar Rainfall Measurement: Steps and Missteps. Weather Radar Technology for Water Resources Management (eds. B. Braga and O. Massambani) UNESCO Press, Montevideo, Chapter 1.

Atlas, D., Ulbrich, C. W., Marks Jr, F. D., Amitai, E., & Williams, C. R. (1999). Systematic variation of drop size and radar-rainfall relations. Journal of Geophysical Research: Atmospheres, 104(D6), 6155-6169.

Austin, P. M. (1987). Relation between measured radar reflectivity and surface rainfall. Monthly Weather Review, 115(5), 1053-1070.

Avtar, R., Yunus, A. P., Kraines, S., & Yamamuro, M. (2015). Evaluation of DEM generation based on Interferometric SAR using TanDEM-X data in Tokyo. Physics and Chemistry of the Earth, Parts A/B/C, 83, 166-177.

Baade, J., & Schmullius, C. (2016). TanDEM-X IDEM precision and accuracy assessment based on a large assembly of differential GNSS measurements in Kruger National Park, South Africa. ISPRS Journal of Photogrammetry and Remote Sensing, 119, 496-508.

Baghdadi, N., Cavelier, S., Chiles, J. P., Bourgine, B., Toutin, T. H., King, C., ... & Truffert, C. (2005). Merging of airborne elevation data and Radarsat data to develop a Digital Elevation Model. International Journal of Remote Sensing, 26(1), 141-166.

Baldonado, F. D. (1996). Experiments in Determination of Radar Reflectivity–Rainfall Intensity (ZR) Relations in the Philippines. Philippine Atmospheric, Geophysical and Astronomical Services Administration-AGSSB Abstracts.

Bangen, S. G., Wheaton, J. M., Bouwes, N., Bouwes, B., & Jordan, C. (2014). A methodological intercomparison of topographic survey techniques for characterizing wadeable streams and rivers. Geomorphology, 206, 343-361.

Barbarella, M., Fiani, M., & Zollo, C. (2017). Assessment of DEM derived from very high-resolution stereo satellite imagery for geomorphometric analysis. European Journal of Remote Sensing, 50(1), 534-549.

Bárdossy, A., & Pegram, G. (2017). Combination of radar and daily precipitation data to estimate meaningful sub-daily point precipitation extremes. Journal of Hydrology, 544, 397-406.

Barnes, M. L., Welty, C., & Miller, A. J. (2018). Impacts of development pattern on urban groundwater flow regime. Water Resources Research, 54, 5198– 5212.

Basile, A., & Butini, F. (1993). Rainfall Estimation by Means of a Meteorological Radar: an Innovative Approach Using Neural Networks. EARSeL Advances in Remote Sensing, Vol.2, No.2 – VI.

Bates, P. D. (2004). Remote sensing and flood inundation modelling. Hydrological processes, 18(13), 2593-2597.

Bates, P. D., Horritt, M. S., & Fewtrell, T. J. (2010). A simple inertial formulation of the shallow water equations for efficient two-dimensional flood inundation modelling. Journal of Hydrology, 387(1-2), 33-45.

Abstract-TH-2793_156104035

Bates, P. D. (2012). Integrating remote sensing data with flood inundation models: how far have we got?. Hydrological processes, 26(16), 2515-2521.

Battan, L. J. (1973). Radar observation of the atmosphere (No. 04; QC973. 5, B3.).

Blanchard, D. C. (1953). Raindrop size-distribution in Hawaiian rains. Journal of Atmospheric Sciences, 10(6), 457-473.

Bellal, M., Sillen, X., & Zech, Y. (1996). Coupling GIS with a distributed hydrological model for studying the effect of various urban planning options on rainfall-runoff relationship in urbanized watersheds. IAHS Publications-Series of Proceedings and Reports-Intern Assoc Hydrological Sciences, 235, 99-106.

Bellon, A., & Austin, G. L. (1978). The evaluation of two years of real-time operation of a short-term precipitation forecasting procedure (SHARP). Journal of Applied Meteorology, 17(12), 1778-1787.

Berthier, E., Andrieu, H., & Creutin, J. D. (2004). The role of soil in the generation of urban runoff: development and evaluation of a 2D model. Journal of hydrology, 299(3-4), 252-266.

Berthier, E., Arnaud, Y., Kumar, R., Ahmad, S., Wagnon, P., & Chevallier, P. (2007). Remote sensing estimates of glacier mass balances in the Himachal Pradesh (Western Himalaya, India). Remote Sensing of Environment, 108(3), 327-338.

Bhaskar, A. S., Welty, C., Maxwell, R. M., & Miller, A. J. (2015). Untangling the effects of urban development on subsurface storage in Baltimore. Water Resources Research, 51(2), 1158-1181.

Bi, H., Zheng, W., Ge, W., Zhang, P., Zeng, J., & Yu, J. (2018). Constraining the distribution of vertical slip on the South Heli Shan Fault (northeastern Tibet) from high-resolution topographic data. Journal of Geophysical Research: Solid Earth, 123(3), 2484-2501.

Boulton, S. J., & Stokes, M. (2018). Which DEM is best for analyzing fluvial landscape development in mountainous terrains?. Geomorphology, 310, 168-187.

Bowler, N. E., Pierce, C. E., & Seed, A. (2004). Development of a precipitation nowcasting algorithm based upon optical flow techniques. Journal of Hydrology, 288(1-2), 74-91.

Bowler, N. E., Pierce, C. E. and Seed, A. W. (2006). STEPS: A probabilistic precipitation forecasting scheme which merges an extrapolation nowcast with downscaled NWP. Q.J.R. Meteorol. Soc., 132: 2127–2155.

Bremnes, J. B. (2004). Probabilistic forecasts of precipitation in terms of quantiles using NWP model output. Monthly Weather Review, 132(1), 338-347.

Bringi, V. N., & Chandrasekar, V. (2001). Polarimetric Doppler weather radar: principles and applications. Cambridge university press.

Bringi, V. N., Rico-Ramirez, M. A., & Thurai, M. (2011). Rainfall estimation with an operational polarimetric C-band radar in the United Kingdom: Comparison with a gauge network and error analysis. Journal of Hydrometeorology, 12(5), 935– 954.

Abstract-TH-2793_156104035

Brommundt, J., & Bárdossy, A. (2007). Spatial correlation of radar and gauge precipitation data in high temporal resolution. Advances in Geosciences, 10, 103-109.

Buch, T., Hamann, S., Niebuhr, A., & Rossen, A. (2014). What Makes Cities Attractive? The Determinants of Urban Labour Migration in Germany. Urban Studies, 51(9), 1960–1978.

Calder, I. R., Harding, R. J., & Rosier, P. T. W. (1983). An objective assessment of soil-moisture deficit models. Journal of Hydrology, 60(1-4), 329-355.

Calheiros, R. V., & Zawadzki, I. (1987). Reflectivity-rain rate relationships for radar hydrology in Brazil. Journal of Applied Meteorology and Climatology, 26(1), 118-132.

Carlino, G. A., & Saiz, A. (2019). Beautiful city: Leisure amenities and urban growth. Journal of Regional Science, 59(3), 369-408.

Carlson, P. E. (1970, January). Problems of Snowfall Measurement by Radar. In BULLETIN OF THE AMERICAN METEOROLOGICAL SOCIETY (Vol. 51, No. 8, p. 776). 45 BEACON ST, BOSTON, MA 02108-3693: AMER METEOROLOGICAL SOC.

Carr, R. S., & Smith, G. P. (2007). Linking of 2D and Pipe hydraulic models at fine spatial scales. Water Practice and Technology, 2(2).

Cataneo, R. (1969). A method for estimating rainfall rate-radar reflectivity relationships. Journal of Applied Meteorology and Climatology, 8(5), 815-819.

Cataneo, R., & Vercellino, D. L. (1972). Estimating rainfall rate-radar reflectivity relationships for individual storms. Journal of Applied Meteorology, 11(1), 211-213.

Chandrasekar, V., Keränen, R., Lim, S., & Moisseev, D. (2013). Recent advances in classification of observations from dual polarization weather radars. Atmospheric Research, 119, 97– 111.

Chaney, N. W., Metcalfe, P., & Wood, E. F. (2016). HydroBlocks: a field-scale resolving land surface model for application over continental extents. Hydrological processes, 30(20), 3543-3559.

Chen, A. S., Djordjevic, S., Leandro, J., & Savic, D. (2007). The urban inundation model with bidirectional flow interaction between 2D overland surface and 1D sewer networks. NOVATECH 2007.

Chen, A. S., Hsu, M. H., Teng, W. H., Huang, C. J., Yeh, S. H., & Lien, W. Y. (2006). Establishing the database of inundation potential in Taiwan. Natural hazards, 37(1-2), 107-132.

Chen, J., Hill, A. A., & Urbano, L. D. (2009). A GIS-based model for urban flood inundation. Journal of Hydrology, 373(1-2), 184-192.

Chen, Y., & Zhou, Q. (2013). A scale-adaptive DEM for multi-scale terrain analysis. International Journal of Geographical Information Science, 27(7), 1329-1348.

Chow, T. E., & Hodgson, M. E. (2009). Effects of lidar post-spacing and DEM resolution to mean slope estimation. International Journal of Geographical Information Science, 23(10), 1277-1295.

Chow, V.T., Maidment, D.R., Mays, L.W. (1988). Applied Hydrology, McGraw-Hill, New York. 350-379.

Abstract-TH-2793_156104035

Chow, V.T., Maidment, D.R. and L.W. Mays. (2010). Applied hydrology. Tata McGraw-Hill Education.

Cluckie, I. D., Rico-Ramirez, M. A., Xuan, Y., & Szalinska, W. (2006). An experiment of rainfall prediction over the Odra catchment by combining weather radar and a numerical weather model. In 7th International Conference on Hydroinformatics, Nice, France.

Congalton, R. G., & Green, K. (2019). Assessing the accuracy of remotely sensed data: principles and practices. CRC press.

Crosson, W. L., Duchon, C. E., Raghavan, R., & Goodman, S. J. (1996). Assessment of rainfall estimates using a standard ZR relationship and the probability matching method applied to composite radar data in central Florida. Journal of Applied Meteorology and Climatology, 35(8), 1203-1219.

Daliakopoulos, I. N., &Tsanis, I. K. (2012). Aweather radar data processing module for storm analysis. Journal of Hydroinformatics, 14(2), 332-344.

Das, A., Agrawal, R., & Mohan, S. (2015). Topographic correction of ALOS-PALSAR images using InSAR-derived DEM. Geocarto International, 30(2), 145-153.

Das, M., & Das, A. (2019). Dynamics of Urbanization and its impact on Urban Ecosystem Services (UESs): A study of a medium size town of West Bengal, Eastern India. Journal of Urban Management, 8(3), 420-434.

Deilami, K., & Hashim, M. (2011). Very high resolution optical satellites for DEM generation: A review. European Journal of Scientific Research, 49(4), 542-554.

DHI Group (2009a), MOUSE pipe flow reference manual, DHI Software, Horsolm, Debmark.

Digital Globe, (2016). Accuracy of world view products, white papers.

Dixon, M., & Wiener, G. (1993). TITAN: Thunderstorm identification, tracking, analysis, and nowcasting—A radar-based methodology. Journal of atmospheric and oceanic technology, 10(6), 785-797.

Djordjević, S., Ivetić, M., Maksimović, C., & Rajcević, A. (1991). An approach to the simulation of street flooding in the modeling of surcharged flow in storm sewers. Proceedings: New Technologies in Urban Drainage, 101-8.

Djordjević, S., Prodanović, D., Maksimović, Č., Ivetić, M., & Savić, D. (2005). SIPSON–Simulation of Interaction between Pipe flow and Surface Overland flow in Networks. Water Science and Technology, 52(5), 275-283.

Dolcine, L., Andrieu, H., Sempere-Torres, D., & Creutin, D. (2001). Flash flood forecasting with coupled precipitation model in mountainous Mediterranean basin. Journal of Hydrologic Engineering, 6(1), 1-10.

Dong, Z., & Lu, J. (2009). Numerical simulation of urban waterlogging disaster due to plum storm. In Advances in Water Resources and Hydraulic Engineering (pp. 275-280). Springer, Berlin, Heidelberg.

Abstract-TH-2793_156104035

Doswell III, C. A., Brooks, H. E., & Maddox, R. A. (1996). Flash flood forecasting: An ingredients-based methodology. Weather and Forecasting, 11(4), 560-581.

Dotto, C. B., Kleidorfer, M., Deletic, A., Rauch, W., McCarthy, D. T., & Fletcher, T. D. (2011). Performance and sensitivity analysis of stormwater models using a Bayesian approach and long-term high resolution data. Environmental Modelling & Software, 26(10), 1225-1239.

Dutta, D., Sharma, S., Kannan, B. A. M., Venketswarlu, S., Gairola, R. M., Rao, T. N., & Viswanathan, G. (2012). Sensitivity of ZR relations and spatial variability of error in a Doppler Weather Radar measured rain intensity. 92.40. eg; 92.60. jf.

Easterling, D. R., Meehl, G. A., Parmesan, C., Changnon, S. A., Karl, T. R., & Mearns, L. O. (2000). Climate extremes: observations, modeling, and impacts. Science, 289(5487), 2068-2074.

Einfalt, T., Arnbjerg-Nielsen, K., Golz, C., Jensen, N. E., Quirmbach, M., Vaes, G., & Vieux, B. (2004). Towards a roadmap for use of radar rainfall data in urban drainage. Journal of Hydrology, 299(3-4), 186-202.

Einfalt, T., Jessen, M., & Mehlig, B. (2005). Comparison of radar and raingauge measurements during heavy rainfall. Water Science and Technology, 51(2), 195-201.

Elaksher, A. F. (2009). Using LIDAR-based DEM to orthorectify Ikonos panchromatic images. Optics and Lasers in Engineering, 47(6), 629-635.

Ettritch, G., Hardy, A., Bojang, L., Cross, D., Bunting, P., & Brewer, P. (2018). Enhancing digital elevation models for hydraulic modelling using flood frequency detection. Remote sensing of environment, 217, 506-522.

Farr, T. G., Rosen, P. A., Caro, E., Crippen, R., Duren, R., Hensley, S., & Seal, D. (2007). The shuttle radar topography mission. Reviews of geophysics, 45(2).

Fereshtehpour, M., & Karamouz, M. (2018). DEM resolution effects on coastal flood vulnerability assessment: Deterministic and probabilistic approach. Water Resources Research, 54, 4965– 4982.

Fewtrell, T. J., Bates, P. D., Horritt, M., & Hunter, N. M. (2008). Evaluating the effect of scale in flood inundation modelling in urban environments. Hydrological Processes: An International Journal, 22(26), 5107-5118.

Fewtrell, T. J., Duncan, A., Sampson, C. C., Neal, J. C., & Bates, P. D. (2011). Benchmarking urban flood models of varying complexity and scale using high resolution terrestrial LiDAR data. Physics and Chemistry of the Earth, Parts A/B/C, 36(7-8), 281-291.

Fieber, K. D., Mills, J. P., Miller, P. E., Clarke, L., Ireland, L., & Fox, A. J. (2018). Rigorous 3D change determination in Antarctic Peninsula glaciers from stereo WorldView-2 and archival aerial imagery. Remote sensing of environment, 205, 18-31.

FULADLU, K., RİZA, M., & İLKAN, M. (2018). The effect of rapid urbanization on the physical modification of urban area.

Abstract-TH-2793_156104035

Fulton, R. A., Breidenbach, J. P., Seo, D. J., Miller, D. A., & O'Bannon, T. (1998). The WSR-88D rainfall algorithm. Weather and forecasting, 13(2), 377-395.

Friederichs, P., &Hense, A. (2007). Statistical downscaling of extreme precipitation events using censored quantile regression. Monthly weather review, 135(6), 2365-2378.

Foresti, L., Panziera, L., Mandapaka, P. V., Germann, U., & Seed, A. (2015). Retrieval of analogue radar images for ensemble nowcasting of orographic rainfall. Meteorological Applications, 22(2), 141-155.

Foresti, L., Reyniers, M., Seed, A., &Delobbe, L. (2016). Development and verification of a real-time stochastic precipitation nowcasting system for urban hydrology in Belgium. Hydrology and Earth System Sciences, 20(1), 505.

Gamba, P., Dell Acqua, F., & Houshmand, B. (2002). SRTM data characterization in urban areas. International Archives of Photogrammetry Remote Sensing and Spatial Information Sciences, 34(3/B), 55-58.

Garcia-Navarro, P., & Burguete, J. (2005). Numerical methods for the shallow water equations: 1D approach (pp. 387-408). Taylor & Francis, London.

Germann, U., & Zawadzki, I. (2002). Scale-dependence of the predictability of precipitation from continental radar images. Part I: Description of the methodology. Monthly Weather Review, 130(12), 2859-2873.

Germann, U., &Zawadzki, I. (2004). Scale dependence of the predictability of precipitation from continental radar images. Part II: Probability forecasts. Journal of Applied Meteorology, 43(1), 74-89.

Gibson, J. J. (1950). The perception of the visual world.

Göbel, P., Stubbe, H., Weinert, M., Zimmermann, J., Fach, S., Dierkes, C., ... & Coldewey, W. G. (2004). Near-natural stormwater management and its effects on the water budget and groundwater surface in urban areas taking account of the hydrogeological conditions. Journal of Hydrology, 299(3-4), 267-283.

Gochis, D., Schumacher, R., Friedrich, K., Doesken, N., Kelsch, M., Sun, J., ... & Brown, B. (2015). The great Colorado flood of September 2013. Bulletin of the American Meteorological Society, 96(9), 1461-1487.

Golding, B. W. (1998). Nimrod: A system for generating automated very short range forecasts. Meteorological Applications: A journal of forecasting, practical applications, training techniques and modelling, 5(1), 1-16.

Gorokhovich, Y., & Voustianiouk, A. (2006). Accuracy assessment of the processed SRTM-based elevation data by CGIAR using field data from USA and Thailand and its relation to the terrain characteristics. Remote sensing of Environment, 104(4), 409-415.

Goudenhoofdt, E., & Delobbe, L. (2009). Evaluation of radar-gauge merging methods for quantitative precipitation estimates. Hydrology and Earth System Sciences, 13(2), 195-203.

Abstract-TH-2793_156104035

GRASS Development Team, 2018. Geographic Resources Analysis Support System (GRASS) Software, Version 7.4.2. Open Source Geospatial Foundation.

Greenwalt, C. R., & Shultz, M. E. (1962). Principles of error theory and cartographic applications (No. ACIC-TR-96). AERONAUTICAL CHART AND INFORMATION CENTER, ST LOUIS MO, USA.

Grimmond, C. S. B., & Oke, T. R. (1991). An evapotranspiration-interception model for urban areas. Water Resources Research, 27(7), 1739-1755.

Grohmann, C. H. (2018). Evaluation of TanDEM-X DEMs on selected Brazilian sites: Comparison with SRTM, ASTER GDEM and ALOS AW3D30. Remote Sensing of Environment, 212, 121-133.

Guth, P. L. (2006). Geomorphometry from SRTM. Photogrammetric Engineering & Remote Sensing, 72(3), 269-277.

Hall, W., Rico-Ramirez, M. A., & Krämer, S. (2015). Classification and correction of the bright band using an operational C-band polarimetric radar. Journal of Hydrology, 531, 248– 258.

Hamel, P., & Fletcher, T. D. (2014). Modelling the impact of stormwater source control infiltration techniques on catchment baseflow. Hydrological Processes, 28(24), 5817-5831.

Hamill, T. M., Whitaker, J. S., & Wei, X. (2004). Ensemble reforecasting: Improving medium-range forecast skill using retrospective forecasts. Monthly Weather Review, 132(6), 1434-1447.

Han, L., Sun, J., Zhang, W., Xiu, Y., Feng, H., & Lin, Y. (2017). A machine learning nowcasting method based on real-time reanalysis data. Journal of Geophysical Research: Atmospheres, 122(7), 4038-4051.

Han, L., Sun, J., & Zhang, W. (2019). Convolutional Neural Network for Convective Storm Nowcasting Using 3-D Doppler Weather Radar Data. IEEE Transactions on Geoscience and Remote Sensing, 58(2), 1487-1495.

Handwerker, J. (2002). Cell tracking with TRACE3D—A new algorithm. Atmospheric Research, 61(1), 15-34.

Hapuarachchi, H. A. P., Wang, Q. J., & Pagano, T. C. (2011). A review of advances in flash flood forecasting. Hydrological processes, 25(18), 2771-2784.

Hardy, J., Gourley, J. J., Kirstetter, P. E., Hong, Y., Kong, F., & Flamig, Z. L. (2016). A method for probabilistic flash flood forecasting. Journal of Hydrology, 541, 480-494.

Hasan, M. M., Sharma, A., Johnson, F., Mariethoz, G., & Seed, A. (2014). Correcting bias in radar Z–R relationships due to uncertainty in point rain gauge networks. Journal of hydrology, 519, 1668-1676.

Hawker, L. P., Rougier, J., Neal, J. C., Bates, P. D., Archer, L., & Yamazaki, D. (2018). Implications of simulating global digital elevation models for flood inundation studies. Water Resources Research, 54, 7910– 7928.

Abstract-TH-2793_156104035

Hirt, C. (2018). Artefact detection in global digital elevation models (DEMs): the maximum slope approach and its application for complete screening of the SRTM v4. 1 and MERIT DEMs. Remote sensing of environment, 207, 27-41.

Höhle, J., & Höhle, M. (2009). Accuracy assessment of digital elevation models by means of robust statistical methods. ISPRS Journal of Photogrammetry and Remote Sensing, 64(4), 398-406.

Holleman, I. (2006). Bias adjustment of radar-based 3-hour precipitation accumulations. Koninklijk Nederlands Meteorologisch Instituut.

Howard, A. D. (1990). Role of hypsometry and planform in basin hydrologic response. Hydrol. Process., 4: 373–385.

Hsu, M. H., Chen, S. H., & Chang, T. J. (2000). Inundation simulation for urban drainage basin with storm sewer system. Journal of Hydrology, 234(1-2), 21-37.

Huang, L., Li, Z., Han, H., Tian, B., & Zhou, J. (2018). Analysis of thickness changes and the associated driving factors on a debris-covered glacier in the Tienshan Mountain. Remote sensing of environment, 206, 63-71.

Hudlow, M. D., & Arkell, R. E. (1978). Effect of temporal and spatial sampling errors and Z-R variability on accuracy of GATE radar rainfall estimates. In Conference on Radar Meteorology, 18 th, Atlanta, Ga (pp. 342-349).

Huff, F. A. (1967). Time distribution of rainfall in heavy storms. Water Resour. Res., 3(4), 1007–1019.

Hunter, N. M., Bates, P. D., Horritt, M. S., & Wilson, M. D. (2007). Simple spatially-distributed models for predicting flood inundation: A review. Geomorphology, 90(3-4), 208-225.

Hunter, N. M., Bates, P. D., Neelz, S., Pender, G., Villanueva, I., Wright, N. G., ... & Mason, D. C. (2008, February). Benchmarking 2D hydraulic models for urban flooding. In Proceedings of the Institution of Civil Engineers-Water Management (Vol. 161, No. 1, pp. 13-30). Thomas Telford Ltd.

Huynh, H.T., Lai, V.S., Soumaré, I., (2008). Stochastic Simulation and Applications in Finance with MATLAB Programs. John Wiley & Sons Ltd, pp. 338 (ISBN 978-0-470-72538-2).

Hyndman, R. J., & Koehler, A. B, (2006). Another look at measures of forecast accuracy. International journal of forecasting, 22(4), 679-688.

Jarihani, A. A., Callow, J. N., McVicar, T. R., Van Niel, T. G., & Larsen, J. R. (2015). Satellite-derived Digital Elevation Model (DEM) selection, preparation and correction for hydrodynamic modelling in large, low-gradient and data-sparse catchments. Journal of Hydrology, 524, 489-506.

Jencso, K. G., and McGlynn, B. L. (2011), Hierarchical controls on runoff generation: Topographically driven hydrologic connectivity, geology, and vegetation, Water Resour. Res., 47, W11527.

Joe, P., Burgess, D., Potts, R., Keenan, T., Stumpf, G., & Treloar, A. (2004). The S2K severe weather detection algorithms and their performance. Weather and Forecasting, 19(1), 43-63.

Abstract-TH-2793_156104035

Johnson, J. T., MacKeen, P. L., Witt, A., Mitchell, E. D. W., Stumpf, G. J., Eilts, M. D., & Thomas, K. W. (1998). The storm cell identification and tracking algorithm: An enhanced WSR-88D algorithm. Weather and forecasting, 13(2), 263-276.

Jones, D. (1956). Rainfall drop size-distribution and radar reflectivity. Illinois State Water Survey.

Jongman, B., Winsemius, H. C., Aerts, J. C., De Perez, E. C., Van Aalst, M. K., Kron, W., & Ward, P. J. (2015). Declining vulnerability to river floods and the global benefits of adaptation. Proceedings of the National Academy of Sciences, 112(18), E2271-E2280.

Jorgensen, D. P., & Willis, P. T. (1982). A ZR relationship for hurricanes. Journal of Applied Meteorology and Climatology, 21(3), 356-366.

Joss, J. (1990). Applications of Weather Radar Systems. A Guide to Users of Radar Data in Meteorology and Hydrology. Edited by CG Collier. Co-ordinating Editors: JW Mason and DR Slogget. Ellis Horwood Limited Publisher, Chichester. 1989. Pp. 294.£ 44.50. Quarterly Journal of the Royal Meteorological Society, 116(494), 1021-1022.

Kalyanapu, A. J., Burian, S. J., & McPherson, T. N. (2009). Effect of land use-based surface roughness on hydrologic model output. Journal of Spatial Hydrology, 9(2).

Karila, K., Yu, X., Vastaranta, M., Karjalainen, M., Puttonen, E., & Hyyppä, J. (2019). TanDEM-X digital surface models in boreal forest above-ground biomass change detection. ISPRS Journal of Photogrammetry and Remote Sensing, 148, 174-183.

Karmaker, T., & Dutta, S. (2010). Generation of synthetic seasonal hydrographs for a large river basin. Journal of hydrology, 381(3), 287-296.

Karl, T. R., & Knight, R. W. (1998). Secular trends of precipitation amount, frequency, and intensity in the United States. Bulletin of the American Meteorological society, 79(2), 231-241.

Kelleher, C., & McPhillips, L. (2020). Exploring the application of topographic indices in urban areas as indicators of pluvial flooding locations. Hydrological Processes, 34(3), 780-794.

Kent, C. W., Grimmond, S., Gatey, D., & Hirano, K. (2019). Urban morphology parameters from global digital elevation models: Implications for aerodynamic roughness and for wind-speed estimation. Remote sensing of environment, 221, 316-339.

Kim, T. J., Kwon, H. H., & Kim, K. B. (2021). Calibration of the reflectivity-rainfall rate (ZR) relationship using long-term radar reflectivity factor over the entire South Korea region in a Bayesian perspective. Journal of Hydrology, 593, 125790.

Kleidorfer, M., Deletic, A., Fletcher, T. D., & Rauch, W. (2009). Impact of input data uncertainties on urban stormwater model parameters. Water Science and Technology, 60(6), 1545-1554.

Kober, K., Craig, G. C., Keil, C., & Dörnbrack, A. (2012). Blending a probabilistic nowcasting method with a high-resolution numerical weather prediction ensemble for convective precipitation forecasts. Quarterly Journal of the Royal Meteorological Society, 138(664), 755-768.

Abstract-TH-2793_156104035

Kong, F., Xue, M., Thomas, K. W., Wang, Y., Brewster, K., Wang, X., ... &Coniglio, M. C,(2011), Evaluation of caps multi-model storm-scale ensemble forecast for the NOAA HWT 2010 spring experiment, 24th Conference on Weather and Forecasting/20th Conference on Numerical Weather Prediction.

Koutsoyiannis, D., and E. Foufoula-Georgiou (1993). A scaling model of a storm hyetograph. Water Resour. Res.,29(7), 2345–2361.

Krebs, G., Kokkonen, T., Valtanen, M., Setälä, H., & Koivusalo, H. (2014). Spatial resolution considerations for urban hydrological modelling. Journal of Hydrology, 512, 482-497.

Krzywinski, M., Schein, J., Birol, I., Connors, J., Gascoyne, R., Horsman, D., ... & Marra, M. A. (2009). Circos: an information aesthetic for comparative genomics. Genome research, 19(9), 1639-1645.

Kyznarová, H., &Novák, P. (2009). CELLTRACK—Convective cell tracking algorithm and its use for deriving life cycle characteristics. Atmospheric Research, 93(1), 317-327.

Kuiry, S. N., Sen, D., & Bates, P. D. (2010). Coupled 1D–Quasi-2D flood inundation model with unstructured grids. Journal of Hydraulic Engineering, 136(8), 493-506.

Kulp, S. A., & Strauss, B. H. (2018). CoastalDEM: A global coastal digital elevation model improved from SRTM using a neural network. Remote sensing of environment, 206, 231-239.

Leandro, J. (2008). Advanced modelling of flooding in urban areas: integrated 1D/1D and 1D/2D Models.

Leandro, J., Chen, A. S., Djordjević, S., & Savić, D. A. (2009). Comparison of 1D/1D and 1D/2D coupled (sewer/surface) hydraulic models for urban flood simulation. Journal of hydraulic engineering, 135(6), 495-504.

Le Bris, R., & Paul, F. (2015). Glacier-specific elevation changes in parts of western Alaska. Annals of Glaciology, 56(70), 184-192.

Lee, J. G., & Heaney, J. P. (2003). Estimation of urban imperviousness and its impacts on storm water systems. Journal of Water Resources Planning and Management, 129(5), 419-426.

Leon, D. C., French, J. R., Lasher-Trapp, S., Blyth, A. M., Abel, S. J., Ballard, S., ... & Young, G. (2016). The Convective Precipitation Experiment (COPE): Investigating the origins of heavy precipitation in the southwestern United Kingdom. Bulletin of the American Meteorological Society, 97(6), 1003-1020.

Leitao, J. P., Boonya-Aroonnet, S., Prodanović, D., & Maksimović, Č. (2009). The influence of digital elevation model resolution on overland flow networks for modelling urban pluvial flooding. Water Science and Technology, 60(12), 3137-3149.

Leitao, J. P., Simões, N. E., Maksimović, Č., Ferreira, F., Prodanović, D., Matos, J. S., & Sá Marques, A. (2010). Real-time forecasting urban drainage models: full or simplified networks?. Water Science and Technology, 62(9), 2106-2114.

Abstract-TH-2793_156104035

Leitão, J. P., Almeida, M. D. C., Simões, N. E., & Martins, A. (2013). Methodology for qualitative urban flooding risk assessment. Water science and technology, 68(4), 829-838.

Leitão, J. P., Moy de Vitry, M., Scheidegger, A., & Rieckermann, J. (2016). Assessing the quality of digital elevation models obtained from mini unmanned aerial vehicles for overland flow modelling in urban areas. Hydrology and Earth System Sciences, 20(4), 1637-1653.

Leitão, J. P., & de Sousa, L. M. (2018). Towards the optimal fusion of high-resolution Digital Elevation Models for detailed urban flood assessment. Journal of Hydrology, 561, 651-661.

Lhomme, J., Bouvier, C., & Perrin, J. L. (2004). Applying a GIS-based geomorphological routing model in urban catchments. Journal of Hydrology, 299(3-4), 203-216.

Li, L., Schmid, W., & Joss, J. (1995). Nowcasting of motion and growth of precipitation with radar over a complex orography. Journal of applied meteorology, 34(6), 1286-1300.

Lim, J. S. (1990). Two-dimensional signal and image processing. Englewood Cliffs, NJ, Prentice Hall, 536-540.

Lindeberg, T. (1998). Edge detection and ridge detection with automatic scale selection. International Journal of Computer Vision, 30(2), 117-156,

Linsley Jr, R. K., Kohler, M. A., & Paulhus, J. L. (1975). Hydrology for engineers.

Liu, X. (2008). Airborne LiDAR for DEM generation: some critical issues. Progress in physical geography, 32(1), 31-49.

Liu, Y., Xi, D. G., Li, Z. L., & Hong, Y. (2015). A new methodology for pixel-quantitative precipitation nowcasting using a pyramid Lucas Kanade optical flow approach. Journal of Hydrology, 529, 354-364.

Looper, J. P., & Vieux, B. E. (2012). An assessment of distributed flash flood forecasting accuracy using radar and rain gauge input for a physics-based distributed hydrologic model. Journal of Hydrology, 412, 114-132.

Maerker, M., Quénéhervé, G., Bachofer, F., & Mori, S. (2015). A simple DEM assessment procedure for gully system analysis in the Lake Manyara area, northern Tanzania. Natural Hazards, 79(1), 235-253.

Maksimović, Č., Prodanović, D., Boonya-Aroonnet, S., Leitão, J. P., Djordjević, S., & Allitt, R. (2009). Overland flow and pathway analysis for modelling of urban pluvial flooding. Journal of Hydraulic Research, 47(4), 512-523.

Mapiam, P. P., Sriwongsitanon, N., Chumchean, S., & Sharma, A. (2009). Effects of rain gauge temporal resolution on the specification of a Z–R relationship. Journal of Atmospheric and Oceanic Technology, 26(7), 1302-1314.

Mark, O., Weesakul, S., Apirumanekul, C., Aroonnet, S. B., & Djordjević, S. (2004). Potential and limitations of 1D modelling of urban flooding. Journal of Hydrology, 299(3-4), 284-299.

Abstract-TH-2793_156104035

Martha, T. R., Kerle, N., Jetten, V., van Westen, C. J., & Kumar, K. V. (2010). Landslide volumetric analysis using Cartosat-1-derived DEMs. IEEE Geoscience and remote sensing letters, 7(3).

Marra, F., & Morin, E. (2015). Use of radar QPE for the derivation of Intensity–Duration–Frequency curves in a range of climatic regimes. Journal of hydrology, 531, 427-440.

Marshall, J. S., Langille, R. C., & Palmer, W. M. K. (1947). Measurement of rainfall by radar. Journal of Meteorology, 4(6), 186-192.

Marshall, J. S., & Palmer, W. M. K. (1948). The distribution of raindrops with size. Journal of meteorology, 5(4), 165-166.

Marshall, J. S., Hitschfeld, W., & Gunn, K. L. S. (1955). Advances in radar weather. Advances in geophysics, 2, 1-56.

Mason, D. C., Trigg, M., Garcia-Pintado, J., Cloke, H. L., Neal, J. C., & Bates, P. D. (2016). Improving the TanDEM-X Digital Elevation Model for flood modelling using flood extents from Synthetic Aperture Radar images. Remote sensing of environment, 173, 15-28.

Maxwell, J.C. (1960). Quantitative geomorphology of the San Dimas experimental forest, California. Project ONR 389-042, Tech. Report-19, Dept. of Geology, Columbia Univ., New York.

Manton, M. J., Della-Marta, P. M., Haylock, M. R., Hennessy, K. J., Nicholls, N., Chambers, L. E., ... &Inape, K. (2001). Trends in extreme daily rainfall and temperature in Southeast Asia and the South Pacific: 1961–1998. International Journal of Climatology, 21(3), 269-284.

McCuen, R. H., Johnson, P. A., & Ragan, R. M. (1996). Highway hydrology: Hydraulic design series No. 2 (No. FHWA-SA-96-067).

Mecklenburg, S., Joss, J., &Schmid, W. (2000). Improving the nowcasting of precipitation in an Alpine region with an enhanced radar echo tracking algorithm. Journal of Hydrology, 239(1), 46-68.

Moon, S. H., Kim, Y. H., Lee, Y. H., & Moon, B. R. (2019). Application of machine learning to an early warning system for very short-term heavy rainfall. Journal of Hydrology, 568, 1042-1054.

Miliaresis, G. C., & Paraschou, C. V. (2011). An evaluation of the accuracy of the ASTER GDEM and the role of stack number: a case study of Nisiros Island, Greece. Remote Sensing Letters, 2(2), 127-135.

Miller, J. D., Kim, H., Kjeldsen, T. R., Packman, J., Grebby, S., & Dearden, R. (2014). Assessing the impact of urbanization on storm runoff in a peri-urban catchment using historical change in impervious cover. Journal of Hydrology, 515, 59-70.

Mitchell, V. G., Cleugh, H. A., Grimmond, C. S., & Xu, J. (2008). Linking urban water balance and energy balance models to analyse urban design options. Hydrological Processes: An International Journal, 22(16), 2891-2900.

Mtamba, J., Van der Velde, R., Ndomba, P., Zoltán, V., & Mtalo, F. (2015). Use of Radarsat-2 and Landsat TM images for spatial parameterization of Manning's roughness coefficient in hydraulic modeling. Remote sensing, 7(1), 836-864.

Abstract-TH-2793_156104035

Muralikrishnan, S., Pillai, A., Narender, B., Reddy, S., Venkataraman, V. R., & Dadhwal, V. K. (2013). Validation of Indian national DEM from Cartosat-1 data. Journal of the Indian Society of Remote Sensing, 41(1), 1-13.

Muthusamy, M., Casado, M. R., Butler, D., & Leinster, P. (2021). Understanding the effects of Digital Elevation Model resolution in urban fluvial flood modelling. Journal of Hydrology, 596, 126088.

Neigh, C., Masek, J., Bourget, P., Cook, B., Huang, C., Rishmawi, K., & Zhao, F. (2014). Deciphering the precision of stereo IKONOS canopy height models for US forests with G-LiHT airborne LiDAR. Remote Sensing, 6(3), 1762-1782.

Neigh, C. S., Masek, J. G., Bourget, P., Rishmawi, K., Zhao, F., Huang, C., ... & Nelson, R. F. (2016). Regional rates of young US forest growth estimated from annual Landsat disturbance history and IKONOS stereo imagery. Remote sensing of environment, 173, 282-293.

Neteler, M., Bowman, M. H., Landa, M., & Metz, M. (2012). GRASS GIS: A multi-purpose open source GIS. Environmental Modelling & Software, 31, 124-130.

Neteler, M., & Mitasova, H. (2013). Open source GIS: a GRASS GIS approach (Vol. 689). Springer Science & Business Media.

Niipele, J. N., & Chen, J. (2019). The usefulness of alos-palsar dem data for drainage extraction in semi-arid environments in The Iishana sub-basin. Journal of Hydrology: Regional Studies, 21, 57-67.

Nikolakopoulos, K. G., Kamaratakis, E. K., & Chrysoulakis, N. (2006). SRTM vs ASTER elevation products. Comparison for two regions in Crete, Greece. International Journal of remote sensing, 27(21), 4819-4838.

Nitheshnirmal, S., Thilagaraj, P., Rahaman, S. A., & Jegankumar, R. (2019). Erosion risk assessment through morphometric indices for prioritisation of Arjuna watershed using ALOS-PALSAR DEM. Modeling Earth Systems and Environment, 1-18.

Novák, P., Březková, L., &Frolík, P. (2009). Quantitative precipitation forecast using radar echo extrapolation. Atmospheric Research, 93(1-3), 328-334.

Ochoa-Rodriguez, S., Wang, L. P., Gires, A., Pina, R. D., Reinoso-Rondinel, R., Bruni, G., ... & ten Veldhuis, M. C. (2015). Impact of spatial and temporal resolution of rainfall inputs on urban hydrodynamic modelling outputs: A multi-catchment investigation. Journal of Hydrology, 531, 389-407.

Ochoa-Rodriguez, S., Wang, L. P., Willems, P., & Onof, C. (2019). A review of radar-rain gauge data merging methods and their potential for urban hydrological applications. Water Resources Research, 55(8), 6356-6391.

Ogania, J. L., Puno, G. R., Alivio, M. B. T., & Taylaran, J. M. G. (2019). Effect of digital elevation model's resolution in producing flood hazard maps. Global Journal of Environmental Science and Management, 5(1), 95-106.

Abstract-TH-2793_156104035

Ogden, F. L., Sharif, H. O., Senarath, S. U. S., Smith, J. A., Baeck, M. L., & Richardson, J. R. (2000). Hydrologic analysis of the Fort Collins, Colorado, flash flood of 1997. Journal of Hydrology, 228(1-2), 82-100.

Ogden, F. L., Pradhan, N. R., Downer, C. W., and Zahner, J. A. (2011). Relative importance of impervious area, drainage density, width function, and subsurface storm drainage on flood runoff from an urbanized catchment, Water Resour. Res., 47, W12503.

O'Loughlin, G., & Seneviratne, I. (2006). Lessons from Modelling Piped Urban Drainage Catchments. In 7th International Conference on Urban Drainage Modelling and the 4th International Conference on Water Sensitive Urban Design; Book of Proceedings (p. 785). Monash University.

Pan, A., Hou, A., Tian, F., Ni, G., & Hu, H. (2012). Hydrologically enhanced distributed urban drainage model and its application in Beijing city. Journal of Hydrologic Engineering, 17(6), 667-678.

Paradella, W. R., Ferretti, A., Mura, J. C., Colombo, D., Gama, F. F., Tamburini, A., ... & Silva, A. Q. (2015). Mapping surface deformation in open pit iron mines of Carajás Province (Amazon Region) using an integrated SAR analysis. Engineering Geology, 193, 61-78.

Pattanaik, D. R., &Rajeevan, M. (2010). Variability of extreme rainfall events over India during southwest monsoon season. Meteorological Applications, 17(1), 88-104.

Pattani, K. (2010). Evaluation of optimal real-time reflectivity-rainfall rate (ZR) functional relationships. Florida Atlantic University.

Peña, F., & Nardi, F. (2018). Floodplain terrain analysis for coarse resolution 2D flood modeling. Hydrology, 5(4), 52.

Petrucci, G., & Bonhomme, C. (2014). The dilemma of spatial representation for urban hydrology semi-distributed modelling: Trade-offs among complexity, calibration and geographical data. Journal of Hydrology, 517, 997-1007.

Phillips, B. C., Yu, S., Thompson, G. R., & De Silva, N. (2005, August). 1D and 2D Modelling of Urban Drainage Systems using XP-SWMM and TUFLOW. In 10th international conference on urban drainage (pp. 21-26). Copenhagen, Denmark.

Pierce, C., Bowler, N., Seed, A., Jones, A., Jones, D. and Moore, R. (2005), Use of a stochastic precipitation nowcast scheme for fluvial flood forecasting and warning, Atmosph. Sci. Lett., 6: 78–83.

Piman, T., Babel, M. S., Das Gupta, A., & Weesakul, S. (2007). Development of a window correlation matching method for improved radar rainfall estimation. Hydrology and Earth System Sciences, 11(4), 1361-1372.

Press, W. H., Teukolsky, S. A., Vetterling, W. T., & Flannery, B. P, (2007). Numerical recipes 3rd edition: The art of scientific computing. Cambridge university press, pp.100.

Price, R. K. (2011). Urban hydroinformatics: data, models, and decision support for integrated urban water management. IWA publishing.

Abstract-TH-2793_156104035

Rabiei, E., & Haberlandt, U. (2015). Applying bias correction for merging rain gauge and radar data. Journal of Hydrology, 522, 544-557.

Raghavan, S., & Sivaramakrishnan, T. R. (1982). Radar estimation of precipitation around Madras. Mausam (India), 33, 21-28.

Rao, T. N., Rao, D. N., Mohan, K., & Raghavan, S. (2001). Classification of tropical precipitating systems and associated Z-R relationships. Journal of Geophysical Research: Atmospheres, 106(D16), 17699-17711.

Rawls, W. J., Brakensiek, D. L., & Miller, N. (1983). Green-Ampt infiltration parameters from soils data. Journal of hydraulic engineering, 109(1), 62-70.

Reuter, H. I., Neison, A., Strobl, P., Mehl, W., & Jarvis, A. (2009, July). A first assessment of ASTER GDEM tiles for absolute accuracy, relative accuracy and terrain parameters. In 2009 IEEE International Geoscience and Remote Sensing Symposium (Vol. 5, pp. V-240). IEEE.

Rico-Ramirez, M. A., & Cluckie, I. D. (2008). Classification of ground clutter and anomalous propagation using dual-polarization weather radar. IEEE Transactions on Geoscience and Remote Sensing, 46(7), 1892– 1904.

Rinehart, R. E., & Garvey, E. T. (1978), Three-dimensional storm motion detection by conventional weather radar, Nature, 273(5660), 287.

Rodriguez, F., Andrieu, H., & Zech, Y. (2000). Evaluation of a distributed model for urban catchments using a 7-year continuous data series. Hydrological processes, 14(5), 899-914.

Rodriguez, F., Andrieu, H., & Creutin, J. D. (2003). Surface runoff in urban catchments: morphological identification of unit hydrographs from urban databanks. Journal of Hydrology, 283(1-4), 146-168.

Rodriguez, F., Andrieu, H., & Morena, F. (2008). A distributed hydrological model for urbanized areas–Model development and application to case studies. Journal of Hydrology, 351(3-4), 268-287.

Rodriguez, E., Morris, C. S., & Belz, J. E. (2006). A global assessment of the SRTM performance. Photogrammetric Engineering & Remote Sensing, 72(3), 249-260.

Rosenberger, L., Leandro, J., Pauleit, S., & Erlwein, S. (2021). Sustainable stormwater management under the impact of climate change and urban densification. Journal of Hydrology, 596, 126137.

Rosenfeld, D., Atlas, D., & Short, D. A. (1990). The estimation of convective rainfall by area integrals: 2. The Height-Area Rainfall Threshold (HART) method. Journal of Geophysical Research: Atmospheres, 95(D3), 2161-2176.

Rosenfeld, D., Wolff, D. B., & Atlas, D. (1993). General probability-matched relations between radar reflectivity and rain rate. Journal of Applied Meteorology and Climatology, 32(1), 50-72.

Rosenfeld, D., Wolff, D. B., & Amitai, E. (1994). The window probability matching method for rainfall measurements with radar. Journal of Applied Meteorology and Climatology, 33(6), 682-693.

Abstract-TH-2793_156104035

Rossi, C., & Gernhardt, S. (2013). Urban DEM generation, analysis and enhancements using TanDEM-X. ISPRS journal of photogrammetry and remote sensing, 85, 120-131.

Rossman L. A., & Huber, W.C. (2016). Storm Water Management Model Reference Manual Volume I – Hydrology. EPA/600/R15/162A. U.S. Environmental Protection Agency, Cincinnati, OH.

Rounce, D. R., King, O., McCarthy, M., Shean, D. E., & Salerno, F. (2018). Quantifying debris thickness of debris-covered glaciers in the Everest Region of Nepal through inversion of a subdebris melt model. Journal of Geophysical Research: Earth Surface, 123(5), 1094-1115.

Rubinato, M., Shucksmith, J., Saul, A. J., & Shepherd, W. (2013). Comparison between InfoWorks hydraulic results and a physical model of an urban drainage system. Water science and technology, 68(2), 372-379.

Saksena, S., & Merwade, V. (2015). Incorporating the effect of DEM resolution and accuracy for improved flood inundation mapping. Journal of Hydrology, 530, 180-194.

Salvadore, E., Bronders, J., & Batelaan, O. (2015). Hydrological modelling of urbanized catchments: A review and future directions. Journal of Hydrology, 529, 62-81.

Sampson, C. C., Bates, P. D., Neal, J. C., & Horritt, M. S. (2013). An automated routing methodology to enable direct rainfall in high resolution shallow water models. Hydrological Processes, 27(3), 467-476.

Sampson, C. C., Smith, A. M., Bates, P. D., Neal, J. C., & Trigg, M. A. (2016). Perspectives on open access high resolution digital elevation models to produce global flood hazard layers. Frontiers in Earth Science, 3, 85.

Sanders, B. F. (2007). Evaluation of on-line DEMs for flood inundation modeling. Advances in Water Resources, 30(8), 1831-1843.

Sarkar, R., Dutta, S., & Panigrahy, S. (2008). Characterizing overland flow on a preferential infiltration dominated hillslope: Case study. Journal of Hydrologic Engineering, 13(7), 563-569.

Satge, F., Denezine, M., Pillco, R., Timouk, F., Pinel, S., Molina, J., ... & Bonnet, M. P. (2016). Absolute and relative height-pixel accuracy of SRTM-GL1 over the South American Andean Plateau. ISPRS journal of photogrammetry and remote sensing, 121, 157-166.

Schmid, W., Mecklenburg, S., & Joss, J. (2000). Short-term risk forecasts of severe weather. Physics and Chemistry of the Earth, Part B: Hydrology, Oceans and Atmosphere, 25(10-12), 1335-1338.

Schmitt, T. G., Thomas, M., & Ettrich, N. (2004). Analysis and modeling of flooding in urban drainage systems. Journal of hydrology, 299(3-4), 300-311.

Schumann, G., Matgen, P., Hoffmann, L., Hostache, R., Pappenberger, F., & Pfister, L. (2007). Deriving distributed roughness values from satellite radar data for flood inundation modelling. Journal of Hydrology, 344(1-2), 96-111.

Abstract-TH-2793_156104035

Schumann, G., Bates, P. D., Horritt, M. S., Matgen, P., & Pappenberger, F. (2009). Progress in integration of remote sensing–derived flood extent and stage data and hydraulic models. Reviews of Geophysics, 47(4).

Schumann, G. J. P., Bates, P. D., Neal, J. C., & Andreadis, K. M. (2014). Technology: Fight floods on a global scale. Nature, 507(7491), 169.

Seed, A. W. (2003). A dynamic and spatial scaling approach to advection forecasting. Journal of Applied Meteorology, 42(3), 381-388.

Seed, A. W., Pierce, C. E., & Norman, K. (2013). Formulation and evaluation of a scale decomposition-based stochastic precipitation nowcast scheme. Water Resources Research, 49(10), 6624-6641.

Selkowitz, D. J., & Forster, R. R. (2016). Automated mapping of persistent ice and snow cover across the western US with Landsat. ISPRS Journal of Photogrammetry and Remote Sensing, 117, 126-140.

Sempere-Torres, D., Corral, C., Raso, J., & Malgrat, P. (1999). Use of weather radar for combined sewer overflows monitoring and control. Journal of Environmental Engineering, 125(4), 372-380.

Seyoum, S. D., Vojinovic, Z., Price, R. K., & Weesakul, S. (2012). Coupled 1D and noninertia 2D flood inundation model for simulation of urban flooding. Journal of hydraulic engineering, 138(1), 23-34.

Seyoum, S. D. (2013). Framework for Dynamic Modelling of Urban Floods at Different Topographical Resolutions.

Shaker, A., Yan, W. Y., & Easa, S. (2011). Construction of digital 3D highway model using stereo IKONOS satellite imagery. Geocarto International, 26(1), 49-67.

Shakti P.C, Misumi, R., Nakatani, T., Iwanami, K., Maki, M., Seed, A. W., & Hirano, K. (2015). Comparison of rainfall nowcasting derived from the STEPS model and JMA precipitation nowcasts. Hydrological Research Letters, 9(4), 54-60.

Shapiro, M., & Westervelt, J. (1994). r. mapcalc: An algebra for GIS and image processing (No. USACERL-TR-EC-94/13). Construction Engineering Research Lab (ARMY) Champaign IL.

Shean, D. E., Alexandrov, O., Moratto, Z. M., Smith, B. E., Joughin, I. R., Porter, C., & Morin, P. (2016). An automated, open-source pipeline for mass production of digital elevation models (DEMs) from very-high-resolution commercial stereo satellite imagery. ISPRS Journal of Photogrammetry and Remote Sensing, 116, 101-117.

Shen, Y., Goodall, J. L., & Chase, S. B. (2017). Method for rapidly assessing the overtopping risk of bridges due to flooding over a large geographic region. JAWRA Journal of the American Water Resources Association, 53(6), 1437-1452.

Shi, X., Chen, Z., Wang, H., Yeung, D. Y., Wong, W. K., & Woo, W. C. (2015). Convolutional LSTM network: A machine learning approach for precipitation nowcasting. Advances in Neural Information Processing Systems, 2015-January, 802-810.

Abstract-TH-2793_156104035

Simões, N. E., Wang, L. P., Ochoa-Rodríguez, S., Leitao, J., Pina, R., Onof, C., ... & David, L. (2011). A methodology for urban flood forecast based on a network of raingauges. In 12th International Conference on Urban Drainage, Porto Alegre, Brazil.

Sloughter, J. M. L., Raftery, A. E., Gneiting, T., & Fraley, C. (2007). Probabilistic quantitative precipitation forecasting using Bayesian model averaging. Monthly Weather Review, 135(9), 3209-3220.

Smith, M. (2006). Comment on 'Potential and limitations of 1D modeling of urban flooding' by O. Mark et al. [J. Hydrol. 299 (2004) 284-299]. Journal of Hydrology, 321(1-4), 1-4.

Smith, J. A., Miller, A. J., Baeck, M. L., Nelson, P. A., Fisher, G. T., & Meierdiercks, K. L. (2005). Extraordinary flood response of a small urban watershed to short-duration convective rainfall. Journal of Hydrometeorology, 6(5), 599–617.

Smith, J. A., Hui, E., Steiner, M., Baeck, M. L., Krajewski, W. F., & Ntelekos, A. A. (2009). Variability of rainfall rate and raindrop size distributions in heavy rain. Water Resources Research, 45(4).

Smythe, G. R., &Zrnic, D. S. (1983). Correlation analysis of Doppler radar data and retrieval of the horizontal wind. Journal of Climate and applied Meteorology, 22(2), 297-311.

Sokol, Z. (2006). Nowcasting of 1-h precipitation using radar and NWP data. Journal of Hydrology, 328(1-2), 200-211.

Spilhaus, A. F. (1948). Drop size, intensity, and radar echo of rain. Journal of Meteorology, 5(4), 161-164.

SPOT Image. (2004), SPOT DEM Product Description, Airbus defence and space, Satellite imaging corporation. https://www.satimagingcorp.com/satellite-sensors/other-satellite-sensors/spot-5/

Spry, R. B., & Zhang, S. (2006). Modelling of Drainage Systems and Overland Flowpaths at Catchment Scales. In 7th International Conference on Urban Drainage Modelling and the 4th International Conference on Water Sensitive Urban Design; Book of Proceedings (p. 801). Monash University.

Steiner, M., & Houze Jr, R. A. (1993, May). Three-dimensional validation at TRMM ground truth sites: Some early results from Darwin, Australia. In Preprints, 26th Int. Conf. on Radar Meteorology, Norman, OK, Amer. Meteor. Soc (Vol. 417, p. 420).

Steiner, M., Houze Jr, R. A., & Yuter, S. E. (1995). Climatological characterization of three-dimensional storm structure from operational radar and rain gauge data. Journal of Applied Meteorology and Climatology, 34(9), 1978-2007.

Stephens, E., Schumann, G. and Bates, P. (2014), Problems with binary pattern measures for flood model evaluation. Hydrol. Process., 28: 4928-4937.

Stout, G. E., & Mueller, E. A. (1968). Survey of relationships between rainfall rate and radar reflectivity in the measurement of precipitation. Journal of Applied Meteorology and Climatology, 7(3), 465-474.

Abstract-TH-2793_156104035

Straub, C., Tian, J., Seitz, R., & Reinartz, P. (2013). Assessment of Cartosat-1 and WorldView-2 stereo imagery in combination with a LiDAR-DTM for timber volume estimation in a highly structured forest in Germany. Forestry, 86(4), 463-473.

Sugier, J., & Tabary, P. (2006). Evaluation of dual polarization technology at C-band for operational weather radars as part of the EUMETNET OPERA programme. Paper presented at the Fourth European Conference on Radar in Meteorology and Hydrology - ERAD 2006, Barcelona, Spain.

Sujatha, E. R., Selvakumar, R., Rajasimman, U. A. B., & Victor, R. G. (2015). Morphometric analysis of sub-watershed in parts of Western Ghats, South India using ASTER DEM. Geomatics, Natural Hazards and Risk, 6(4), 326-341.

Sun, J., Xue, M., Wilson, J. W., Zawadzki, I., Ballard, S. P., Onvlee-Hooimeyer, J., ... & Pinto, J. (2014). Use of NWP for nowcasting convective precipitation: Recent progress and challenges. Bulletin of the American Meteorological Society, 95(3), 409-426.

Tachikawa, T., Kaku, M., Iwasaki, A., Gesch, D. B., Oimoen, M. J., Zhang, Z., ... & Abrams, M. (2011). ASTER global digital elevation model version 2-summary of validation results. NASA.

Tanoue, M., Hirabayashi, Y., & Ikeuchi, H. (2016). Global-scale river flood vulnerability in the last 50 years. Scientific Reports, 6, 36021.

Tarpanelli, A., Franchini, M., Brocca, L., Camici, S., Melone, F., & Moramarco, T. (2012). A simple approach for stochastic generation of spatial rainfall patterns. Journal of Hydrology, 472, 63-76.

Teague, A., Christian, J., & Bedient, P. (2013). Radar rainfall application in distributed hydrologic modeling for Cypress Creek watershed, Texas. Journal of Hydrologic Engineering, 18(2), 219-227.

Terao, T., Murata, F., Yamane, Y., Kiguchi, M., Fukushima, A., Tanoue, M., ... & Bhagabati, A. K. (2017). Direct validation of TRMM/PR near surface rain over the northeastern Indian subcontinent using a tipping bucket raingauge network. SOLA, 13, 157-162.

Thorndahl, S., & Willems, P. (2008). Probabilistic modelling of overflow, surcharge and flooding in urban drainage using the first-order reliability method and parameterization of local rain series. Water research, 42(1-2), 455-466.

Thorndahl, S. L., Nielsen, J. E., & Rasmussen, M. R. (2013). Review and Comparison of Radar Rainfall Bias Adjustment Methods: applying a 10-year dataset from Denmark. In 11th International Precipitation Conference 2013: Royal Netherlands Meteorological Institute (KNMI) and Hydrology and Quantitative Water Management Group, Wageningen University (p. 217). Wageningen University.

Tielidze, L. G. (2016). Glacier change over the last century, Caucasus Mountains, Georgia, observed from old topographical maps, Landsat and ASTER satellite imagery. The Cryosphere, 10(2), 713-725.

Todini, E., Alberoni, P., Butts, M., Collier, C., Khatibi, R., Samuels, P., &Weerts, A. (2005). ACTIF best practice paper–understanding and reducing uncertainty in flood forecasting. In International conference on innovation, advances and implementation of flood forecasting technology, edited by: Balabanis, P., Lumbroso, D., and Samuels, P., Tromsø, Norway, Vol.1, 1-43.

Abstract-TH-2793_156104035

Toutin, T. (2006). Generation of DSMs from SPOT-5 in-track HRS and across-track HRG stereo data using spatiotriangulation and autocalibration. ISPRS Journal of Photogrammetry and Remote Sensing, 60(3), 170-181.

Tsanis, I. K., Seiradakis, K. D., Daliakopoulos, I. N., Grillakis, M. G., & Koutroulis, A. G. (2014). Assessment of GeoEye-1 stereo-pair-generated DEM in flood mapping of an ungauged basin. Journal of Hydroinformatics, 16(1), 1-18.

Turner, B. J., Zawadzki, I., & Germann, U. (2004). Predictability of precipitation from continental radar images. Part III: Operational nowcasting implementation (MAPLE). Journal of Applied Meteorology and Climatology, 43(2), 231-248.

Tuttle, J. D., & Foote, G. B. (1990). Determination of the boundary layer airflow from a single Doppler radar. Journal of Atmospheric and oceanic Technology, 7(2), 218-232.

Ulbrich, C. W., & Atlas, D. (1977, November). A method for measuring precipitation parameters using radar reflectivity and optical extinction. In Annales des Télécommunications (Vol. 32, No. 11, pp. 415-421). Springer-Verlag.

Ulbrich, C. W. (1983). Natural variations in the analytical form of the raindrop size distribution. Journal of climate and applied meteorology, 22(10), 1764-1775.

UNDESA (2014). World urbanization prospects: The 2014 revision. United Nations Department of Economic and Social Affairs (UNDESA).

United Nations, Department of Economic and Social Affairs, Population Division (UNDESA) (2019). World Urbanization Prospects: The 2018 Revision (ST/ESA/SER.A/420). New York: United Nations.

Vaes, G., Bouteligier, R., Herbos, P., & Berlamont, J. (2004). Modelling of floods caused by urban drainage systems. In Conference Proceedings UDM'04, 6th int. conf. on Urban Drainage Modelling, Date: 2004/09/01-2004/09/09, Location: Dresden, Germany (pp. 141-148).

Valeo, C., & Moin, S. M. A. (2000). Grid-resolution effects on a model for integrating urban and rural areas. Hydrological Processes, 14(14), 2505-2525.

van der Sterren, M., Rahman, A., & Ryan, G. (2014). Modeling of a lot scale rainwater tank system in XP-SWMM: A case study in Western Sydney, Australia. Journal of environmental management, 141, 177-189.

Vojinovic, Z., & Tutulic, D. (2009). On the use of 1D and coupled 1D-2D modelling approaches for assessment of flood damage in urban areas. Urban Water Journal, 6(3), 183-199.

Vojinovic, Z., & Van Teeffelen, J. (2007). An integrated stormwater management approach for small islands in tropical climates. Urban Water Journal, 4(3), 211-231.

Vozinaki, A. E. K., Morianou, G. G., Alexakis, D. D., & Tsanis, I. K. (2017). Comparing 1D and combined 1D/2D hydraulic simulations using high-resolution topographic data: A case study of the Koiliaris basin, Greece. Hydrological sciences journal, 62(4), 642-656.

Abstract-TH-2793_156104035

Wang, G., Liu, L., & Ding, Y. (2012). Improvement of radar quantitative precipitation estimation based on real-time adjustments to ZR relationships and inverse distance weighting correction schemes. Advances in Atmospheric Sciences, 29(3), 575-584.

Wallerman, J., Fransson, J. E., Bohlin, J., Reese, H., & Olsson, H. (2010, July). Forest mapping using 3D data from SPOT-5 HRS and Z/I DMC. In 2010 IEEE International Geoscience and Remote Sensing Symposium (pp. 64-67). IEEE.

Wang, L., Marzahn, P., Bernier, M., Jacome, A., Poulin, J., & Ludwig, R. (2017). Comparison of TerraSAR-X and ALOS PALSAR differential interferometry with multisource DEMs for monitoring ground displacement in a discontinuous permafrost region. IEEE Journal of Selected Topics in Applied Earth Observations and Remote Sensing, 10(9), 4074-4093.

Wang, X., Holland, D. M., & Gudmundsson, G. H. (2018). Accurate coastal DEM generation by merging ASTER GDEM and ICESat/GLAS data over Mertz Glacier, Antarctica. Remote sensing of environment, 206, 218-230.

Wechsler, S. P. (2007). Uncertainties associated with digital elevation models for hydrologic applications: a review. Hydrology and Earth System Sciences, 11(4), 1481-1500.

Wendleder, A., Wessel, B., Roth, A., Breunig, M., Martin, K., & Wagenbrenner, S. (2013). TanDEM-X water indication mask: Generation and first evaluation results. IEEE Journal of Selected Topics in Applied Earth Observations and Remote Sensing, 6(1), 171-179.

Werner, M. (2001). Shuttle Radar Topography Mission (SRTM) Mission Overview, Frequenz, 55(3-4), 75-79.

Wessels H.R.A. (1990). Estimation of the Areal Coverage of Radars and Radar Networks from Radar Site Horizon Data. In: Collier C.G., Chapuis M. (eds) Weather Radar Networking. Springer, Dordrecht., 204-211,

Wessel, B., Huber, M., Wohlfart, C., Marschalk, U., Kosmann, D., & Roth, A. (2018). Accuracy assessment of the global TanDEM-X Digital Elevation Model with GPS data. ISPRS Journal of Photogrammetry and Remote Sensing, 139, 171-182.

Wheaton, J. M., Brasington, J., Darby, S. E., & Sear, D. A. (2010). Accounting for uncertainty in DEMs from repeat topographic surveys: improved sediment budgets. Earth surface processes and landforms: the journal of the British Geomorphological Research Group, 35(2), 136-156.

Willis, M. J., Herried, B. G., Bevis, M. G., & Bell, R. E. (2015). Recharge of a subglacial lake by surface meltwater in northeast Greenland. Nature, 518(7538), 223.

Wilson, J. W., & Brandes, E. A. (1979). Radar measurement of rainfall—A summary. Bulletin of the American Meteorological Society, 60(9), 1048-1060.

Wilson, J. W., Crook, N. A., Mueller, C. K., Sun, J., & Dixon, M. (1998). Nowcasting thunderstorms: A status report. Bulletin of the American Meteorological Society, 79(10), 2079-2100.

Wilson, J. P., & Gallant, J. C. (Eds.). (2000). Terrain analysis: principles and applications. John Wiley & Sons.

Abstract-TH-2793_156104035

Wilson, J. W., Ebert, E. E., Saxen, T. R., Roberts, R. D., Mueller, C. K., Sleigh, M., ... & Seed, A. (2004). Sydney 2000 forecast demonstration project: convective storm Nowcasting. Weather and forecasting, 19(1), 131-150.

Wilson, J. W., Feng, Y., Chen, M., & Roberts, R. D. (2010). Nowcasting challenges during the Beijing Olympics: Successes, failures, and implications for future nowcasting systems. Weather and Forecasting, 25(6), 1691-1714.

Wu, M. C., & Lin, G. F. (2017). The very short-term rainfall forecasting for a mountainous watershed by means of an ensemble numerical weather prediction system in Taiwan. Journal of hydrology, 546, 60-70.

Wurm, M., d'Angelo, P., Reinartz, P., & Taubenböck, H. (2014). Investigating the applicability of Cartosat-1 DEMs and topographic maps to localize large-area urban mass concentrations. IEEE Journal of Selected Topics in Applied Earth Observations and Remote Sensing, 7(10).

Xiao, Q., McPherson, E. G., Simpson, J. R., & Ustin, S. L. (2007). Hydrologic processes at the urban residential scale. Hydrological Processes: An International Journal, 21(16), 2174-2188.

Yadav, S. K., Singh, S. K., Gupta, M., & Srivastava, P. K. (2014). Morphometric analysis of Upper Tons basin from Northern Foreland of Peninsular India using CARTOSAT satellite and GIS. Geocarto International, 29(8), 895-914.

Yao, G., Liu, Z., Guo, X., Wei, C., Li, X., & Chen, Z. (2020, July). Prediction of Weather Radar Images via a Deep LSTM for Nowcasting. In 2020 International Joint Conference on Neural Networks (IJCNN) (pp. 1-8). IEEE.

Yu, D., & Coulthard, T. J. (2015). Evaluating the importance of catchment hydrological parameters for urban surface water flood modelling using a simple hydro-inundation model. Journal of Hydrology, 524, 385-400.

Yu, D., & Lane, S. N. (2006a). Urban fluvial flood modelling using a two-dimensional diffusion-wave treatment, part 1: mesh resolution effects. Hydrological Processes: An International Journal, 20(7), 1541-1565.

Yu, D., Yin, J., & Liu, M. (2016). Validating city-scale surface water flood modelling using crowd-sourced data. Environmental Research Letters, 11(12), 124011.

Yu, P. S., Yang, T. C., Chen, S. Y., Kuo, C. M., & Tseng, H. W. (2017). Comparison of random forests and support vector machine for real-time radar-derived rainfall forecasting. Journal of Hydrology, 552, 92-104.

Zahraei, A., Hsu, K. L., Sorooshian, S., Gourley, J. J., Hong, Y., & Behrangi, A. (2013). Short-term quantitative precipitation forecasting using an object-based approach. Journal of hydrology, 483, 1-15.

Zhang, S., & Pan, B. (2014). An urban storm-inundation simulation method based on GIS. Journal of hydrology, 517, 260-268.

Abstract-TH-2793_156104035

Zhang, Y., & Smith, J. A. (2003). Space–time variability of rainfall and extreme flood response in the Menomonee River basin, Wisconsin. Journal of Hydrometeorology, 4(3), 506-517.

Zhang, J., Howard, K., Langston, C., Vasiloff, S., Kaney, B., Arthur, A., ... & Dempsey, C. (2011). National Mosaic and Multi-Sensor QPE (NMQ) system: Description, results, and future plans. Bulletin of the American Meteorological Society, 92(10), 1321-1338.

Zhang, J., Howard, K., Langston, C., Kaney, B., Qi, Y., Tang, L., Grams, H., Wang, Y., Cocks, S., Martinaitis, S. & Arthur, A. (2016). Multi-Radar Multi-Sensor (MRMS) quantitative precipitation estimation: Initial operating capabilities. Bulletin of the American Meteorological Society, 97(4), 621-638.

Zhang, K., Gann, D., Ross, M., Robertson, Q., Sarmiento, J., Santana, S., ... & Fritz, C. (2019). Accuracy assessment of ASTER, SRTM, ALOS, and TDX DEMs for Hispaniola and implications for mapping vulnerability to coastal flooding. Remote sensing of environment, 225, 290-306.

Zhao, S., Chigira, M., & Wu, X. (2019). Gigantic rockslides induced by fluvial incision in the Diexi area along the eastern margin of the Tibetan Plateau. Geomorphology, 338, 27-42.

Abstract-TH-2793_156104035

Appendix A

RADAR REFLECTIVITY RAINFALL RATE RELATIONSHIP

Abstract-TH-2793_156104035

A.1 Radar images before and after post-processing

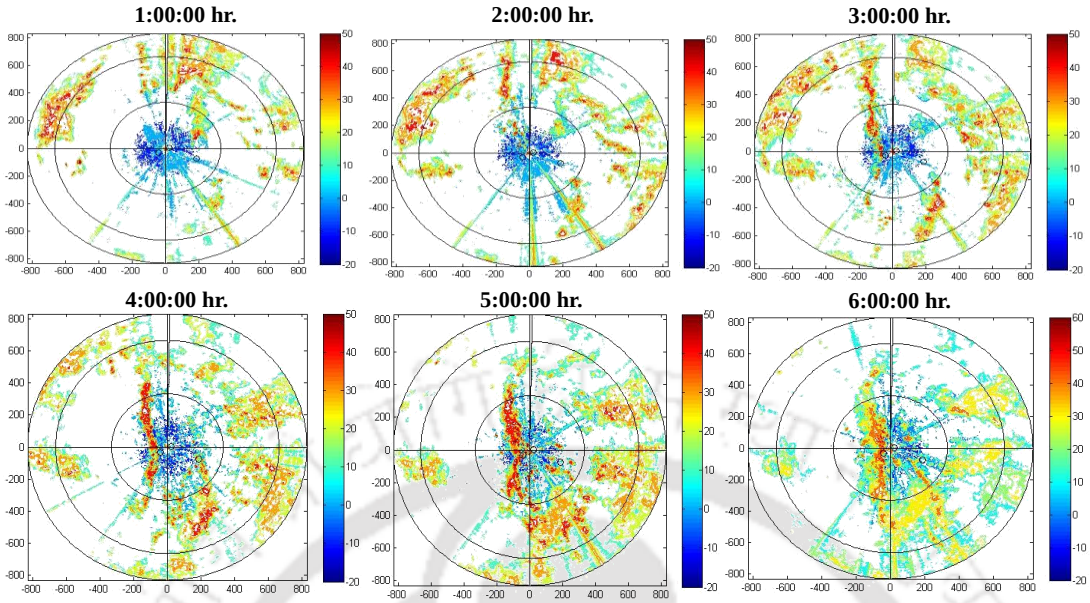

Figure A1. Plan Position Indicator (PPI) plots of 20th July, 2013 before processing data.

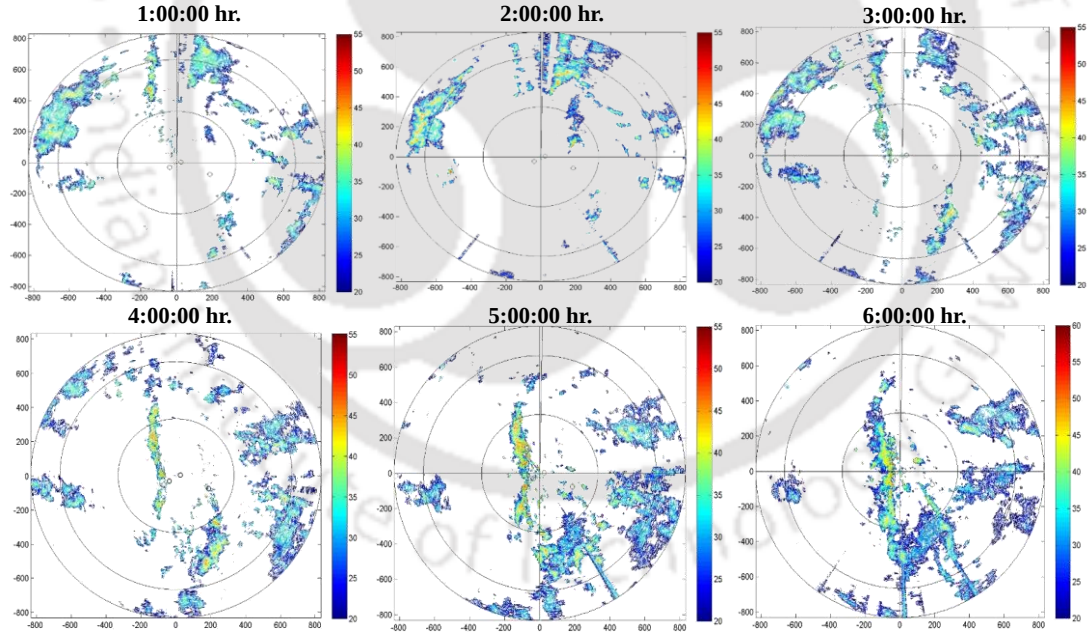

Figure A2. Plan Position Indicator (PPI) plots of 20th July, 2013 after post-processing data.

A.2 Automatic Weather Stations details

The details of Automatic Weather Station (AWS) network considered for this study which follows with in 100km of radar coverage are provided below.



Figure A3. Radar Station and AWS rain gauge network and its location (© Google Earth, Landsat)

Table A1. Radar Station and AWS rain gauge network and its location

Gauge Station	state	Latitude(^{0}N)	Longitude(^{0}E)	Distance from Radar Station (Km)	Direction from North (degree)	Elevation angle of point 1km above raingauge station, Sin(Θ)	Θ in Rad	Θ in deg	CAPPI Bins
Akshardham	Delhi	28.61	77.27	5.205	64˚25'33"	0.18491059	0.185981	10.6559	nc7
Ayanagar	Delhi	28˚29'	77˚07'	15.68	220˚59'39"	0.060559992	0.060597	3.4720	nc4
Bawal	Haryana	28.1	76.6	81.67	228˚19'24"	0.00699638	0.006996	0.4009	nc
Bhiwani	Haryana	28.8	76.1	111.9	282˚19'33"	0.002027804	0.002028	0.1162	nc
Bhopani	Haryana	28.2	77.2	43.4	182˚50'05"	0.019658293	0.01966	1.1264	nc2
Bulandeswar	UP	28.4	77.8	60.31	110˚20'46"	0.012434555	0.012435	0.7125	nc1
Delhi university	Delhi	28˚41'	77˚13'	10.41	357˚11'24"	0.09199567	0.092126	5.2784	nc5
Faridabad	Haryana	28.3	77.2	32.3	183˚48'24"	0.027945398	0.027949	1.6014	nc2
Indirpuram	UP	28.64	77.4	18.26	72˚09'23"	0.051721015	0.051744	2.9647	nc3
Jafarpur	Delhi	28.59	76.9	31.43	270˚07'03"	0.028822793	0.028827	1.6517	nc2
Jagdishpur	Haryana	29	77	50.48	334˚41'22"	0.01612601	0.016127	0.9240	nc1
Jhajjar	Haryana	28.6	76.7	50.97	271˚24'00"	0.015913568	0.015914	0.9118	nc1
Mandkola	Haryana	28.1	77	58.63	201˚47'28"	0.012991494	0.012992	0.7444	nc1
Meerut	UP	29	77.7	65.2	45˚29'31"	0.010947808	0.010948	0.6273	nc1
Mungeshpur	Delhi	28˚48'	76˚58'	34.15	313˚15'18"	0.026219601	0.026223	1.5024	nc2
Najafgarh	Delhi	28.64	77	22.37	284˚30'15"	0.041778951	0.041791	2.3945	nc3
Narela	Delhi	28.8	77.04	29.34	322˚50'31"	0.03113079	0.031136	1.7840	nc2
NCMRWF	UP	28.62	77.36	13.89	75˚58'48"	0.068588673	0.068643	3.9329	nc4
NUH	Haryana	28.1	76.99	59	202˚40'35"	0.012866595	0.012867	0.7372	nc1
Pitampura	Delhi	28˚42'	77˚09'	14.12	330˚13'19"	0.067444576	0.067496	3.8672	nc4
PUSA_Delhi_Agro	Delhi	28˚38'	77˚09'	8.526	304˚36'39"	0.112570387	0.11281	6.4635	nc6
Rohtak	Haryana	28.9	76.6	69.76	299˚47'05"	0.009712839	0.009713	0.5565	nc1
Sports complex	Delhi	28.66	77.31	11.61	47˚44'48"	0.082353088	0.082446	4.7238	nc5
Ujha_Panipat	Haryana	29.4	77	92.64	346˚34'55"	0.004952773	0.004953	0.2838	nc

Appendix B

REFLECTIVITY HYETOGRAPH PREDICTION

Abstract-TH-2793_156104035

B.1 Accuracy error matrices used for performance evaluation of propose technique

The reliability of hyetograph prediction is quantified using the Root Mean Square Error (RMSE), Nash-Sutcliffe Efficiency (NSE) metrics, mean error (BIAS), mean continuous ranked probability score (CRPS), the temporal mean of ensemble root mean squared error (MRMSE) [Perera et al., 2016]. The accuracy at the tail end of reflectivity hyetograph was analyzed using Symmetric Mean Absolute Percentage Error (sMAPE), Geometric Mean Relative Absolute Error (GMRAE) and Mean Absolute Scaled Error (MASE) [Hyndman & Koehler, 2006]. The used error matrices are listed below:

$$RMSE = \sqrt{\frac{1}{n}\sum_{t=1}^{n}\left(Z_o(t) - Z_s(t)\right)^2} \quad \text{(Eq. B1)}$$

Where n is the total number of observations, $Z_o(t)$ is the observed reflectivity depth (dBZ), and $Z_s(t)$ is the simulated reflectivity depth (dBZ) for each time step t.

The NSE [Nash & Sutcliffe, 1970] can be used to access the predictive power of the mode. The ideal value of NSE is 1. The negative value indicates that the mean of observations is a better predictor than the model.

$$NSE = 1 - \frac{\sum_{t=1}^{n}\left(Z_s(t) - Z_o(t)\right)^2}{\sum_{t=1}^{n}\left(Z_o(t) - \overline{Z_o}\right)^2} \quad \text{(Eq. B2)}$$

The mean error or BIAS is

$$BIAS = \frac{1}{n}\sum_{t=1}^{n}\left(\overline{Z_s(t)} - Z_o(t)\right) \quad \text{(Eq. B3)}$$

The mean Continuous Ranked Probability Score (CRPS)

$$MeanCRPS = \frac{1}{n}\sum_{t=1}^{n}\int_{-\infty}^{\infty}\left(F(Z_s(t)) - F(Z_o(t))\right)^2 \quad \text{(Eq. B4)}$$

$$F(Z_o(t)) = \begin{cases} 0, & Z(t) < Z_o(t) \\ 1, & Z(t) \geq Z_o(t) \end{cases} \quad \text{(Eq. B5)}$$

The temporal Mean of the no. of Predicted hyetographs Root Mean Squared Error (MRMSE)

$$MRMSE = \frac{1}{n}\sum_{t=1}^{n}\sqrt{\frac{1}{N}\sum_{i=1}^{N}\left(Z_o(t,i) - Z_s(t,i)\right)^2} \quad \text{(Eq. B6)}$$

Abstract-TH-2793_156104035

Where N is the number sample generated hyetographs. The higher score of MRMSE and mean CRPS indicates that the predictions become more error biased or the less reliable (or both), the scores leads to 0 for perfect spread or reliable.

Pearson correlation coefficient (PCC), Modified correlation coefficient or Index (rM) were also calculated for comparing predicted hyetograph with observed hyetograph. The PCC(r) is the most frequently used index for evaluating the goodness of fit between two graphs, which is inadequate for comparing observed and simulated because it is insensitive to differences in the size of the two-time series graphs. The hyetograph should be recognized as a specific example of time series, so the Modified correlation index (rM) can be used to regenerate the time series curves [MuCuen &Snyder, 1975]. In this present study, both of the indices were used for validating.

$$r = \frac{\sum_{t=1}^{n}\left(Z_o(t)-\overline{Z_o}\right)\left(Z_s(t)-\overline{Z_s}\right)}{\sqrt{\sum_{t=1}^{n}\left(Z_o(t)-\overline{Z_o}\right)^2}\sqrt{\sum_{t=1}^{n}\left(Z_s(t)-\overline{Z_s}\right)^2}} \quad \text{(Eq. B7)}$$

Where, $\bar{Z}_0$ is the mean value of observed reflectivity, and $\bar{Z}_s$ is the mean value of simulated reflectivity.

In modified correlation index (r_M) the denominator term (Z_i) depends on the size and shape of the curve.

$$r_M = \frac{\sum_{t=1}^{n}\left(Z_o(t)-\overline{Z_o}\right)\left(Z_s(t)-\overline{Z_s}\right)}{\sum_{t=1}^{n}\left(Z_i(t)-\overline{Z_i}\right)^2} \quad \text{(Eq. B8)}$$

$Z_i \to Z_o$ If the simulated curve is underpredicted than observed.

$Z_i \to Z_s$ If the simulated curve is overpredicted than observed.

Correlation coefficient ranges from -1 to 1. The ideal value of r and rM is 1. Zero value indicates no correlation between data.

Percentage Error (% Error):

$$\%Error = \frac{\left|Z_s(t)-Z_o(t)\right|}{\left|Z_o(t)\right|}\times 100 \quad \text{(Eq. B9)}$$

Abstract-TH-2793_156104035

Symmetric Mean Absolute Percentage Error (sMAPE):

$$sMAPE = \frac{200}{n} \times \sum_{t=1}^{n} \frac{\left|Z_s(t) - Z_o(t)\right|}{\left|Z_o(t)\right| + \left|Z_s(t)\right|} \quad \text{(Eq. B10)}$$

Geometric Mean Relative Absolute Error (GMRAE):

$$r_t = \left| \frac{Z_o(t) - Z_s(t)}{Z_o(t) - Z_s(t)^*} \right| \quad \text{(Eq. B11)}$$

Where $Z_s(t)^*$ is the simulated error observed with respect to the benchmark. The value can be obtained by benchmark method, which is the random walk where simulated values are equal to the last observation or using Naïve forecast model as a benchmark.

$$GMRAE = \sqrt[n]{\prod \left| \frac{Z_o(t) - Z_s(t)}{Z_o(t) - Z_s(t)^*} \right|} \quad \text{(Eq. B12)}$$

Mean Absolute Scaled Error (MASE):

$$MASE = \frac{1}{n} \times \sum_{t=1}^{n} \left(\frac{\left|Z_s(t) - Z_o(t)\right|}{\frac{1}{T-m} \sum_{t=m+1}^{n} \left|Z_o(t) - Z_o(t-1)\right|} \right) \quad \text{(Eq. B13)}$$

Where m is the seasonal period, which is 1 for non-seasonal time series.

B.2 Decomposition of random variables for generating random numbers using Cholesky decomposition

X is an n-dimensional random vector matrix, then

$$X_n = LZ_n \quad \text{(Eq. B14)}$$

$$cov(X_n, X_n^T) = \Delta_x \quad \text{(Eq. B15)}$$

For special and more efficient triangular decomposition, the square matrix Δx to be symmetric and positive definite. Cholesky decomposition [Huynh et al., 2008; Press et al., 2007] constructs a lower triangular matrix L and upper triangular matrix as the transpose of lower triangular matrix L^T. In other words

$$cov(X_n, X_n^T) = \Delta_x = LL^T \quad \text{(Eq. B16)}$$

Then L matrix can subsequently be obtained with the decomposition of LL^T of Δx.

Abstract-TH-2793_156104035

B.3 Linear and Nonlinear interdependency between variables.

The Pearson correlation matrix and Spearman rank coefficient matrix computed and plotted to check the linear and nonlinear interdependency between random variables.

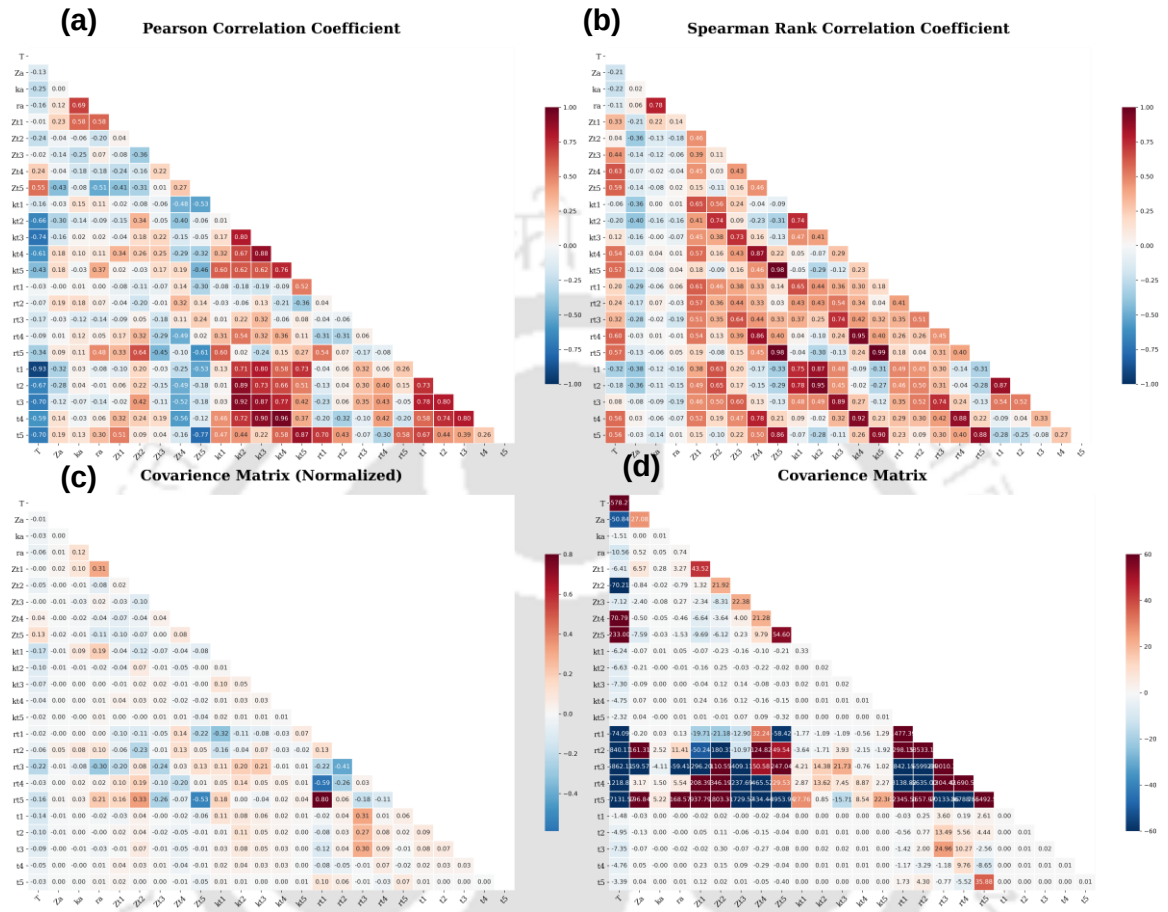

Figure B1. (a) Pearson Correlation matrix (linear); (b) Spearman Correlation matrix (nonlinear); (c) Covariance matrix (Normalized average); (d) Covariance matrix

Abstract-TH-2793_156104035

B.4 Regression equations for fitted parameters and variables to generate random numbers

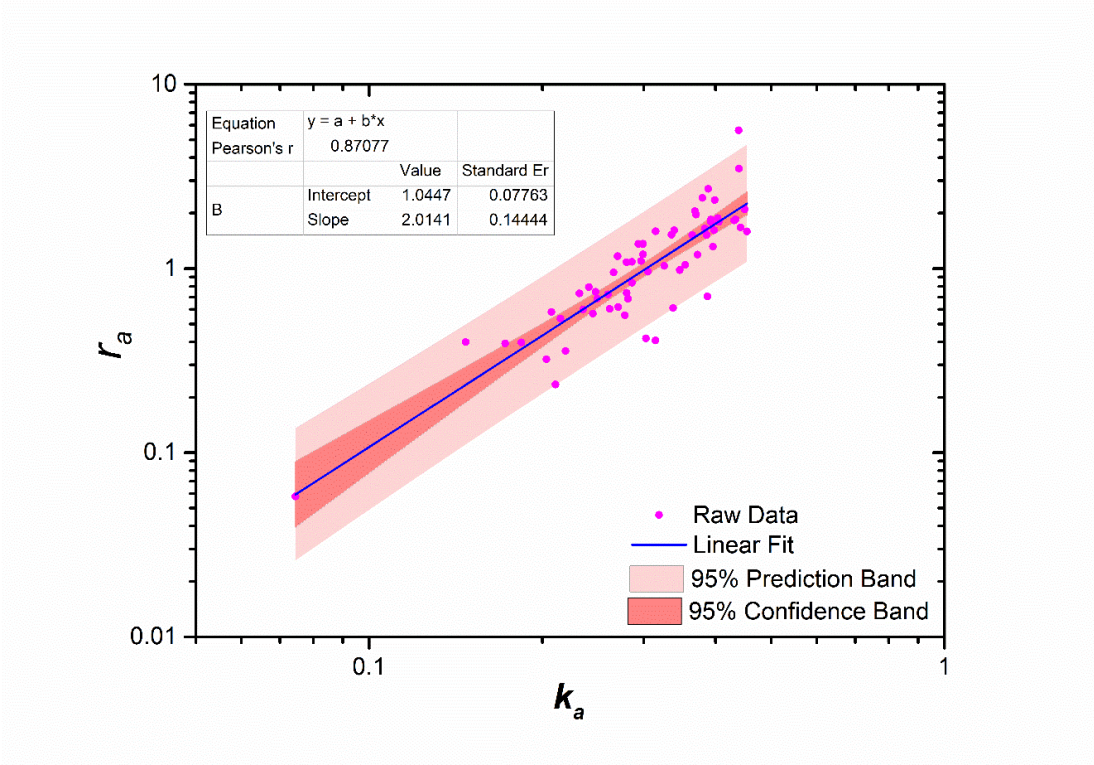

Figure B2. The regression fit between atmospheric wave fitted parameters K_a and r_a.

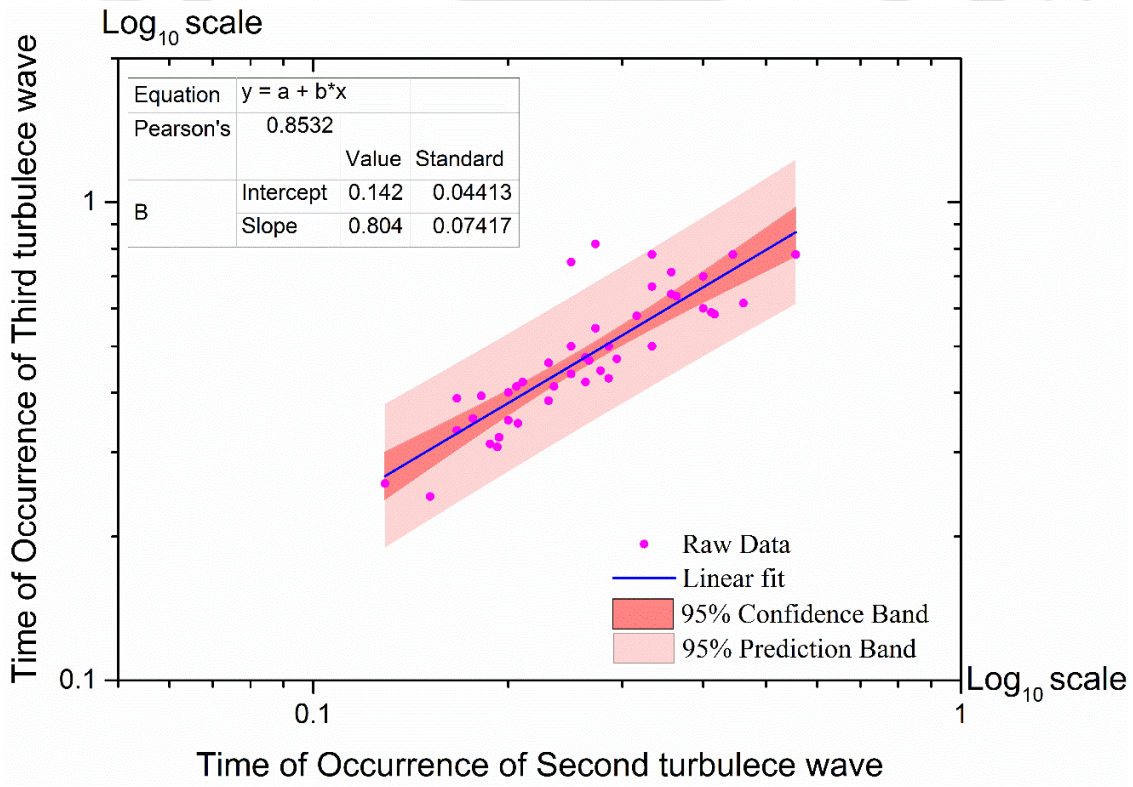

Figure B3. The regression fit between time of occurrence of second and third turbulence waves with 95% confidence and prediction bands.

Abstract-TH-2793_156104035

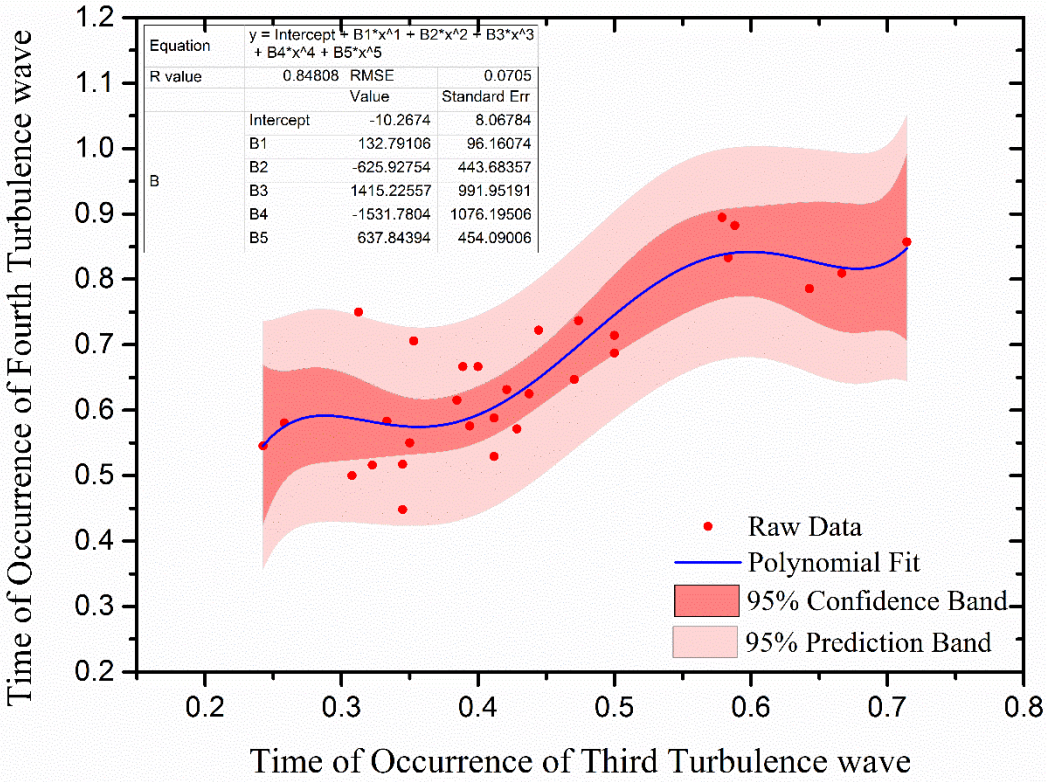

Figure B4. The regression fit between time of occurrence of third and fourth turbulence waves with 95% confidence and prediction bands.

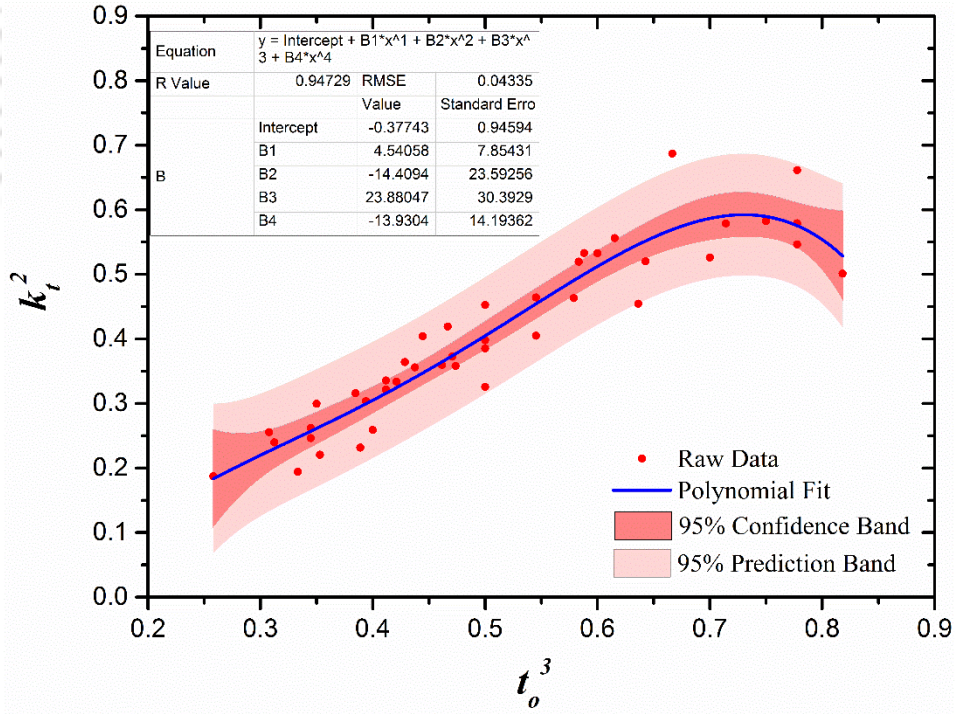

Figure B5. The regression fit between time of occurrence of third turbulence wave ($\mathbf{t_0^3}$) and second turbulence wave fitted parameter ($\mathbf{k_t^2}$) with 95% confidence and prediction bands.

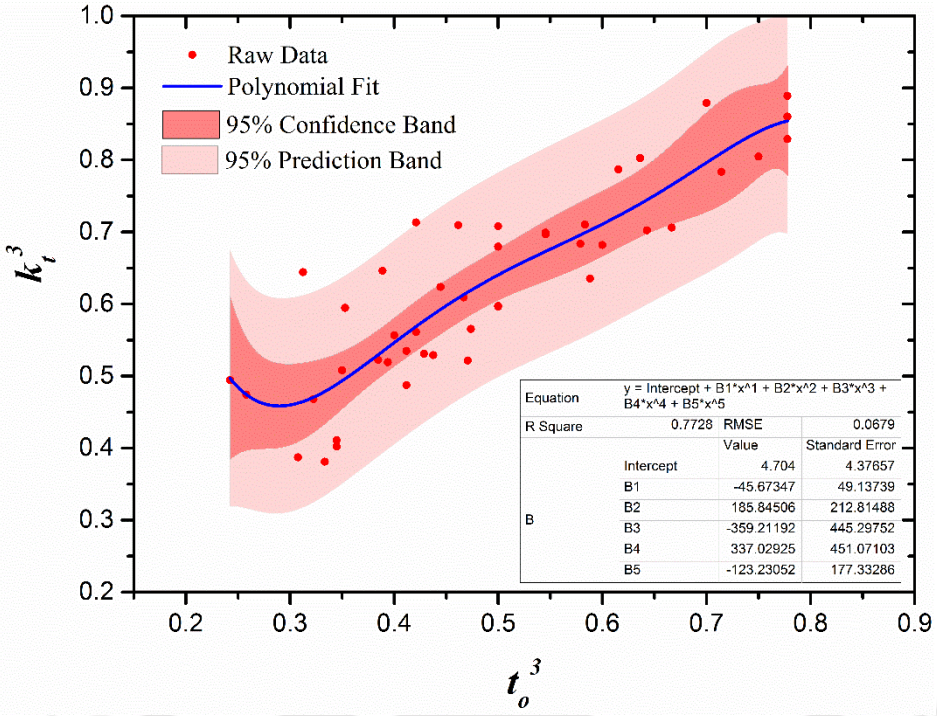

Figure B6. The regression fit between time of occurrence of third turbulence wave ($\mathbf{t_0^3}$) and third turbulence wave fitted parameter ($\mathbf{k_t^3}$) with 95% confidence and prediction bands.

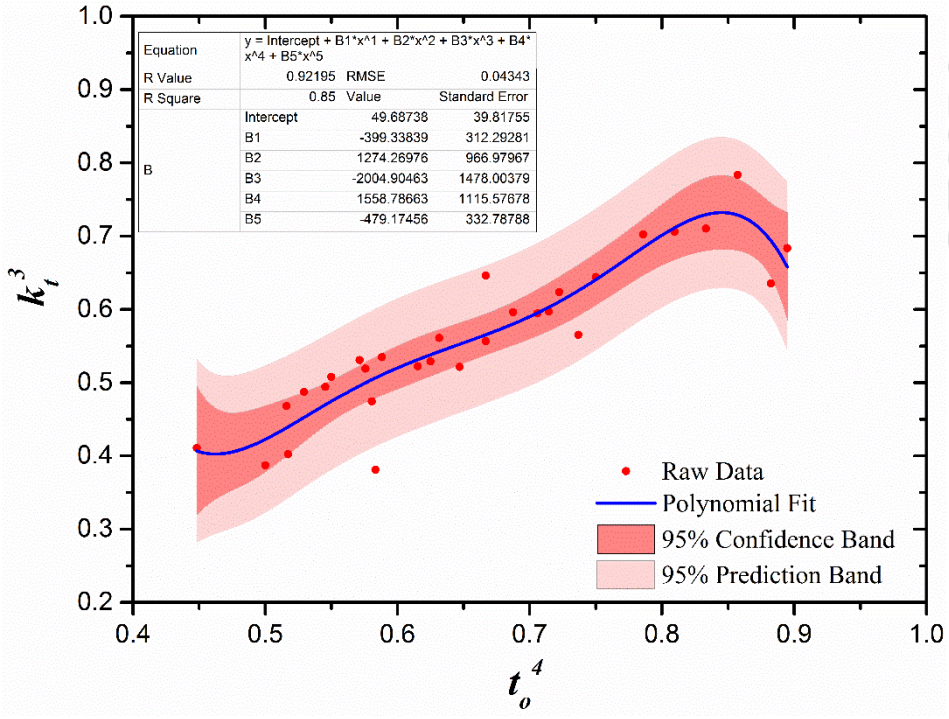

Figure B7. The regression fit between time of occurrence of fourth turbulence wave ($\mathbf{t_0^4}$) and third turbulence wave fitted parameter ($\mathbf{k_t^3}$) with 95% confidence and prediction bands.

Abstract-TH-2793_156104035

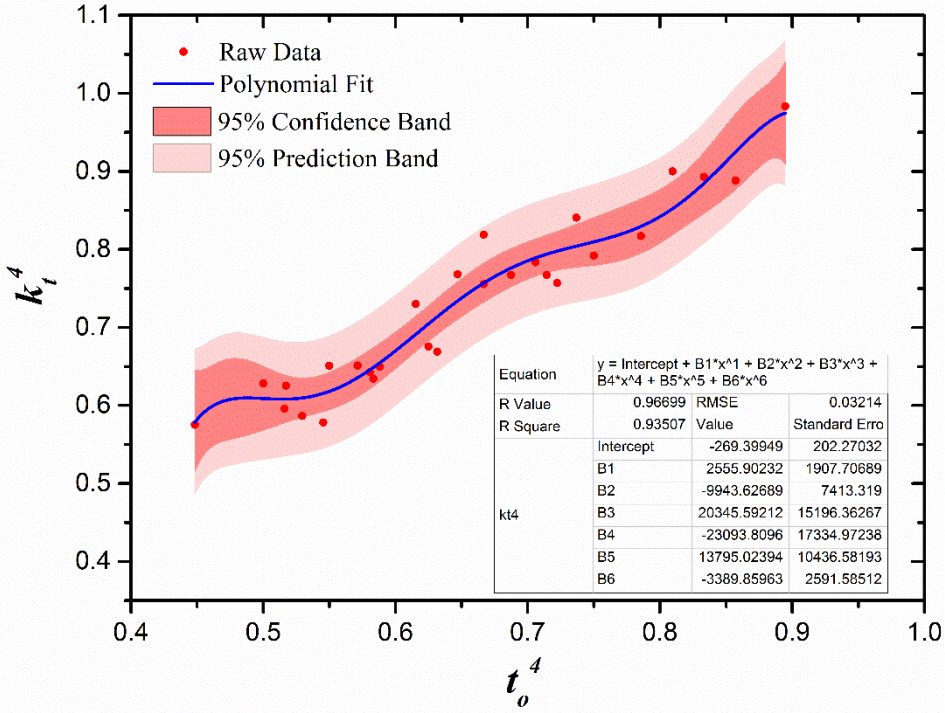

Figure B8. The regression fit between time of occurrence of fourth turbulence wave ($\mathbf{t_0^4}$) and fourth turbulence wave fitted parameter ($\mathbf{k_t^4}$) with 95% confidence and prediction bands.

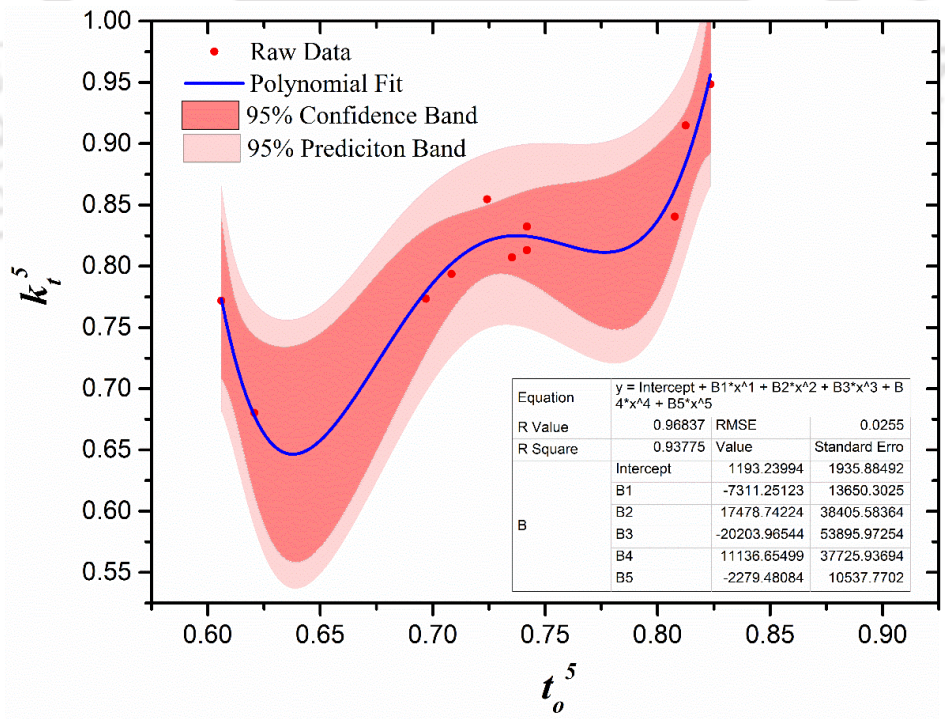

Figure B9. The regression fit between time of occurrence of fifth turbulence wave ($\mathbf{t_0^5}$) and fifth turbulence wave fitted parameter ($\mathbf{k_t^5}$) with 95% confidence and prediction bands.

Abstract-TH-2793_156104035

Table B1: Statistical metrics for prediction performance of generated hyetographs with a random number generated from the parent distributions.

Sample Size	Statistical Verification Score	Storm Duration (min)			
		70	120	190	310
n = 2	RMSE (mean) dBZ	6.06 (2.42)	5.03 (3.11)	6.64 (4.66)	7.07 (6.52)
	NSE (mean)	0.63 (0.75)	0.79 (0.79)	0.63 (0.71)	0.66 (0.71)
	BIAS (mean) dBZ	1.07	-3.71	1.58	-1.78
	Mean CRPS dBZ	2.09	4.11	4.81	3.17
	MRMSE dBZ	5.59	4.32	5.84	6.64
n = 3	RMSE (mean) dBZ	5.54 (1.71)	5.47 (2.82)	4.68 (2.93)	6.70 (6.24)
	NSE (mean)	0.67 (0.87)	0.73 (0.83)	0.82 (0.88)	0.69 (0.73)
	BIAS (mean) dBZ	-0.78	0.81	0.62	-1.72
	Mean CRPS dBZ	2.33	3.90	2.06	4.71
	MRMSE dBZ	5.64	4.98	4.14	5.28
n = 5	RMSE (mean) dBZ	4.35 (1.48)	5.35 (2.65)	6.17 (2.73)	7.42 (5.81)
	NSE (mean)	0.81 (0.91)	0.75 (0.85)	0.67 (0.90)	0.61 (0.77)
	BIAS (mean) dBZ	-0.32	-0.24	-1.12	-1.41
	Mean CRPS dBZ	1.55	2.76	2.36	4.08
	MRMSE dBZ	4.10	4.87	5.61	6.90
n = 7	RMSE (mean) dBZ	5.88 (1.43)	4.84 (1.94)	6.18 (2.44)	7.11 (4.75)
	NSE (mean)	0.64 (0.91)	0.78 (0.92)	0.66 (0.92)	0.64 (0.85)
	BIAS (mean) dBZ	0.68	-0.55	1.56	0.01
	Mean CRPS dBZ	1.90	2.19	1.85	3.33
	MRMSE dBZ	5.99	4.77	5.67	6.73
n = 8	RMSE (mean) dBZ	6.75 (1.37)	5.68 (1.81)	5.66 (2.57)	7.19 (4.70)
	NSE (mean)	0.54 (0.92)	0.70 (0.93)	0.73 (0.91)	0.63 (0.85)
	BIAS (mean) dBZ	-0.81	0.22	0.30	-3.25
	Mean CRPS dBZ	2.52	2.57	2.35	3.79
	MRMSE dBZ	6.85	5.64	5.34	6.74
	RMSE (mean) dBZ	5.23 (1.28)	3.84 (1.90)	5.74 (2.33)	7.01 (4.60)

n = 10	NSE (mean)	0.72 (0.93)	0.87 (0.92)	0.71 (0.93)	0.65 (0.86)
	BIAS (mean) dBZ	-1.24	0.05	1.83	-1.90
	Mean CRPS dBZ	1.75	2.17	2.13	2.66
	MRMSE dBZ	5.21	3.21	5.41	6.69
n = 15	RMSE (mean) dBZ	5.72 (1.17)	5.32 (1.66)	6.24 (1.84)	7.86 (4.40)
	NSE (mean)	0.66 (0.94)	0.75 (0.94)	0.66 (0.95)	0.57 (0.87)
	BIAS (mean) dBZ	-0.30	1.04	1.66	-1.69
	Mean CRPS dBZ	1.72	2.47	2.26	3.93
	MRMSE dBZ	5.78	5.24	6.19	7.47
n = 20	RMSE (mean) dBZ	5.59 (1.11)	6.06 (1.74)	6.83 (2.19)	6.72 (3.96)
	NSE (mean)	0.68 (0.95)	0.67 (0.93)	0.60 (0.94)	0.68 (0.89)
	BIAS (mean) dBZ	-1.08	0.46	1.99	-1.30
	Mean CRPS dBZ	1.79	2.24	1.99	2.82
	MRMSE dBZ	5.68	6.01	6.85	6.49

*average values are given; **The value given in bracket is the 5% confidence value for RMSE and 95% confidence value for NSE

B.5 Evaluation with cumulative distribution curves, ran histograms and tail end error analysis

Cumulative distribution of simulated with observed reflectivity hyetograph and rank histogram approach were performed to estimate the limit of error and to evaluate the reliability of model respectively. Considering the random nature of atmospheric lift, turbulence lifts and time of occurrence of turbulence waves, storm hyetographs for 70, 120, 190 and 310min duration were generated. The obtained Chi-squares values 7.75, 10.76, 5.97 and 4.05 for 70, 120, 190, and 310-min storm duration were above the lower limit of 2.73 and much below the upper limit of 15.5 with an acceptance level at 8˚ of freedom and 95% confidence limit [Kreyszig, 2010]. The ranges of cumulative probability between simulated and observed were in acceptable range and rank histograms are shown graphically in Figure B.9. The rank histogram for all durations shows that the generated samples were evenly spread (flat rank histogram), which indicates the developed methodology is reliable. Overall, aforementioned results suggest that the proposed approach provides a satisfactory prediction of storm reflectivity hyetograph for forecasting flash floods.

Abstract-TH-2793_156104035

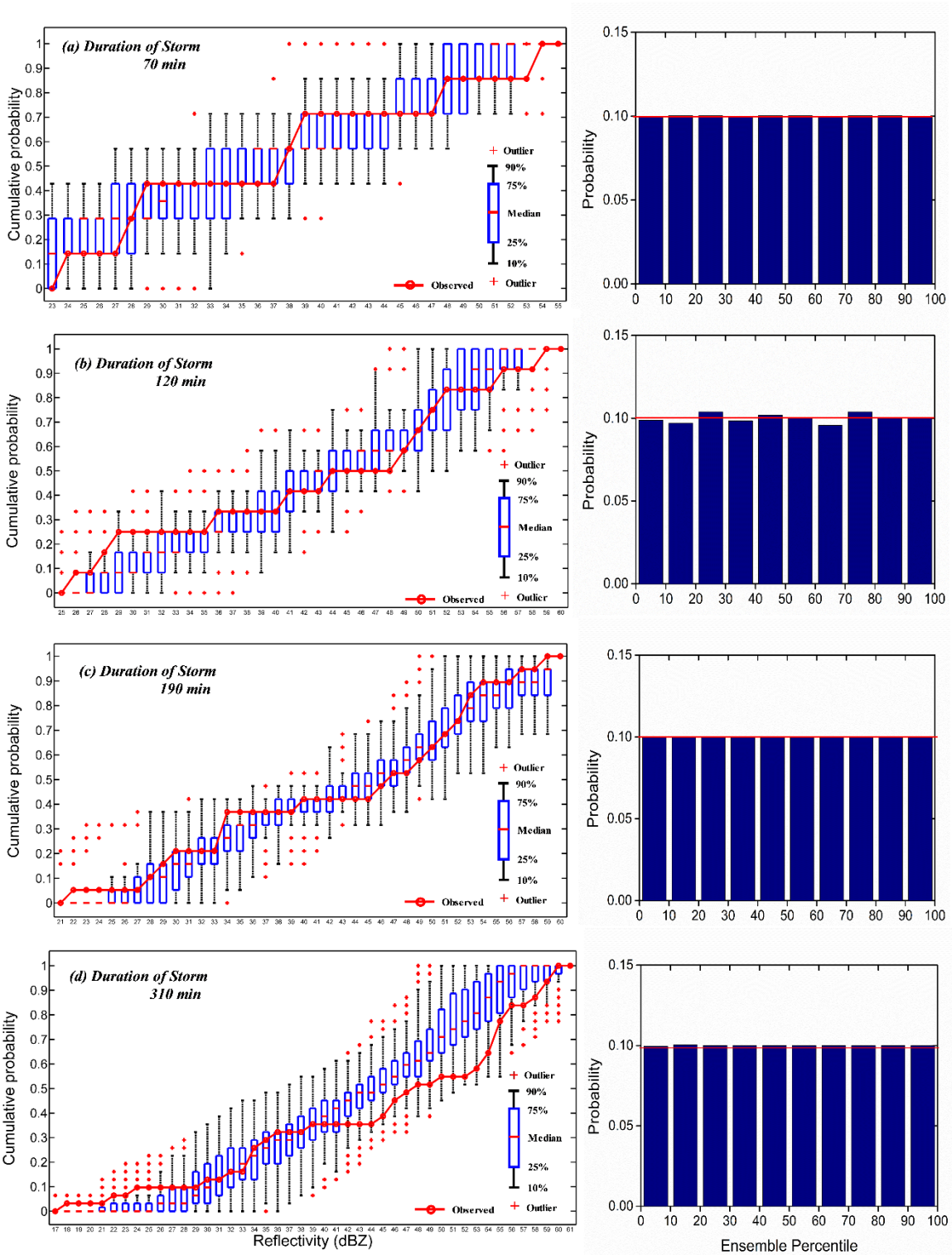

Figure B9. Evaluation of the proposed method at different storm duration groups: Cumulative frequency function for storm durations (a) 70min, (b) 90min, (c) 120min and (d) 310min.

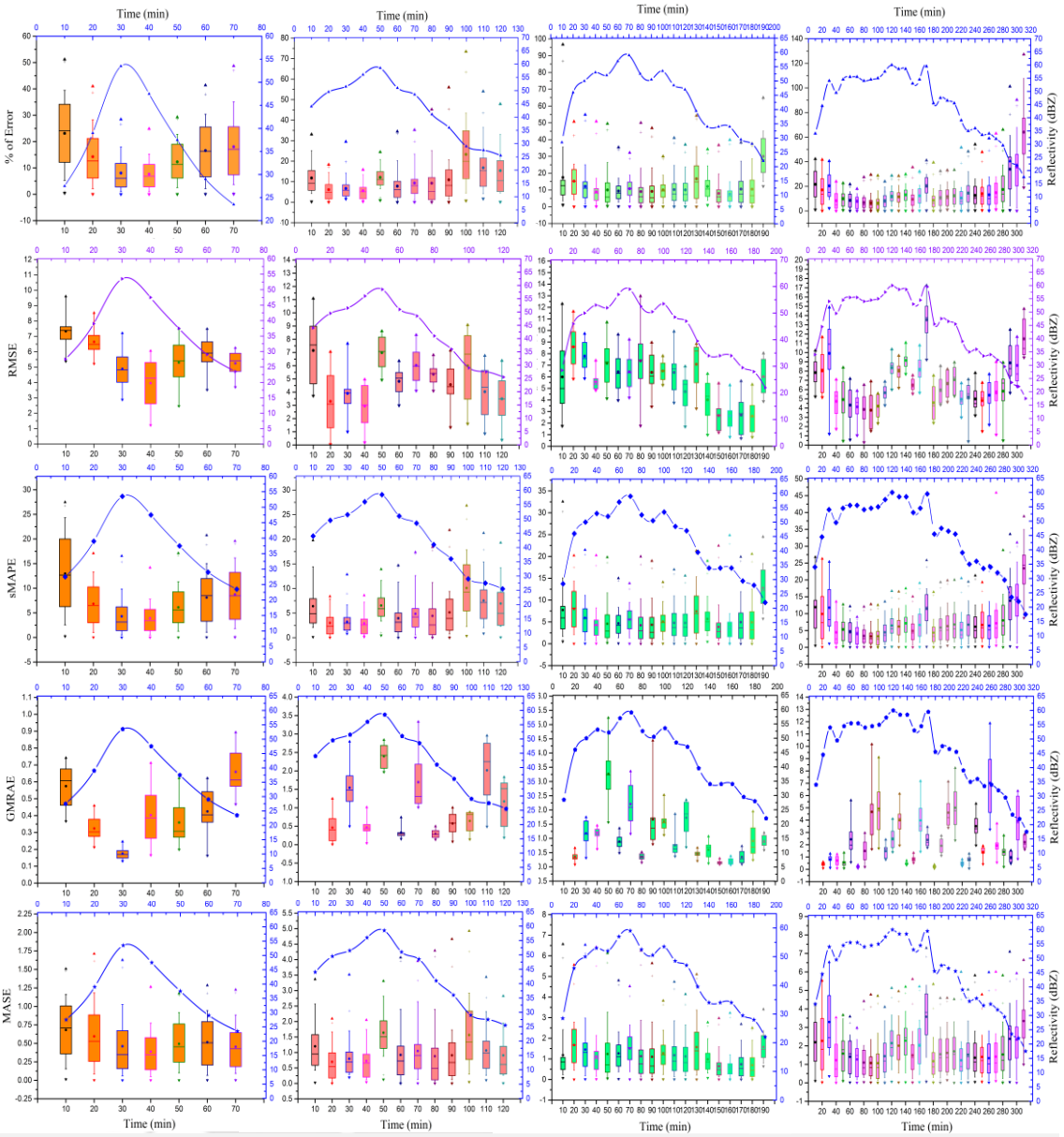

RMSE – Root Mean Squared Error
sMAPE – Symmetric Mean Absolute Percentage Error
GMRAE – Geometric Mean Relative Absolute Error
MASE – Mean Absolute Scaled Error [*Hyndman and Koehler,* 2006]

Figure B10. Tail end error analysis at each time step throughout the reflectivity hyetographs

Abstract-TH-2793_156104035

This Page Intentionally Left Blank

Abstract-TH-2793_156104035

Appendix C

ASSESSMENT OF OPEN-SOURCE DEMS

Abstract-TH-2793_156104035

C.1 Description of Selected DEMs

ALOS

The both ALOS AW3D and ALOS 12.5 considered here are the product of Advanced Land Observing Satellite (ALOS) launched by the Japan Aerospace Exploration Agency (JAXA). The optical sensor PRISM (Panchromatic Remote-sensing Instrument for Stereo Mapping) and microwave sensor PALSAR (Phased Array type L-band Synthetic Aperture Radar) onboard the ALOS satellite on 2006 for generating ALOS AW3D 30m and ALOS 12.5m respectively. The detailed description of ALOS products is given by Tadono et al. (2014) and Das et al. (2015).

ASTER

A Japanese optical and Near Infra-Red Sensor Advanced Spaceborne Thermal and Emission and Reflection Radiometer (ASTER) was onboard the Terra Satellite launched in 1999 by NASA. ASTER GDEM provides maximum spatial resolution of 30m. The more detailed description of ASTER is given by Tachikawa et al. (2011).

CARTOSAT

Cartosat-1 is an Indian satellite launched under Indian Remote Sensing programme with optical sensor onboard in 2005 by ISRO. It provides the high-resolution DEM of 5m commercially and 30m spatial resolution for open access. The more specifications of the product are given by Muralikrishnan et al. (2013).

EU-DEM

It is a hybrid data product by a fusion of SRTM, ASTER GDEM and other sources. It provides Pan-European topographic data at 30m (1 arc-second) interval spatial resolution. Mainly it covers 33-member states and 6 cooperating states of European Union. The other specifications and fusion techniques of data can be found in Bashfield and Keim (2011); Gras (2014); Florinsky et al. (2019).

NED

The National Elevation Dataset (NED) is a data of the Contiguous United States and other US territories. It is primary elevation product developed by the U.S. Geological Survey (USGS) derived from many sources of data sets. It provides the data at 1m, 1/9, 1/3, and 1 arc-second interval of spatial resolution. Other details like its background and preparation given by Gesch et al. (2002).

SRTM

The Shuttle Radar Topography Mission was widely used DEM for flood mapping and processes. Two C-band and X-band sensor systems onboard on the STS-99 Endeavour Space Shuttle in 2000. In this study a C-band, generated DEM used to evaluate in the

Abstract-TH-2793_156104035

context of urban flood mapping. The more details of SRTM missioned data is given by Farr et al. (2007).

C.2 Descriptive Statistics Tables of Elevations

DEM	Minimum	Maximum	Range	Mean	Median	Std dev	skew	kurt	p25	p75
Surveyed	776.44	1285.42	508.98	898.49	871.39	83.50	1.46	4.80	841.64	934.24
NED 10m	786.01	1261.80	475.79	898.94	871.99	83.75	1.42	4.67	839.84	935.88
NED 30m	786.01	1248.00	461.99	897.63	871.16	82.63	1.42	4.65	839.38	933.58
SRTM 30m	793.96	1253.30	459.34	905.16	879.27	80.36	1.43	4.68	849.74	938.32
ASTER 30m	748.03	1230.30	482.27	875.86	849.74	83.72	1.41	4.71	816.93	912.07
ALOS AW3D 30m	784.12	1279.50	495.38	905.41	879.27	83.21	1.44	4.77	849.74	941.60
ALOS 12.5m	787.40	1279.50	492.10	899.90	872.70	84.97	1.42	4.67	839.90	938.32

Table C1. Descriptive statistics of Elevation - Simi Valley Urban, California.

DEM	Minimum	Maximum	Range	Mean	Median	Std dev	skew	kurt	p25	p75
Surveyed	338.20	344.60	6.40	341.66	341.49	1.22	0.09	2.56	340.82	342.62
SRTM 30m	338.00	347.00	9.00	342.53	342.00	1.89	0.02	2.74	341.00	344.00
ASTER 30m	338.00	354.00	16.00	344.88	344.00	3.35	0.23	2.40	342.00	348.00
ALOS AW3D 30m	340.00	350.00	10.00	344.92	345.00	1.98	0.27	2.80	343.25	346.00
EU-DEM	340.62	349.18	8.56	343.95	343.36	1.97	0.71	2.85	342.75	345.19
EU-DEM 1.1	340.40	349.54	9.14	344.10	343.57	2.11	0.65	2.77	342.76	345.46

Table C2. Descriptive statistics of Elevation – Riom City, France.

DEM	Minimum	Maximum	Range	Mean	Median	Std dev	skew	kurt	p25	p75
Surveyed	207.00	218.95	11.95	213.37	213.79	1.48	-1.53	7.48	212.63	214.22
SRTM 30m	202.00	237.00	35.00	218.16	218.00	3.73	-0.08	4.01	216.00	220.00
ASTER 30m	191.00	254.00	63.00	218.01	218.00	8.17	0.27	4.13	213.00	223.00
ALOS AW3D 30m	206.00	236.00	30.00	217.33	217.00	3.84	0.49	3.83	215.00	220.00
ALOS 12.5m	200.43	236.43	36.00	218.25	218.43	3.73	-0.10	3.97	216.43	220.43
CARTOSAT 30m	208.43	237.43	29.00	221.09	221.43	3.63	0.03	3.77	218.43	223.43

Table C3. Descriptive statistics of Elevation – New Delhi, India.

DEM	Minimum	Maximum	Range	Mean	Median	Std dev	skew	kurt	p25	p75
SRTM 30m	868.00	961.00	93.00	904.28	905.00	15.46	0.14	2.67	893.00	914.00
ASTER 30m	838.00	962.00	124.00	904.49	904.00	17.70	0.09	2.81	893.00	916.00
ALOS AW3D 30m	864.00	963.00	99.00	905.64	905.00	15.46	0.18	2.82	895.00	915.00
ALOS 12.5m	866.30	962.30	96.00	904.11	904.30	15.50	0.12	2.66	893.30	914.30
CARTOSAT 30m	871.30	959.30	88.00	906.20	906.30	15.46	0.21	2.73	895.30	916.30

Table C4. Descriptive statistics of Elevation – Bangalore, India.

DEM	Minimum	Maximum	Range	Mean	Median	Std dev	skew	kurt	p25	p75
Surveyed	100.40	104.79	4.39	102.82	102.73	1.05	0.21	1.84	101.87	103.72
SRTM 30m	99.00	105.00	6.00	102.24	103.00	1.30	-0.29	2.80	101.00	103.00
ASTER 30m	85.00	106.00	21.00	96.03	96.00	6.14	-0.13	2.01	91.00	101.00
ALOS AW3D 30m	101.00	105.00	4.00	103.18	103.00	0.81	-0.34	3.46	103.00	104.00
ALOS 12.5m	98.71	104.71	6.00	102.02	102.71	1.40	-0.42	2.80	100.71	102.71
CARTOSAT 30m	101.71	107.71	6.00	103.55	103.71	1.46	0.33	3.03	101.71	104.71

Table C5. Descriptive statistics of Elevation – Jorhat, India.

Abstract-TH-2793_156104035

DEM	Minimum	Maximum	Range	Mean	Median	Std dev	skew	kurt	p25	p75
Surveyed	47.10	54.49	7.39	48.77	48.85	0.60	2.16	17.04	48.39	49.07
SRTM 30m	45.00	55.00	10.00	49.20	49.00	1.53	-0.02	3.06	48.00	50.00
ASTER 30m	25.00	58.00	33.00	42.59	42.00	5.31	0.06	3.13	39.00	46.00
ALOS AW3D 30m	45.00	56.00	11.00	47.89	48.00	1.25	1.94	12.22	47.00	48.00
ALOS 12.5m	45.44	56.44	11.00	49.23	48.44	1.63	0.54	3.01	48.44	50.44
CARTOSAT 30m	46.44	57.44	11.00	50.26	50.44	1.28	1.39	7.59	49.44	50.44

Table C6. Descriptive statistics of Elevation – Pachoria, Guwahati, India.

C.3 Descriptive Statistics Tables of Slopes

DEM	Minimum	Maximum	Range	Mean	Median	Std dev	skew	kurt	p25	p75
Surveyed	0.00	67.20	67.20	3.50	1.76	5.01	4.16	27.97	1.07	3.75
SRTM 30m	0.00	5.27	5.27	1.45	1.23	0.99	0.98	4.73	0.80	2.09
ASTER 30m	0.39	15.12	14.73	3.98	3.58	2.54	1.45	6.19	2.14	4.98
ALOS AW3D 30m	0.00	3.88	3.88	1.49	1.40	0.92	0.44	2.64	0.87	2.09
EU-DEM	0.08	2.49	2.40	1.06	1.06	0.52	0.34	2.72	0.62	1.39
EU-DEM 1.1	0.08	3.78	3.71	1.18	1.11	0.72	0.74	3.64	0.58	1.66

Table C7. Descriptive statistics of slopes – Riom City, France.

DEM	Minimum	Maximum	Range	Mean	Median	Std dev	skew	kurt	p25	p75
Surveyed	0.00	38.33	38.33	1.35	0.57	2.92	5.66	42.24	0.26	1.18
SRTM 30m	0.00	15.11	15.11	3.24	2.76	2.05	1.25	5.40	1.75	4.35
ASTER 30m	0.00	33.50	33.50	6.37	5.60	4.03	1.55	7.91	3.49	8.51
ALOS AW3D 30m	0.00	19.49	19.49	3.31	2.76	2.40	1.51	7.17	1.45	4.59
ALOS 12.5m	0.00	21.72	21.72	4.16	4.04	2.62	1.14	5.63	2.29	5.42
CARTOSAT 30m	0.00	15.71	15.71	2.83	2.42	1.86	1.58	7.34	1.45	3.70

Table C8. Descriptive statistics of slopes – New Delhi, India.

Abstract-TH-2793_156104035

DEM	Minimum	Maximum	Range	Mean	Median	Std dev	skew	kurt	p25	p75
Surveyed	0.00	83.74	83.74	8.46	4.79	9.11	1.66	5.40	2.07	11.49
NED 10m	0.00	41.29	41.29	5.67	1.51	7.27	1.51	4.47	0.65	9.02
NED 30m	0.01	28.76	28.75	4.83	1.50	5.94	1.46	4.24	0.64	7.63
SRTM 30m	0.00	28.03	28.03	4.17	2.27	4.35	1.67	5.40	1.14	5.73
ASTER 30m	0.00	32.33	32.33	5.65	4.09	4.70	1.70	6.22	2.41	7.36
ALOS AW3D 30m	0.00	35.67	35.67	4.95	2.30	5.52	1.66	5.33	1.14	6.95
ALOS 12.5m	0.00	35.59	35.59	5.72	2.43	7.18	1.39	4.03	0.00	9.16

Table C9. Descriptive statistics of slopes - Simi Valley Urban, California.

DEM	Minimum	Maximum	Range	Mean	Median	Std dev	skew	kurt	p25	p75
SRTM 30m	0.00	17.88	17.88	2.70	2.40	1.68	1.22	6.23	1.47	3.62
ASTER 30m	0.00	36.77	36.77	6.98	6.31	4.11	0.94	4.29	3.96	9.34
ALOS AW3D 30m	0.00	41.05	41.05	3.48	2.65	3.16	2.77	16.23	1.47	4.47
ALOS 12.5m	0.00	37.78	37.78	3.37	3.24	2.21	1.32	9.24	2.29	4.57
CARTOSAT 30m	0.00	28.41	28.41	3.64	2.96	2.82	1.94	9.31	1.68	4.78

Table C10. Descriptive statistics of slopes – Bangalore, India.

DEM	Minimum	Maximum	Range	Mean	Median	Std dev	skew	kurt	p25	p75
Surveyed	0.01	56.38	56.37	7.17	5.83	6.24	1.44	6.62	2.09	10.61
SRTM 30m	0.00	4.11	4.11	1.53	1.45	1.01	0.57	2.60	0.64	2.20
ASTER 30m	2.42	14.30	11.88	8.23	7.66	3.41	0.32	1.99	5.31	10.77
ALOS AW3D 30m	0.34	2.42	2.08	0.98	0.97	0.59	1.10	3.46	0.49	1.08
ALOS 12.5m	0.00	6.50	6.50	2.12	2.29	1.69	0.51	2.64	0.81	3.24
CARTOSAT 30m	0.34	4.01	3.67	1.39	0.77	1.16	1.07	2.84	0.49	2.22

Table C11. Descriptive statistics of slopes – Jorhat, India.

Abstract-TH-2793_156104035

DEM	Minimum	Maximum	Range	Mean	Median	Std dev	skew	kurt	p25	p75
Surveyed	0.00	19.54	19.54	0.58	0.31	0.82	4.90	50.81	0.18	0.60
SRTM 30m	0.00	5.31	5.31	1.64	1.53	0.90	0.81	3.93	1.03	2.17
ASTER 30m	0.00	15.23	15.23	5.39	5.05	2.90	0.66	3.12	3.16	7.20
ALOS AW3D 30m	0.00	5.51	5.51	1.15	1.03	0.77	1.92	9.50	0.69	1.45
ALOS 12.5m	0.00	8.84	8.84	2.32	2.29	2.00	0.39	2.13	0.00	4.04
CARTOSAT 30m	0.00	5.34	5.34	0.80	0.77	0.76	1.80	9.24	0.34	1.08

Table C12. Descriptive statistics of slopes – Pachoria, Guwahati, India.

C.4 Descriptive Statistics Table of Contour Lines

Study Area	DEM	Length (m)	Count
Simi Valley, USA (2*ft* contour interval)	Surveyed 1ft	6034041.02	44035
	NED 10 m	3930263.74	1141
	NED 30 m	3596778.50	1070
	SRTM 30 m	3035469.63	1070
	ASTER 30 m	4407664.24	2289
	ALOS AW3D 30 m	4020967.93	1892
	ALOS 12.5 m	4066390.08	1175
Riom, France (0.5m contour interval)	Surveyed 1m	10568.92	214
	SRTM 30 m	5926.96	26
	ASTER 30 m	18580.29	115
	ALOS AW3D 30 m	5830.28	32
	EU-DEM 25 m	3406.76	18
	EU-DEM v.1.1 25 m	3926.91	23
Ashok Vihar, New Delhi, India (0.5m contour interval)	Surveyed 1m	168832.53	920
	SRTM 30 m	470048.35	1210
	ASTER 30 m	953311.93	2584
	ALOS AW3D 30 m	595406.68	2081
	ALOS 12.5m	505111.34	1278
	CARTOSAT 30m	433774.09	1483
Challagatta Valley, Bangalore, India (0.5m contour interval)	SRTM 30 m	4390515.45	6794
	ASTER 30 m	11893036.22	27606
	ALOS AW3D 30 m	6926649.94	19314
	ALOS 12.5m	4777392.82	7565
	CARTOSAT 30m	7300047.75	23445
Jorhat, India (0.1m contour interval)	Surveyed 0.9 m	30200.50	703
	SRTM 30 m	7950.43	100
	ASTER 30 m	40582.65	461
	ALOS AW3D 30 m	5607.07	168
	ALOS 12.5m	11001.22	113

Abstract-TH-2793_156104035

	CARTOSAT 30m	7968.14	90
Pachoria, Guwahati, India (0.5m contour interval)	Surveyed 0.9 m	9699.40	56
	SRTM 30 m	34320.84	131
	ASTER 30 m	110756.45	451
	ALOS AW3D 30 m	29945.00	138
	ALOS 12.5m	41199.36	163
	CARTOSAT 30m	17356.22	74

Table C13. Total length (m) and count of contour lines for each DEM at all study areas.

C.5 Descriptive Statistics Tables of DoDs

DEM	Minimum	Maximum	Range	Mean	Median	Std dev	skew	kurt	p25	p75
NED 10m	-66.37	73.45	139.82	-0.35	0.41	10.46	-0.52	8.11	-2.99	3.04
NED 30m	-88.53	89.83	178.36	1.07	0.99	13.32	-0.20	9.78	-2.18	3.91
SRTM 30m	-92.15	59.80	151.96	-6.46	-7.79	10.45	0.89	8.15	-11.50	-3.59
ASTER 30m	-65.06	106.55	171.61	23.14	22.17	15.08	0.23	4.43	13.95	31.59
ALOS AW3D 30m	-72.92	46.33	119.25	-6.08	-6.55	7.36	0.37	9.10	-9.43	-4.17
ALOS 12.5m	-74.26	56.11	130.37	-1.08	0.28	9.53	-0.81	6.97	-3.82	2.94

Table C14. Simi Valley statistics of difference in elevation: surveyed (1ft) - DEMs

DEM	Minimum	Maximum	Range	Mean	Median	Std dev	skew	kurt	p25	p75
SRTM 30m	-4.83	3.63	8.46	-0.79	-0.43	1.64	-0.26	2.10	-2.21	0.40
ASTER 30m	-11.00	4.54	15.54	-2.95	-2.78	2.82	-0.22	2.50	-5.01	-0.80
ALOS AW3D 30m	-7.60	1.44	9.04	-3.14	-2.82	1.70	-0.41	2.23	-4.45	-1.82
EU-DEM	-5.51	1.32	6.83	-2.10	-2.10	1.63	-0.07	1.75	-3.50	-0.60
EU-DEM 1.1	-5.86	1.03	6.89	-2.23	-2.00	1.59	-0.28	1.91	-3.55	-0.83

Table C15. Riom statistics of difference in elevation: surveyed (1m) - DEMs

Abstract-TH-2793_156104035

DEM	Minimum	Maximum	Range	Mean	Median	Std dev	skew	kurt	p25	p75
SRTM 30m	-21.34	9.00	30.34	-4.80	-4.83	3.21	0.00	4.03	-6.77	-2.85
ASTER 30m	-41.03	26.00	67.03	-4.65	-4.88	8.12	-0.06	4.16	-9.76	0.20
ALOS AW3D 30m	-22.02	7.03	29.05	-3.96	-3.52	3.33	-0.67	3.40	-6.18	-1.20
ALOS 12.5m	-21.59	8.54	30.13	-4.88	-4.89	3.26	0.02	3.87	-6.87	2.92
CARTOSAT 30m	-23.09	8.11	31.20	-7.71	-7.73	3.11	-0.14	3.67	-9.68	-5.66

Table C16. New Delhi statistics of difference in elevation: surveyed (5m) - DEMs

DEM	Minimum	Maximum	Range	Mean	Median	Std dev	skew	kurt	p25	p75
SRTM 30m	-21.04	14.98	36.03	-0.16	-0.13	1.46	-0.18	3.14	-0.97	0.67
ASTER 30m	-49.99	47.74	97.73	-0.4	-0.12	8.52	-0.11	0.86	-5.61	5.05
ALOS AW3D 30m	-62.74	21.2	83.94	-1.64	-1.53	4.28	-1.30	9.06	-3.78	0.87
CARTOSAT 30m	-38.42	21.15	59.57	-2.16	-2.01	3.99	-0.73	3.58	-4.25	0.19

Table C17. Bangalore statistics of difference in elevation: ALOS PALSAR (12.5m) – DEMs

DEM	Minimum	Maximum	Range	Mean	Median	Std dev	skew	kurt	p25	p75
SRTM 30m	-3.35	4.49	7.85	0.46	0.60	1.40	-0.38	2.94	-0.28	1.41
ASTER 30m	-4.25	18.58	22.83	6.23	5.90	5.08	0.20	2.44	2.26	9.75
ALOS AW3D 30m	-3.52	2.41	5.93	-0.43	-0.36	0.99	-0.35	2.64	-1.14	0.33
ALOS 12.5m	-3.22	5.03	8.25	0.67	0.84	1.55	-0.38	2.94	-0.26	1.77
CARTOSAT 30m	-4.33	2.90	7.23	-0.68	-0.62	1.55	0.11	2.24	-1.92	0.44

Table C18. Jorhat statistics of difference in elevation: surveyed (0.9m) – DEMs

DEM	Minimum	Maximum	Range	Mean	Median	Std dev	skew	kurt	p25	p75
SRTM 30m	-5.45	3.50	8.95	-0.42	-0.58	1.47	0.16	2.93	-1.48	0.44
ASTER 30m	-10.05	23.89	33.95	6.27	6.32	5.02	-0.03	3.22	3.20	9.45
ALOS AW3D 30m	-3.35	4.14	7.50	0.88	0.95	1.03	-0.17	3.42	0.18	1.51
ALOS 12.5m	-4.99	3.64	8.63	-0.45	-0.15	1.53	-0.30	2.55	-1.56	0.59
CARTOSAT 30m	-4.47	1.99	6.46	-1.47	-1.33	0.89	-0.49	3.40	-1.93	-0.93

Table C19. Guwahati statistics of difference in elevation: surveyed (0.9m) - DEMs

Abstract-TH-2793_156104035

C.6 Error metrics of DEMs compared to Surveyed data with assuming normal distribution

Surveyed - DEM	Study Area	ME	RMSE	STDE	LE90	LE95	LE99
SRTM 30 m	Simi Valley	-1.97	3.75	3.19	5.24	6.05	9.56
	Riom	-0.79	1.82	1.64	2.70	3.12	4.93
	New Delhi	-4.80	5.77	3.21	5.28	6.10	9.64
	Guwahati	-0.42	1.53	1.47	2.41	2.79	4.40
	Jorhat	0.46	1.48	1.40	2.30	2.66	4.20
ASTER 30 m	Simi Valley	7.05	8.42	4.60	7.56	8.73	13.79
	Riom	-2.95	4.09	2.82	4.64	5.36	8.47
	New Delhi	-4.65	9.36	8.12	13.36	15.44	24.37
	Guwahati	6.27	8.03	5.02	8.25	9.53	15.05
	Jorhat	6.23	8.03	5.08	8.35	9.65	15.23
ALOS AW3D 30 m	Simi Valley	-2.04	3.03	2.24	3.69	4.26	6.73
	Riom	-3.14	3.57	1.70	2.80	3.23	5.10
	New Delhi	-3.96	5.18	3.33	5.48	6.33	10.00
	Guwahati	0.88	1.36	1.03	1.70	1.96	3.10
	Jorhat	-0.43	1.07	0.99	1.62	1.87	2.96
ALOS 12.5 m	Simi Valley	-0.33	2.92	2.90	4.78	5.52	8.71
	New Delhi	-4.88	5.87	3.26	5.37	6.20	9.79
	Guwahati	-0.45	1.59	1.53	2.51	2.90	4.58
	Jorhat	0.67	1.69	1.55	2.56	2.95	4.66
CARTOSAT 30 m	New Delhi	-7.71	8.32	3.11	5.11	5.90	9.32
	Guwahati	-1.47	1.72	0.89	1.47	1.69	2.67
	Jorhat	-0.68	1.69	1.55	2.55	2.94	4.65
NED 30 m	Simi Valley	0.32	4.07	4.06	6.68	7.72	12.18
NED 10 m	Simi Valley	-0.11	3.19	3.19	5.24	6.06	9.56
EU DEM 25 m	Riom	-2.10	2.66	1.63	2.68	3.09	4.88
EU DEM v1 25 m	Riom	-2.23	2.74	1.59	2.62	3.02	4.77

*ME: Mean Error; RMSE: Root Mean Square Error; STDE: Standard Deviation Error; LE90: Linear Error at 90% confidence; LE95: Linear Error at 95% confidence; LE99: Linear Error at 99.73% (3σ) confidence. All are in meters

Table C20. Error metrics of selected DEMs with respect to surveyed data by assuming DoDs distributed normally.

Abstract-TH-2793_156104035

C.7 Error metrics of DEMs compared to Surveyed data without assuming normal distribution

Surveyed DEM	Study Area	Min	Max	Mean	Median	STDE	LE 10	LE 90	LE95	LE99
SRTM 30 m	Simi Valley	0.00	28.09	3.08	2.70	2.14	0.88	5.60	7.13	10.48
	Riom	0.00	4.83	1.42	1.09	1.14	0.15	3.19	3.54	4.18
	New Delhi	0.00	21.34	5.03	4.86	2.83	1.39	8.82	9.95	12.50
	Guwahati	0.00	5.45	1.23	1.02	0.91	0.14	2.53	2.96	3.72
	Jorhat	0.00	4.49	1.20	1.02	0.86	0.20	2.41	2.84	3.39
ASTER 30 m	Simi Valley	0.00	32.48	7.31	6.80	4.17	2.33	12.82	15.11	19.66
	Riom	0.00	11.00	3.27	2.84	2.44	0.38	6.82	8.01	9.19
	New Delhi	0.00	41.03	7.45	6.44	5.67	1.21	14.58	17.38	28.08
	Guwahati	0.00	23.89	6.85	6.36	4.19	1.64	12.28	14.24	17.91
	Jorhat	0.00	18.58	6.63	5.90	4.54	1.18	13.83	15.48	17.09
ALOS AW3D 30 m	Simi Valley	0.00	22.23	2.50	2.11	1.72	0.87	4.63	5.92	8.75
	Riom	0.00	7.60	3.14	2.82	1.69	1.06	5.66	6.26	6.82
	New Delhi	0.00	22.02	4.09	3.54	3.17	0.57	8.61	9.82	12.84
	Guwahati	0.00	4.14	1.11	1.00	0.79	0.15	2.19	2.48	3.15
	Jorhat	0.00	3.52	0.85	0.70	0.66	0.12	1.73	2.23	2.90
ALOS 12.5 m	Simi Valley	0.00	22.63	1.87	0.98	2.25	0.17	4.89	6.70	10.46
	New Delhi	0.00	21.59	5.12	4.93	2.88	1.42	9.01	10.22	12.56
	Guwahati	0.00	4.99	1.25	1.01	0.99	0.16	2.63	3.11	4.06
	Jorhat	0.00	5.03	1.40	1.27	0.96	0.25	2.76	3.13	3.97
CARTOSAT 30 m	New Delhi	0.00	23.09	7.73	7.73	3.06	3.80	11.46	12.75	15.64
	Guwahati	0.00	4.47	1.50	1.33	0.85	0.51	2.82	3.33	3.62
	Jorhat	0.00	4.33	1.39	1.25	0.96	0.21	2.77	2.96	3.75
NED 30 m	Simi Valley	0.00	27.38	2.36	0.99	3.32	0.16	6.55	9.48	16.10
NED 10 m	Simi Valley	0.00	22.39	1.95	0.92	2.53	0.15	5.29	7.46	11.78
EU DEM 25 m	Riom	0.00	5.51	2.16	2.10	1.55	0.22	4.27	4.63	5.17
EU DEM v1 25 m	Riom	0.00	5.86	2.25	2.00	1.57	0.32	4.54	4.87	5.51

* STDE: Standard Deviation Error; LE90: Linear Error at 90% confidence; LE95: Linear Error at 95% confidence; LE99: Linear Error at 99.73% (3σ) confidence. All are in meters.

Table C21. Error metrics of selected DEMs with respect to surveyed data for actual DoDs distribution.

Abstract-TH-2793_156104035

DEM	Features by Visual Identification					Statistical Analysis			Elevation Differences (DoDs)	Storage Holding Capacity	Flood Identification			Overall Performance
	Buildings	Water bodies	Roads	Channel Network	Vegetation	Elevations	Slopes	Contours			Depth	Flood Extent	Peak & HG	
ALOS PALSAR (12 m)	1, -, 1, 2, 1, -	1, -, -, 4, -, 1	1, 1, 1, 1, 1, -	4, -, 2, 2, -, -	1, -, 1, 2, -, 2	2, -, 2, 3, 3, 2	3, -, 3, 3, 2, 3	3, -, 3, 3, 2, 3	3, -, 4, -, 3, 3	2, -, 4, 3, -, 3	3.5, -, 2, , 3.5, -	4, -, -, , -, -	2, -, 3, , 3, -	2.38
ALOS AW3D (30 m)	4, 3, 4, 4, 2, -	4, -, -, 4, -, 2	3, 1, 2, 2, 1, -	4, 3, 4, 3, -, -	2, 2, 3, 2, -, 2	3, 3, 4, 4, 3, 4	4, 3, 3, 4, 2, 4	4, 3, 3, 4, 2, 4	4, 2, 4, -, 4, 4	5, 4, 4, 4, -, 4	3.25, 4, 3.5, , 3.5, -	3, -, -, , -, -	5, 3, 4, , 4, -	3.46
ASTER GDEM (30 m)	1, 1, 1, 1, 1, -	1, -, -, 1, -, 1	1, 1, 1, 1, 1, -	1, 1, 1, 3, -, -	1, 2, 1, 2, -, 2	1, 2, 1, 2, 1, 1	2, 2, 2, 2, 2, 2	2, 2, 2, 2, 2, 2	1, 1, 1, -, 1, 1	3, 2, 4, 4, -, 1	2, -, 0, , 3.5, -	4, -, -, , -, -	1, -, -, , 3, -	1.62
CARTOSAT (30m)	-, -, 4, 4, 1, -	-, -, -, 2, -, 1	-, -, 2, 2, 1, -	-, -, 3, 3, -, -	-, -, 2, 2, -, 2	-, -, 4, 4, 3, 3	-, -, 3, 4, 2, 5	-, -, 3, 4, 2, 5	-, -, 3, -, 3, 3	-, -, 4, 2, -, 3	-, -, 2.5, , 1.5, -	-, -, -, , -, -	-, -, 2, , 3, -	2.75
EU DEM (~25 m)	-, 1, -, -, -, -	-, -, -, -, -, -	-, 1, -, -, -, -	-, 2, -, -, -, -	-, 2, -, -, -, -	-, 4, -, -, -, -	-, 3, -, -, -, -	-, 3, -, -, -, -	-, 3, -, -, -, -	-, 1, -, -, -, -	-, -, -, , -, -	-, -, -, , -, -	-, -, -, , -, -	2.22
EU DEM V1 (~25 m)	-, 1, -, -, -, -	-, -, -, -, -, -	-, 1, -, -, -, -	-, 2, -, -, -, -	-, 2, -, -, -, -	-, 2, -, -, -, -	-, 2, -, -, -, -	-, 2, -, -, -, -	-, 3, -, -, -, -	-, 1, -, -, -, -	-, -, -, , -, -	-, -, -, , -, -	-, -, -, , -, -	1.89
NED (10 m)	1, -, -, -, -, -	1, -, -, -, -, -	1, -, -, -, -, -	4, -, -, -, -, -	1, -, -, -, -, -	5, -, -, -, -, -	3, -, -, -, -, -	3, -, -, -, -, -	2, -, -, -, -, -	2, -, -, -, -, -	4, -, -, , -, -	4, -, -, , -, -	4, -, -, , -, -	2.69
NED (30 m)	1, -, -, -, -, -	1, -, -, -, -, -	1, -, -, -, -, -	4, -, -, -, -, -	1, -, -, -, -, -	4, -, -, -, -, -	3, -, -, -, -, -	3, -, -, -, -, -	1, -, -, -, -, -	2, -, -, -, -, -	4, -, -, , -, -	4, -, -, , -, -	2, -, -, , -, -	2.38
SRTM (30 m)	2, 2, 2, 3, 1, -	1, -, -, 3, -, 1	1, 1, 1, 2, 1, -	3, 3, 2, 2, -, -	2, 2, 2, 2, -, 2	3, 3, 4, 3, 3, 2	3, 3, 3, 3, 2, 3	3, 3, 3, 3, 2, 3	3, 4, 4, -, 3, 3	4, 4, 4, 3, -, 3	2.5, 2, 2, , 3.5, -	3, -, -, , -, -	4, 1, 1, , 4, -	2.69

* Ratings given from 0-5 and Colour Order followed: Simi Valley; Riom; New Delhi; Bangalore; Jorhat; and Guwahati

Table C22. Ranking matrix given from grim (1) to very good (5) towards each feature identification at each study area for all Dems

C.9 Photogrammetry vs Interferromerty over urban features

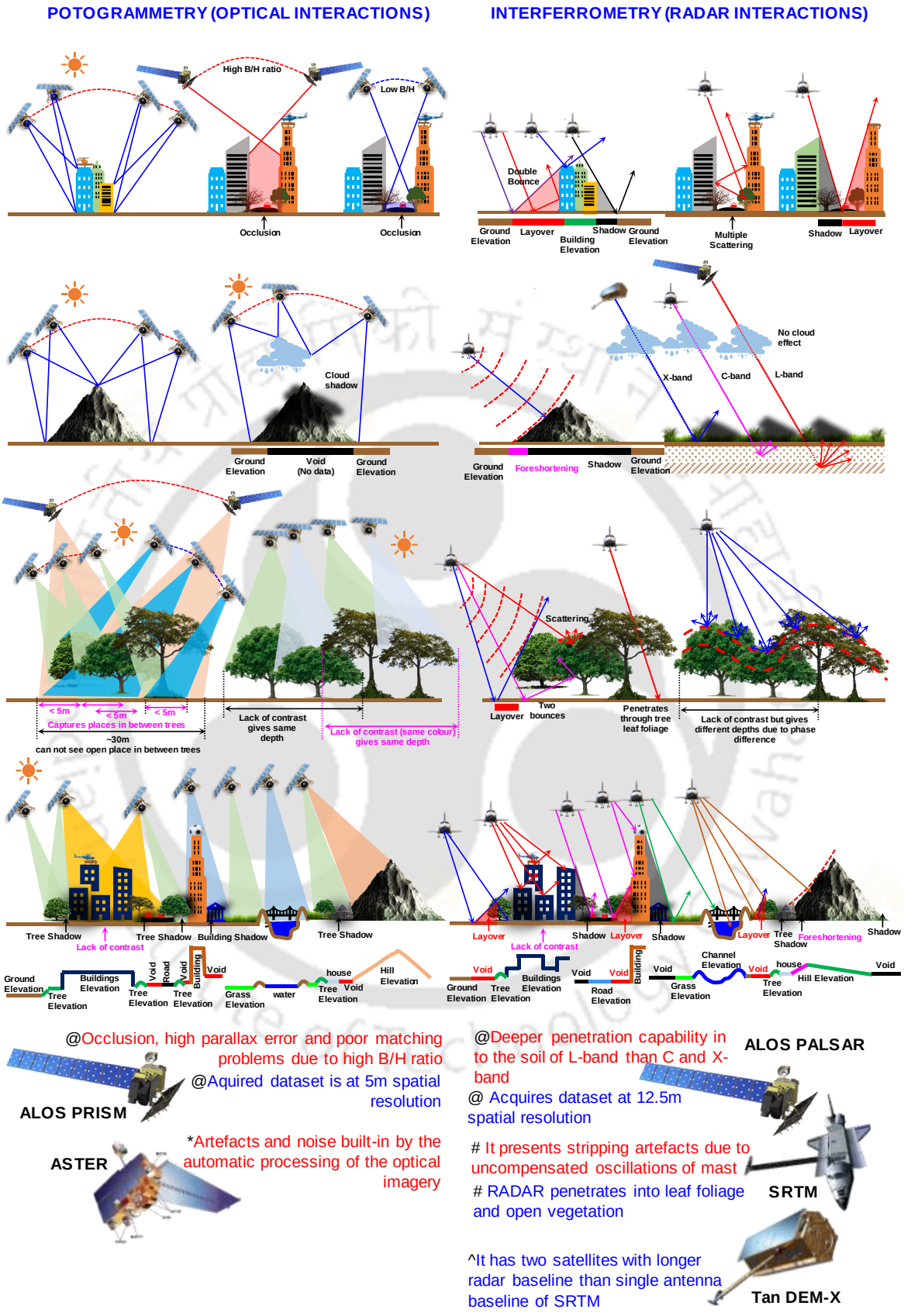

Figure CF1. Conceptual Sketch of Optical and Microwave interactions with urban features.

C.10 Satellites images of the selected study regions

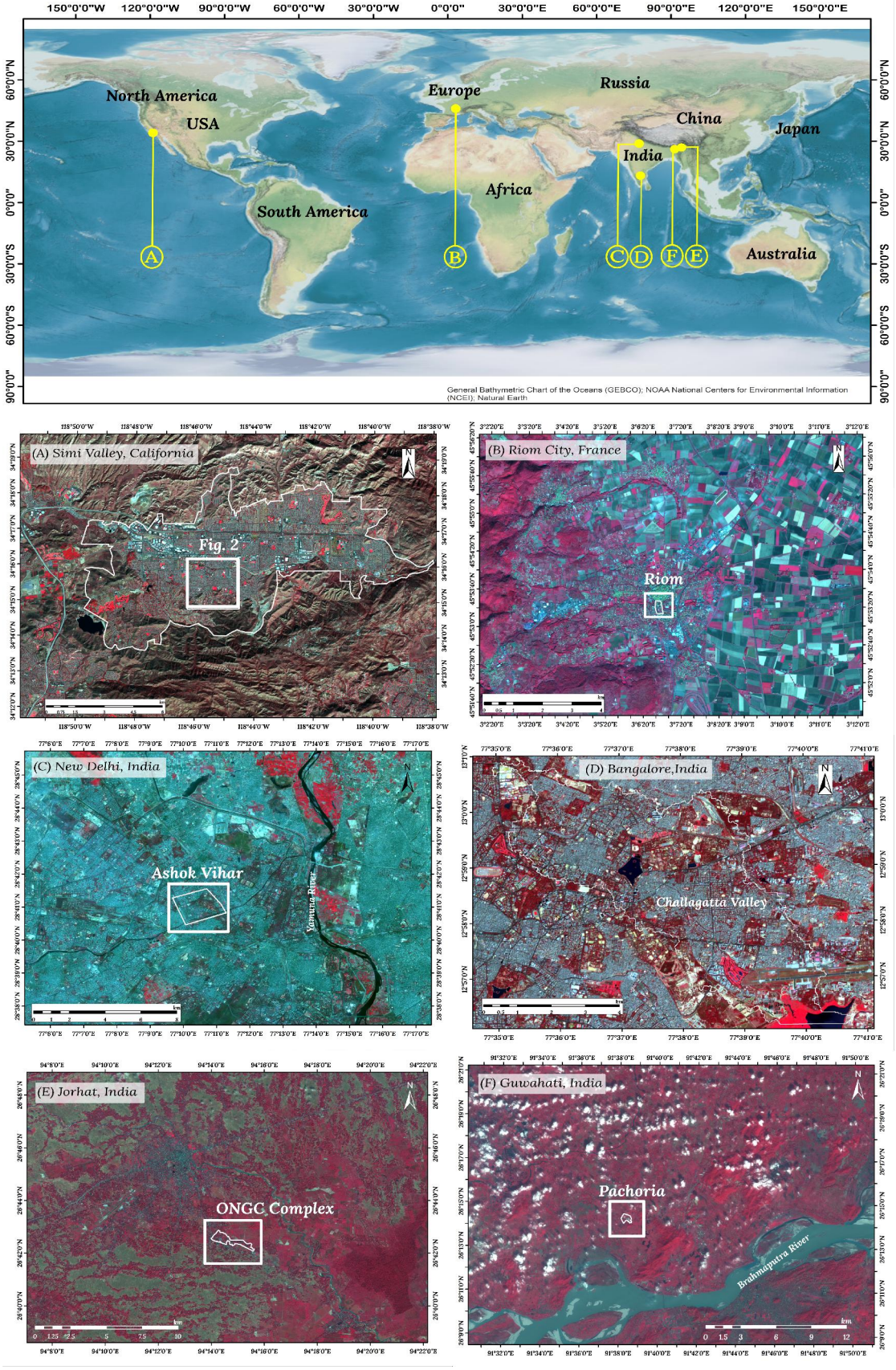

Figure CF2. Sentinel false colour composition satellite imagery of considered study areas with indication of places referred in the text.

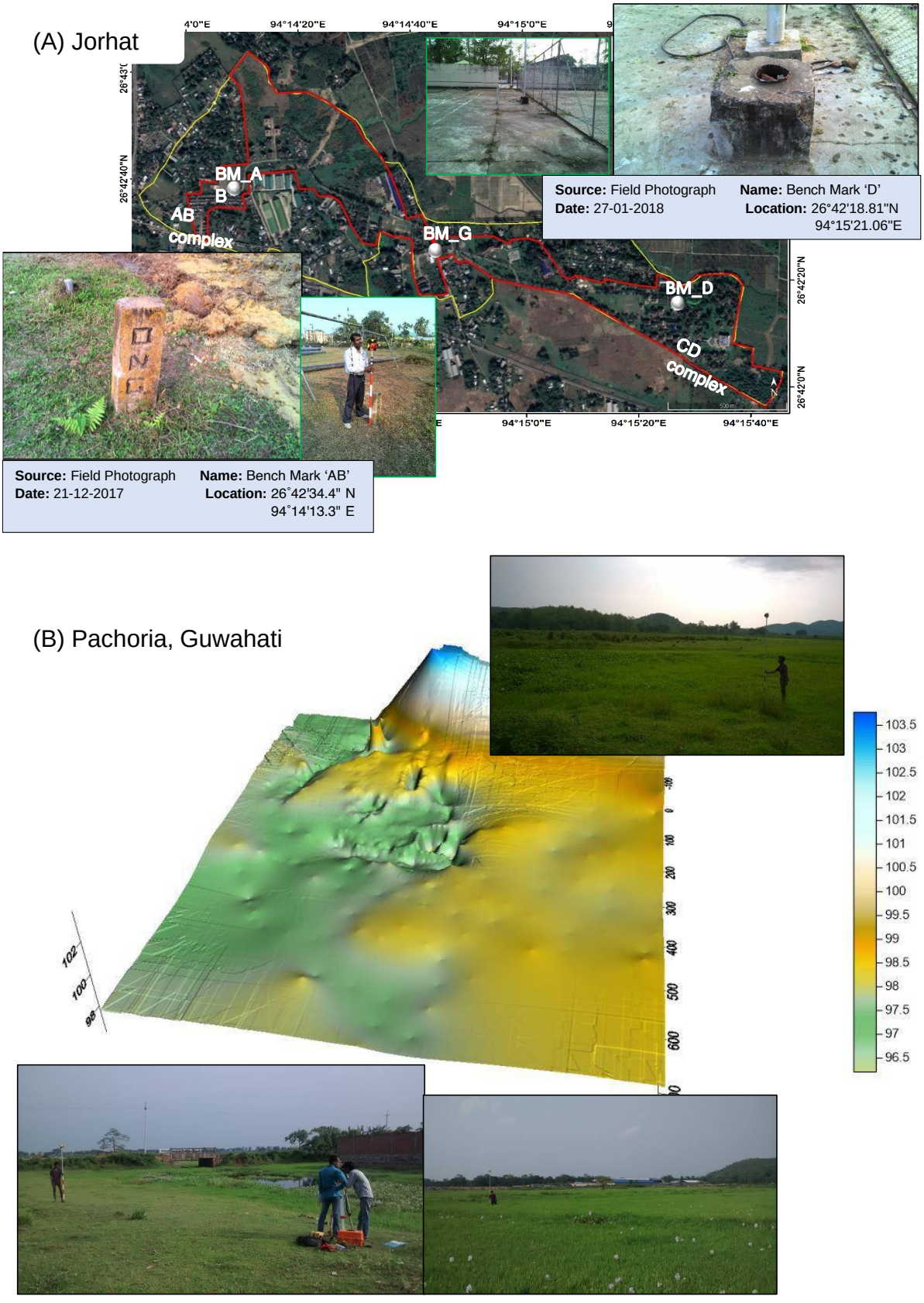

Figure CF3. Ground Elevation Data Collection using Total Station Survey at. A) Jorhat, 0.9 m interval; B) Pachoria, Guwahati, 1 m interval.

C.11 Shaded relief images of different DEMs of the selected study regions

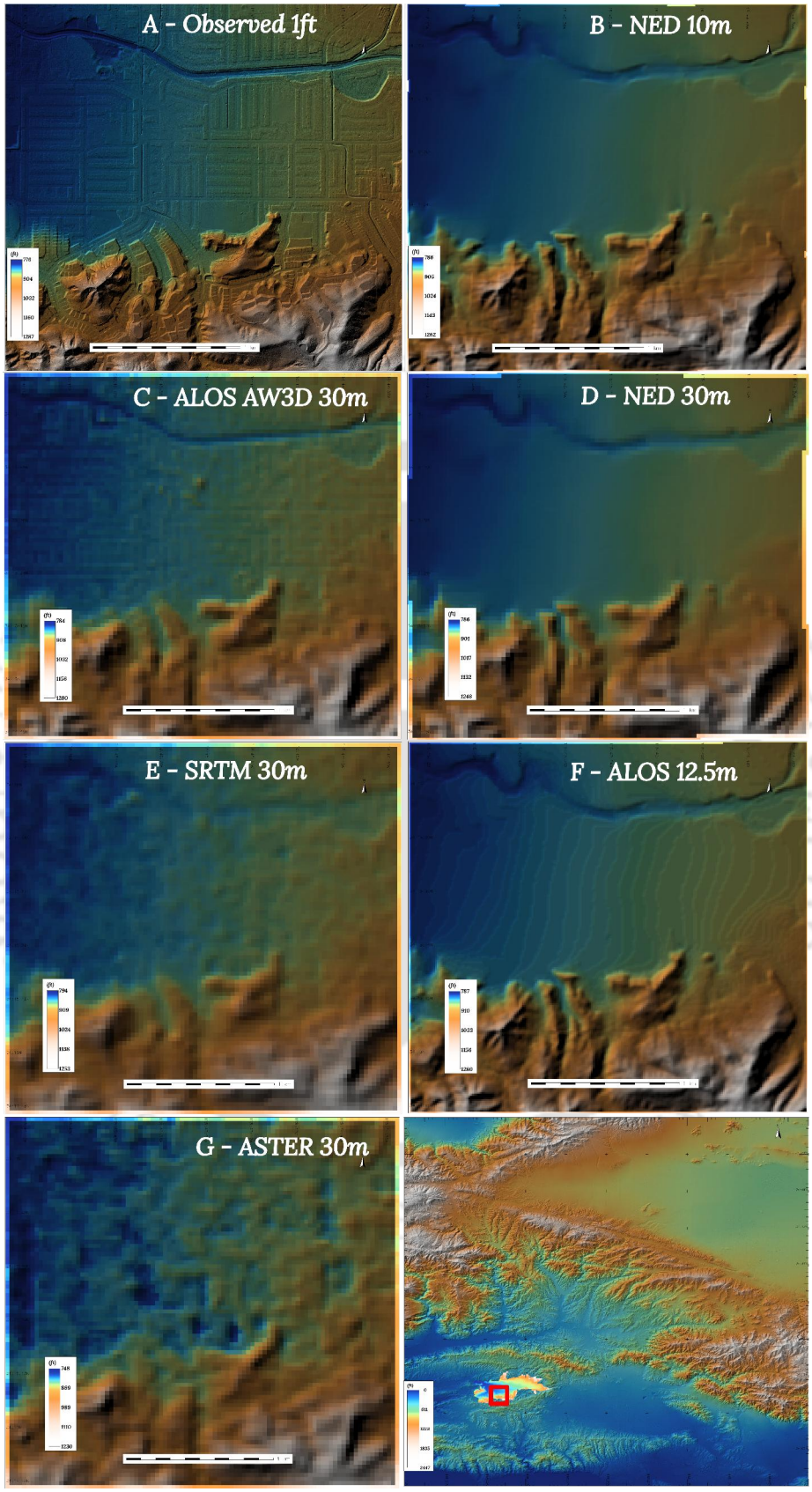

Figure CF4. Shaded relief datasets for Simivalley area. A) Observed DEM, 1 ft resolution; B) NED, 10 m resolution; C) ALOS AW3D, 30 m resolution; D) NED, 30 m resolution; E) SRTM, 30 m resolution; F) ALOS, 12.5 m resolution; G) ASTER, 30 m resolution.

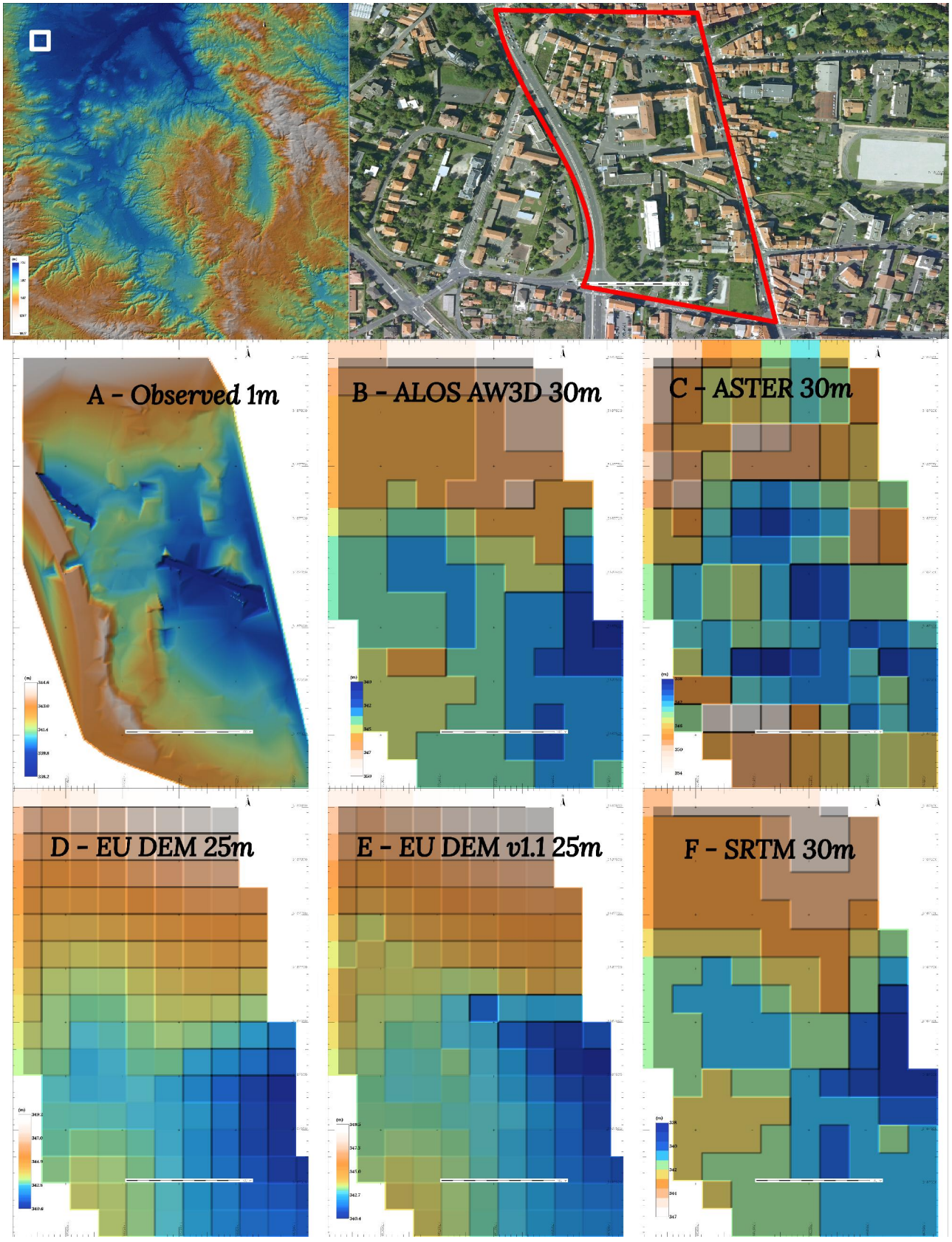

Figure CF5. Shaded relief datasets for Riom area. A) Observed DEM, 1 m resolution; B) ALOS AW3D, 30 m resolution; C) ASTER, 30 m resolution; D) EU DEM, 25 m resolution; E) EU DEM v1.1, 25 m resolution; F) SRTM, 30 m resolution.

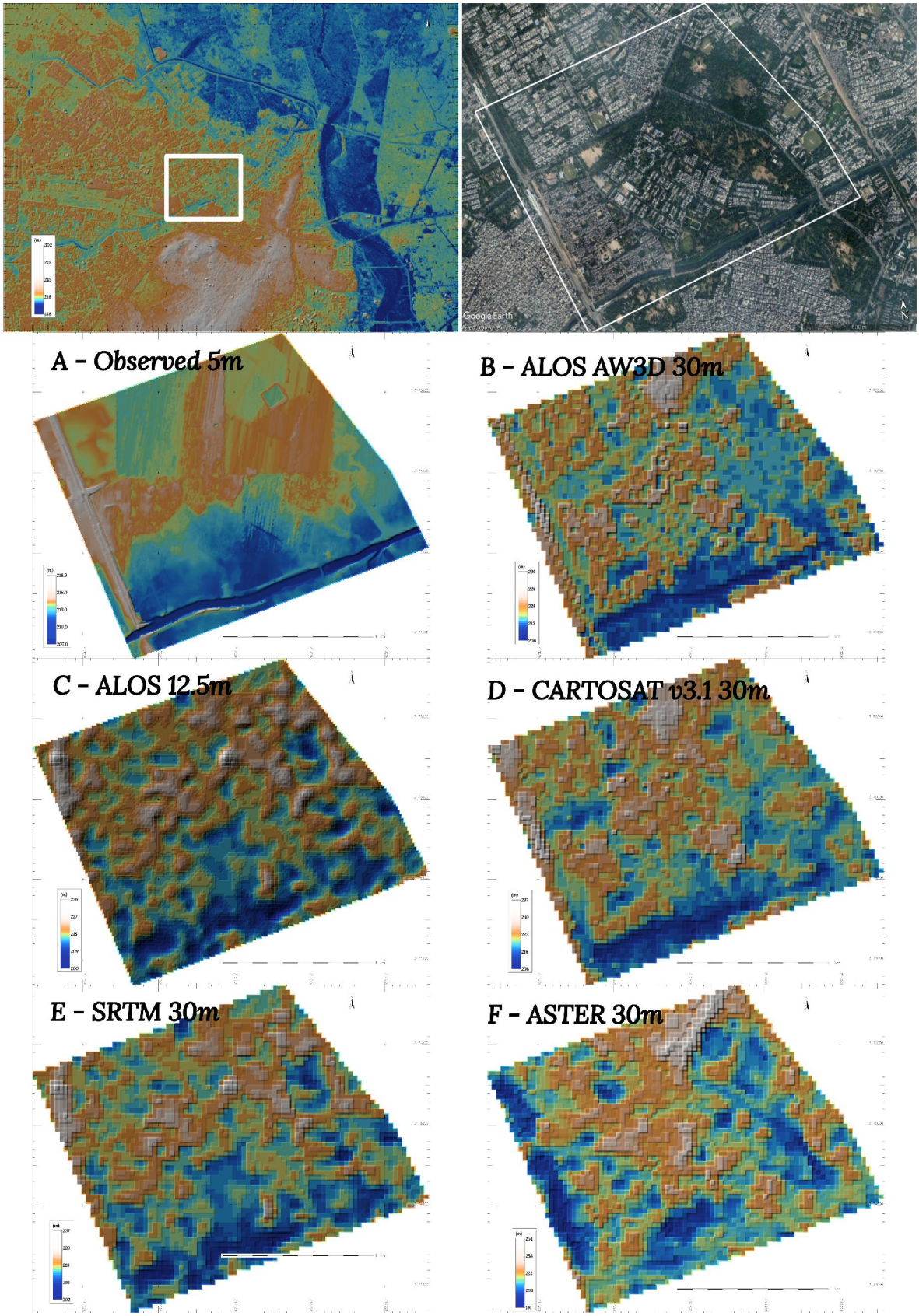

Figure CF6. Shaded relief datasets for Ashok Vihar, New Delhi, India area. A) Observed DEM, 5 m resolution; B) ALOS AW3D, 30 m resolution; C) ALOS, 12.5 m resolution; D) CARTOSAT v3R1, 30 m resolution; E) SRTM, 30 m resolution; F) ASTER, 30 m resolution.

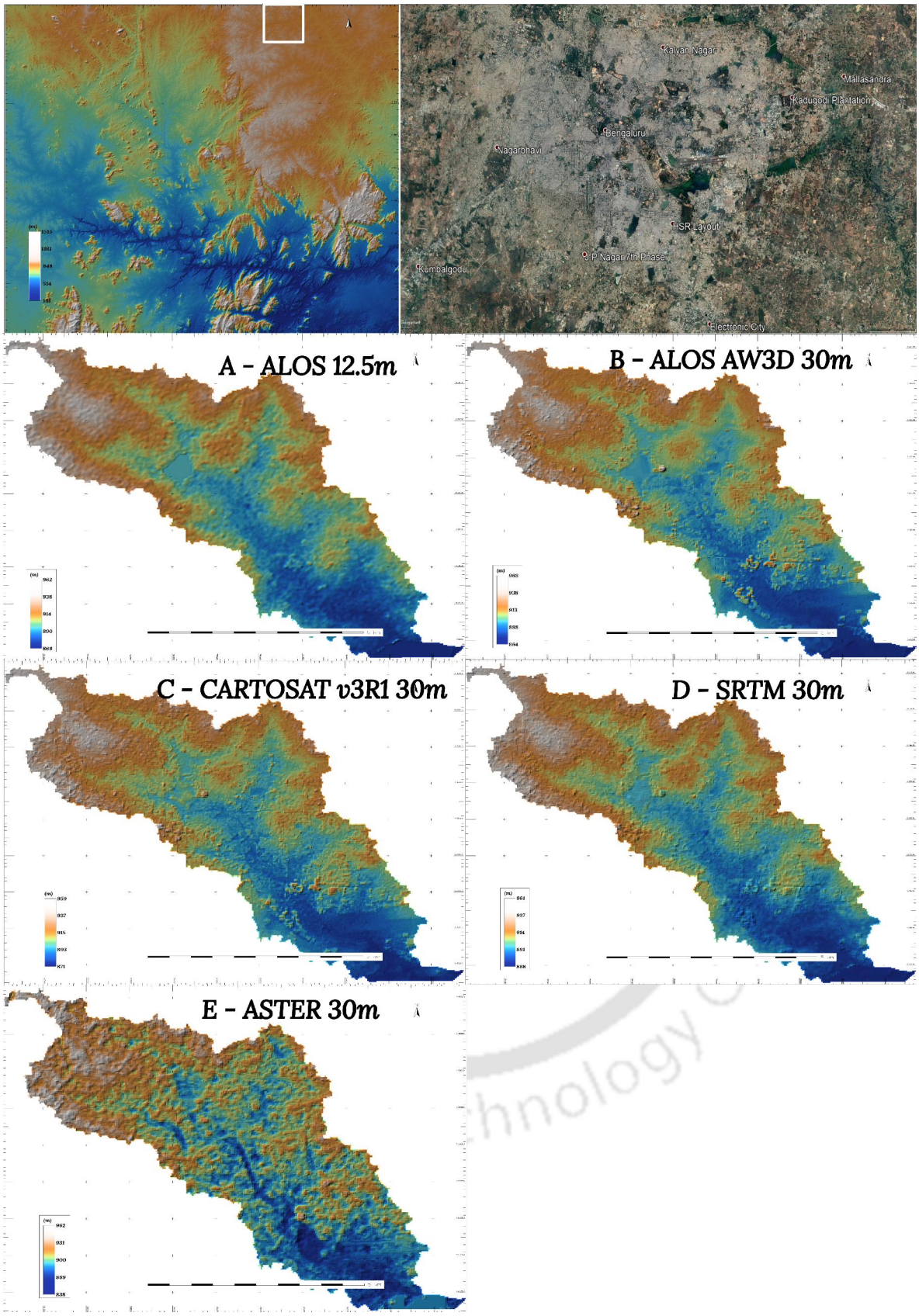

Figure CF7. Shaded relief datasets for Challagatta Valley, Bangalore, India area. A) ALOS, 12.5 m resolution; B) ALOS AW3D, 30 m resolution; C) CARTOSAT v3R1, 30 m resolution; D) SRTM, 30 m resolution; E) ASTER, 30 m resolution.

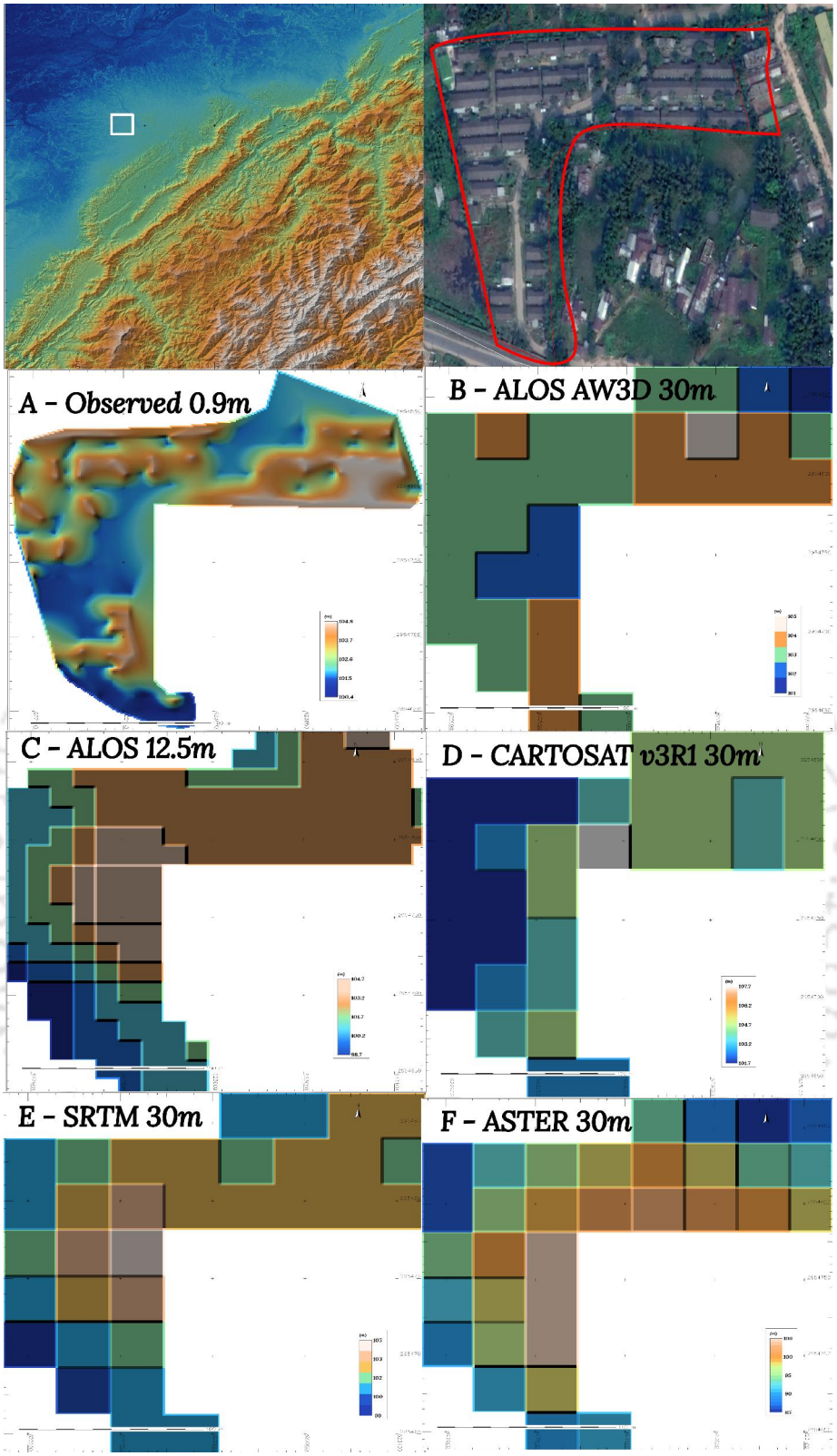

Figure CF8. Shaded relief datasets for ONGC colony, Jorhat, India area. A) Surveyed DEM, 0.9 m resolution; B) ALOS AW3D, 30 m resolution; C) ALOS, 12.5 m resolution; D) CARTOSAT v3R1, 30 m resolution; E) SRTM, 30 m resolution; F) ASTER, 30 m resolution.

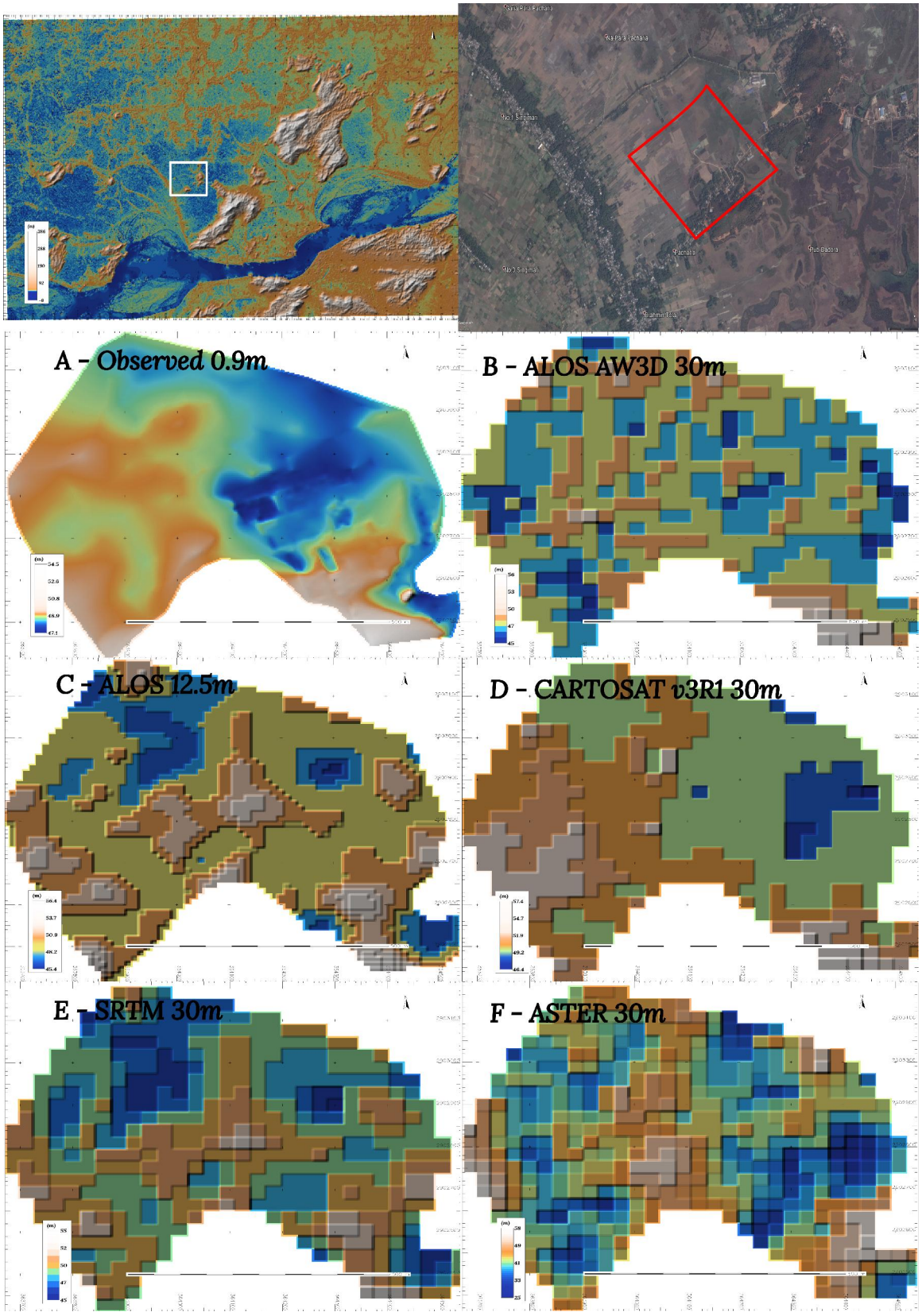

Figure CF9. Shaded relief datasets for Pachoria, Guwahati, India area. A) Observed DEM, 0.9 m resolution; B) ALOS AW3D, 30 m resolution; C) ALOS, 12.5 m resolution; D) CARTOSAT v3R1, 30 m resolution; E) SRTM, 30 m resolution; F) ASTER, 30 m resolution.

C.12 Slope maps of different DEMs of the selected study sites

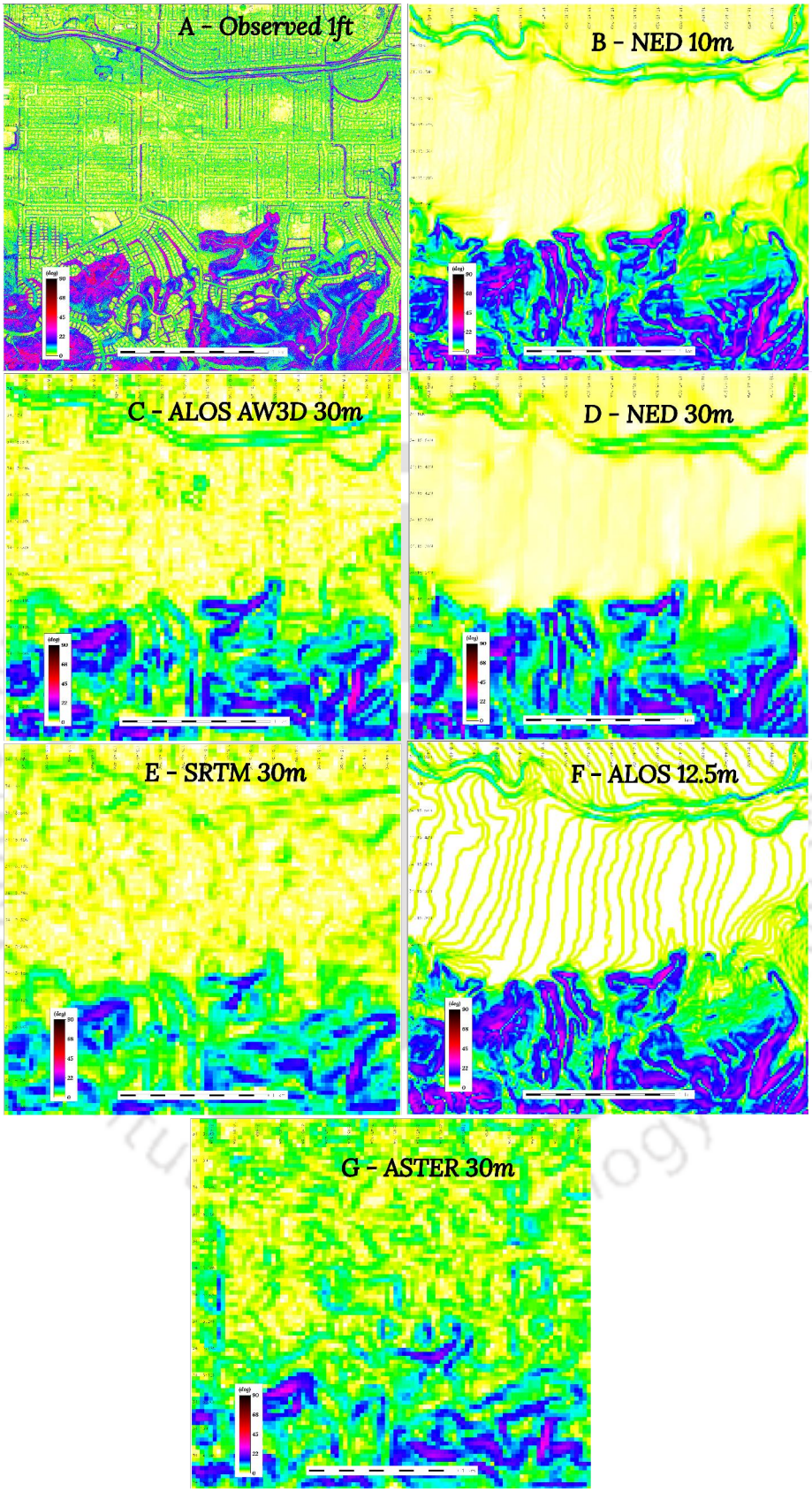

Figure CF10. Slope maps for Simivalley area. A) Observed DEM, 1 ft resolution; B) NED, 10 m resolution; C) ALOS AW3D, 30 m resolution; D) NED, 30 m resolution; E) SRTM, 30 m resolution; F) ALOS, 12.5 m resolution; G) ASTER, 30 m resolution.

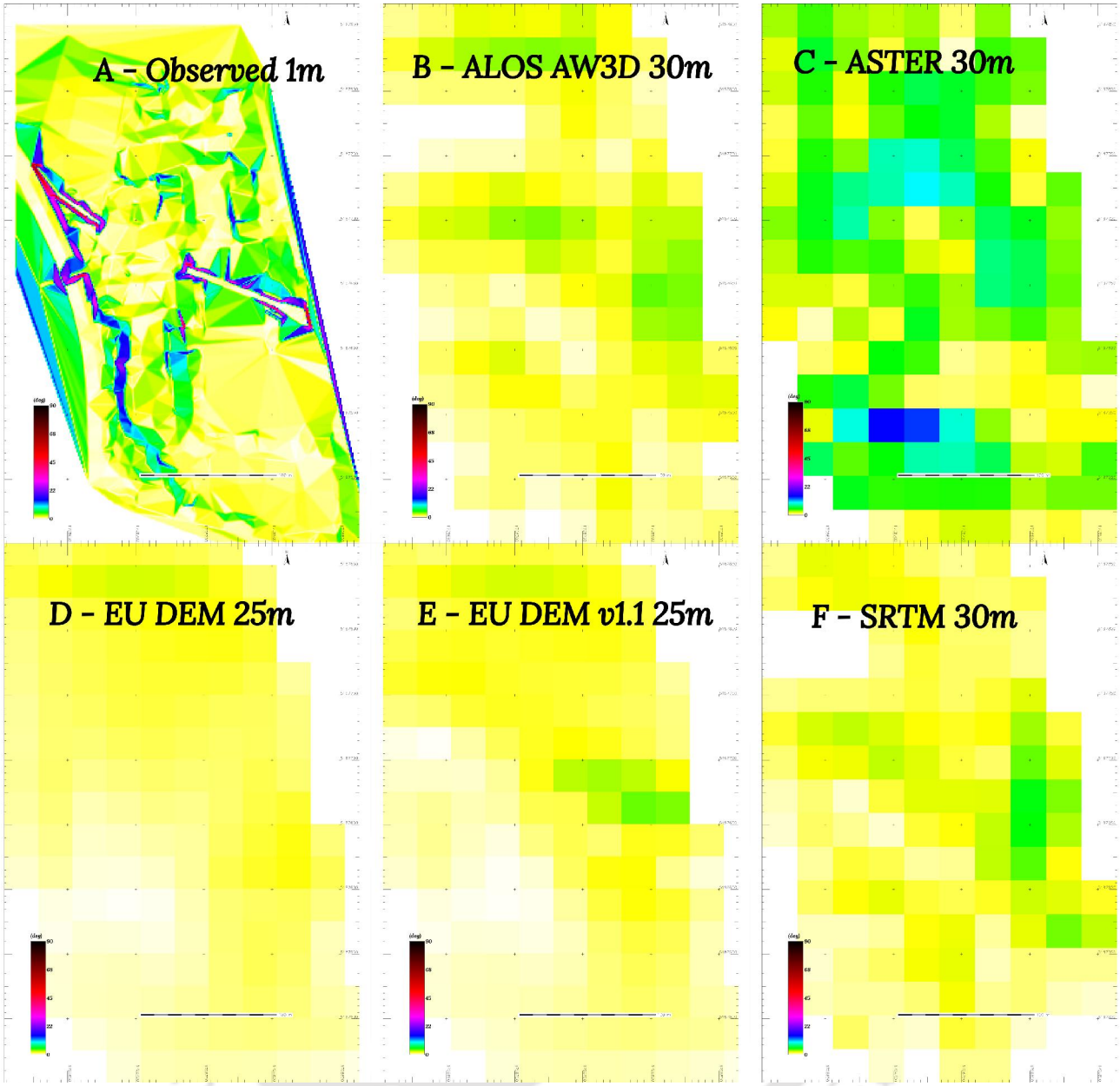

Figure CF11. Slope maps for Riom area. A) Observed DEM, 1 m resolution; B) ALOS AW3D, 30 m resolution; C) ASTER, 30 m resolution; D) EU DEM, 25 m resolution; E) EU DEM v1.1, 25 m resolution; F) SRTM, 30 m resolution.

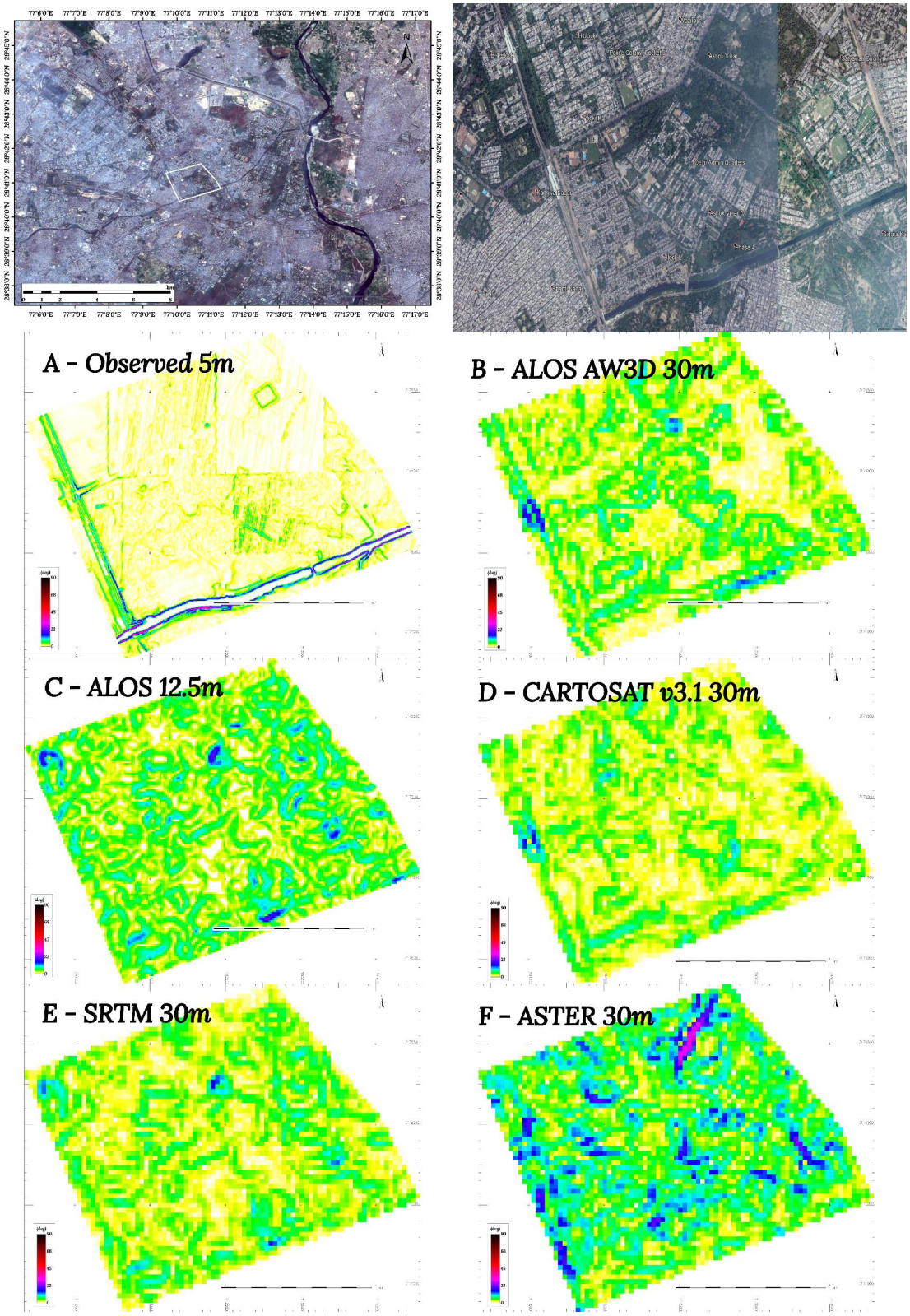

Figure CF12. Slope maps for Ashok Vihar, New Delhi area. A) Observed DEM, 5 m resolution; B) ALOS AW3D, 30 m resolution; C) ALOS, 12.5 m resolution; D) CARTOSAT v3R1, 30 m resolution; E) SRTM, 30 m resolution; F) ASTER, 30 m resolution.

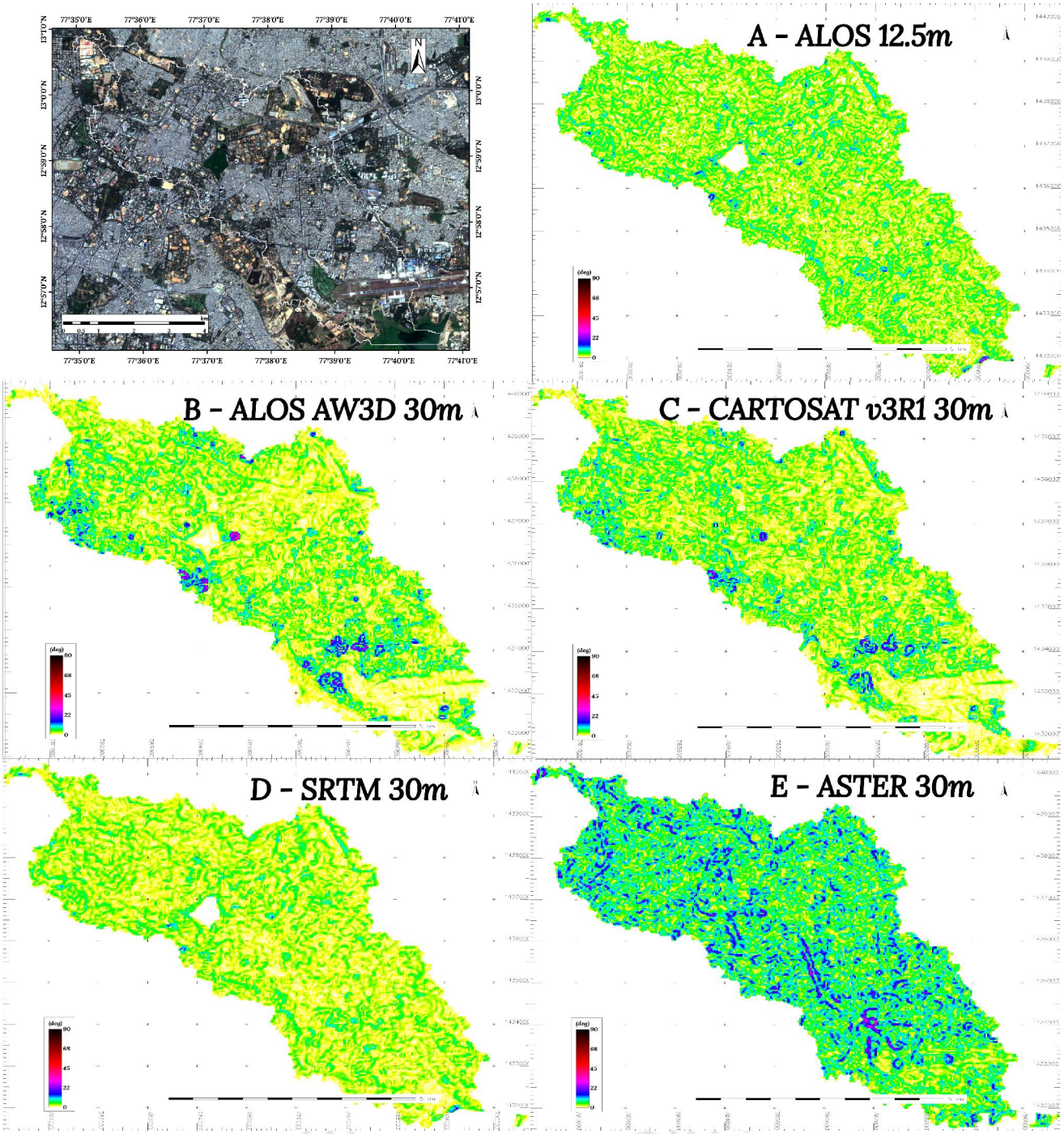

Figure CF13. Slope maps for Challagatta Valley, Bangalore, India area. A) ALOS, 12.5 m resolution; B) ALOS AW3D, 30 m resolution; C) CARTOSAT v3R1, 30 m resolution; D) SRTM, 30 m resolution; E) ASTER, 30 m resolution.

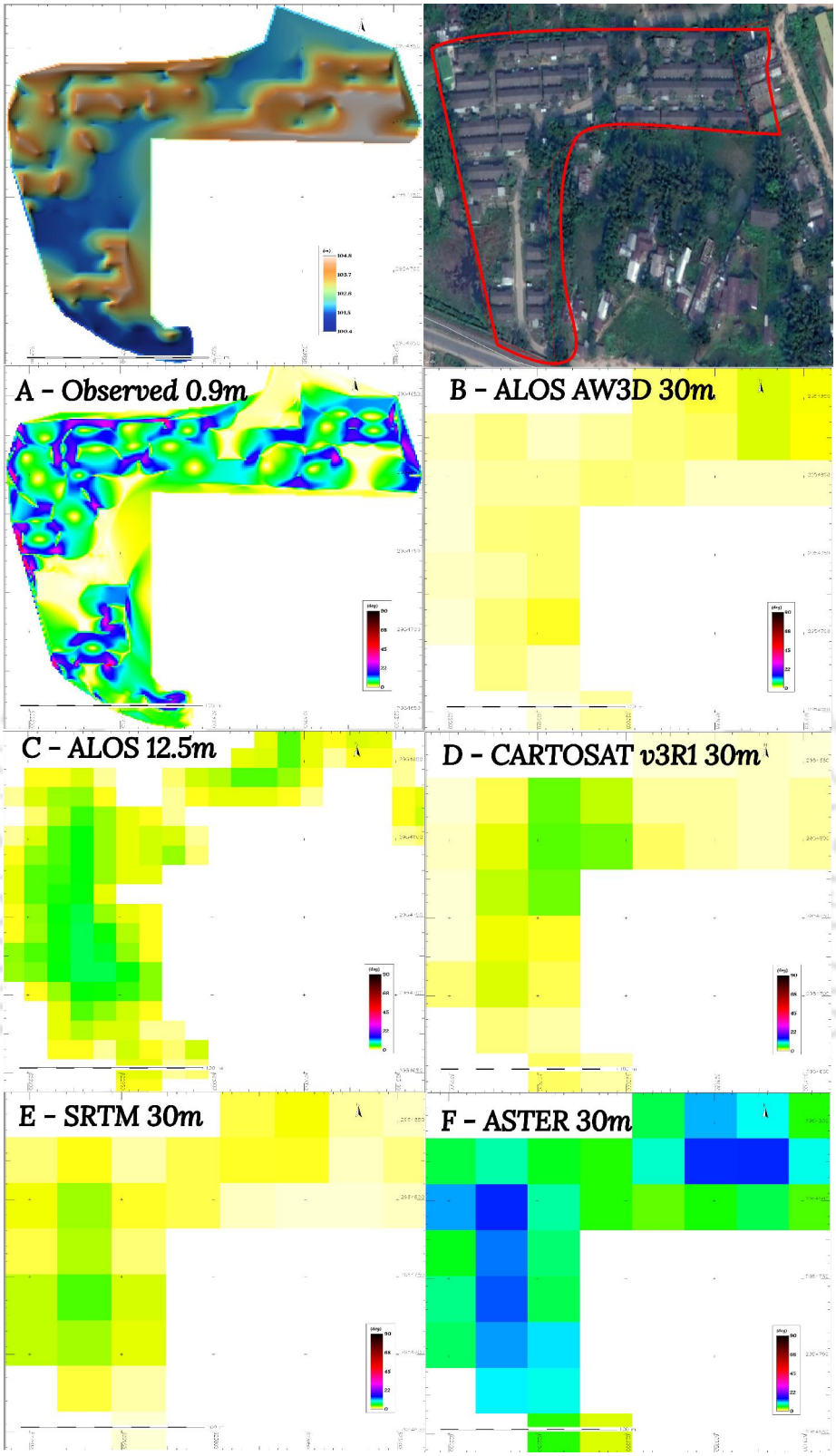

Figure CF14. Slope maps for ONGC colony, Jorhat, India area. A) Surveyed DEM, 0.9 m resolution; B) ALOS AW3D, 30 m resolution; C) ALOS, 12.5 m resolution; D) CARTOSAT v3R1, 30 m resolution; E) SRTM, 30 m resolution; F) ASTER, 30 m resolution.

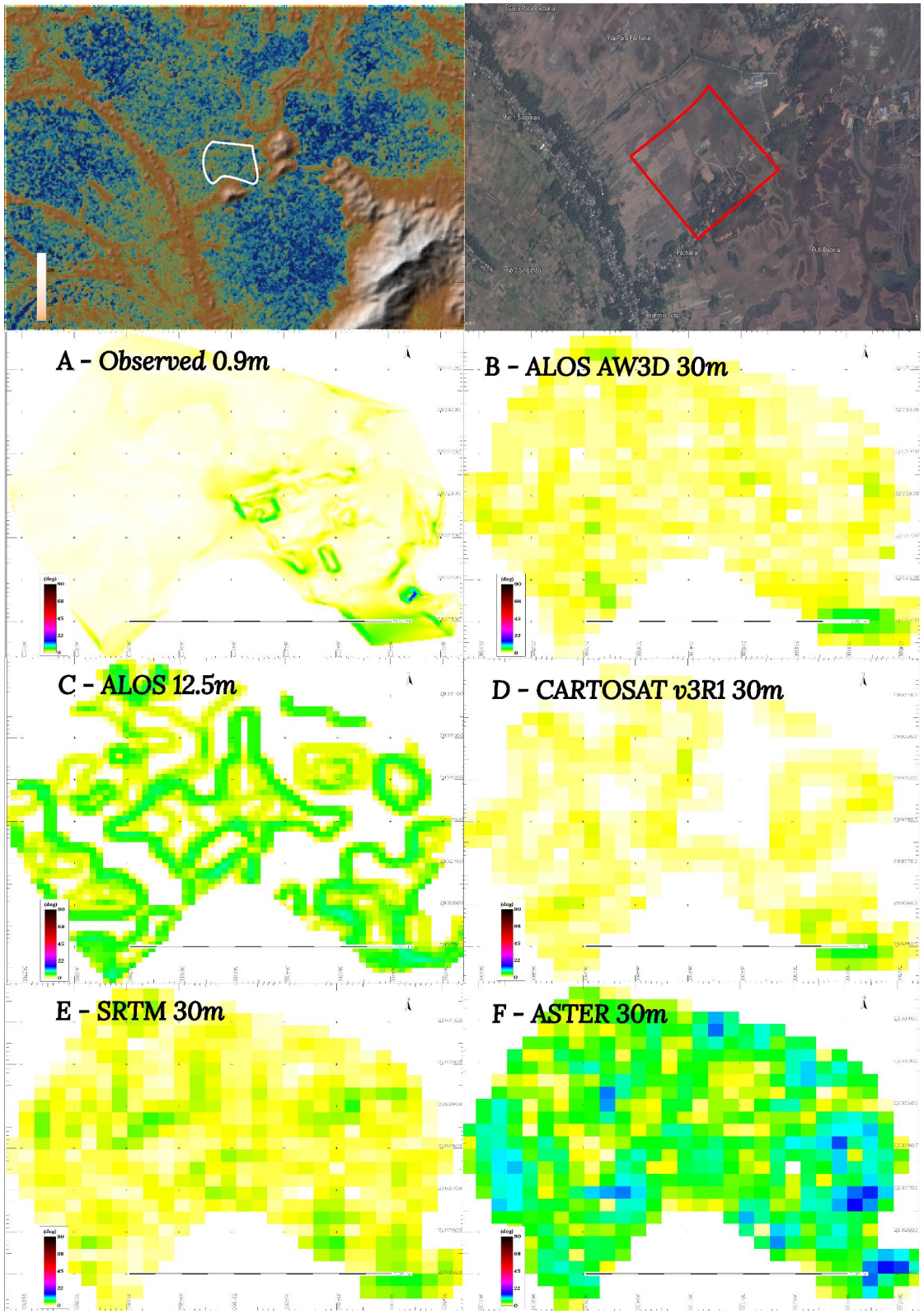

Figure CF15. Slope maps for Pachoria, Guwahati, India area. A) Observed DEM, 0.9 m resolution; B) ALOS AW3D, 30 m resolution; C) ALOS, 12.5 m resolution; D) CARTOSAT v3R1, 30 m resolution; E) SRTM, 30 m resolution; F) ASTER, 30 m resolution.

C.13 Plots of Mean Slope × Elevation

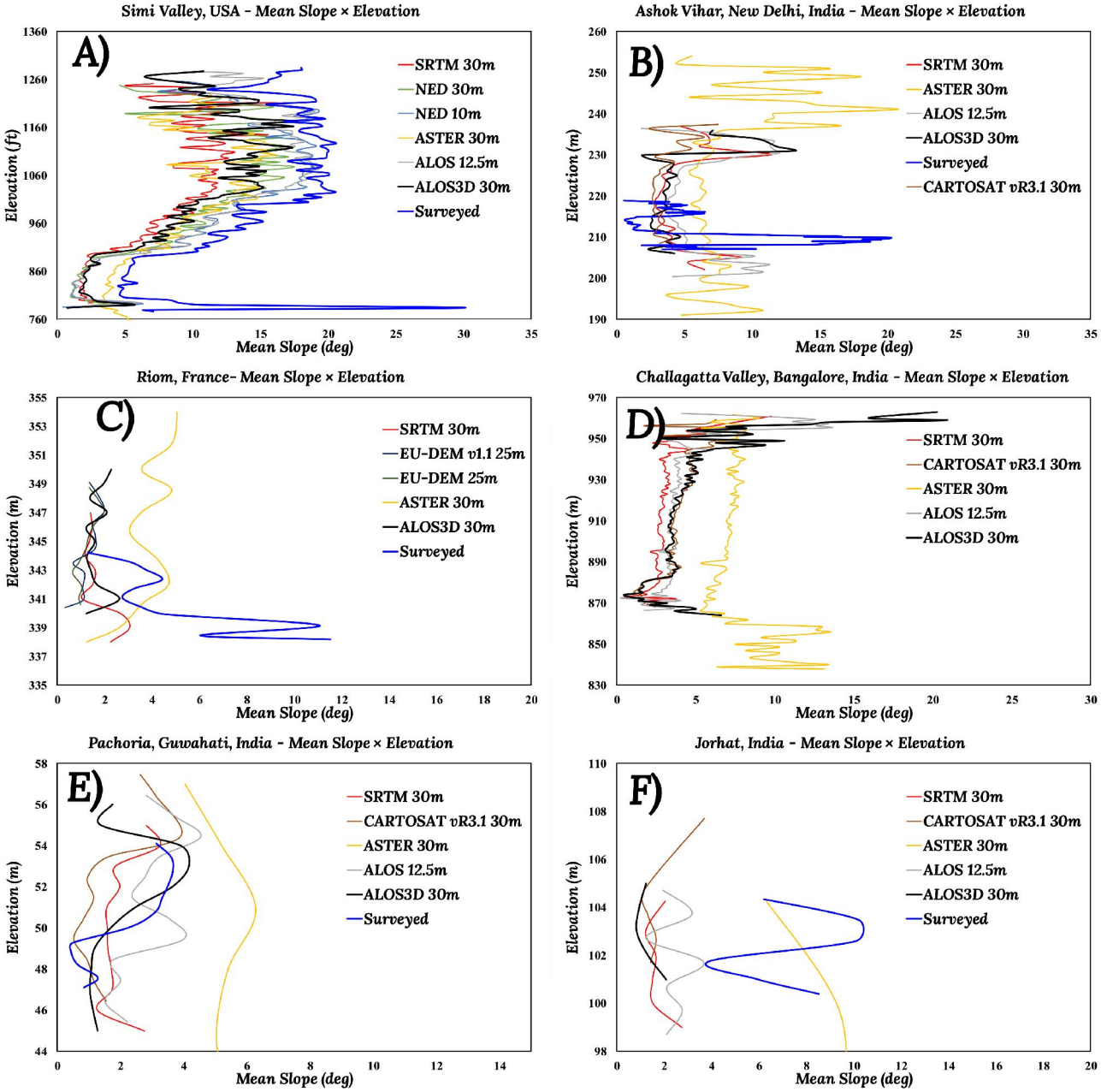

Figure CF16. Figures of mean slope × elevation for all study areas. A) Simi Valley, USA; B) Ashok Vihar, New Delhi, India; C) Riom, France; D) Challagatta Valley, Bangalore, India; E) Pachoria, Guwahati, India; F) ONGC residential Colony, Jorhat, Inida.

C.14 Cumulative sum of contour lengths for considered study areas

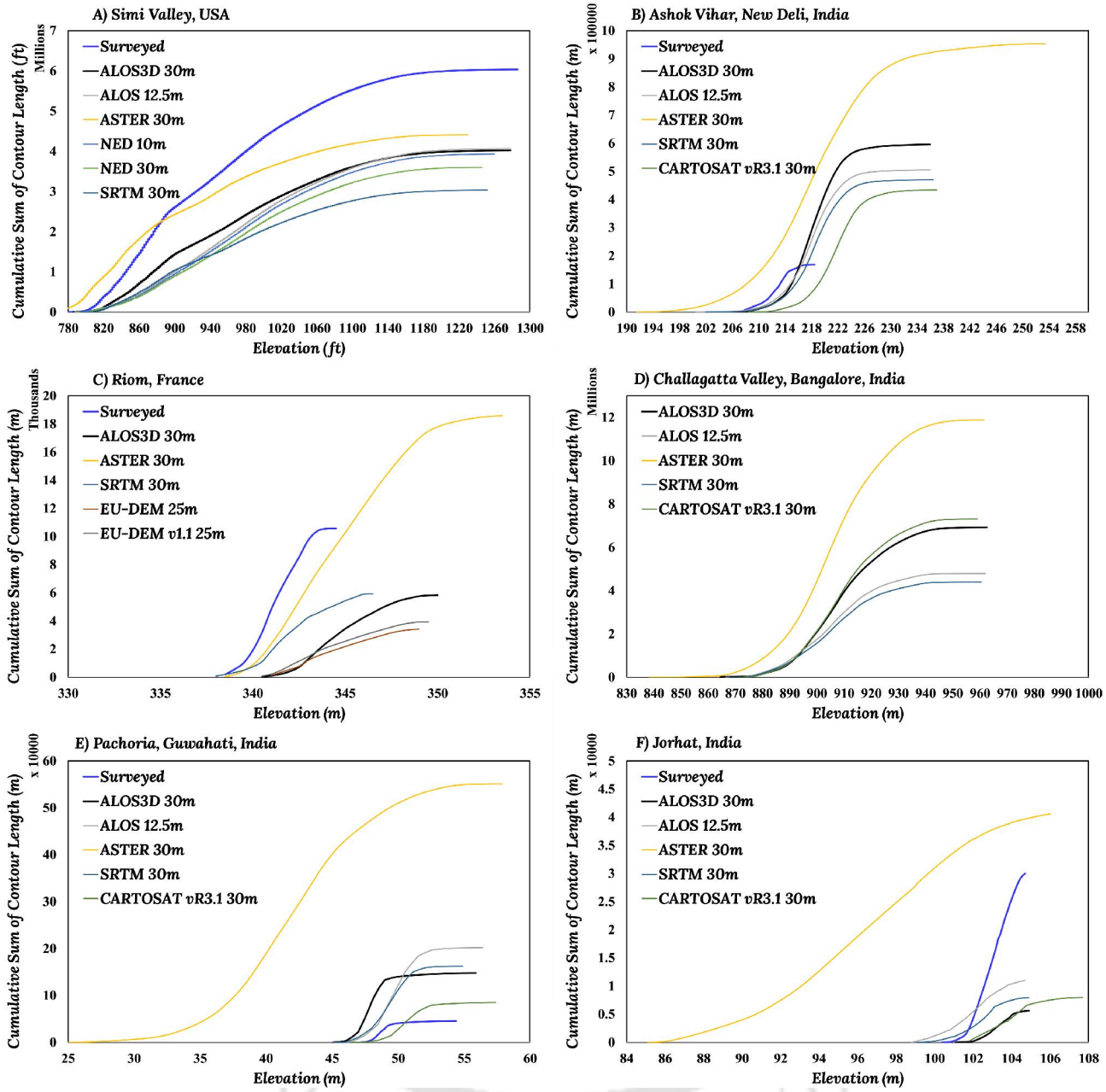

Figure CF17. Figures of cumulative sum of contour lengths for all study areas. A) Simi Valley, USA; B) Ashok Vihar, New Delhi, India; C) Riom, France; D) Challagatta Valley, Bangalore, India; E) Pachoria, Guwahati, India; F) ONGC residential Colony, Jorhat, Inida.

C.15 Cumulative sum of contour counts for considered study areas

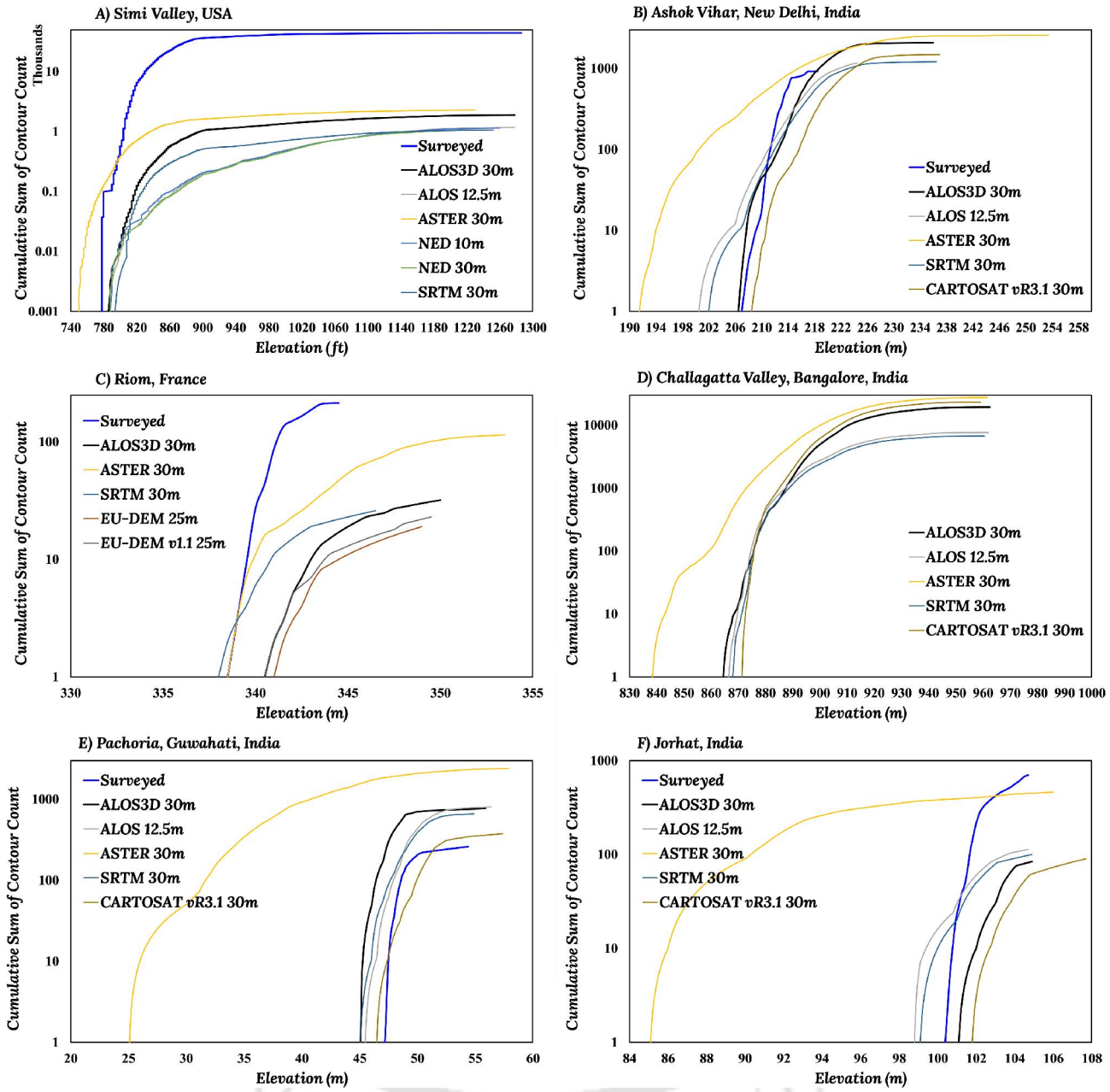

Figure CF18. Figures of cumulative sum of contour counts for all study areas. A) Simi Valley, USA; B) Ashok Vihar, New Delhi, India; C) Riom, France; D) Challagatta Valley, Bangalore, India; E) Pachoria, Guwahati, India; F) ONGC residential Colony, Jorhat, Inida.

C.16 Maps of difference in elevation of DEMs compared to observed or surveyed data

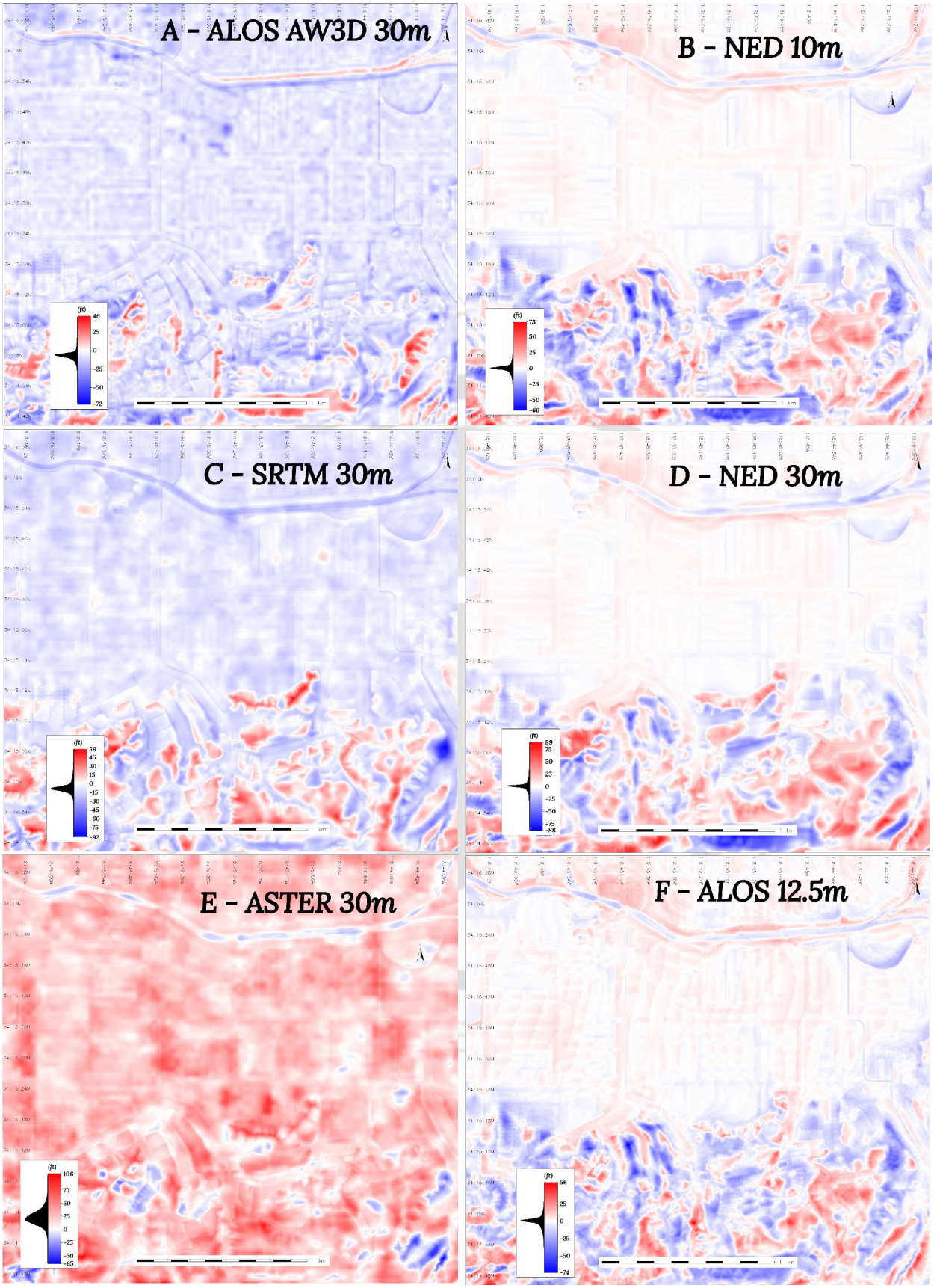

Figure CF19. Maps of difference in elevation about observed data (Observed - DEMs) for Simivalley area. A) ALOS AW3D, 30 m resolution; B) NED, 10 m resolution; C) SRTM, 30 m resolution; D) NED, 30 m resolution; E) ASTER, 30 m resolution; F) ALOS, 12.5 m resolution.

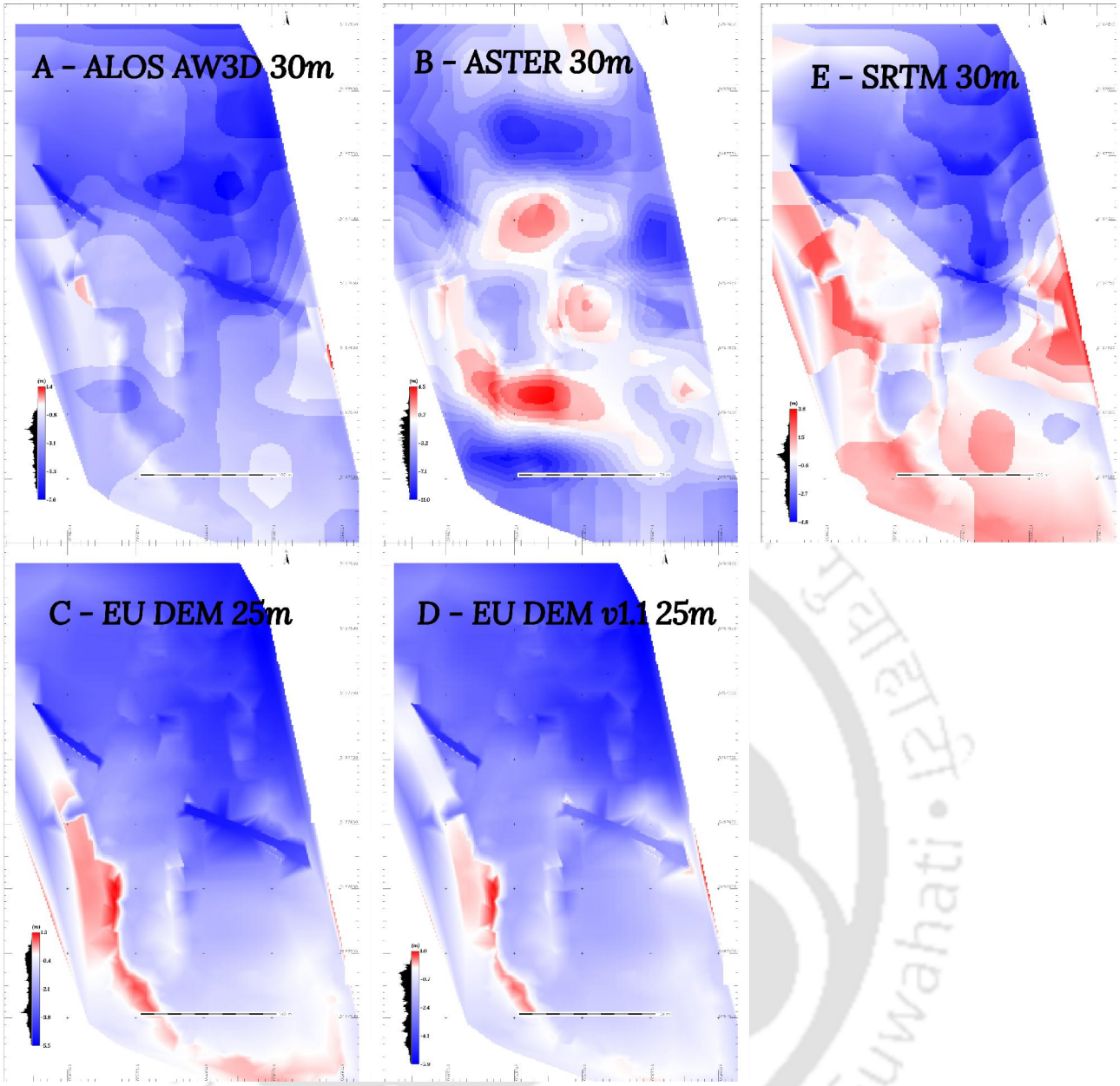

Figure CF20. Maps of difference in elevation about observed data (Observed - DEMs) for Riom area. A) ALOS AW3D, 30 m resolution; B) ASTER, 30 m resolution; C) EU DEM, 25 m resolution; D) EU DEM v1.1, 25 m resolution; E) SRTM, 30 m resolution.

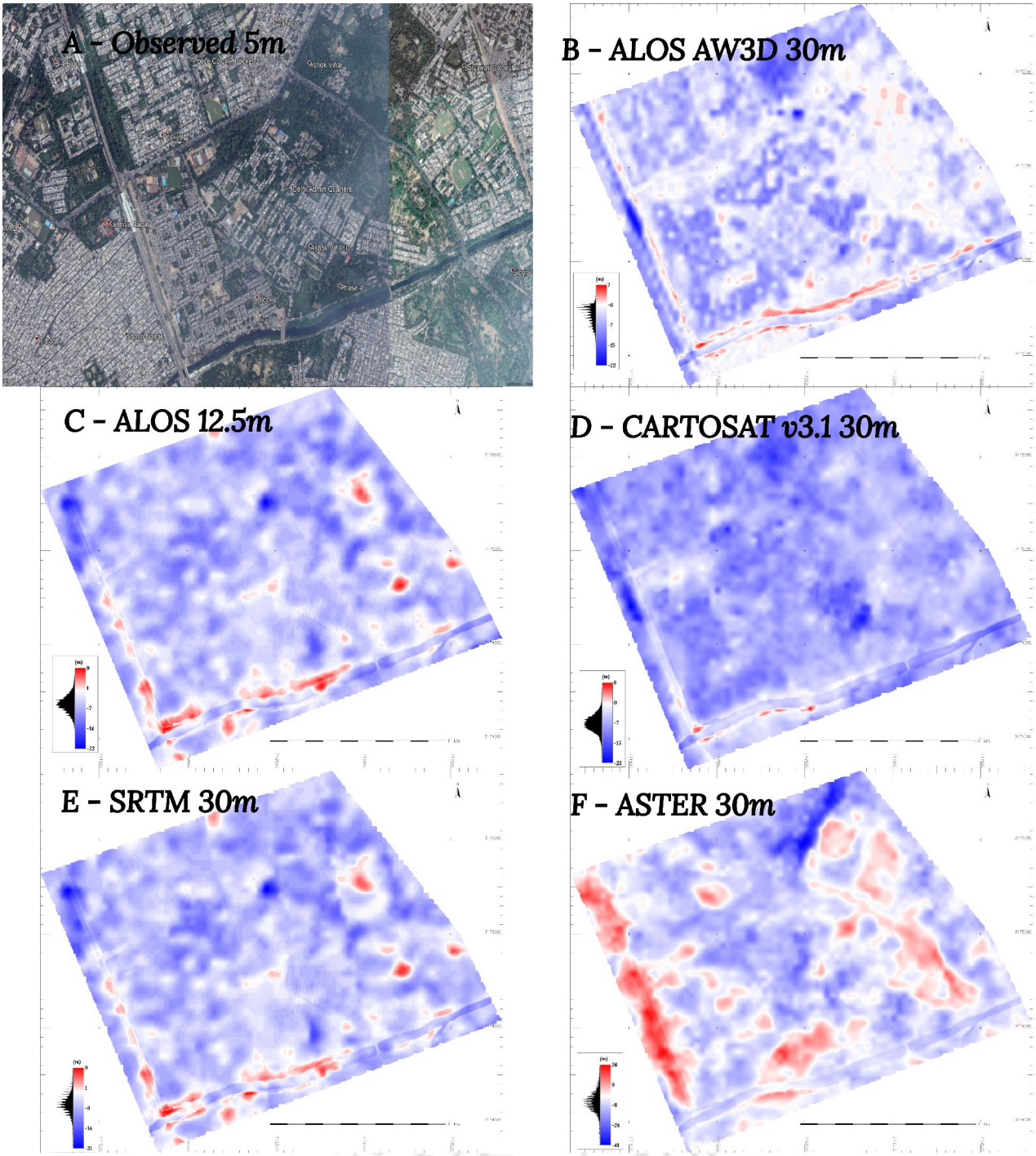

Figure CF21. Maps of difference in elevation about observed data (Observed - DEMs) for Ashok Vihar, New Delhi area. A) Google Earth image; B) ALOS AW3D, 30 m resolution; C) ALOS, 12.5 m resolution; D) CARTOSAT v3R1, 30 m resolution; E) SRTM, 30 m resolution; F) ASTER, 30 m resolution.

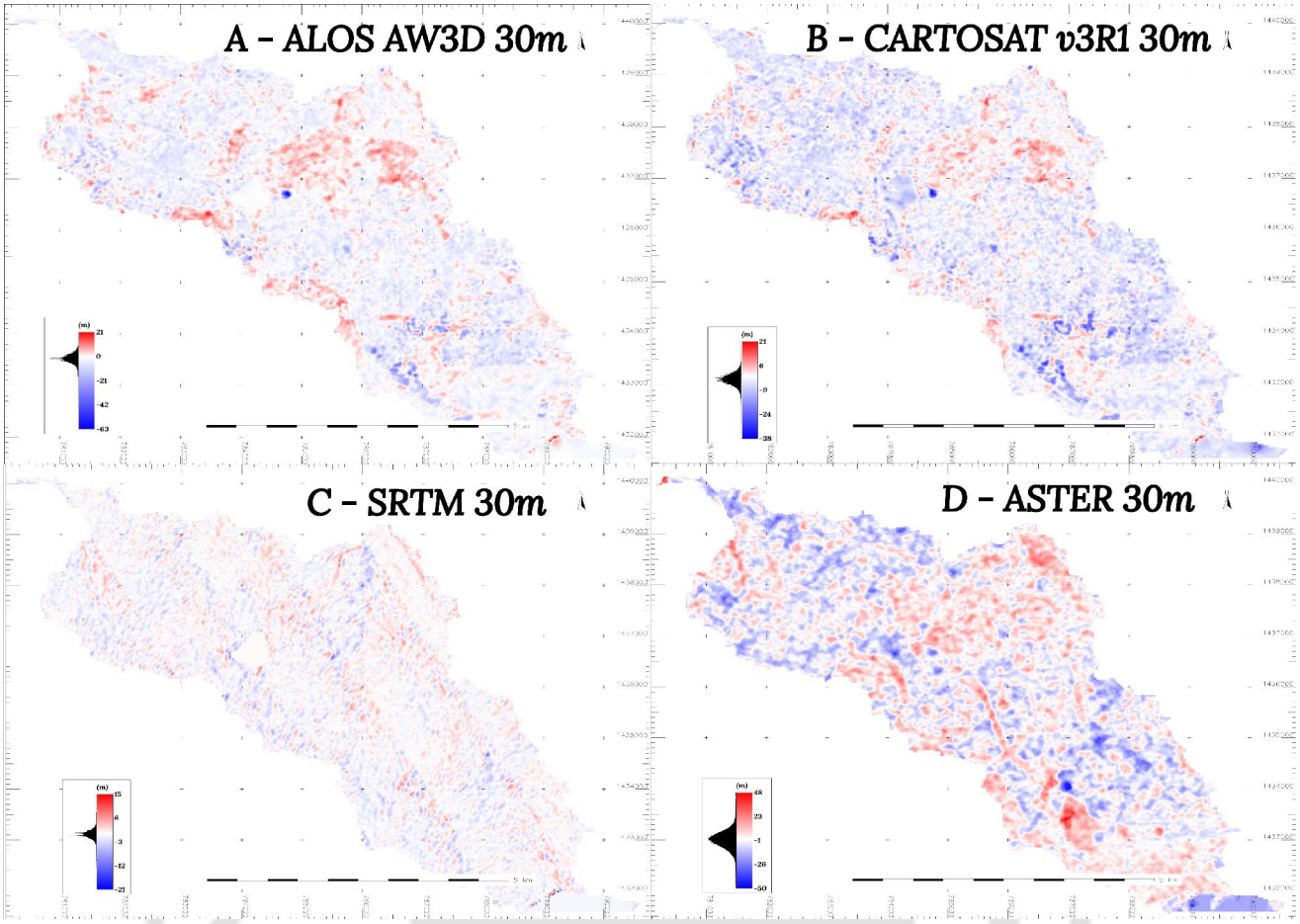

Figure CF22. Maps of difference in elevation about ALOS 12.5m data (ALOS 12.5m - DEMs) for Challagatta Valley, Bangalore, India area. A) ALOS AW3D, 30 m resolution; B) CARTOSAT v3R1, 30 m resolution; C) SRTM, 30 m resolution; D) ASTER, 30 m resolution.

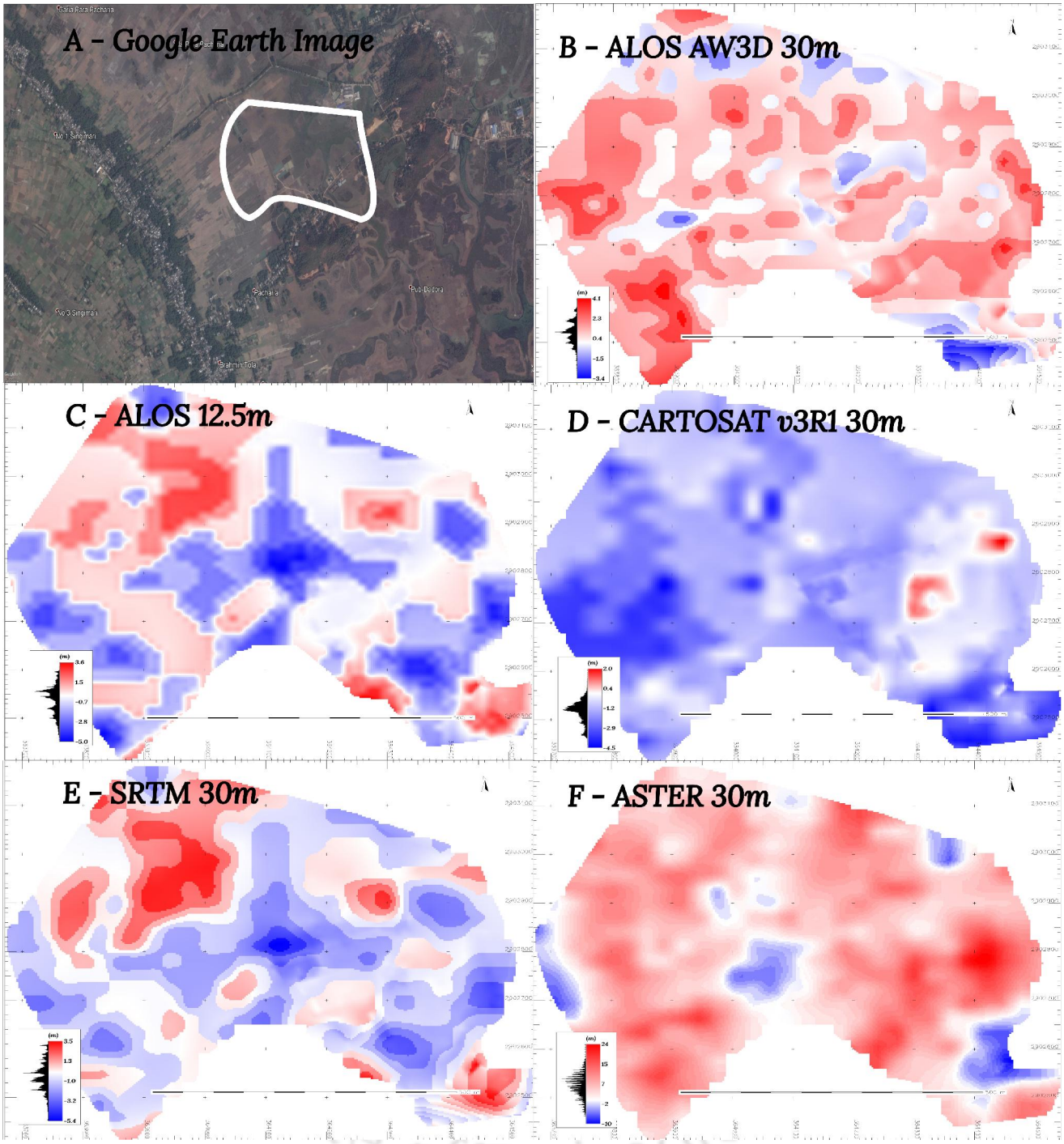

Figure CF23. Maps of difference in elevation about observed data (Observed - DEMs) for Pachoria, Guwahati area. A) Google Earth image; B) ALOS AW3D, 30 m resolution; C) ALOS, 12.5 m resolution; D) CARTOSAT v3R1, 30 m resolution; E) SRTM, 30 m resolution; F) ASTER, 30 m resolution.

C.17 Histograms of DoD about to observed or surveyed topographic data

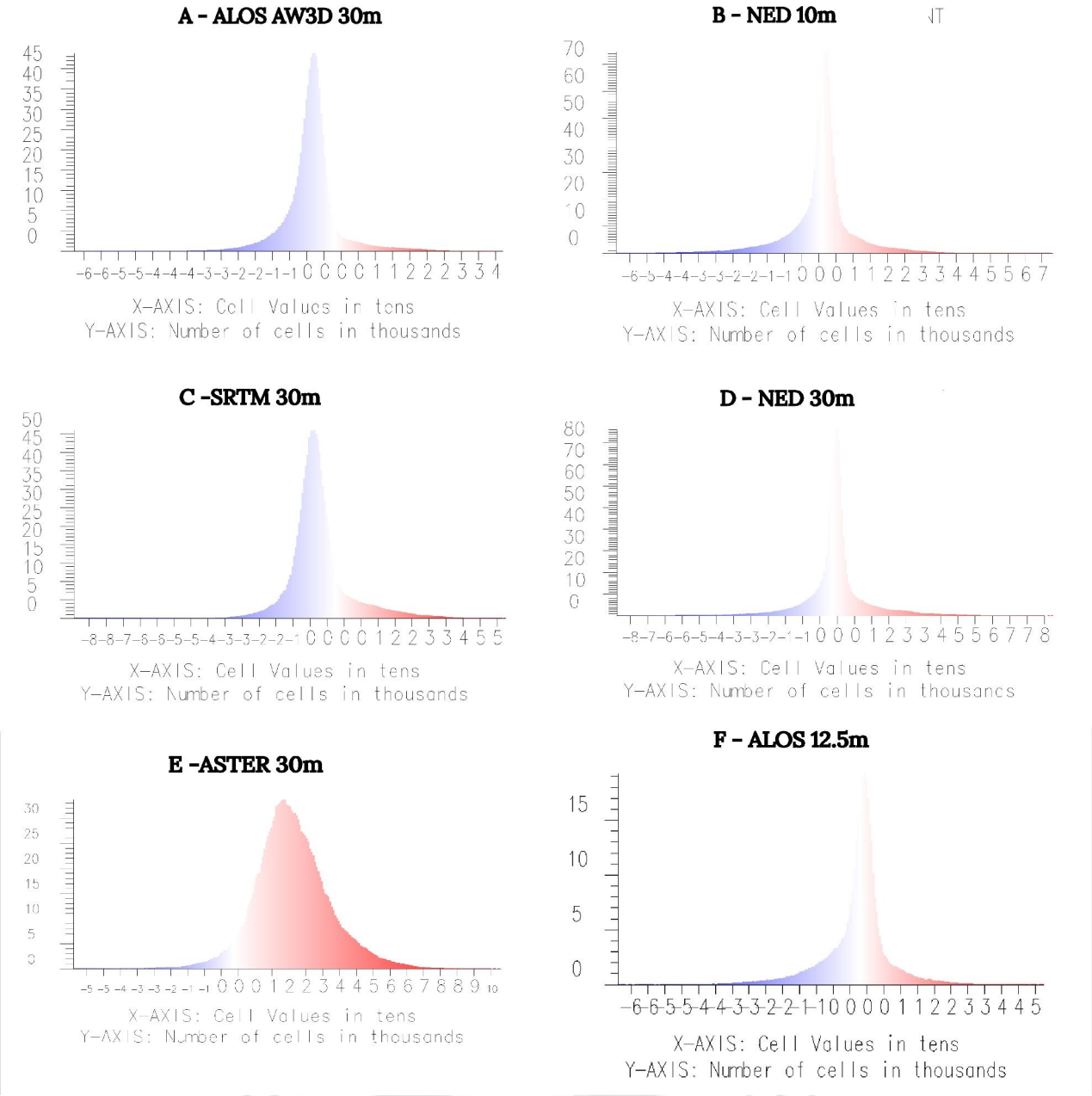

Figure CF24. Histograms of difference in elevation about observed data (Observed - DEMs) for Simivalley area. A) ALOS AW3D, 30 m resolution; B) NED, 10 m resolution; C) SRTM, 30 m resolution; D) NED, 30 m resolution; E) ASTER, 30 m resolution; F) ALOS, 12.5 m resolution.

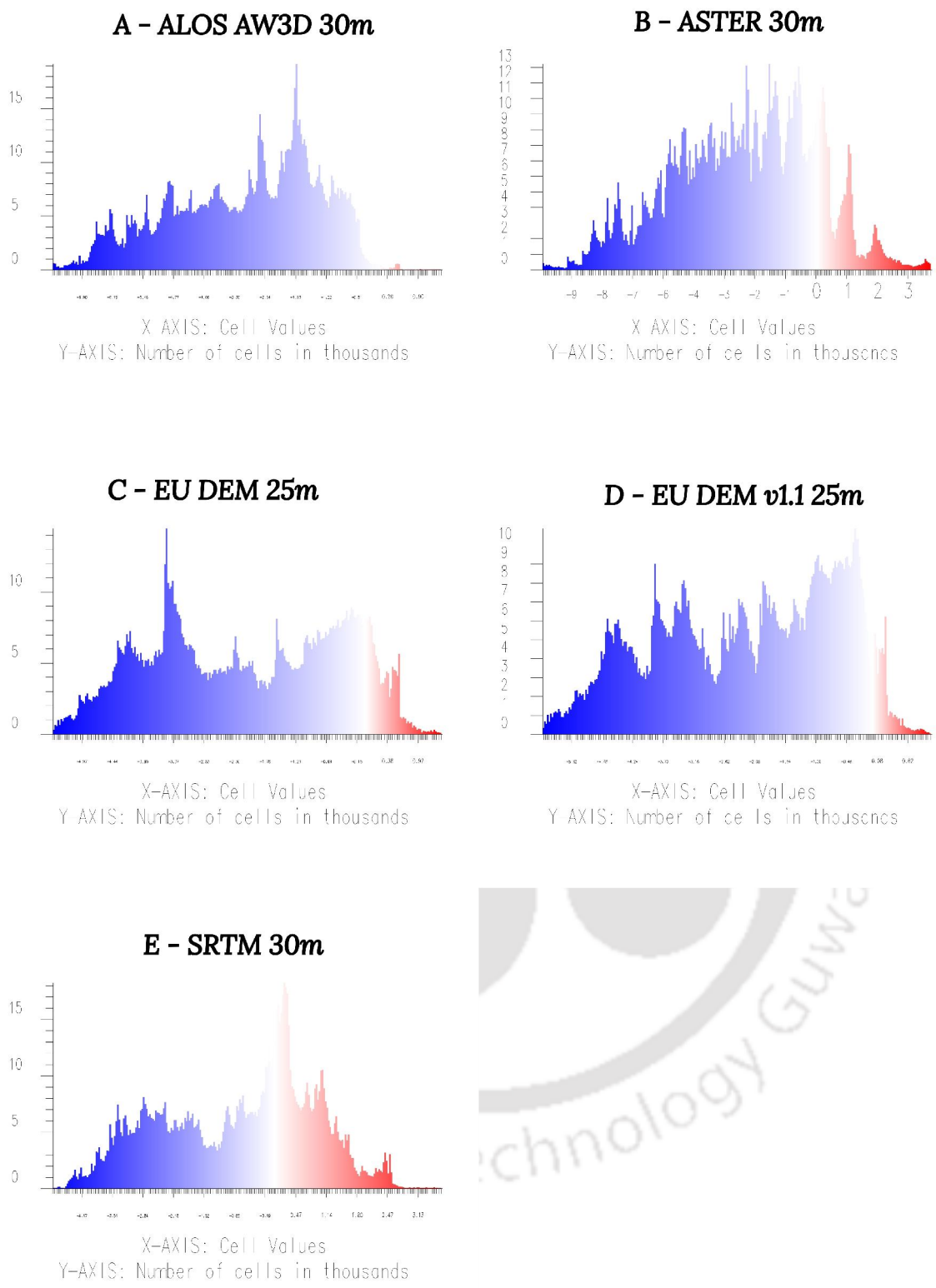

Figure CF25. Histograms of difference in elevation about observed data (Observed - DEMs) for Riom area. A) ALOS AW3D, 30 m resolution; B) ASTER, 30 m resolution; C) EU DEM, 25 m resolution; D) EU DEM v1.1, 25 m resolution; E) SRTM, 30 m resolution.

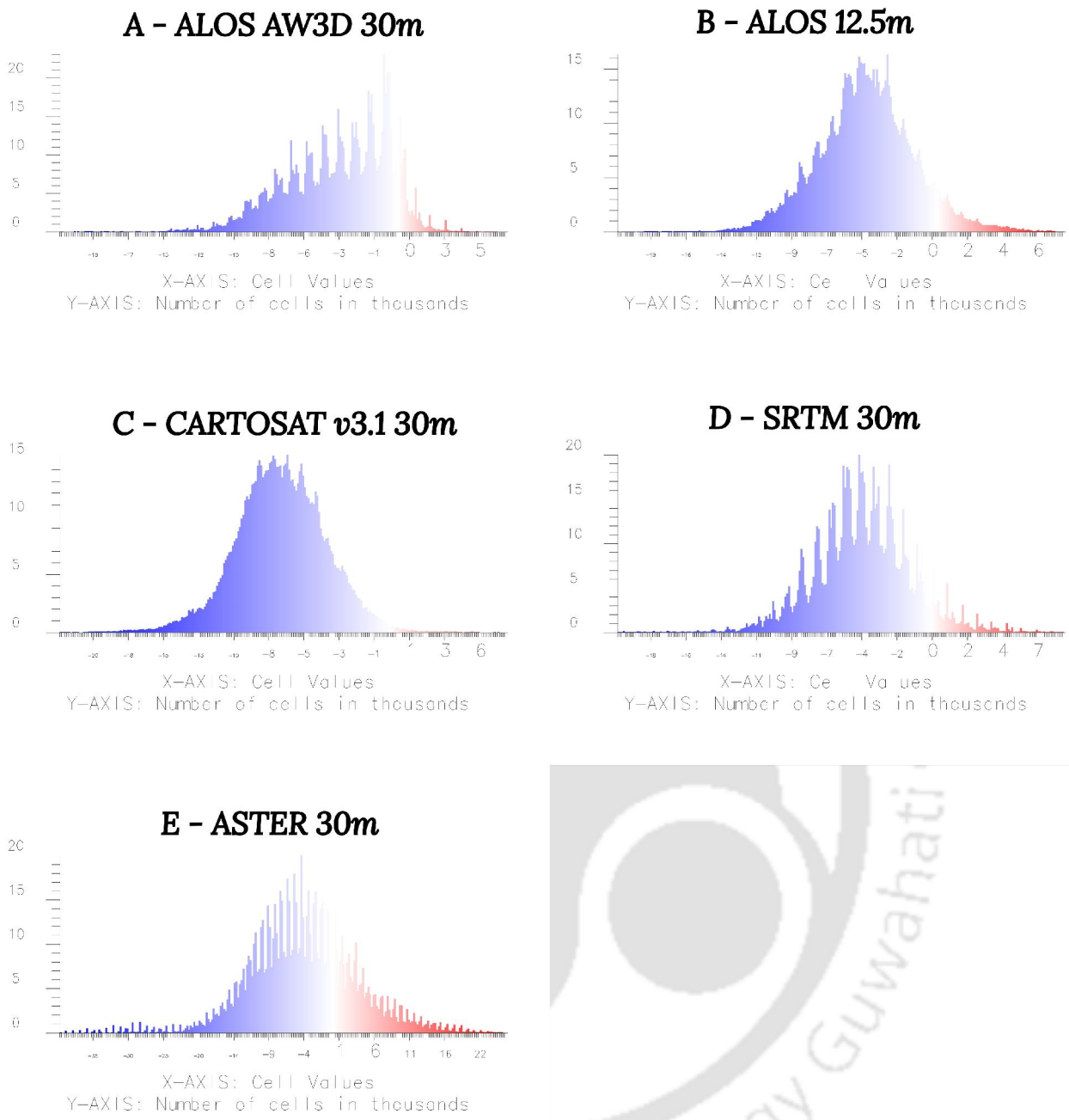

Figure CF26. Histograms of difference in elevation about observed data (Observed - DEMs) for Ashok Vihar, New Delhi area. A) ALOS AW3D, 30 m resolution; B) ALOS, 12.5 m resolution; C) CARTOSAT v3R1, 30 m resolution; D) SRTM, 30 m resolution; E) ASTER, 30 m resolution.

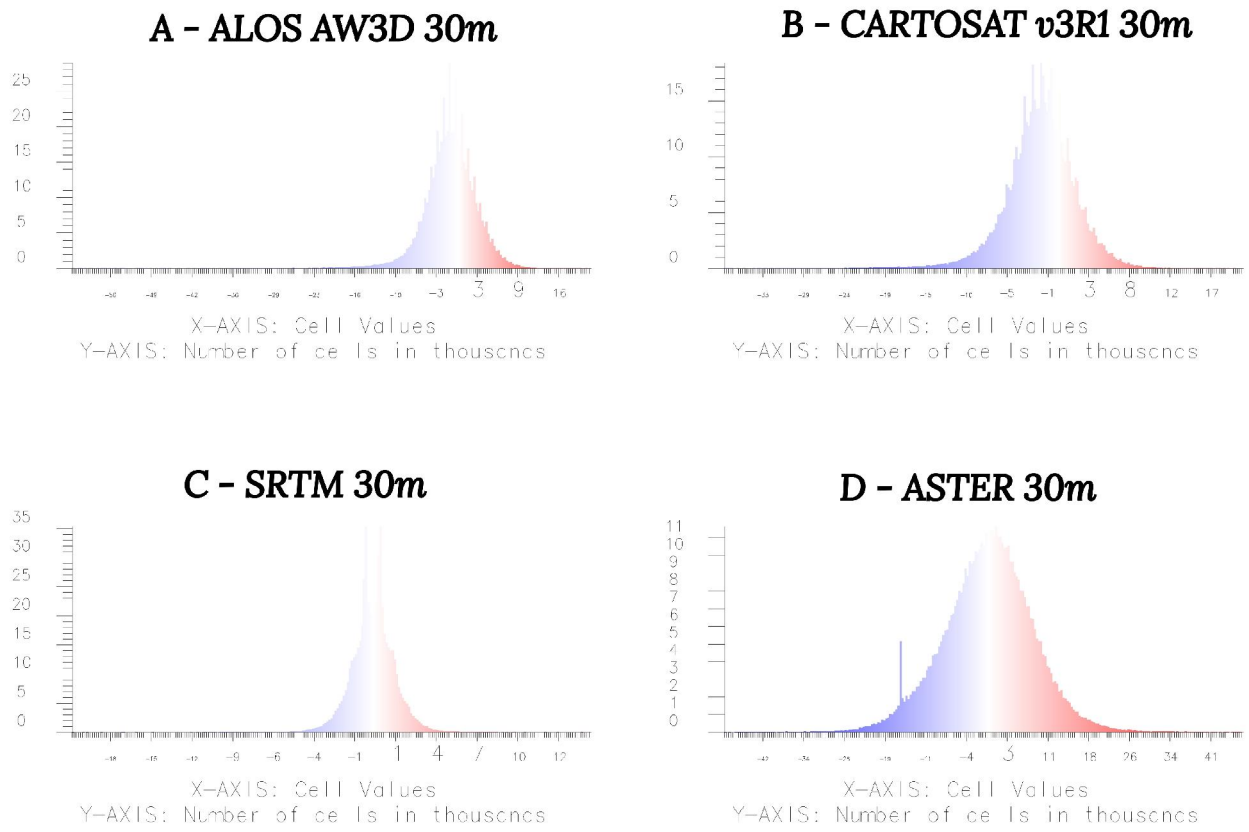

Figure CF27. Histograms of difference in elevation about ALOS 12.5m data (ALOS 12.5m - DEMs) for Challagatta Valley, Bangalore, India area. A) ALOS AW3D, 30 m resolution; B) CARTOSAT v3R1, 30 m resolution; C) SRTM, 30 m resolution; D) ASTER, 30 m resolution.

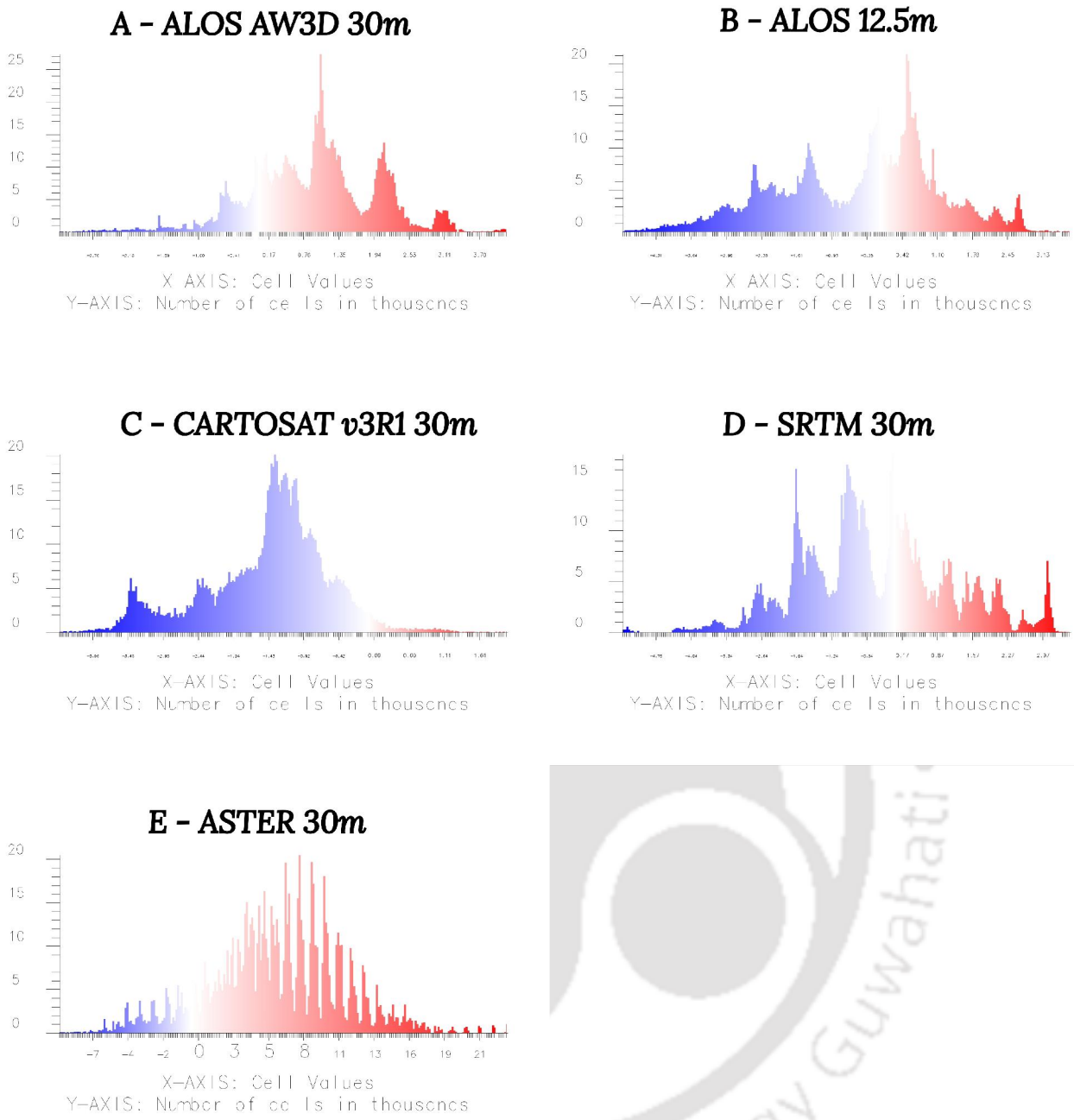

Figure CF28. Histograms of difference in elevation about observed data (Observed - DEMs) for Pachoria, Guwahati area. A) ALOS AW3D, 30 m resolution; B) ALOS, 12.5 m resolution; C) CARTOSAT v3R1, 30 m resolution; D) SRTM, 30 m resolution; E) ASTER, 30 m resolution.

C.18 Scatterplots of Aspect × Differences

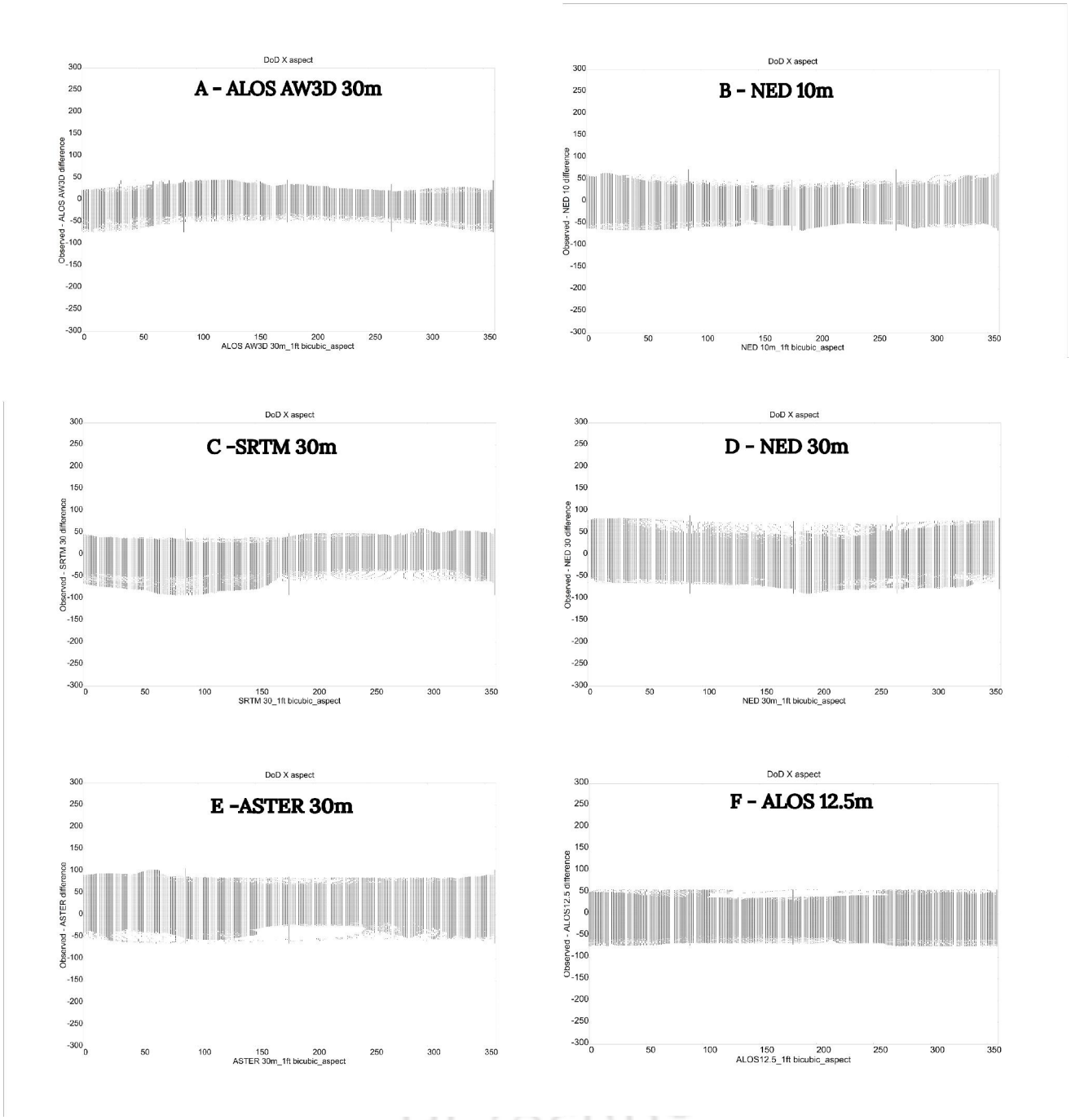

Figure CF29. Scatterplots of aspect × DoDs for Simivalley area. A) ALOS AW3D, 30 m resolution; B) NED, 10 m resolution; C) SRTM, 30 m resolution; D) NED, 30 m resolution; E) ASTER, 30 m resolution; F) ALOS, 12.5 m resolution.

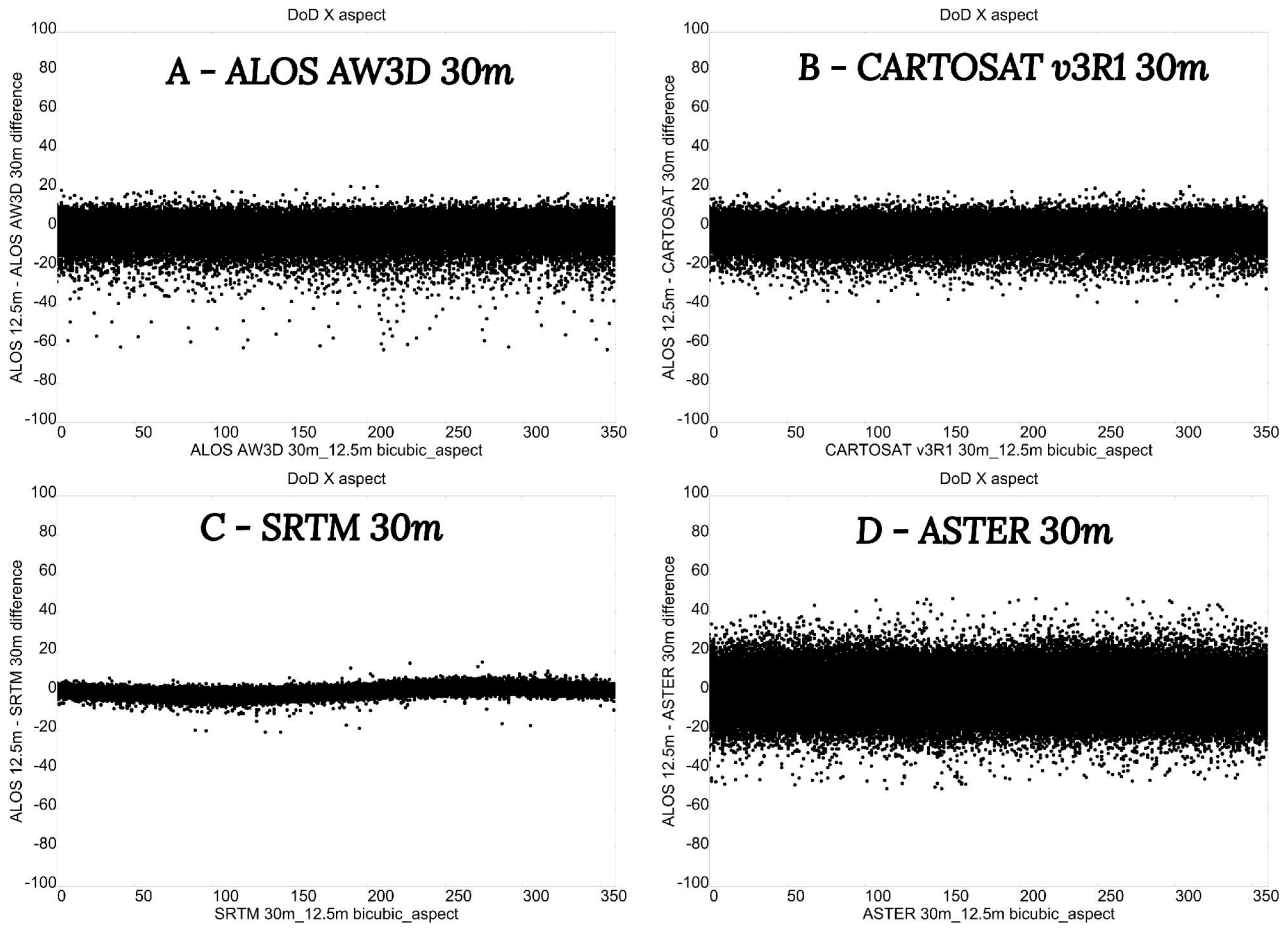

Figure CF30. Scatterplots of aspect × DoDs for Challagatta Valley, Bangalore, India area. A) ALOS AW3D, 30 m resolution; B) CARTOSAT v3R1, 30 m resolution; C) SRTM, 30 m resolution; D) ASTER, 30 m resolution.

C.19 Scatterplots of Elevation between Observed and other DEMs

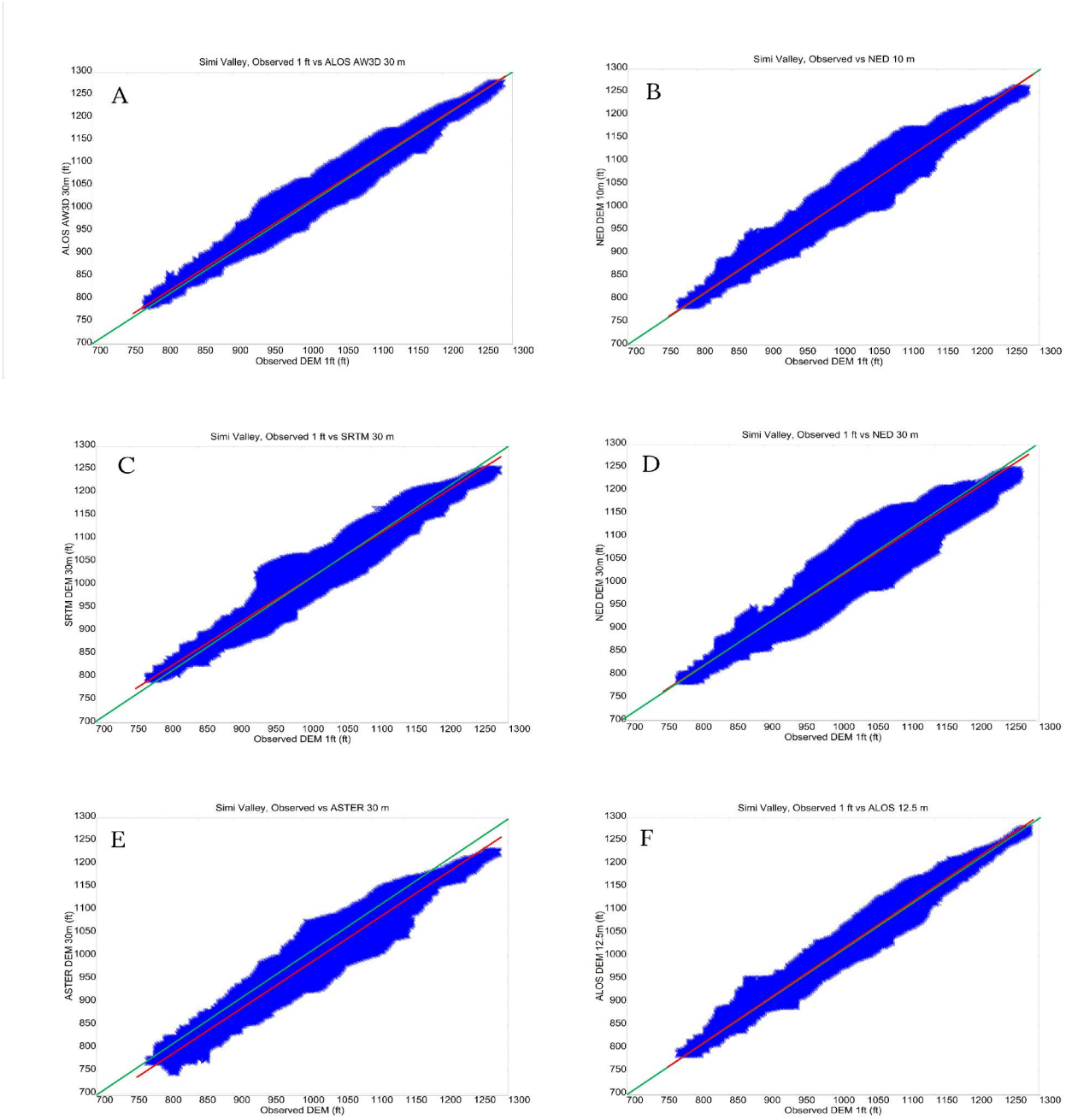

Figure CF31. Scatterplots of elevation for Simivalley area. A) ALOS AW3D, 30 m resolution; B) NED, 10 m resolution; C) SRTM, 30 m resolution; D) NED, 30 m resolution; E) ASTER, 30 m resolution; F) ALOS, 12.5 m resolution.

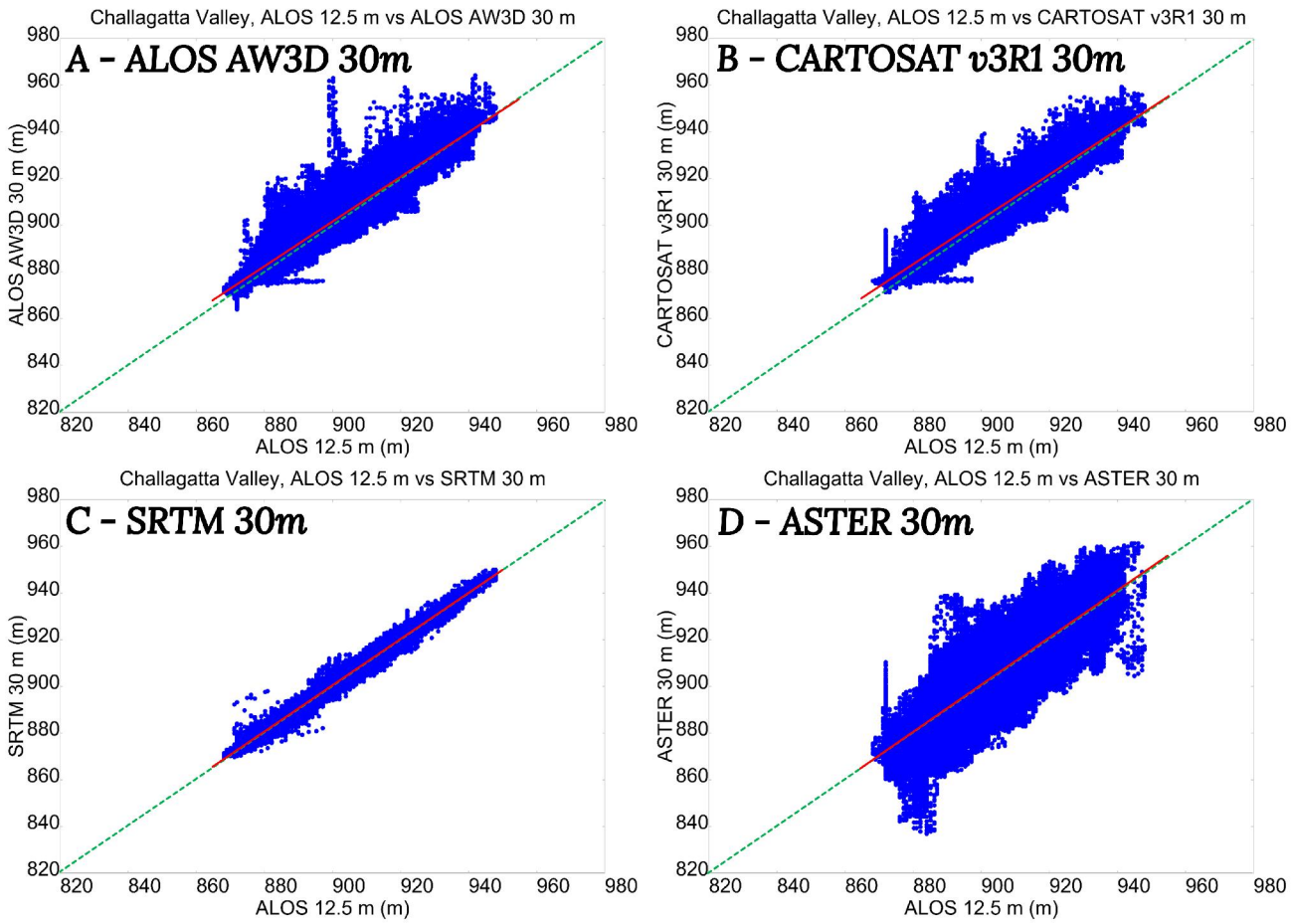

Figure CF32. Scatterplots of elevation for Challagatta Valley, Bangalore, India area. A) ALOS AW3D, 30 m resolution; B) CARTOSAT v3R1, 30 m resolution; C) SRTM, 30 m resolution; D) ASTER, 30 m resolution.

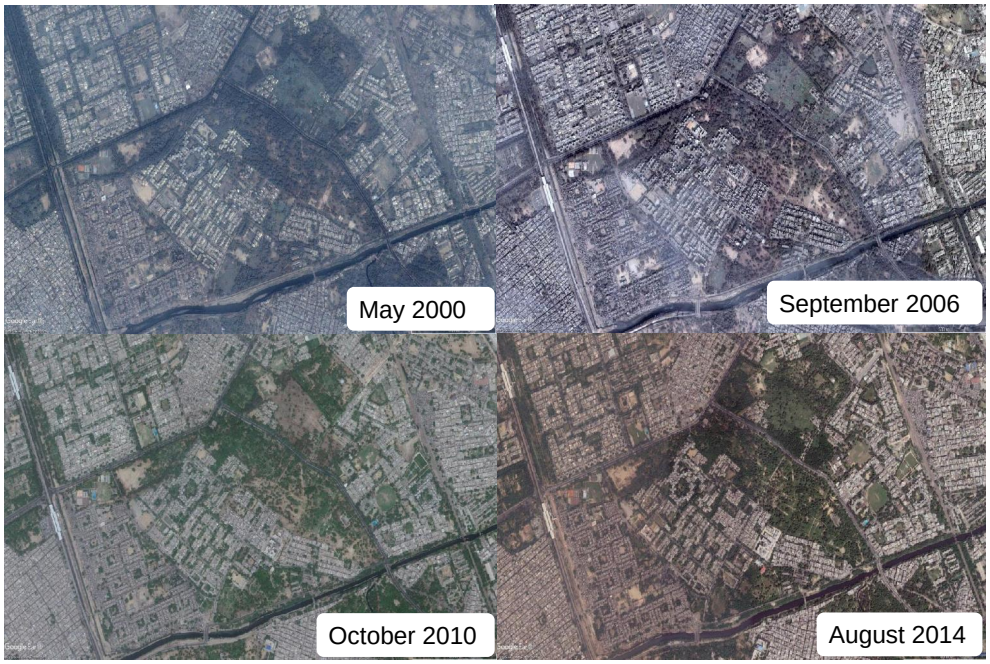

Figure CF33. Natural Changes in the environment at Ashok Vihar, New Delhi, India. ©Powered by Google Earth

C.20 Storage - Elevation Curves

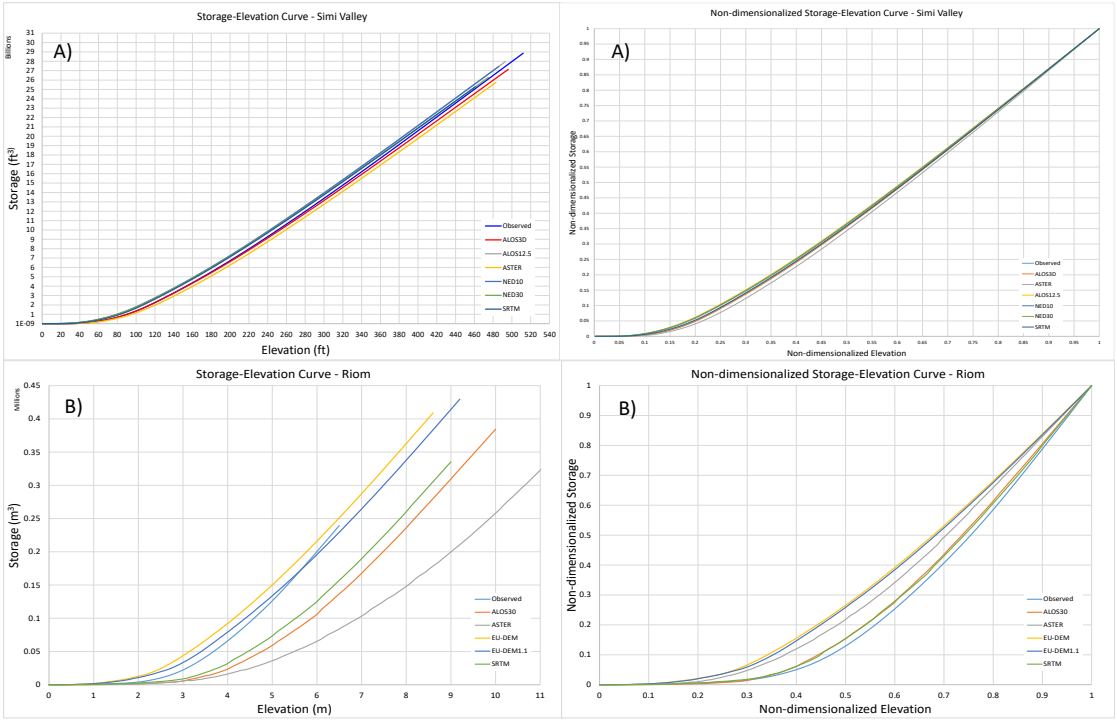

Figure CF34. Storage-Elevation curves: dimensional and non-dimensional for Simi Valley urban watershed

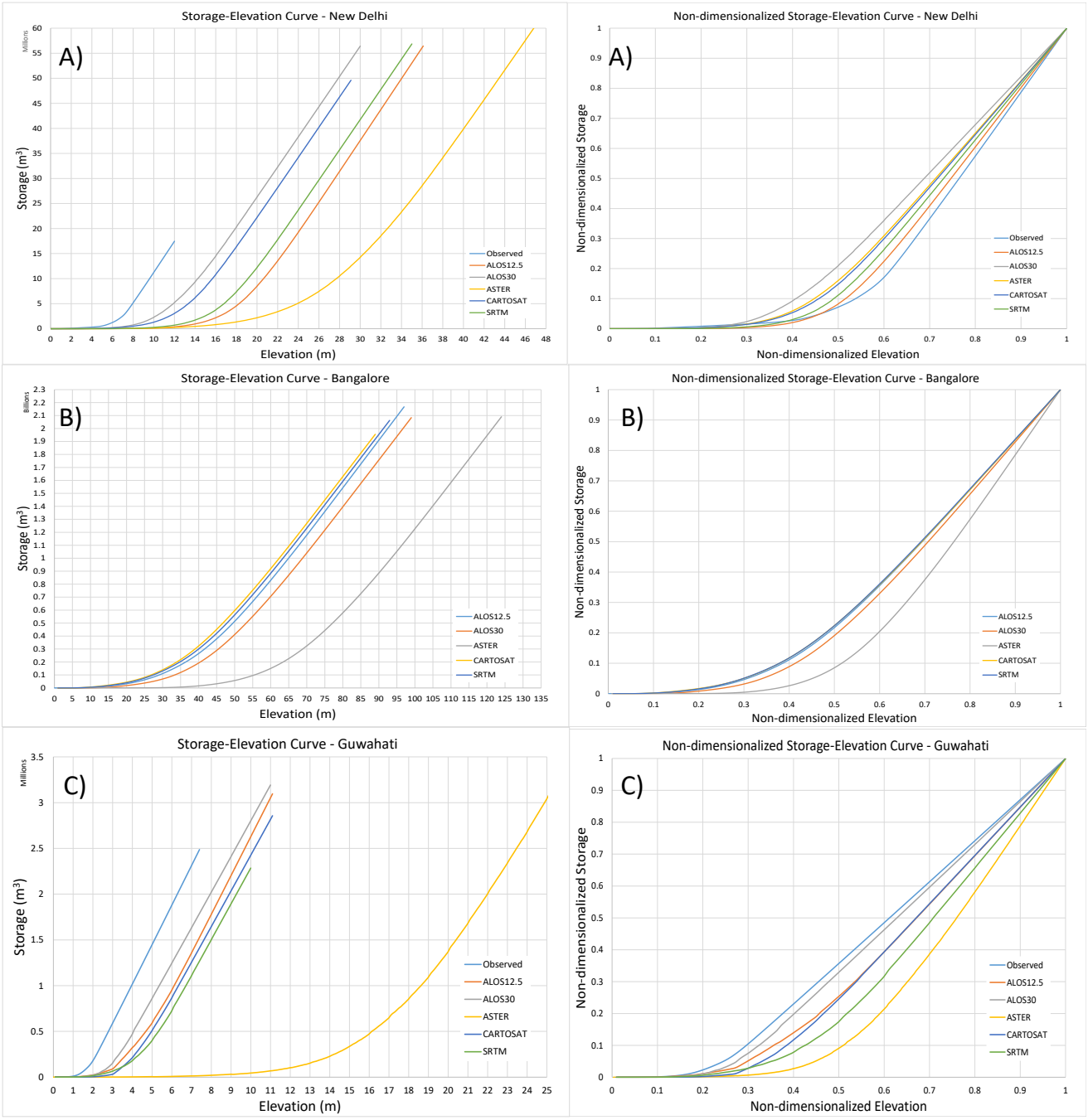

Figure CF35. Storage-Elevation curves: dimensional and non-dimensional for A) New Delhi; B) Bangalore; C) Pachoria, Guwahati

Appendix D

INFLUENCE OF DEMs ON SWMM MODEL

Abstract-TH-2793_156104035

D.1 Descriptive Statistics Tables of model simulated depths

DEM	Minimum	p25	Median	p75	Maximum	Mean	Std dev	RMSE	ME	MAE	STDE
Surveyed	0.00	0.02	0.07	0.16	3.61	0.14	0.26				
ALOS 12.5m	0.00	0.03	0.06	0.10	4.25	0.09	0.19	0.13	-0.02	0.07	0.13
ALOS AW3D 30m	0.00	0.02	0.08	0.32	5.33	0.35	0.75	0.15	0.02	0.06	0.15
ASTER 30m	0.00	0.05	0.23	1.29	9.14	1.03	1.63	0.96	-0.21	0.28	0.94
NED 10m	0.00	0.02	0.05	0.09	3.61	0.08	0.18	0.11	-0.01	0.07	0.11
NED 30m	0.00	0.02	0.04	0.08	4.20	0.08	0.21	0.11	0.01	0.06	0.11
SRTM 30m	0.00	0.01	0.05	0.32	9.47	0.38	0.93	0.20	0.02	0.06	0.20

Table DT1. Descriptive statistics of model simulated depths - Simi Valley Urban, California.

DEM	Minimum	p25	Median	p75	Maximum	Mean	Std dev
Surveyed	0.01	0.56	0.94	1.49	3.44	1.14	0.86
ALOS AW3D 30m	0.01	0.64	1.33	2.19	3.46	1.49	0.97
SRTM 30m	0.01	0.48	0.81	1.77	2.81	1.09	0.81

Table DT2. Descriptive statistics of model simulated depths – Riom City, France.

DEM	Minimum	p25	Median	p75	Maximum	Mean	Std dev	RMSE	ME	MAE	STDE
Surveyed	0.25	0.68	1.09	1.46	1.9	1.05	0.54				
ALOS 12.5m	0.25	0.41	0.76	0.99	1.5	0.74	0.37	0.74	-0.25	0.62	0.72
ALOS AW3D 30m	0.22	0.435	0.59	0.82	2.08	0.71	0.47	0.57	-0.28	0.44	0.51
CARTOSAT	0.14	0.38	0.54	1.13	1.51	0.67	0.44	0.68	-0.32	0.53	0.61
SRTM 30m	0.08	0.35	0.59	0.91	1.5	0.66	0.44	0.79	-0.38	0.68	0.72

Table DT3. Descriptive statistics of model simulated depths – New Delhi, India.

DEM	Minimum	p25	Median	p75	Maximum	Mean	Std dev	RMSE	ME	MAE	STDE
Surveyed	0.18	0.33	0.49	0.57	0.82	0.46	0.17				
ALOS 12.5m	0.05	0.18	0.33	0.62	2.8	0.62	0.77	0.79	0.15	0.46	0.80
ALOS AW3D 30m	0.15	0.29	0.45	0.79	2	0.64	0.49	0.54	0.18	0.31	0.53
ASTER 30m	0.05	0.14	0.28	0.52	2.68	0.54	0.74	0.71	0.08	0.43	0.73
CARTOSAT	0.1	0.24	0.45	0.92	3.02	0.75	0.85	0.84	0.28	0.46	0.82
SRTM 30m	0.19	0.34	0.5	0.73	2.7	0.72	0.66	0.66	0.26	0.35	0.62

Table DT4. Descriptive statistics of model simulated depths – Bangalore, India.

DEM	Minimum	p25	Median	p75	Maximum	Mean	Stddev	RMSE	ME	MAE	STDE
Surveyed	0.02	0.12	0.24	0.34	0.57	0.24	0.14				
ALOS 12.5m	0.01	0.03	0.08	0.49	0.94	0.24	0.25	0.26	0.00	0.20	0.26
ALOS AW3D30m	0.01	0.03	0.2	0.36	0.8	0.24	0.24	0.27	0.00	0.21	0.27
ASTER 30m	0.01	0.03	0.06	0.50	0.82	0.22	0.25	0.26	-0.04	0.21	0.26
CARTOSAT	0.01	0.06	0.5	0.64	0.78	0.38	0.28	0.30	0.13	0.24	0.28
SRTM 30m	0.01	0.04	0.09	0.44	0.8	0.22	0.24	0.25	-0.02	0.21	0.26

Table DT5. Descriptive statistics of model simulated depths – Jorhat, India

D.2 Peaks and Error metrics Table of model simulated peaks and hydrographs at outlet

Study Area	Dataset	Peaks (m^3/s)	ME	MAE	RMSE
Simi Valley, USA	Surveyed	18.30			
	ALOS 12.5m	16.16	-0.40	0.40	0.42
	ALOS AW3D 30m	21.92	0.02	0.02	0.08
	ASTER 30m	3.44	-2.46	2.46	2.50
	NED 10 m	15.36	-0.05	0.05	0.14
	NED 30 m	16.31	-0.19	0.19	0.21
	SRTM 30m	21.98	0.03	0.03	0.11
Ashok Vihar, New Delhi, India	Surveyed	4.31			
	ALOS 12.5m	4.25	-0.58	0.59	0.82
	ALOS AW3D 30m	4.1	-0.12	0.17	0.24
	CARTOSAT 30m	3.11	-0.40	0.41	0.64
	SRTM 30m	3.09	-0.77	0.77	1.07
Riom, France	Surveyed	54.95			
	ALOS AW3D 30m	28.66	-7.32	7.34	12.50
	SRTM 30m	9.26	-11.74	11.74	20.19
Challagatta Valley, Bangalore, India	Surveyed	22.23			
	ALOS 12.5m	8.46	-0.53	0.53	1.67
	ALOS AW3D 30m	21.64	0.00	0.01	0.03
	ASTER 30m	5.78	-0.64	0.64	1.98
	CARTOSAT 30m	6.37	-0.61	0.61	1.91
	SRTM 30m	22.23	0.00	0.01	0.06
Jorhat, India	Surveyed	0.85			
	ALOS 12.5m	0.31	-0.10	0.10	0.21
	ALOS AW3D 30m	0.16	-0.13	0.13	0.26
	ASTER 30m	0.02	-0.14	0.14	0.30
	CARTOSAT 30m	0.01	-0.15	0.15	0.31
	SRTM 30m	0.33	-0.09	0.09	0.20

*ME: Mean Error; RMSE: Root Mean Square Error; MAE: Mean Absolute Error;

Table DT6. Error metrics of selected DEMs with respect to surveyed data by assuming DoDs distributed normally.

Abstract-TH-2793_156104035

This Page Intentionally Left Blank

Abstract-TH-2793_156104035

Appendix E
DISTRIBUTED URBAN HYDROLOGICAL MODEL

Abstract-TH-2793_156104035

E.1 Manning Roughness and Impervious Factor values for each Land Use and Land Cover subclasses

Class	Impervious Factor	Roughness category	Manning's Roughness	*n* Range	Reference
Building Roofs					
Asphalt	1	-	0.011	-	MuCuen et al. [1996] - PCSWMM
Concrete	1	Ordinary Concrete	0.013	-	MuCuen et al. [1996] - PCSWMM
	1	Smooth Concrete	0.012	-	MuCuen et al. [1996] - PCSWMM
	1	Rough Concrete	0.017	-	MuCuen et al. [1996] - PCSWMM
Tile Roof Clay Roof Vitrified Clay	1 1 1	-	0.015	-	-
Metal Roof	1	Steel Roof	-	-	-
Roads and Pavements					
Asphalt Road	1	Smooth Asphalt	0.011	-	-
	1	Rough Asphalt	0.017	-	Open Channels, ASCE (1982) – PCSWMM
Concrete Road	1	-	0.017	-	Yen [2001], SWMM Hydrology Manual
	1	Ordinary Concrete	0.013	-	-
Rough Concrete Road	1	-	0.017	-	-
Cement Rubble Surface Road	1	Cement Rubble Surface	0.024	-	-
Perforated Blocks Pavement	1	-	-	-	-
Permeable Pavement	1	Permeable Road	-	-	-
Parking Lots					
Perforated Blocks Parking Lot	1	Perforated Blocks	-	-	-
Permeable Surface	1	-	-	-	-
Good Wood	1	-	0.014	-	MuCuen et al. [1996] - PCSWMM
Cast Iron	1	-	0.015	-	MuCuen et al. [1996] - PCSWMM
Brick with Cement Mortar	1	-	0.014	-	MuCuen et al. [1996] - PCSWMM

Abstract-TH-2793_156104035

Open Land					
Fallow Soil	0	-	0.05	-	MuCuen et al. [1996] - PCSWMM
Natural Cultivated Soil	0	-	0.13	-	MuCuen et al. [1996] - PCSWMM
Packed Clay	0	-	0.03	-	Crawford & Linsley [1966], SWMM Manual
Bare Sand	0	-	0.010	-	Engman [1986], SWMM Hydrology Manual
Graveled Surface	0	-	0.020	-	Engman [1986], SWMM Hydrology Manual
Erodible Bar Clay-Loam	0	-	0.020	-	Engman [1986], SWMM Hydrology Manual
Smooth Impervious Surface	0	-	0.013	-	Yen [2001], SWMM Hydrology Manual
Rough Impervious Surface	0	-	0.019	-	Yen [2001], SWMM Hydrology Manual
Smooth Bare Packed Soil	0	-	0.021	-	Yen [2001], SWMM Hydrology Manual
Rough Bare Packed Soil	0	-	0.038	-	Yen [2001], SWMM Hydrology Manual
Moderate Bare Packed Soil	0	-	0.030	-	Yen [2001], SWMM Hydrology Manual
Gravel Soil	0	-	0.032	-	Yen [2001], SWMM Hydrology Manual
Vegetation					
Sparse Vegetation	0	-	0.0585	0.032 – 0.071	Sarkar & Dutta, [2008] ASCE Journal
Moderate Vegetation	0	-	0.062	0.039 – 0.085	Sarkar & Dutta, [2008] ASCE Journal
Dense Vegetation	0	-	0.077	0.044 – 0.110	Sarkar & Dutta, [2008] ASCE Journal
Short Grass	0	-	0.15	-	MuCuen et al. [1996] - PCSWMM
Dense Grass	0	-	0.24	-	MuCuen et al. [1996] - PCSWMM
Bermuda Grass	0	-	0.41	-	MuCuen et al. [1996] - PCSWMM
Light Underbush Woods	0	-	0.40	-	MuCuen et al. [1996] - PCSWMM
Dense Underbush Woods	0	-	0.80	-	MuCuen et al. [1996] - PCSWMM
Light Turf	0	-	0.20	-	Crawford & Linsley [1966], SWMM Manual
Dense Turf	0	-	0.35	-	Crawford & Linsley [1966], SWMM Manual

Abstract-TH-2793_156104035

Dense Shrub	0	-	0.4	-	Crawford & Linsley [1966], SWMM Manual
Forest litter	0	-	0.4	-	Crawford & Linsley [1966], SWMM Manual
Bluegrass Sod	0	-	0.45	-	Engman [1986], SWMM Hydrology Manual
Short Grass Prairie	0	-	0.15	-	Engman [1986], SWMM Hydrology Manual
Mowed Poor Grass	0	-	0.038	-	Yen [2001], SWMM Hydrology Manual
Average Grass	0	-	0.050	-	Yen [2001], SWMM Hydrology Manual
Closely Clipped Sod	0	-	0.050	-	Yen [2001], SWMM Hydrology Manual
Pasture	0	-	0.055	-	Yen [2001], SWMM Hydrology Manual
Timberland	0	-	0.090	-	Yen [2001], SWMM Hydrology Manual
Residential and Commercial					
Business Land	1	-	0.022	-	Yen [2001], SWMM Hydrology Manual
Semi-Business Land	1	-	0.035	-	Yen [2001], SWMM Hydrology Manual
Industrial Land	1	-	0.035	-	Yen [2001], SWMM Hydrology Manual
Dense Residential Land	1	-	0.040	-	Yen [2001], SWMM Hydrology Manual
Suburban Residential Land	1	-	0.055	-	Yen [2001], SWMM Hydrology Manual
Park	0	-	0.075	-	Yen [2001], SWMM Hydrology Manual
Lawn	0	-	0.075	-	Yen [2001], SWMM Hydrology Manual
Waterbody	0	-	0.035	-	Kalyanapu et al. [2009]; Shen et al. [2017]
Wetland	0	-	-	-	-
Swamp	0	-	0.270	-	Mtamba et al. [2015]
Open Land	0	-	-	-	-

Table ET1. Manning's roughness coefficients and impervious factors used in the hydrological model

Abstract-TH-2793_156104035

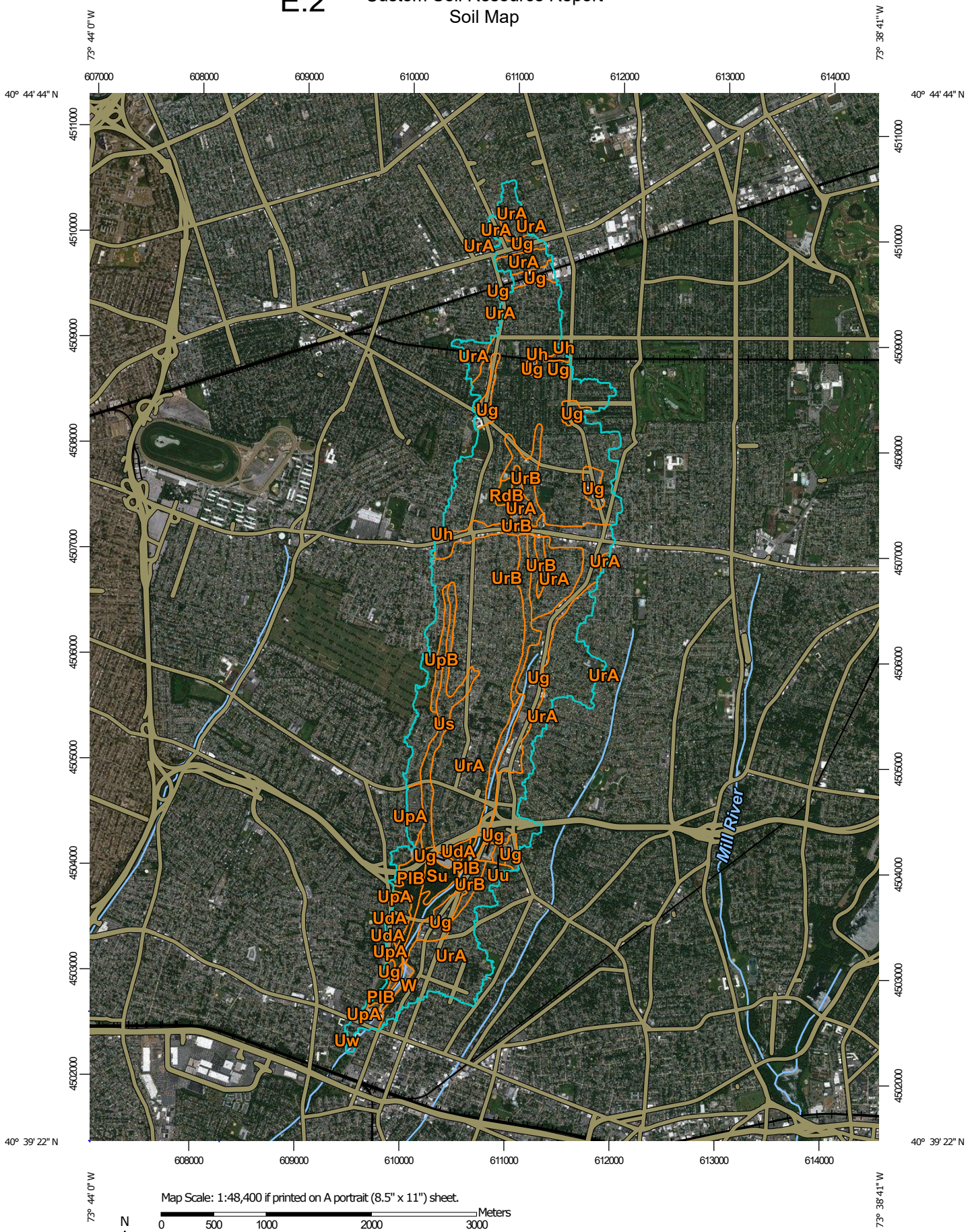
73° 44' 0" W
73° 38' 41" W
40° 44' 44" N
40° 39' 22" N
607000
608000
609000
610000
611000
612000
613000
614000
4511000
4510000
4509000
4508000
4507000
4506000
4505000
4504000
4503000
4502000
UrA
Ug
Uh
UrB
RdB
UpB
Us
UpA
UdA
PIB
Su
Uu
W
Uw
Mill River
Map Scale: 1:48,400 if printed on A portrait (8.5" x 11") sheet.
N
Meters
0 500 1000 2000 3000
Feet
0 2000 4000 8000 12000
Map projection: Web Mercator Corner coordinates: WGS84 Edge tics: UTM Zone 18N WGS84

MAP LEGEND

Area of Interest (AOI)
- Area of Interest (AOI)

Soils
- Soil Map Unit Polygons
- Soil Map Unit Lines
- Soil Map Unit Points

Special Point Features
- Blowout
- Borrow Pit
- Clay Spot
- Closed Depression
- Gravel Pit
- Gravelly Spot
- Landfill
- Lava Flow
- Marsh or swamp
- Mine or Quarry
- Miscellaneous Water
- Perennial Water
- Rock Outcrop
- Saline Spot
- Sandy Spot
- Severely Eroded Spot
- Sinkhole
- Slide or Slip
- Sodic Spot
- Spoil Area
- Stony Spot
- Very Stony Spot
- Wet Spot
- Other
- Special Line Features

Water Features
- Streams and Canals

Transportation
- Rails
- Interstate Highways
- US Routes
- Major Roads
- Local Roads

Background
- Aerial Photography

MAP INFORMATION

The soil surveys that comprise your AOI were mapped at 1:24,000.

Please rely on the bar scale on each map sheet for map measurements.

Source of Map: Natural Resources Conservation Service
Web Soil Survey URL:
Coordinate System: Web Mercator (EPSG:3857)

Maps from the Web Soil Survey are based on the Web Mercator projection, which preserves direction and shape but distorts distance and area. A projection that preserves area, such as the Albers equal-area conic projection, should be used if more accurate calculations of distance or area are required.

This product is generated from the USDA-NRCS certified data as of the version date(s) listed below.

Soil Survey Area: Nassau County, New York
Survey Area Data: Version 15, Sep 3, 2018

Soil map units are labeled (as space allows) for map scales 1:50,000 or larger.

Date(s) aerial images were photographed: Dec 31, 2009—Oct 5, 2016

The orthophoto or other base map on which the soil lines were compiled and digitized probably differs from the background imagery displayed on these maps. As a result, some minor shifting of map unit boundaries may be evident.

E.3 Soil composition, land settings and zone properties

MU Symbol	Map Unit (MU) Name	Soil Components (%)		Land Form	Parent Material	Slope (%)
		Map Soil	Minor Soil			
At	Atsion loamy sand	90	10	Depressions	Sandy marine	0 – 2
PlB	Plymouth loamy sand	85	15	Outwash plains, Moraines	Acid Sandy glaciofuluvial/delatic	3 – 8
RdB	Riverhead sandy loam	90	10	Moraines, outwash plains	Loamy glaciofluvial overlying stratified sand and gravel	3 – 8
Su	Sudbury sandy loam	80	20	Outwash plains	Sandy and gravelly glaciofluvial	0 – 3
UdA	Udipsamments	90	10	-	-	0 – 8
Ue	Udipsamments, wet substratum	90	10	-	-	0 – 3
Ug	Urban land	90	10	-	-	-
Uh	Urban land-Hempstead complex	75, 20	5	Outwash plains	A silty mantle over highly siliceous stratified sandy and gravelly glaciofluvial	0 – 3
UpA	Urban land-Plymouth complex	65, 20	15	Moraines, outwash plains	Acid Sandy glaciofuluvial/delatic	0 – 3
UpB	Urban land-Plymouth complex	65, 20	15	Moraines, outwash plains	Acid Sandy glaciofuluvial/delatic	3 – 8
UrA	Urban land-Riverhead complex	65, 20	15	Moraines, outwash plains	Loamy glaciofluvial overlying stratified sand and gravel	0 – 3
UrB	Urban land-Riverhead complex	65, 20	15	Moraines, outwash plains	Loamy glaciofluvial overlying stratified sand and gravel	3 – 8
Us	Urban land-Sudbury complex	70, 20	10	Outwash plains	Sandy and gravelly glaciofluvial derived mainly from crystalline rock	0 – 3
Uu	Urban land-Udipsamments	70, 25	5	-	-	0 – 3
Uw	Urban land-Udipsamments	70, 25	5	-	-	0 – 3
W	Water	100	0	-	-	-

Abstract-TH-2793_156104035

E.4 Soil profile, properties and qualities

MU Symbol	Map Unit (MU) Name	Typical Profile *(in)*					Natural Drainage	Ksat *(in/hr)*	water table *(in)*	Soil Group
		Oa, Oi	H1	H2	H3	H4				
At	Atsion loamy sand	0 – 2, highly decomposed plant material	2 – 7, loamy sand	7 – 36, loamy sand	36 – 60, coarse sand	-	Poorly drained	0.2 – 5.95	0 – 12	A/D
PIB	Plymouth loamy sand	0 – 2, slightly decomposed plant material	2 – 7, loamy sand	7 – 28, loamy sand	28 – 60, gravelly coarse sand	-	Excessively drained	0.2 – 5.95	> 80	A
RdB	Riverhead sandy loam	0 – 1, slightly decomposed plant material	1 – 4, sandy loam	4 – 25, sandy loam	25 – 36, loamy sand	36 – 60, Stratified gravelly sand	Well drained	0.2 – 5.95	> 80	A
Su	Sudbury sandy loam	-	0 – 5, sandy loam	5 – 18, sandy loam	18 – 28, gravelly loamy sand	28 – 60, Stratified gravelly sand	Moderately well drained	1.98 – 5.95	18 - 36	B
UdA	Udipsamments	-	0 – 72, coarse sand	-	-	-	Somewhat excessively drained	19.98	> 80	A
Ue	Udipsamments, wet substratum	-	0 – 72, coarse sand	-	-	-	Moderately well drained	19.98	> 80	A
Ug	Urban land	-	-	-	-	-	-	-	-	-
Uh	Urban land-Hempstead complex	-	0 – 11, silt loam	11 – 29, silt loam	19 – 33, very gravelly	33 – 60, Stratified	Well drained	0.57 – 1.98	> 80	-

Abstract-TH-2793_156104035

					loamy sand	gravelly sand				
UpA	Urban land-Plymouth complex	0 – 2, slightly decomposed plant material	2 – 7, loamy sand	7 – 28, loamy sand	28 – 60, gravelly coarse sand	-	Excessively drained	0.2 – 5.95	> 80	-
UpB	Urban land-Plymouth complex	0 – 2, slightly decomposed plant material	2 – 7, loamy sand	7 – 28, loamy sand	28 – 60, gravelly coarse sand	-	Excessively drained	0.2 – 5.95	> 80	-
UrA	Urban land-Riverhead complex	0 – 1, slightly decomposed plant mat.	1 – 4, sandy loam	4 – 25, sandy loam	25 – 36, loamy sand	36 – 60, Stratified gravelly sand	Well drained	0.2 – 5.95	> 80	-
UrB	Urban land-Riverhead complex	0 – 1, slightly decomposed plant mat.	1 – 4, sandy loam	4 – 25, sandy loam	25 – 36, loamy sand	36 – 60, Stratified gravelly sand	Well drained	0.2 – 5.95	> 80	-
Us	Urban land-Sudbury complex	-	0 – 5, sandy loam	5 – 18, sandy loam	18 – 28, gravelly loamy sand	28 – 60, Stratified gravelly sand	Moderately well drained	1.98 – 5.95	18 - 36	-
Uu	Urban land-Udipsamments	-	0 – 72, coarse sand	-	-	-	Somewhat excessively drained	19.98	> 80	-
Uw	Urban land-Udipsamments	-	0 – 72, coarse sand	-	-	-	Somewhat excessively drained	19.98	> 80	-
W	Water	-	-	-	-	-	-	-	-	-

Abstract-TH-2793_156104035

This Page Intentionally Left Blank

Abstract-TH-2793_156104035

PUBLICATIONS

Journals

- Akkimi, A., & Dutta, S. (2021). Suitable DEM Assessment Study for Data Scarce Cities Towards Urban Extreme and Nuisance Flood Mapping. ISPRS Annals of the Photogrammetry, Remote Sensing and Spatial Information Sciences, 4, 161-168.

- Akkimi, A., Dutta, S., & Ray, K. Hierarchical Supervised Machine Learning based Stochastic Generation and Prediction of High Intensity Rainfall Hyetograph (*Submitted*).

- Akkimi, A., & Dutta, S. Assessment Framework to Select Open-Source Global DEMs for Urban Flooding (*Submitted*).

- Akkimi, A., & Dutta, S. Diagnostic Analysis of SWMM Model Sensitivity with Different Open-Source Global DEMs (*to be submitted*).

- Akkimi, A., Dutta, S., & Ray, K. Gravity – Turbulence Spectral Width Thresholds based Radar Reflectivity Rainfall Rate Relationship Establishment (*In preparation*).

- Akkimi, A., & Dutta, S. Physically based Urban Runoff Accounting Hydrological Modeling Framework to Forecast Flash Floods Over Heterogeneous Urban Landscapes (*In preparation*).

Conferences

International

- Akkimi, A., Dutta, S., & Ray, K. (2021). "A Physical-based Distributed Urban Hydrological Model (PURAHM) Integrated with Weather RADAR Rainfall to Assess the Influence of Climatic and Anthropogenic Stressors on Urban Flood Patterns". **AGU Fall Meeting**, **New Orleans**, USA.

- Akkimi, A., Dutta, S., & Ray, K. (2019). "Flash Flood Generated Short Term Precipitation Forecast System in Heterogeneous Urban Landscape using Weather RADAR". **AGU Fall Meeting**, **San Francisco**, USA, 101st Edition, A53L-3067. https://ui.adsabs.harvard.edu/abs/2019AGUFM.A53L3067A

- Akkimi, A., Dutta, S., & Ray, K. (2019). "Establishing Radar Reflectivity - Rainfall Rate Relationship in terms of Spectral Width thresholds". **39th International Conference on Radar Meteorology** (ICRM), NARA, **JAPAN**. https://cscenter.co.jp/icrm2019/program/data/abstracts/Poster3-96.pdf

- Akkimi, A., & Dutta, S. (2019). "Evaluation of Satellite DEMs on Selected Urban Settings: Comparison with high resolution data for Urban Flood Inundation Modelling". 16th Asia Oceania Geosciences Society (**AOGS**) meeting, **SINGAPORE**. HS13-A025. https://www.asiaoceania.org/aogs2019/public.asp?page=browse_abstract.htm

- Akkimi, A., Dutta, S., & Ray, K. (2019). "Short term Precipitation Forecast System in Heterogeneous Urban Landscape in Delhi City using Weather Radar". Asian Precipitation Experiments (**AsiaPEX**) Kickoff Conference, SAPARRO, **JAPAN**. http://rfweb.ed.kagawau.ac.jp/dav/asiapex_abstract/Poster2/05_P2_043_2_JapnApex_Precipitation_nowcat_abstract_final.pdf

- Akkimi, A., Ray, K., & Dutta, S. (2017). "Hydrological Model Development for Urban Flash Flood Early Warning System Using Weather Radar and TRMM Products as Input". 14th Asia Oceania Geosciences Society (**AOGS**) meeting, **SINGAPORE**. HS14-A016. https://www.meetmatt-svr3.net/aogs/aogs2017/ mars2/pubViewAbs.asp

National

- Akkimi, A., Dutta, S., & Ray, K. (2020). "Generation of Synthetic Weather Radar Reflectivity Hyetograph to Nowcast High Intensity Rainfall in Urban Landscape". ISRS - ISG National Symposium, Space Application Centre, Ahmedabad, INDIA.

- Akkimi, A., Dutta, S., & Ray, K. (2019). "Nowcasting of Extreme Strom Hyetograph for Flash Flood Forecast in Urban Landscape using Doppler Weather Radar", ISRS - ISG National Symposium, North East Space Application Centre, Shillong, INDIA.

- Akkimi, A., Ray, K., & Dutta, S. (2016). "Urban Flash Flood Early Warning System using Weather RADAR Input". ISRS - ISG National Symposium, Indian Institute of Remote Sensing, Dehradun, INDIA.

SPECIAL ACKNOWLEDGEMENTS

- India Meteorological Department (IMD) (RMC, New Delhi and IMD, New Delhi)
- Mr. B. A. M. Kannan and his team, India Meteorological Department, New Delhi
- Indian Institute of Sciences Bangalore (Prof. P. P. Mujumdar and Team)
- Indian Institute of Technology Delhi (Prof. A. K. Gosain, Dr. C. T. Dhanya, and team)
- Computation Hydraulic Institute (CHI) (Nandana Perara and Team)
- American Geophysical Union (AGU) – for AGU 2019 Travel grant
- American Meteorological Society (AMS) – for ICRM 2019 Travel grant
- United States Geological Survey (USGS), USA
    - Earth Explorer
    - National Map 3DEP
    - National Water Information
- National Aeronautics and Space Administration (NASA), USA
- Japan Aerospace Exploration Agency (JAXA), Japan
- Indian Space Research Organization (ISRO), India
- Grass-GIS Team
- National Oceanic Atmospheric Administration (NOAA), USA
    - Data Access Viewer
    - National Centers for Environmental Information (NCEI)
- National Agriculture Imagery Program (NAIP), USA
- United States Department of Agriculture Natural Resources Conservation Service, USA
- IOWA State University (IOWA Environmental Mesonet)
- Google Earth
- Google Chrome

Department of Civil Engineering
Indian Institute of Technology Guwahati



Abstract-TH-2793_156104035

© U.S. National Oceanic and Atmospheric Administration, Wikimedia Commons
(https://commons.wikimedia.org/wiki/File:Katrina-new-orleans-flooding3-2005.jpg)